HIGH-RESOLUTION 3D GEOCELLULAR FACIES AND PROPERTY MODELING OF BENTIU-1 RESERVOIR INTERVAL, JACK OILFIELD, FULA SUB-BASIN, SUDAN

BY

Mohammed Ali Hammad Jabir

A Thesis Presented to the
DEANSHIP OF GRADUATE STUDIES

KING FAHD UNIVERSITY OF PETROLEUM & MINERALS

DHAHRAN, SAUDI ARABIA

In Partial Fulfillment of the
Requirements for the Degree of

MASTER OF SCIENCE

In

GEOLOGY

June 2015

KING FAHD UNIVERSITY OF PETROLEUM & MINERALS

DHAHRAN- 31261, SAUDI ARABIA

DEANSHIP OF GRADUATE STUDIES

This thesis, written by **MOHAMMED ALI HAMMAD JABIR** under the direction of his thesis advisor and approved by his thesis committee, has been presented and accepted by the Dean of Graduate Studies, in partial fulfillment of the requirements for the degree of **MASTER OF SCIENCE IN GEOLOGY.**

Dr. Osman Abdullatif
(Advisor)

Dr. Ali Sahin
(Co-Advisor)

Dr. Gabor Korvin
(Member)

Dr. Mohammad Makkawi
(Member)

Dr. SanLinn Kaka
(Member)

Dr. Abdulaziz Al-Shaibani
Department Chairman

Dr. Salam A. Zummo
Dean of Graduate Studies

16/6/15
Date

To My Family

ACKNOWLEDGMENTS

Acknowledgments are due to King Fahd University of Petroleum and Minerals for giving me the opportunity to pursue my Master's degree and Ministry of Petroleum, Republic of Sudan for supporting me with the data and permission to publish this thesis.

I would like to express my sincere appreciation to my thesis advisors Dr. Osman Abdullatif and Dr. Ali Sahin for their guidance support and the critical review of this manuscript. Sincere gratitude is also due to the thesis committee members Prof. Gabor Korvin, Dr. Mohamad Makkawi, and Dr. Sanlinn Kaka for their continuous guidance throughout my study at KFUPM and their excellent advice and comments during my thesis writing.

Gratitude and appreciation are due to the chairman of Earth Sciences Department Dr. Abdulaziz Al Shaibani and the faculty, staff, and colleagues of the department for their support and encouragement.

Words of thanks are due to Mr. Abdullbagi Awad and Mr. Ali Mahmoud for their technical and professional support. Thanks are also expressed to the Sudanese community at King Fahd University of Petroleum and Minerals.

At last, a sincere gratitude to my family and friends in Sudan for their continuous support and encouragements during the period of my study.

TABLE OF CONTENTS

LIST OF TABLES

LIST OF FIGURES

ABSTRACT

Full Name : Mohammed Ali Hammad Jabir

Thesis Title : HIGH-RESOLUTION 3D GEOCELLULAR FACIES AND PROPERTY MODELING OF BENTIU-1 RESERVOIR INTERVAL, JACK OILFIELD, FULA SUB-BASIN, SUDAN.

Major Field : Geology

Date of Degree : June, 2015

The thick sandstone sequences of the Bentiu-1 Reservoir Interval represents the most prolific oil bearing zones in the northeastern part of the Muglad Rift Basin. However, the lithofacies heterogeneity coupled with rifting complex structural and stratigraphic settings have resulted in complex reservoir geometries and highly variable petrophysical properties. This study aimed to establish a 3-D stochastic geocellular model characterizing the lithofacies heterogeneity and major reservoir architectures that control the reservoir properties and consequent fluid flow pathways. A comprehensive lithofacies classification, petrophysical analyses, and stochastic modeling workflow were used to deliver the objective of this study. The lithofacies classification revealed the prevalence of thee distinctive lithofacies: sand, shaly-sand, and shale. The petrophysical analysis of the porosity, permeability and water saturation revealed that these properties occur over specific zones. These zones, in turn, were easily correlated with the lithofacies identified. Four locally fining upward lithological cycles have been observed from the 3-D stochastic simulation of the lithofacies. Each one of cycles dominated by sand at the bottom and capped with shale at the top. The 3-D stochastic models of the petrophysical properties have confirmed the results of the lithofacies modeling. Four petrophysical units were firmly identified by the presence of three marker-beds. The marker beds were characterized by low porosity, low permeability and high water saturation corresponding to the shale situated at the top of each unit. The findings of this study provided a detailed structural, geological and petrophysical models for the Bentiu-1 reservoir Interval. These findings increase the current knowledge understanding and prediction of the reservoir geometries and reservoir potential in addition to providing a new insight into the petroleum exploration and future development of the study interval.

ملخص الدراسة

الاسم الكامل: محمد علي حماد جابر

عنوان الرسالة: النمزجة الدقيقة ثلاثية الابعاد لسحنات وخصائص مكامن بانتيو-1، حقل الجيك، تحت حوض الفولة، السودان

التخصص: جيولوجيا

تاريخ الدرجة العلمية: يونيو 2015

تمثل تتابعات الحجر الرملي في عضو بانتيو-1 اهم النطاقات المحتوية على النفط في الجزء الشمالي الشرقي من حوض المجلد الاخدودي. حيث أنتج التباين السحني الناتج عن تاريخ تركيبي وتطبقي معقد، أنتج خصائص متعددة ومتغايرة للمكمن النفطية، هذه الدراسة تهدف الي انشاء نمازج ثلاثية الابعاد لوصف التباين السحني والمعالم الرئيسية التي تتحكم في خصائص المكامن وما يتبعها من سمات. لذلك، مخطط شامل لتصنيف السحنات الرسوبية، التحليل البتروفيزيائي، والنمزجة العشوائية استخدم لتحقيق اهداف هذه الدراسة. التصنيف السحني اظهر وجود ثلاث: حجر رملي، رمل طفلي وطفل. التحليل البتروفيزيائي للمسامية، النفاذية والتشبع بالماء اثبت ان هذه العناصر تتقسم في نطاقات محددة. هذه النطاقات بالمقابل يمكن بيسر ربطها بالسحنات التي تم تعريفها. تم تعريف أربع دورات صخرية تتميز بنعومة الي اعلي من خلال النمزجة العشوائية للسحنات الرسوبية. أي من هذه الدورات تتسم بسيادة حجر رملي في اسفلها ومغطاة بطفل في الأعلى. النماذج ثلاثية الابعاد للخصائص البتروفيزيائية اكدت نتائج نمزجه السحنات. حيث تم تعريف أربع وحدات بتروفيزيائية بوجود ثلاث طبقات معرفة. هذه الطبقات المعرفة تتسم بمسمية ونفاذية منخفضتين وتشبع عالي بالماء حيث تم ربطها بالطفل المتواجد في اعلي كل وحدة صخرية. نتائج هذه الدراسة توفر نمازج مفصلة عن التراكيب، السحنات الرسوبية والخصائص البتروفيزيائية للمكامن المتواجدة بعضو بانتيو-1 والتي تزيد من معرفة و فهم و التنبؤ بخصائص وإمكانيات هذه المكامن. مما يساعد فى عمليات التنقيب و التطوير لهذا المكمن البترولى الهام.

CHAPTER 1

INTRODUCTION

1.1 Overview

Fula Sub-basin which comprises the oilfield under consideration represents the fault bounded northeastern depression of Muglad Rift Basin (Figure 1.1). The stratigraphy of Fula Sub-basin follows the same general stratigraphy identified throughout the Muglad Rift Basin, in which Abu Gabra Formation (Lower Cretaceous) represents the main source rock for the entire basin, Bentiu Formation (Albian-Cenomanian) contains the major reservoir intervals, and Aradeiba Formation (Senonian-Turonian) mudstone exhibit the regional cap rock for the underlying reservoir intervals (Figure 1.2).

The Albian-Cenomanian Bentiu Formation of predominant sandstone sequences were deposited during the first of three rifting phases (Figure 1.2). The accumulation of these thick sandstone sequences was due to the expansion of fluvial and floodplain environments related to the rifting and subsidence processes during the first phase (Schull (1988). These thick sequences (about 1500m in depo-center) were deposited in braided and meandering streams environment. The Bentiu Formation is subdivided into three main parts (Lower, Middle, and Upper); each part is characterized by distinct facies assemblage and different depositional patterns (Idriss, 2002 and Petroenergy E&P, 2006).

The main scope of this study is the modeling of the lithofacies and petrophysical properties of the Upper Member of Bentiu Formation which is termed as the Bentiu-1Reservoir Interval (Petroenergy E&P, 2006). The data for this study were acquired from the Jake-South Oilfield in the Northwestern part of the Fula Sub-Basin (Figure 1.1). This data consist of a 3-D cropped seismic cube of 20 km^2 covering the whole oilfield and data from 20 wells including well-logging data, core analysis reports, and cutting samples.

The hierarchical approach of geostatistics and the stochastic modeling workflow were used to generate high-resolution 3-D model of the lithofacies and associated petrophysical properties (porosity, permeability, and water saturation). The basic question about the necessity of stochastic modeling is addressed by Haldorsen and Damsleth (1990) where they listed the following points; (1) the incomplete information regarding the reservoirs (dimensions, internal architecture, rock property and their property at all scales), (2) complex spatial allocation of the reservoir building blocks or facies, (3) difficulty in capturing rock properties variability and the structure of the variability with spatial position, (4) the scale problem indicated by the unknown relationships between the property values and the overall value rock volume, (5) realistic abundance of the static data over the dynamic data, and (6) convenience and speed (difficulty and time consumption).

1.2 Study Area

The Muglad Basin represents one of the largest rift basins of interior Sudan with respect to smaller basins, such as Melut, White Nile, and Blue Nile Rift Basins (Figure 1.1a).

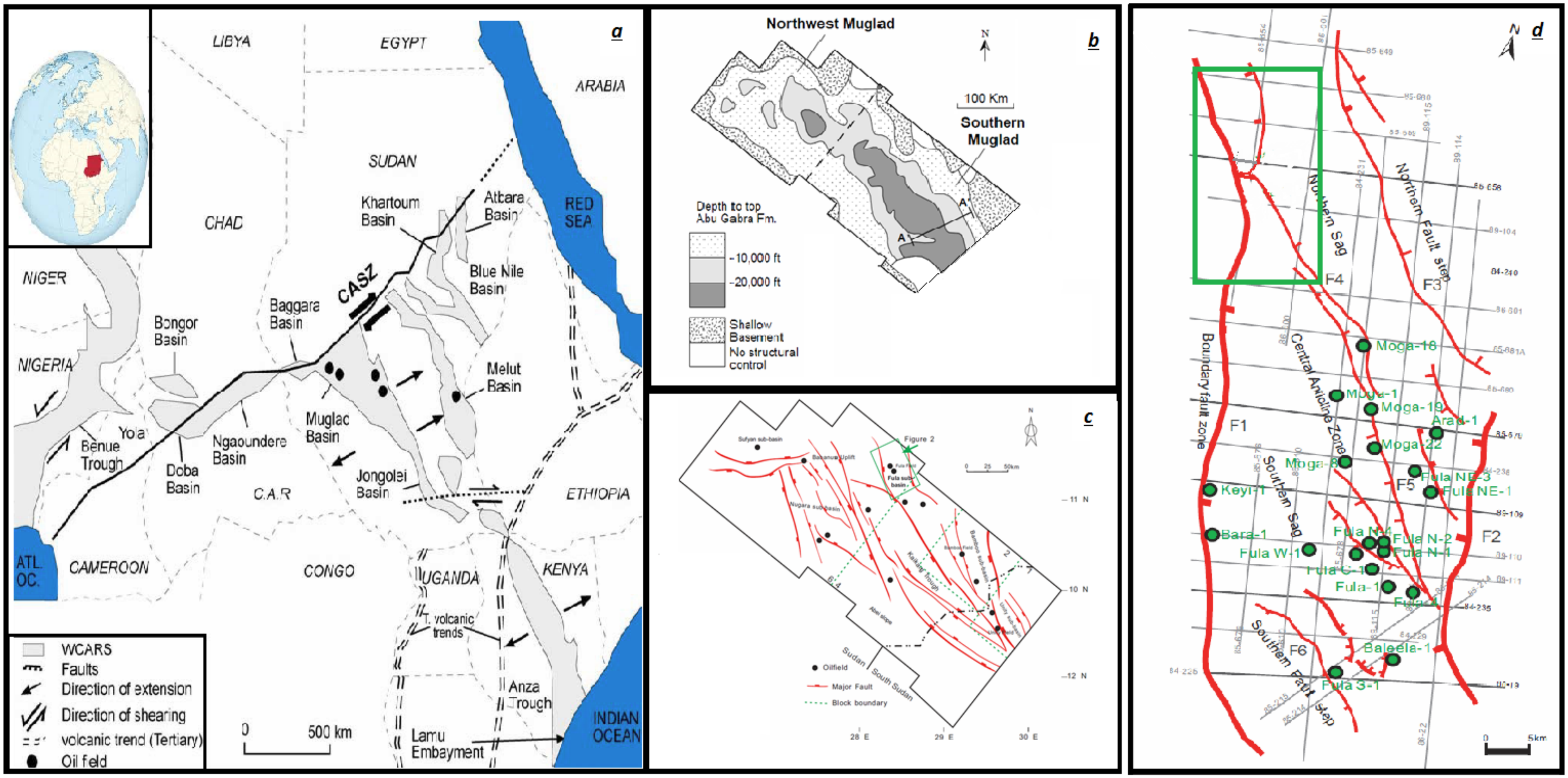

Figure 1.1 Illustrates; (a) the geographic location of Sudan interior rift basins in general and Muglad Basin in particular and the relation of the rift basins with CASZ (Fairhead, 1988), (b) simplified depth-structural map over the top of Abo Gabra Formation (Sch ull, 1988), (c) structural map of central and northern part of Muglad Basin illustrating the main structural units in this part of the basin and the location of Fula Sub-Basin in the Northeastern part of Muglad Basin (modified from Dou Lirong et al., 2013), (d) Fula Sub-Bain structural map illustrating the five structural zones (North Fault Zone, Northern Sub-depression, Central Faulted Uplift, Southern Sub-depression, and Southern Fault Zone) and the major bounding NW-SE trending faults (Dou Lirong et al., 2013)

The Basin extends from South Sudan Republic to the western and southern Kordofan State in southern-central Sudan (Hussein, 2012). The Muglad Bain, as the other rift basins of Sudan, represents one of a series of intra-cratonic rift basins that have formed following the Cretaceous splitting of the South American-African Pangaea and the Atlantic Ocean formation in the Early Cretaceous. This ocean was formed when a right-lateral-slip movement ruptures begin to develop across the center of Africa resulting in the Central African Shear Zone (CASZ). Consequently, a series of passive rift basins started to form due to CASZ to the south of its eastern margin (Giedt, 1990; and Mourlin et at., 2010). Towards the end of the Late Cretaceous, the Muglad Basin suffered from both compressional and slipping movements. The compressional structures were formed along the major basin boundaries and the slipping structures formed along the faults resulted from the CASZ. Eventually, three types of fault-bounded sub-basin were formed: reverse extinction and compressional fault-bounded sub-basins, constructed extensional slipping fault-bounded sub basins, and unconstructed extensional fault-bounded sub-basins (Yu et al., 2009).

Structurally, the Muglad Basin was subjected to three stages of structural evolution: pre-rifting, syn-rifting, and post-rifting. The whole block had been a stable craton during the pre-rifting stage in the Paleozoic and the Lower Mesozoic. While during the syn-rifting in the Early Cretaceous, the South America-African Pangea split apart to form the first extensional sub-basin in the Muglad Basin. Moreover, a second extensional fault-bounded sub-basin was formed towards the end of the Late Cretaceous following the opening of the Proto-Atlantic Ocean. The post rifting stage took place in the Cenozoic when a regional subsidence occurred and the original fault-bounded basin evolved into the extensional sag basin (Yamin and Qin, 2011). According to the tectonic evolution and the structural style in Muglad Basin, it can be subdivided into five sub-basins: Fula, Nugara, Bamboo, Abo-Sufyan and Unity sub-basins associated with the Babanousa Uplift, Kikang Trough, and Abyi slope (Figure 1.1c).

The fault-bounded Fula Sub-basin is located at the NE part of the Muglad Basin (Figure 1.1c and 1.1d). This sub-basin covers an area of 5000 km^2. The sub-basin is a north-south striking strip and structurally subdivided into five structural zones: Northern Fault Zone, Northern Sub-depression, Central Faulted Uplift, Southern Sub-depression, and Southern Fault Zone (Dou Lirong et al., 2013). The Sub-basin is characterized by N-NE striking structural belt and N-S structural rupture forming diagonally spreaded and structurally regular sub-basin (Dou Lirong et al., 2013).

The exploration activities in the Fula Sub-basin started at 1974 by the Chevron Overseas Inc. Although, oil patches have been encountered in Abo Gabra Formation, the field was abandoned. However, the renewed 1996 exploration program resulted in the discovery of eleven commercial and non-commercial oil fields (Arad, Moga, Fula, Keyi, Fula North, Fula South, Fula Northeast, Fula West, Jake , and Jake South) (Schull, 1988).

In Fula Sub-basin, the Lower cretaceous Abo Gabra Formation represents the major source rock, as it is the case for the entire Muglad Basin. While the Albian-Cenomanian Bentiu Formation contains a massive oil pool throughout the Sub-basin and the Senonian-Turonian, mudstone of Darfur Group represents a regional cap rock of the underlying Bentiu Reservoirs throughout the Muglad Basin (Figure 2.1).

The Albian-Cenomanian Bentiu Formation was only discovered in the subsurface and subdivided into three main parts. The Lower Bentiu, which lies directly on top of the clystones of Abo Gabra Formation (Figure 2.1). This member was deposited in moderately deep, mixed-load, high sinuosity streams. The Middle Bentiu, which reflects deposition in low sinuosity braided sand-bed dominated streams. The Upper Bentiu, which is also known as the Bentiu-1 consists mainly of gravel sandstone and sandstone facies. The Bentiu-1 facies assemblage along with distinct depositional pattern indicates deposition in outwash plain of low sinuosity braided shallow channel (Idriss, 2002). The Bentiu-1 is the main oil bearing interval in the study area. The thickness of this reservoirs interval ranges between 90 m and 250 m and contains over ten productive zones (Petroenergy E&P, 2006).

1.3 Problem Statment

The heterogeneity of the lithofacies coupled with the complex stratigraphic settings resulting from the rifting and subsidence processes and the variable depositional environments have led to a complex reservoirs geometries and highly variable petrophysical properties. These indicate that there is an obvious need for a detailed geological model for the reservoirs in the study area.

This geological model can provide an improved understanding of reservoir internal geometries, structural control, and inherent petrophysical properties. Although the Bentiu-1 is the most prolific reservoir interval in the Fula Sub-basin, no comprehensive geological and petrophysical assessment has been conducted to provide a basis for realistic oil recovery forecasts, future production plans, and decision-making. This study can provide such basis to fulfill various aspects with high-resolution and geologically sound realizations integrating various types of available data.

The value of this study emerges from the understanding that characterization of a reservoir internal geometries and associated petrophysical properties based on sparse well data and coarser low-resolution seismic data is a very questionable (Haldor and Demsleth, 1990). The geostatistical approach is capable of yielding realistic images of the reservoir. These “synthetic” images or models of reservoir can establish a corner stone in predicting the reservoir architecture, facies distribution, and properties distribution by considering the different stratigraphic envelopes and the structural framework.

1.4 Scope and Objectives

The main scope of this study is to establish a high-resolution 3-D geocellular model for the Bentiu-1 reservoir in the Jack-South oil field within the Fula Sub-basin located in the northwestern part of the Muglad Rift Basin. The main aim behind this model is to utilize the geostatistical approaches to incorporate the geological/petrophysical and geophysical data to delineate the lithological heterogeneities as well as the inherent petrophysical properties.

This generalized scope can be divided into a number of tasks that will ultimately lead to fulfill the main scope of this study;

- Establishing a comprehensive structural framework to determine the major reservoirs architectures and geometries in terms of faults and horizons.

- Building a 3-D litho-stratigraphic grid controlled by the previously established structural framework and populating this grid with lithofacies determined form the well-log interpretation, well report (core sample alternative), cutting samples, and previous studies.
- Building 3-D property models of the previously determined petrophysical parameters (porosity, permeability, and water saturation) based on well-log interpretation, and well reports.
- Mapping back the generated petrophysical models to the structurally controlled 3-D litho-stratigraphic model with lithofacies providing as geological constraints.
- Establishing the final high-resolution 3-D geocellular models for reservoir under consideration.
- Performing different realizations for the established models and quantifying the uncertainties of the simulation procedure and ranking the realizations.

1.5 Data and Methods

1.5.1 Data

The available data to fulfill the objectives of this study are listed as follows;

1. 3-D cropped seismic cube covering the Jack South Oilfield in Fula Sub-basin.
2. Well-logging information representing 20 wells drilled in the oilfield.
3. Selected cutting samples of the Bentiu-1 interval.
4. Core analysis and well completions reports, and master logs.

1.5.2 Methods

The methods adopted to fulfill the objective of this study can be outlined in three main sections as follows.

A. Structural Analysis

The main aim of the structural analysis is to produce the general framework of the reservoir in terms of faults (polygons, surfaces, and sticks) and the bounding surfaces (top and bottom horizons, and isochores). In this section, a 3-D structural model of the Bentiu-1 reservoir was established based on the interpretation of the 3-D seismic data integrated by the well data. This requires the identification of the regional horizons from the well logs, correlation between the wells, and calibrating the seismic data with the well data.

B. Facies Classification and Petrophysical Analysis

In this section, both lithofacies and petrophysical properties were determined. Firstly, the lithofacies within the reservoir interval were established to serve as a geological and stratigraphic constrains (envelopes) to the petrophysical properties during the stochastic modeling. The lithofacies were determined using a module implemented in the Interactive Petrophysics (IP) software called “cluster analysis”. This module helped in identification of electro-facies based on certain log integrations (Serra and Abbot 1980). The resulting electro-facies have been integrated with core description reports, lithology description from the master logs and previous studies within the vicinity of the study area. The later process was used mainly for the validation of the electro-facies generated.

Secondly, the petrophysical properties were derived from the well data, well completion report, and core analysis reports. First, the shale content was evaluated to remove the shale effect form the subsequent analysis of the porosity and water saturation. In this regard, Larinove (1969) equation for the older rocks (Eq. 3.3) was adopted for shale/clay volume determination. Next, the porosity values were determined from the density log, sonic log, neutron log, and density-neutron combination. The average porosity was taken for the modeling study after the integration of the core porosity to neglect the effect of washout in certain depths. The water saturation values were derived according to the Indonesia Equation (Eq. 3.17). Finally, the permeability values were calculated according a predefined relation between the porosity and permeability (Eq. 4.1) obtained from core analysis reports.

C. Geostatistics Approach

The previous information were analyzed and integrated in a progressive hierarchical approach as outlined in the following paragraphs:

I. Descriptive statistics

Statistical analyses of all the lithofacies data and petrophysical values were performed. The univariate statistics were used to describe the distribution of the data through parameters such as measures of the location, measures of the shape, and measures of the spread. Various plots such as histograms, PDF and CDF were generated to obtain the data distribution. The final step in this descriptive statistics was the testing of the normality of data providing information about the data transformation. Accordingly, the normal score transformations were applied to the porosity and water saturation values because of their deviation from the Gaussian behavior. The logarithmic transformation was applied to permeability data.

II. Estimation and Simulation

This step involved the following tasks:

a) Dividing the rock volume (reservoir) acquired earlier form the seismic 3-D interpretation and structural modeling into a cellular 3-D grid defined by the inline-crossline geometry in the horizontal scale and well logs resolution in the vertical scale.

b) Upscaling the well-derived properties to the 3-D grid scale by averaging process.

c) Modeling the spatial variability by means of experimental semivariograms in the three principal directions (two major direction and vertical direction).

d) Applying the ordinary kriging to estimate the values at unsampled locations.

e) Applying the sequential indicator simulation (SIS) to model the lithofacies defined earlier. In addition, the Sequential Gaussian Simulation was employed to model the petrophysical parameters within the individual lithofacies.

1.6 Previous Works and Studies

Over the past 50 years, many published and unpublished works and studies were conducted on the Muglad Basin. Prior to the works conducted by the Chevron Overseas Petroleum Inc. in the early 1970s, the general consent was that the area was a site of a shallow intra-cratonic sag basin where a few thousand meters of Quaternary, Tertiary, and Cretaceous were accumulated. This earlier thought was based on the scattered wells and sparse outcrop information (Mohammed and Mohammed, 2008). By the beginning of the year 1975, the Chevron Overseas started heavily to explore the previously unexplored interior basins of Sudan. These major exploration efforts resulted in several significant oil discoveries about eight years later. The major accumulations were recovered in the Heglig and the Unity oilfields (about 204-300 MBBl of recoverable oil reserves) from thick fluvial deposits known as the Bentiu Formation (Schull, 1988).

The availability of various types of data and continuous exploration efforts resulted in the emergence of extensive published studies by the early 1980s covering various aspects of the Muglad Basin. These include tectonic evolution, sedimentology, petroleum geology, paleontology, and reservoir characterization. These studies started with Browne and Fairhead work (1983) who studied the architecture of Abu Gabra Rift (currently known as the Muglad Basin) based on gravity data. This study outlined the major structural controls of the basin. In 1988, Thomas Schull, a geologist with the Chevron Overseas published one of the comprehensive and detailed studies about the rift basins of interior Sudan and the Muglad Basin in particular. His study is considered one of the main references on the Muglad Basin. He described the main geological keys of the exploration potential and categorized the tectonic evolution into three rift phases, each one ending with extensive sag phase. Moreover, Schull (1988) characterized the structural style of the basin within the context of extensional movement and productive versus unproductive basin wide structures. In the same year, Fairhead (1988) also illustrated the tectonic development and structural controls on the Muglad Basin. The same subject was tackled by later studies including McHargue and others (1992) and Guiraud and Maurin (1992). On the other hand, aspects such as thick skin and thin skin features, volcanic activities, tectono-stratigraphic studies were published by Mann (1989); Wycisk et al., (1992); and Willson and Guiraud (1992), respectively. Shandelmir (1993) proposed the concept of intra-cratonic mantle pluming process, in which he suggested that the rift basins of Sudan were formed due to plate divergence during the tectonic activity in the Proto-Indian Ocean and the resultant sea floor spreading.

All this previous studies have established the tectonic and structural framework of the Muglad Basin. By no coincidence, the later studies have tackled the stratigraphic, petroleum, and sedimentlogical aspects. Kaska (1989) studied the polymorphs assemblage of the basin, which resulted in subdivision of the fluvio-lacustrine deposits previously described by Schull (1988) into five bio-stratigraphic zones. Giedt (1990) described the geological aspects that resulted in the first oil discovery in the Unity Oilfield in the southern part of the Muglad Basin in a detailed atlas. Hewang and others (1994) discussed the role of geological and geochemical processes associated with varying oil compositions within the heterogeneous reservoirs in the Muglad Basin. Babiker (1993) and Ahmed (1994) focused on the sedimentological, paleoclimatic and tectonic evolution aspects of the basin. Abdullatif (1992) integrated the sedimentological, mineralogical, and geochemical approaches to address the evolution of the basin. Mohammed and other (1999) constructed a model for the burial and migration history of the basin in the Heglig Oilfield. Mohammed et al (2001) established a conceptual structural model to reveal the ambiguity about the crustal extension in the Unity-Kikang province in central Muglad Basin. Abdullatif (2002) discussed the role of burial digenesis and organic maturity in oil generation in the NW of Muglad Basin. Consequently, Idriss (2002) delineated the depositional environment and reservoirs heterogeneity of the Bentiu Formation, in which they classified the formation into upper, middle, and lower parts according to their distinctive facies assemblage and depositional patterns. Saida and Abdullatif (2002) described the reservoir quality of the Zarqa Formation in the Heglig and Unity oilfields. Idriss (2002) addressed the implication of faulting in oil escape from Aradeiba Formation as a significant part of a basin wide study. Mustafa and Tyson (2002) were able to analyze the source rock of the Muglad Basin using an integration of palynomorphs and organic geochemistry. The estimation of the hydrocarbon generation in the NW part of Muglad Basin was carried out by Mohammed and others (2002). Dou Lirong and others (2002) followed by Tong and others (2004) have discussed the petroleum geology and petroleum system of the Muglad Basin. These two studies have indicated that Abo Gabra Formation is the most significant and efficient source rock present in the area. This was based on comparison between the biomarkers characteristics and bulk parameters of oil and source rocks extractions. Idriss (2005) studied the Aradeiba and Bentiu plays as an integrated petroleum system. Trivedi and others (2005) illustrated the depth-porosity relationship in the Neem Oilfeild in the southern part of the basin. Dou Lirong and others (2006) studied the role and the implication of Aradeiba muds as a regional seal on the hydrocarbon entrapment in the Muglad Basin. Mohammed (2006) discussed the role of the reservoir modeling in siliciclastic multilayer reservoir such as the Bentiu sand in order to enhance the oil in place recovery in the Eltoor Oilfield in the southern part of the basin. Eltom (2007) in his master thesis addressed the sedimentological and sequence stratigraphic framework of the first rifting cycle (Abo Gabra and Bentiu formations), in which he characterized the depositional environment, associated lithofacies, and their stratigraphic sequence. He concluded by the delineation of four lithofacies types in the Bentiu Formation that were deposited in fluvial system, minor lacustrine, braided and meandering environments. Yamin and Qin (2011) utilized the petroleum system theory to study the Fula Sub-basin characteristics. This study revealed that the petroleum system in the Muglad Basin composed of the lacustrine mudstone facies of the Abo Gabra as an efficient and mature source rock, the fluvial sandstone facies of the Bentiu and the Upper Abo Gabra the prominent reservoir rocks and the mudstones of the Aradeiba Formation regional cap rock (Figure 2.1). Dou Lirong and others (2013) amended this study on their article about the petroleum geology of the Fula Sub-basin and they correlated the oil in the Bentiu and sandy part of Aradeiba formations to the Abo Gabra Formation despite the varying characteristics related to the migration and accumulation processes. Mohammed and Mohammed (2008) modified the stratigraphic column of the Muglad Basin illustrating the role of tectonic evolution. In their modified column, they pointed out the major lithofacies, formations maximum thicknesses, and oil producing horizons in the context of the evolution history. Hussein (2012) studied the sedimentary facies and their sequence stratigraphy in the Fula Sub-basin. Khairalla and Ibrahim (2012) used a multi-geophysical data to characterize the reservoir within the Shelingo Oilfield in the Muglad Basin, where they concluded that the basin-wide deposition of high-energy fluvial sandstone of the Bentiu Formation and Aradeiba Sandstone exhibit an excellent reservoir interval. Shauib (2013) in his master thesis integrated the petrophysical and seismic attributes to model the reservoir characteristics of the Aradeiba-D Member in the Muglad Basin.

CHAPTER 2

Geologic and Tectonostratigraphic Settings

2.1 Introduction

The rift basins of the southern and central Sudan represent one of the world's major rift systems, forming a part of continent wide linked intracratonic rift system that wonder across Central Africa. The Muglad Basin is the largest among them covering an area of about 120,000 km^2 and locally accounting for up to 13 km thick of the Mesozoic and Cenozoic sediments. Further to the northwest. This rift system appears to break against the Central African Shear Zone (CASZ) that extends form Chad through Cameron to Sudan (Figure 1.1a). On the contrary, the southeastern limit of the extensional systems is undefined (Fairhead, 1988). However, some authors speculated that the Muglad Basin might extend to the southeast and coalesce with the Anza Rift in Kenya (Figure 1.1a).

2.2 Tectonic Evolution

Thomas Schull (1988) described the evolutionary sequence of the Muglad Basin, which starts with a pre-rifting phase, followed by three rifting phases and a sag phase. These tectonic evolution periods were well documented by regional geology, geophysical surveys, and well data interpretation.

2.2.1 Pre-rifting Phase

Towards the end of the Pan-African orogeny (550 Ma ± 100 m.y.), the region has consolidated into a platform. The highlands of the platform supplied the subsiding surrounding areas with sediments during the Late Paleozoic and the Early Mesozoic times. The continental sediments near the Libyan-Chadian border in northwestern Sudan represent the nearest preserved Paleozoic records. Schull (1988) also suggested that the absence of rock fragments in the rift sediments implies the insignificance of the sedimentary succession prior to the rifting in the early-consolidated platform.

2.2.2 Rifting Phase

According to Browne and Fairhead (1983), the isostatic subsidence mechanism inferred in the Muglad Basin was provided by three prominent rifting periods as a resultant of the crustal extension. The crustal extension resulting from the parallel to subparallel (to the basin margins) normal faults have aided the subsidence. In the deepest part of the basin, the Neocomian-Barramian lacustrine claystone and siltstones have been deposited. A thick pile of older sediments (undated) has been detected away from deep-seated wells. Another claystone, siltstone, and halite deposits of a probable Jurassic age were encountered in the northern Blue Nile block.

In the light of the available yet dispersed penetrations, it was believed that the Jurassic-Early Cretaceous period probably is the starting point of rifting initiation (Schull, 1988). Both seismic and well control data have proved that the initial (which was the strongest) rifting phase took place until the end of the Albian time. There was no volcanic activity during this phase. The deposition of basin wide thick sandstone deposits of the Bentiu Formation mark graphically the termination of the initial rifting phase.

The Turonian-Late Senonian time witnessed the triggering of the second rifting phase, which resulted in the deposition of basin wide floodplain and lacustrine siltstones and clystones. This phase represents an abrupt termination of the sandstone deposition making up the Bentiu Formation. On the contrary to first rifting phase, this phase was accompanied by minor volcanic activity. Moreover, the well information acquired from the northwest Muglad Basin indicated presence of 91-meter thick dolerite sill dated to 82 Ma ± 8 m.y. Moreover, the Senonian andesite tuff encountered in the adjacent Melut Basin is approximately (90 Ma) in age. This date is cited as one of two igneous activity periods in central and northern Sudan (Vail, 1978). The deposition of progressively sand-rich sequence terminated by thick sandstones of the Amal Formation marked the end of this rifting phase.

The third and final rifting phase initiated towards the Late Eocene-Oligocene and reflected in a thick sequence of floodplain and lacustrine siltstones and claystones. Whereas the volcanic evidence was absent in the Muglad Basin, the occurrence of a thin Late Eocene basalt flow in the southern Melut Basin near the Ethiopian border represents the sole evidence of the volcanism in this rifting phase (Vail, 1978). Throughout the Late Oligocene-Miocene after this rifting period the deposition changed into more sand-rich sediments.

2.2.3 Sag Phase

In the middle of Miocene, the Muglad Basin was subjected to a very gentle intracratonic sagging phase, which is associated with minor or no faulting. Restricted volcanic rock outcrops in the southeastern Muglad Basin were dated at 5.6 Ma ± 0.6 m.y. and 2.7 Ma ± 0.8 m.y. (Browne and Fairhead, 1985).

2.3 Stratigraphic Units of Muglad Basin

2.3.1 Precambrian Basement Complex

The term “Basement Complex” is widely used to describe all crystalline Precambrian rocks found in the Sudan (Vail 1978). This complex crops out in the Northeastern, northwestern, and southeastern margins of the Muglad Basin. In northeastern part and in Nuba Mountains the Basement Complex consists of granites, granodiorites, gneisses, mica-schists, meta-volcanics and gabbroic rocks. In the southwestern margins (equatorial province), the complex consists of various types of gneisses, amphibolites, graphitic schists and marbles (Vail 1978). While in the northwestern margins (Darfur province), it consists of gneisses, and quartzites (Vial 1988). In the subsurface, basement of granodioritic genesis of Cambrians age (540 Ma ± 40 m.y.) has been recorded (Schull 1988).

2.3.2 Cretaceous Units

The Cretaceous succession in the Muglad basin contain mainly three formations; the Neocomian-Barremian Sharaf Formation, the Aptian-Early Albian Abu Gabra Formation, the Albian-Ceneomenian Bentiu Formation, and the Turonian-Late Senonian Darfur Group (Figure 2.1).

The Sharaf Formation consists predominantly of organic reach shales, siltstones and fine-grained sandstones. This formation is grading into a coarser sequence towards the margins of Muglad Basin where the amount of shale is substantially reduced. The depositional environment of the Sharaf Formation was fluvial-floodplain and lacustrine environment (Schull, 1988).

The Aptian-Early Albian Abu Gabra Formation (Figure 2.1) represents a deposition in a massive lacustrine development period, indicating a deposition in a probably humid climate and external drainage lacking (sealed basin). Several thousand meters of lacustrine shales and organic rich claystones were deposited. They are interbeded by silts and fine-grained sands based on the information from the majority of wells penetrated in the northwestern part of the Muglad Basin.

The Albian-Cenomanian Bentiu Formation (Figure 2.1) represents a deposition of a predominantly thick sandstone sequences. This formation consists of sandstones interbedded with shaly mudstones and siltstones thinner beds. The maximum thickness of the Bentiu formation is about 5000 feet that show good reservoir qualities. Polynological studies of Kaska (1989) proved the presence of abundant miospores and freshwater algae, which suggest that the Bentiu formation is predominantly deposited in braided meandering streams with restricted lacustrine pulses.

The Turonian-Late Senonian Darfur Group (Figure 2.1) is the name suggested by the Chevron Inc. to include both the differentiated and undifferentiated Turanian- Senonian strata in the SE and NW parts of the Muglad Basin, respectively. This period is characterized by a deposition of fine to coarse-grained sediments. The Aradeiba and the

Zarqa Formations represent the lower part of the group. These formations are characterized by predominance of claystones, siltstones, and shales. The excellent basin wide correlation of these two formations indicates the major impact of tectonic on the sedimentation, where the lacustrine and floodplain deposits were widespread and the deposition in shallow, well-oxygenated water was inferred from the low organic contents in these sediments. These two formations may represent a period of partial sealing of the basin. Throughout the Muglad Basin, the lower part of Darfur Group provides an important seal rock.

The Cretaceous time was concluded by a deposition of increasingly coarser-grained sediments, representing higher sand percentage in the Gazal and the Baraka Formation (Figure 2.1). They were deposited in a sand-rich alluvial and fluvial fan environments that prograded from the basin flanks.

2.3.3 Tertiary Units

The Tertiary sediments are formally known as the Kordofan Group (Figure 2.1). Form bottom to top this group consists of Amal, Nayil, Adok and Zeraf Formation. These units are undistinguishable from the Pleistocene-Holocene overlying alluvium sediments. No exact date had been given to these deposits due to the few fossils retrieved from the succession. A thick secession of the Tertiary sediments has been penetrated in the subsurface (Figure 2.1). The subsurface Tertiary strata starts with a deposition of a medium to coarse-grained clastics, overlaid by a sole cycle of fine to coarse-grained sediments marking the final rifting phase.

The thick sandstone pile of Paleocene Amal Formation (Figure 2) reaching up to 762 meter are mainly composed of coarse to medium-grained quartz arenites. This Formation represents a deposition in a high energy in an extensive basin wide alluvial-plain environment associated with braided streams and alluvial fans. The Amal Formation sandstones represent a potential good reservoir.

The Middle and Upper Kordofan Group sediments represent a coarsening-upward dispositional sequence covering the Eocene-Middle Miocene time. Nyile and Tendi Formation at the lower part are characterized by fine-grained sediments, which represent an extensive lacustrine and fluvial-floodplain environment. The lacustrine sediments of these units are known to have only minor source potential. However, they make up an excellent seal for the underneath sandstones of Amal Formation.

The Upper Kordofan Group is generally characterized by the interbeded claystone and sandstone with increasing sand content. This reflects a deposition of the Adok and the Zaraf formationsin a fluvial-floodplain and restricted lacustrine environment (Vail, 1978).

2.4 Stratigraphic History of the Rifting

The Muglad Basin has experienced three major extensional tectonic episodes. The early episode occurred approximately 140 to 95 Ma. in the Early Cretaceous. A second episode took place in Late Cretaceous approximately between 95-65 Ma. While the last rifting episode about 65-30 Ma in the Paleogene. The identification of three depositional cycles,

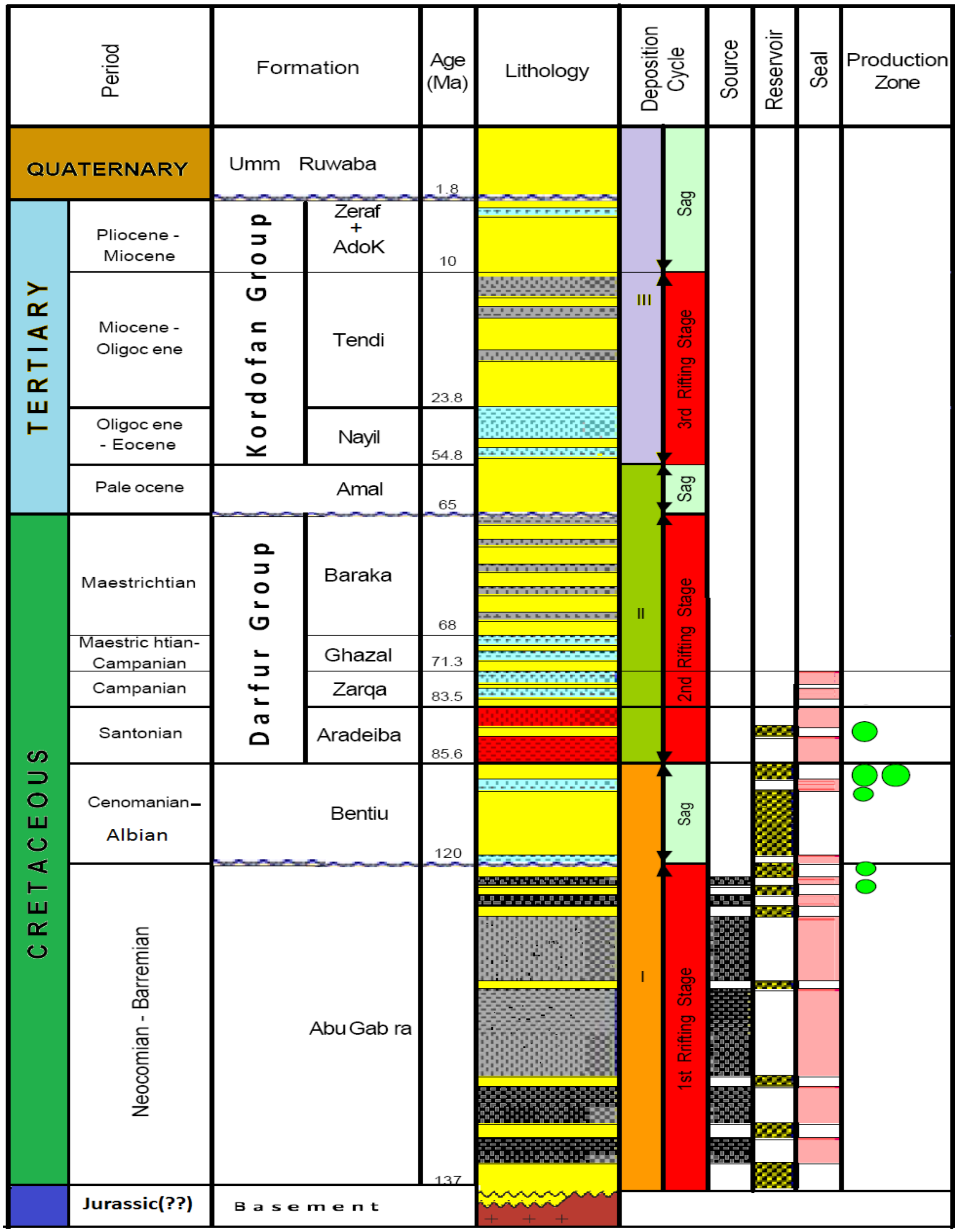

Figure 2.1 Generalized stratigraphic column of Fula Sub-Basin illustrating the formations, rifting cycles, and the petroleum system (Modified from Schull, 1988; Yamin and Qin 2011; and Dou Lirong et al., 2013).

which are regionally correlative, is the basis for the three separate rifting episode recognition. These depositional cycles which are of explicit existence in the Muglad Basin are indicated locally by delicate angular unconformity surfaces (McHargue et al., 1992).

Stratigraphically, each rift correlated depositional cycle starts about near the margins of the rift with basal sand overlaid by a shale-dominated interval, which reflects basin deepening. Each of these shaly intervals occurs as a base of coarsening upwards section grading from lacustrine shale into fluvial and lacustrine sandstone and mudstone when fully developed.

Each of these shaly intervals occurs as a base of coarsening upwards section grading from lacustrine shale into fluvial and lacustrine sandstone and mudstone when fully developed.

The later, in turn, is capped with the fluvial sandstones that are regionally extensive. The sediments of the three rifting episodes in the Muglad Basin attain a thickness of about 5400, 4200 and 5400 meters, respectively. After the Oligocene time only sand dominated sediments of about 750 meters were deposited in the basin.

The Muglad Basin stratigraphic succession represents a good example relating sedimentation to the contemporaneous tectonism. The stratigraphy can be seen as a result of rhythmic high sediment influx rate into depressions during episodes of cyclic alteration and subsidence patterns. The lithofacies association can be interpreted in light of different subsidence rate for various sub-basins. When subsidence was enormous during time of active rifting, shale-dominated sediments were deposited. While during time of low subsidence most likely during thermal sag phases, sand dominated sequence accumulated (Figure 2.2).

Throughout each tectonic cycle, a broad area reflects an influence of the initial subsidence, although the subsidence rate was slow. This pattern may explain the existence of regional unconformity overlaid by the basal sand-dominated unit. This unit is sandiest at the margins of the rift and often shaly towards the depo-center. The first depositional cycle (sand unit) have been penetrated only at the rift (Basin) margins, hence the geographic representation of this unit remains uncertain. On the contrary, the basal sand unit of the second depositional cycle (Upper Bentiu), and the third depositional cycle (Upper Amal) interfingers towards the axis of the rift with suspended-load fluvial and shaly lacustrine accumulations. This modality is thought to be applicable for the sand unit of the first depositional cycle.

Following the accumulation of few hundred meters of the sand-dominated basal unit by the initial extension the phase of active rifting initiated. This initiation is marked by a rapid subsidence of the hanging wall close to the main sub-basin boundary-faults. During this rifting phase, the topographic relief postulated to be at maximum while the sediment accumulation rate was high, yet unable to keep pace with the rapid fault-activated subsidence. At that time, the basin was characterized by close/sluggish drainage system linking a series of swaps and lakes. Each fault-bounded sub-basin behaved as a trap for the sediment where a thick shale-dominated section has been developed. Periods and areas of rapid subsidence were dominated by shales, either due to the sediments accumulation in long-lived outspread lakes or due to rapid descending of the deposited sediments beneath the erosional base and quick burial. In both cases, sediments were suffered a little and/or winnowing after accumulation and the predominant shaly composition indicated the introduction of mostly fine clastics into the basin.

Each of the three tectonic phases witnessed incoming coarse clastics form outside of the basin. This is supported by the presence of thick sandstone accumulations along the margins of the rift and their insignificance among the sediments accumulated near the intra-basinal highs during the main tectonic phases. The syn-rift sediments of the first tectonic cycle (Sharaf and Abo Gabra Formations) were associated with the extensive lacustrine shale (Figure 2.2) where the water of these lacustrine were stratified enough to prevent the accumulation and subsequent preservation of organic reach kerogen shales representing the source rock of the oil in the Muglad basin (Schull, 1988). The second tectonic cycle syn-rift deposits (Lower Darfour Group) and the third tectonic syn-rift deposits (Nayil and Tendi Formations) again comprised mostly of lacustrine shales and fluvial overbank deposits. These shales do not represent petroleum sources where they have been penetrated, while the sand deposited within these sequences represent premium reservoirs in the southern parts of the Muglad Basin.

Towards the end of each tectonic cycle, the subsidence was altered gradually by a relatively slower rate of thermal down-warping basin-wide. The sediment influx during this stage took over the sub-basinal topography. Hence, the slow rate of subsidence allowed the continuous reworking by the bedload streams, which penetrates the mud transported downstream outside the basin by the drainage system. The rest of the sediments were preserved as sheets of amalgamated fluvial sand throughout the whole basin (Lower Bentiu, Lower Amal, and Adok Formation).

The distribution and thicknesses of sediments accumulated during each rifting phase of each tectonic cycle indicate that more influence of subsidence can be observed during first tectonic rifting cycle than other cycles. Similar to the subsidence related to the tectonic rifting, the thermal rifting through the sag phase following the first tectonic cycle was greater than the other subsequent two cycles. Moreover, the thermal sag subsidence was positioned above the proceeding subsidence of the below rifting phase for each tectonic cycle.

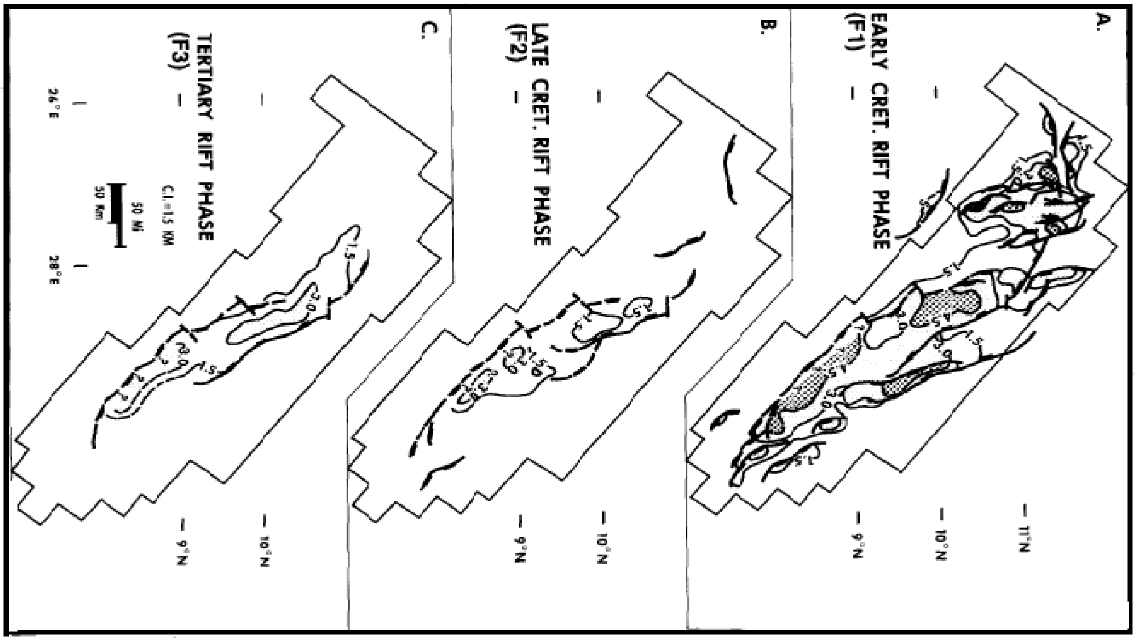

Figure 2.2 Isopach maps of the strata accumulated as a result of sagging phases that follows each of the three tectonic rift cycles in Muglad Basin. A Bentiu Fomation, B. Amal Formation, and C. Adok and Zeraf Formation. (Mchargue et al., 1992).

2.5 Structural Framework

Sudan interior rift basins composed of complicated systems of crustal extension and transtentionl sub-basins. These sub-basins are typically characterized by sub-graben geometries, which were modified by subsequent reactivation during younger rift cycles. The asymmetry of initial half-graben was reserved by opposed younger superimposed graben. Moreover, the thick-skinned detachment fault across the syn-tectonic sediment rift introduced additional complications to the final structural geometry (Mann, 1989). The extension of the upper crust by simple shear is believed to have involved development of planer and listric faults (domino and rigid body rotation) (McHaurge et al., 1992).

The variety in fault types have played major role in the development of Sudan interior basins structurally. The dominant structural controls in the Muglad Basin are the dip-slip normal faults. The long complex history of horst and graben development and formation of complicated fault systems are the main result of the three rift phases. These predominant rifting-resulted faults are oriented parallel or sub-parallel to the basin margins (Figure 2.3). The complicated fault system in the Muglad Basin exhibits a wide range in geometry displacement and growth history. The complex history of extension resulted in prominent productive and prospective structures, which were categorized to: rotated fault blocks, reverse and drape folds. The rotated fault blocks represent the common and important traps across the basin. The drape folds were formed in the upthrow side of the deep-seated normal faults. They have been found in areas where the faults were formed during the early rifting phase. In some areas, a downthrown rollover anticlines were formed as result of rotation along listric faults (Figure 2.3) (Shull, 1988).

2.6 Petroleum System

The Abo Gabra Formation represents the active/proven source rock consisting of a 2000 meter thick dark claystones and mudstones with high organic matter content. In the depocenter of the Muglad Basin as well as the Fula Sub-basin, the burial depth of this formation exceeds 5000 meters with maximum R_o exceeding 1.3 %, which indicates mature to post mature source rock. There are mainly two sets of effective reservoir intervals within the basin. The first interval lies within the Abo Gabra Formation.

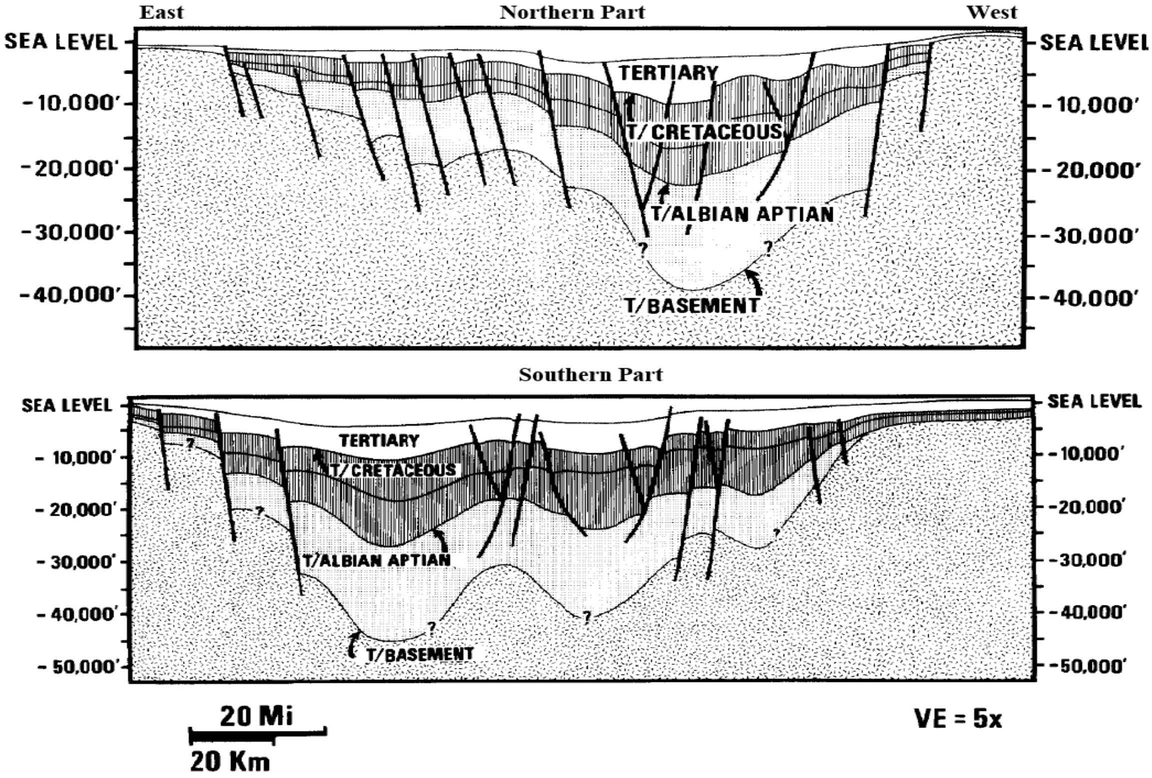

Figure 2.3 A structural profile across the northern and southern part of Muglad basin (Shull, 1988).

This interval represents a deltaic facies that are well developed making up to 43 % of the entire sequence with 2 to 8 meters thick individual beds with maximum thickness of up to 15 meter. The porosity of these reservoir zones ranges from 10 to 28 % while the permeability values ranges from 2.325 mD up to 3 Darcie's. The second reservoir interval lies within the Bentiu Formation, which is thick blocky sandstone sequence of fluvial facies. The individual beds of this reservoir ranges from 8 to 10 meter in thickness, while the porosity values range from 20 to 35 %, and a permeability values about 100 mD to 5

Darcy. This formation represents the main reservoir zone throughout the Basin (Yamin and Qin, 2011).

Two sets of basin wide cap rocks have been identified in the basin. The first one is the mudstone and lacustrine shale of the Abo Gabra Formation with individual beds of over 100 meters thick. The second set is the claystone and mudstone of lower part of Darfur group with a maximum thickness of over 1200 meters. The latter extensively overlies the reservoir zones within the Bentiu Formation throughout the Bain (Dou et al., 2006) (Figure 2.4).

The burial history (Figure 2.5) of the Fula Sub-Basin as an analogous for the Muglad Basin revealed that the source sediments within the Abo Gabra Formation started to deposition about 135 Ma ago and that the hydrocarbon generation was initiated 25 Ma later. From geological point of view, the migration and the accumulation of the hydrocarbons occurred over a short span of time nearly 90 Ma. The main reservoir bearing formation (Bentiu Formation) was deposited from 97 to 110 Ma, whereas the regional cap rock within the Lower Darfur Group deposited around 97 to 90 Ma (Tarken and Ferwin, 2000) ago.

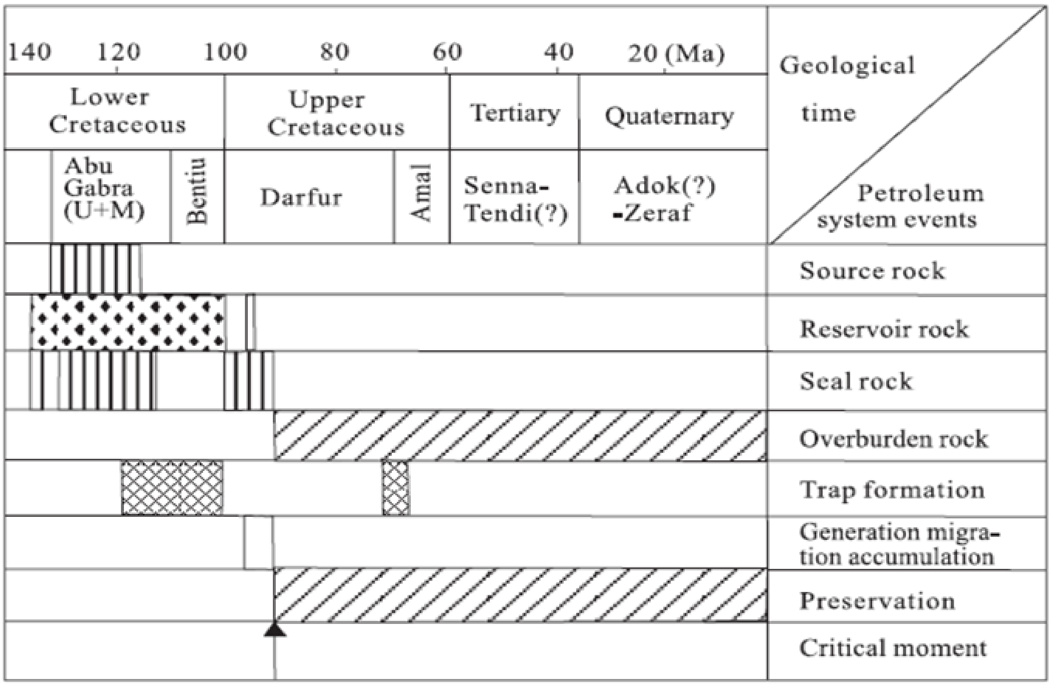

Figure 2.4 Event map of the petroleum system in Fula Sub-Basin as analogues for Muglad Basin (Yamin and Qin, 2011).

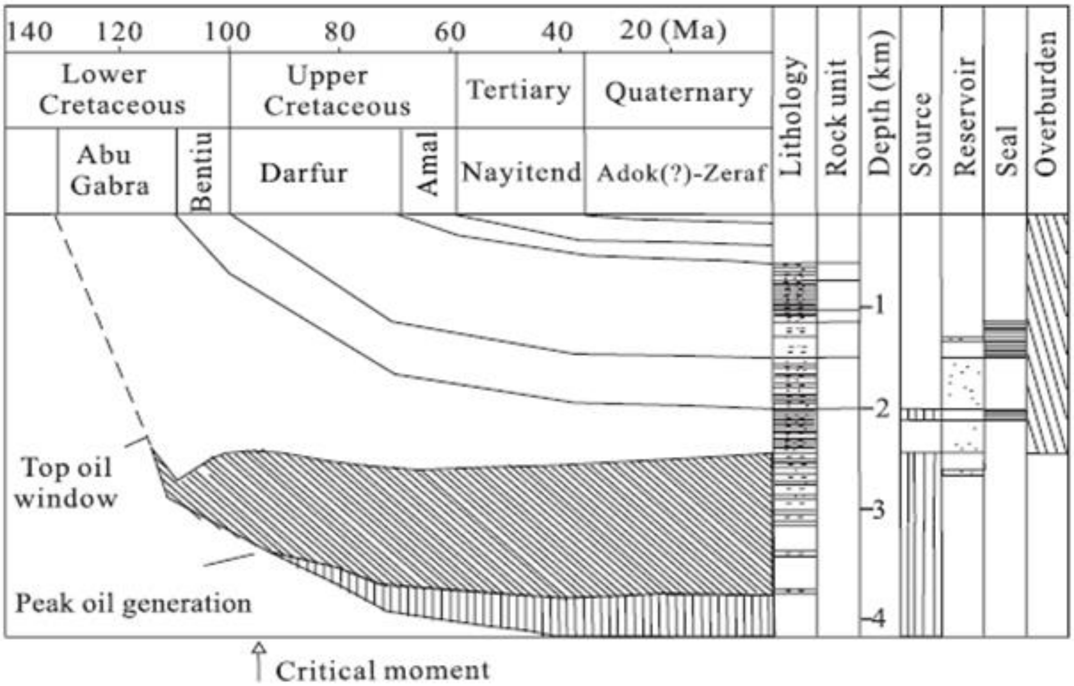

Figure 2.5 Fula Sub-Basin history match map (Yamin and Qin, 2011).

CHAPTER 3

Methods of Investigations

3.1 Introduction

This chapter is divided into two main sections. The first section is dedicated to petrophysics and lithofacies analysis. The second section will provide general insights into the theories and concepts of the geostatistical techniques including the outline of modules that were used in this study.

3.2 Petrophysical and Lithofacies Analysis

The repeated recording down a borehole for specific physical properties produces certain responses known as the geophysical well logs. The well logs or well logging plays a major role in the evaluation of hydrocarbon reservoirs. The main objective of evaluating, analyzing and interpreting the geophysical well logs is to determine the reservoirs key parameters that govern the hydrocarbons flow. The first aim is to evaluate and to quantify the porosity of the reservoir unit. Secondly, it is necessary to quantify the hydrocarbon fraction of the fluid within the rock mass “water saturation”. A third aim is to asses and approximate areal extent of the lithofacies within the reservoir. The fourth and last aim is to quantify the permeability of the reservoir. A number of empirical approaches are utilized to obtain this property from the well logs with different degrees of success.

3.2.1 Shale Volume Evaluation

The shale/clay presence in the reservoir can yield erroneous results for the porosity and the water saturation. These erroneous readings result from the influence of the shale minerals on the measurements characteristics of logs such as gamma ray, spontaneous potential, neutron porosity, sonic porosity, density porosity, and deep resistivity. Gamma Ray logs are one of the traditional logs that are used to evaluate the shale content within reservoirs. The first step in the calculation of shale volume from the gamma ray log is the determination of the gamma ray index (Eq. 3.1)

$$I_{GR}= \frac{GR_{log} - GR_{min}}{GR_{max} - GR_{min}} \tag{3.1}$$

Hence, the evaluation of the shale volume from the gamma ray log can be accomplished using one of the linear and nonlinear empirical equations (Eq. 3.2 to 3.6) as illustrated in Figure 3.1. The nonlinear equations yields values lower than the linear one. The shale volume (Vsh) is expressed in either percentage or decimal fractions.

Linear equation:

$$V_{sh}=I_{GR}= \frac{GR_{log} - GR_{min}}{GR_{max} - GR_{min}} \tag{3.2}$$

Nonlinear equation:

Larionov (1969) for older rocks: $V_{sh} = 0.33 \times (2^{2I_{GR}} - 1)$ (3.3)

Larionov (1969) for younger (Tertiary) rocks: $V_{sh} = 0.083 \times (2^{3.7_{GR}} - 1)$ (3.4)

Steiber (1970): $V_{sh} = \frac{I_{GR}}{3-2\times I_{GR}}$ (3.5)

Clavier (1971): $$V_{sh} = 1.7 - [3.38 - (I_{GR} + 0.7)^2]^{\frac{1}{2}} \quad (3.6)$$

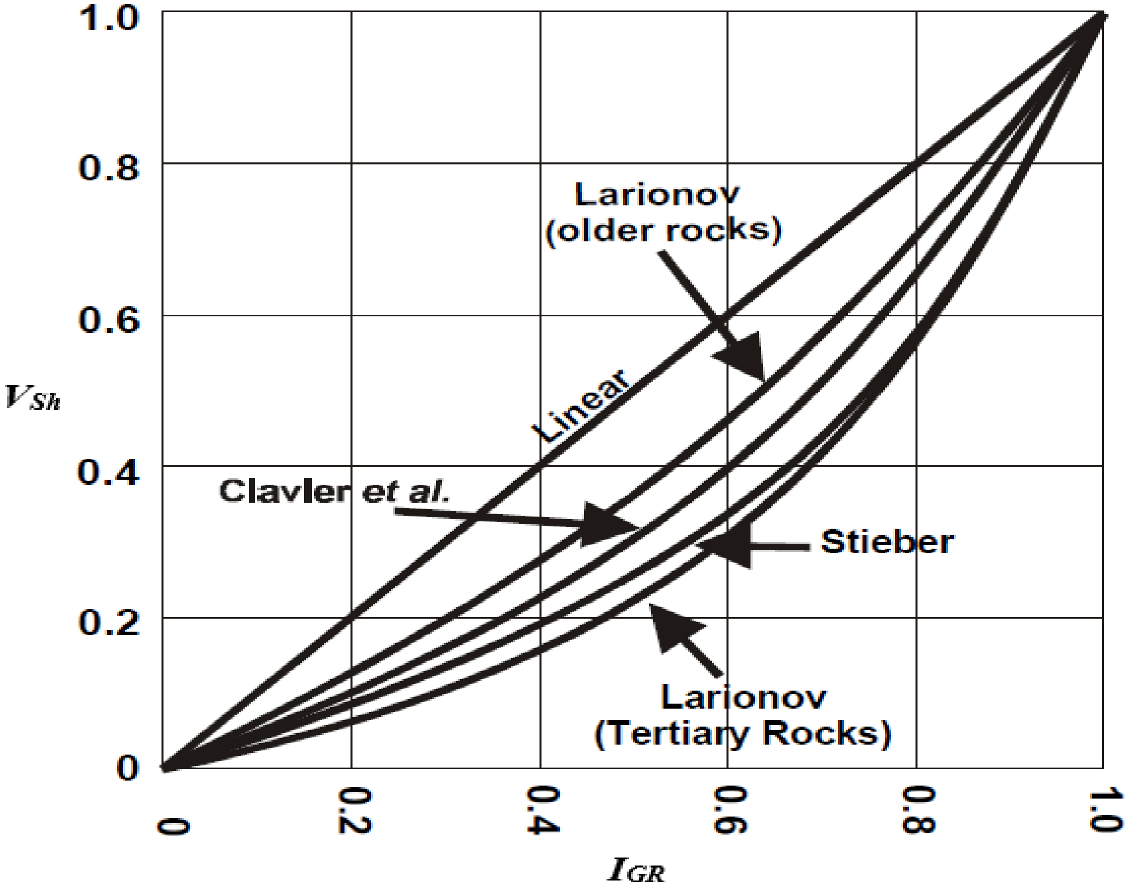

Figure 3.1 The empirical linear and nonlinear equations for shale volume determination.

3.2.2 Porosity Evaluation

Porosity (*Φ*) is defined as the ratio between the volumes of nonsolid portion of the rock occupied by fluids to the total rock volume. Often, the porosity is divided into two main types: primary porosity and secondary porosity. The primary porosity is regarded as porosity that has developed during the original sedimentation processes. On the other hand, the secondary porosity is defined as the porosity that has developed after the rock was formed and may be due to such as diagensis, dissolution and compaction. There are additional two terms related to porosity: total porosity and effective porosity. Total porosity may include both primary and secondary. The effective porosity is the total porosity after applying the shale/clay correction; hence, in the shale free zones the total porosity is equal to the effective porosity.

The determination of the porosity from the well logs necessitates the understanding of the relationship between the pores within a porous media and the physics behind the logging tool that indirectly used to drive the porosity. In general, there are three models for driving the porosity from the well logs responses.

Variety of well logs including neutron, density and sonic logs can be used to drive the porosity. All these logging tools are affected by the pores and the fluids within these pores. The responses of these tools can be related to porosity if the matrix effect and the fluid effects are known or could be determined. All these logging tool respond to the rock characteristics directly adjacent to the wellbore. The investigation depth of these three techniques is shallow (few inches) which is generally within the flushed zone. Beside the effect of the porosity on the response of these tools, the lithology of the matrix, nature and amount of pores, nature and volume of the shale are also important.

Sonic Porosit: the sonic logging tools measure the interval transit time (Δt), which is the ability of the formation to transmit seismic waves. This ability varies geologically with the rock texture and the dominant lithology, but the response is generally inversely proportional to the effective porosity. Many models have been proposed to delineate the relationship between the Δt and the porosity. In general, there are two empirical models for delineating the porosity-Δt relation. The first model is the Wyllie time-average model introduced by Wyllie and others (1958). This model is proposed for application in clean and non-consolidated formation with small pores of uniform distribution. The relationship between the Δt and porosity is given by Eq. 3.7.

$$\Phi_S = \frac{\Delta t_{log} - \Delta t_{max}}{\Delta t_f - \Delta t_{max}} \tag{3.7}$$

Where; Δt_{log} is the sonic tool reading in µsec/m, Δt_{max} is the transit time of the matrix material (182 µsec/m for sand), Δt_f is the transit time of the saturating fluids.

If the formation is not well compacted, then the porosity values will be underestimated by this formula. However, the porosity Δt will stand approximately linear. Hence, an empirical correction factor (C_p) is applied to yield a porosity values that are corrected for the compaction (Eq. 3.8)

$$\Phi_{Scrr} = \frac{\Delta t_{log} - \Delta t_{max}}{\Delta t_f - \Delta t_{max}} \times \frac{1}{C_p} \tag{3.8}$$

Where: C_p is determined by comparing the porosity values obtained from Eq. 3.7 with true porosity obtained from the core analysis for instance.

A second model for the porosity-Δt relation is called Raymer-Hunt transform (Eq. 3.9). This model was built based on the extensive field experiments between the porosity and transit time.

$$\Phi_S = C \; \frac{\Delta t_{log} - \Delta t_{max}}{\Delta t_{log}} \tag{3.9}$$

Where C is constant (0.67)

Density Porosity: the density logging tools provides a continuous record of the bulk density of the formation down the borehole. Geologically, the bulk density is a direct function of the matrix (forming minerals) and the content of the pore system. Hence, the density or litho-density logging tools are primarily used for porosity and lithology determination along other uses such as mineral identification, gas detection, hydrocarbons density determination, etc. Considering the fact that the measured bulk density depends only on the matrix density and the fluid density, the porosity can be directly related to the measured bulk density (Eq. 3.10). This relationship is appropriate for the clean, wet formation (sandstone and limestone formations). On the contrary, the shale can yield drastic density porosity values resulting from the variability in the clay minerals. In such cases, slight modification is necessary to account for the shaliness in the reservoir (Eq.3.11).

$$\Phi_D = \frac{\rho_{max} - \rho_b}{\rho_{max} - \rho_f} \tag{3.10}$$

$$\Phi_{Dcrr} = \left[\frac{\rho_{max} - \rho_b}{\rho_{max} - \rho_f}\right] - V_{Sh}\left[\frac{\rho_{max} - \rho_{Sh}}{\rho_{max} - \rho_f}\right] \tag{3.11}$$

Where: ρ_b is the bulk density measured form the density logging tool, ρ_{max} is the matrix density, ρ_f is the fluid density, ρ_{sh} is the density of the shale zone.

Neutron Porosity: the neutron logging tools is used primarily for porous formations and porosity determination. The tools respond to principally to the hydrogen content in the formations. In the oil-filled, clean formation, the neutron tools measures the liquid-filled amount of the porosity. The gas-filled zones can be identified by combining the neutron tools response with another tool reading such as the litho-density tools. Integrating the neutron tool responses with another porosity logs often yields accurate porosity estimation. In general there are three basic neutron logging tools (SNP, CNL, and DNL) each operating with specific source-receiver combination and detecting specific neutron type. The presence of the shale often leads to overestimation in the neutron porosity due to the hydrogen attached to the shale minerals. Hence, the neutron porosity readings must be corrected to the shale effect (Eq. 3.12)

$$\Phi_{Ncrr} = \Phi_{N\,log} - V_{sh}\,\Phi_{Nsh} \tag{3.12}$$

3.2.3 Permeability Evaluation

Permeability (K) is a measure of the tendency of materials (such as rocks) to transmit fluids such as water and hydrocarbons or simply the ability of rocks to permit the fluid flow. The fundamental physical low that governs this phenomenon is called Navier-Stocks equation. This equation is a very complex equation that can be simplified in form of the Poiseuille's equation (Eq. 3.13). For the purposes of linear flow in cylindrical tube this equation can be written as

$$Q = \frac{\pi\, r^4 (P_i - P_o)}{8\mu\, L} \tag{3.13}$$

Where; Q is the flow rate in cm^3/s, r is the tube radius in cm, P_o is the outlet fluid pressure in dynes/cm^2 , P_i is the inlet fluid pressure dynes/cm^2, μ is the viscosity in poise , L is the tube length in cm.

Henery Darcy (1803- 1858) performed an experiment on sand packs and developed an empirical equation used for the permeability determination. Darcy's equation has been tested and validated to the most rocks types and for certain fluids types. It can be expressed in the form of equation given below (Eq. 3.14):

$$Q = \frac{k\, A\, (P_{i-}\, P_o)}{\mu\, L} \tag{3.14}$$

Where: K is the material permeability in darcy or cm^3, and A is the sample area in cm^3.

3.2.4 Water Saturation Evaluation

Water saturation (S_w) is a measure of pore volume of rock that is filled with water or the fraction of the formation water in the undisturbed zone. This parameter represents one of the most critical petrophysical parameters and is utilized to quantify the hydrocarbon saturation ($1-S_w$). A number of techniques have been developed for the determination of water saturation. Among these techniques, the determination of water saturation from the well logs which is commonly used in the oil industry. There are four approaches on application of this technique. The first approach aims to quantify the S_w from the resistivity well logs by a model relating the S_w to the porosity, resistivity of the formation water, and number of electrical properties of the rocks. A second approach involves calculating the S_w by a series of equations that relate the S_w to the capillary pressure-saturation by laboratory experiments. The latter relates the S_w to the height above the free water level and fluids properties. A third approach for calculating the S_w uses the Dean-Stark method for water volume determination by employing oil-based mud. A last approach is achieved by using a combination of these methods depending on the availability of the data.

The resistivity well logs represent the most routinely used approach to calculate and quantify the water saturation. A number of both theoretical and empirical models (Eq.

3.14 to 3.17) have been developed to relate the water saturation to the porosity, true resistivity (R_t) and formation water resistivity (R_w) among other parameters depending on the formation and the nature of matrix.

Archie model for clean sand: $$S_w = \left(\frac{aR_w}{R_t \Phi^m}\right)^{\frac{1}{n}} \tag{3.15}$$

Simandux model: $$\frac{1}{R_t} = \frac{\Phi^m \times S_w^n}{a \times R_w} + \frac{V_{sh} \times S_w}{R_{sh}} \tag{3.16}$$

Dual Water model: $$\frac{1}{R_t} = \frac{\Phi^m \times S_{wT}^n}{a} \times \left(\frac{1}{R_w} + \frac{S_{wb}}{S_{wT}}\left(\frac{1}{R_{wb}} - \frac{1}{R_w}\right)\right) \tag{3.17}$$

Indonesian model for shaly formation: $$\frac{1}{\sqrt{R}_t} = \left(\sqrt{\frac{\Phi^m}{a \times R_w}} + \frac{V_{sh}^{(1-(V_{sh}/2))}}{\sqrt{R_{sh}}}\right) \times S_w^{n/2} \tag{3.18}$$

Where; R_w is the formation water resistivity, R_{wb} is the bound water resistivity, R_t is the true resistivity, R_{sh} is the shale resistivity, m is the cementation factor, n is the saturation exponent, a is the tortuosity factor.

3.2.5 Lithofacies Analysis (Electro-Facies)

Before 1970, the core data was the only source for studying and describing the lithological and sedimentological characteristics (lithofacies) of a given formation. Serra and Abbott (1982) introduced the term “Electro-Facies” as a “set of logging measurements that can characterize a unit allowing being distinguished from the others”. Hence, the lithofacies definition has been extended to include the electro-facies that are based on the well logging responses at any given interval. Evidently, the log measurements are responses to the physical characteristics of the rock(s), therefore an electro-facies might be linked to one or more geologic lithofacies. There are a number of methods for identifying the electro-facies ranging from manual, semiautomatic, to automatic methods (Serra and Abbot, 1982). The traditional way of determining the electro-facies is by manually correlating the different responses of the various logs with help of some graphical techniques. Several semiautomatic and automatic methods have been developed including Multivariate Analysis and Nonparametric Regressions, Principal Component Analysis; Artificial Intelligence based techniques, Classification Trees, and Cluster Analysis (Kumar and Kishore, 2006).

The Cluster Analysis technique is main approach for lithofacies analysis in this study. It aims to subdivide the input data into classes that are homogenous internally and isolated externally based on the similarity and dissimilarity among the classes. The principal consideration in cluster analysis is to use a set of suitable logs that are sensitive to lithology, and hence can be operated as lithology discriminators. The cluster analysis techniques involve two main steps. First, compiling a database of the logs measurements that attributes to objects (classes) to be clustered (Figure 3.2a). Second, a matrix of statistical distance or similarities is computed between the classes based on attributes collective treatment. The clustering algorithms that are applied to the matrix of similarity operate as an iterative process. As a result, a given pair of classes with highest resemblances will be merged and the matrix is recalculated. This process is repeated until all classes are merged together in a hierarchical fashion (Figure 3.2b).

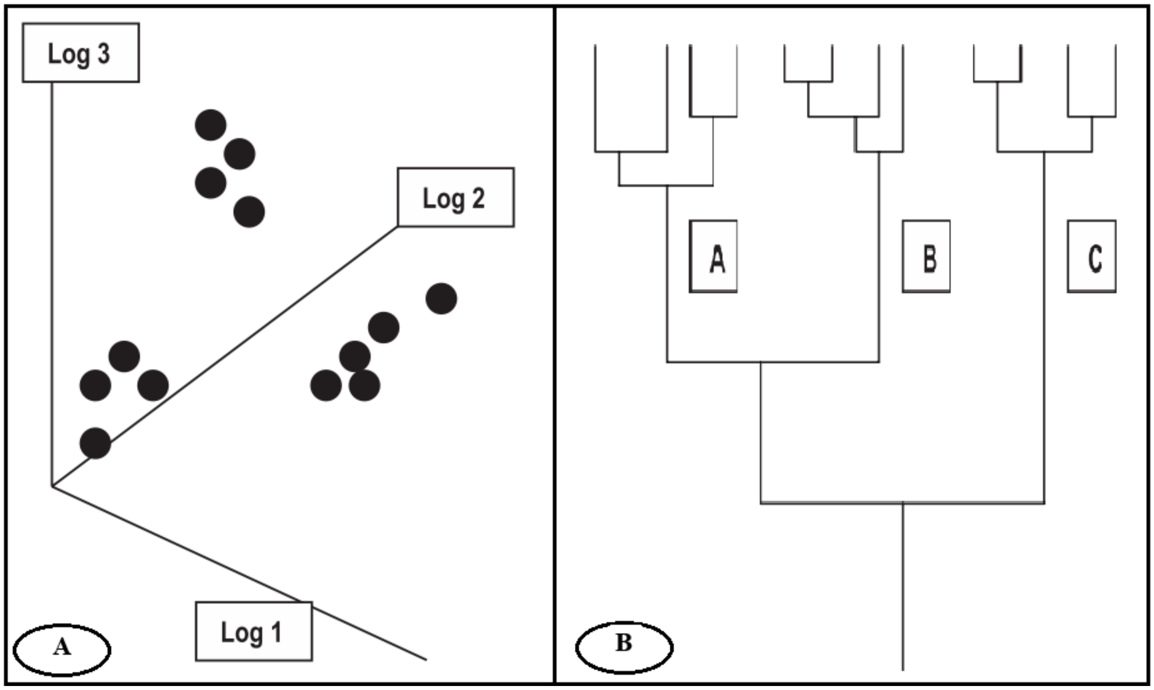

Figure 3.2 The two key steps in cluster analysis. A, the clustering by multivariate into a set of classes. B, dendrograms of the classes in a hierarchical manner based on the similarities (Kumar and Kishore, 2006).

3.3 Geostatistics

3.3.1 Background

Since the early 1950s, Geostatistics have been utilized as major tool for spatial modeling in variety of fields. A mining engineer from South Africa named, Daniel Krige, set the initial concepts for gold grade estimation (Krige, 1951). The theory was developed later by a mathematician (Georges Matheron) in Fontainebleau, France (Matheron, 1962 and Matheron, 1965). The basic aim of this approach was to provide accurate estimations for the spatial characteristics. The minimum estimation variance is provided by Kriging at the unknown location through a set of linear combination of the surrounding values. The minimum error with local accuracy results in smooth maps. This may be adequate for a number of operations such as mining, where the local estimation is important. However, Kriging is not satisfactory for reservoir modeling as it leades to loss of the critical information due to smoothing. Hence, the stochastic modeling approach has been introduced to reproduce the spatial variability and to deliver maps that displays the spatial variations based on a given variogram model (Matheron, 1973; and Journel, 1977a and b). Several different yet, equiprobable realizations can be generated by the Conditional Stochastic simulation for the same set of data. This approach has become a standard tool in reservoir modeling to address the reservoir heterogeneity and the subsequent spatial uncertainty assessment. Nevertheless, the curvilinear shapes and other complex patterns cannot be adequately reproduced by two-point Geostatistics, which is based on variogram modeling (Traditional Geostatistics). Hence, Object-based modeling was proposed to address the spatial architecture of the complex facies pattern or associations (Haldorsen and Damsleth, 1990). With this approach, the undulant geometries can be reproduced by parameterizing the shape parameters. Although, Object-based modeling is straightforward approach to delineate the complex geometries, yet it turns out to be challenging to condition to data, either in numbers or types (Holden et al., 1998). To maintain both data conditioning flexibility and to reproduce the curvilinear geometries, a new approach known as the Multi-point Geostatistics was introduced (Journel, 1992; and Guardiano and Srivastava, 1993). This approach makes possible to simulate facies architecture by utilizing a training images, and anchoring them to particular reservoir parameters. These training images are conceptual in their origin and can be as simple as hand drawing diagrams (Journel and Zhang, 2006).

3.3.2 Univariate Statistics

Univariate statistics are used to describe the distribution of one independent variable from a set of different variables (Davis, 2002). The univariate data are data set of a single variable representing for instance; porosity, permeability, water saturation, or lithofacies clusters. Three sets of numerical measures as well as two graphical representation techniques are used to describe the distribution of a data set. These measures and the graphical representations are briefly outlined in the following paragraphs.

A. Measures of Location

One of the routine uses of statistics is to identify the center of distribution. In this sense, a number of measurements are frequently used (Isaaks and Srivastava, 1989):

- **Mean (m):** the customary measure of the center of any distribution. This measure is strongly influenced by extreme values in data set. Hence, it may not correspond to the intuitive sense of the middle of distribution**.**

$$Mean = m = \sum_{i=1}^{n} Vi\,/n \qquad (3.19)$$

- **Median (M):** represents the midpoint of the observations when they are sorted in ascending or descending order. If there are even number values, the median will be the average of the middle two values. This implies that, half of the observations fall above the median value, the other half below it. Contrary to the mean, median is not influenced by extreme values; it is rather sensitive to the gaps in the middle of data.
- **Mode:** represents the observation that appears most often in the data set.
- **Minimum (min):** the smallest value in the data set.

- **Maximum (max)**: the largest value in the data set.
- **Quartile**: It provides two useful measures of location, by considering the minimum and maximum values.
    - Lower (first) quartile (Q_1): an observation below which 25% of data falls.
    - Upper (third) quartile (Q_3): an observation above which 25% of data falls.

B. Measures of Spread

These measures indicate spreading of the data around the center of the distribution. In other words, they are measures of variability. Hence, they describe whether the data are tightly grouped or scattered away from the center. In this regard, the most commonly used statistics are the Variance (S^2), Standard Deviation (SD), and Interquartile Range (IQR).

- **Variance (S^2):** the average squared difference of the observations from the arithmetic mean value.

$$S^2 = \frac{1}{n}\sum_{i=1}^{n}(Vi - m)^2 \qquad (3.20)$$

- **Standard deviation (SD):** is the square root of the variance. However, due to the averaging process, both the variance and standard deviation are both sensitive to the extreme values.
- **Interquartile range (IQR):** This parameter is the arithmetic difference between the upper and lower quartiles. Hence, it provides a quick measure of the spread. It is not sensitive to extreme values in the population.

C. Measures of Shape

These measures are used to describe the shape of the distribution.

- **Coefficient of Skewness (CS):** is a measure of the asymmetry in the data distribution around the mean. The value of this measure can be positive or negative depending on the data distribution.

$$CS = [\sum_{i=1}^{n}(Vi - m)^{3]} / S^{3} \tag{3.21}$$

IF: CS = 0 the observations are symmetrical around the mean (m=M).

CS = + ve value: the majority of observations lie in the lower end of the distribution.

CS = - ve value: the majority of observations lie in the higher end of the distribution

- **Coefficient of variation (CV):** represents the ratio of the standard deviation to the mean. This is an important measure when comparing the variability of two distributions. It may also be used in selecting the type of geostatistics to be used (whether linear or nonlinear geostatistics).

$$CV = S/m \tag{3.22}$$

IF: CV< 1 linear geostatistics will be used.

CV= 1-2 linear or nonlinear geostatistics can be used with caution.

CV> 2 nonlinear geostatistics must be used.

- **Kurtosis (k):** describes the flatness or peakedness of the distribution.

IF: K< 3 the distribution has a flat top (platykurtic).

K = 3 the observations are normally distributed with a moderate peak (mesokurtic distribution).

K >3 the observations are distributed with a sharp peak (leptokurtic).

Probability Density Function

The probability density function (pdf) is a function describing the relative probability (likelihood) for the specific interval of a random variable in a graphical view by dividing the observation into particular groups (regions). Hence, the pdf is a tool by which the statistical distribution of a variable can be readily represented and summarized. The statistical characteristics and parameters of the variable can be calculated and derived from the pdf plot.

Cumulative Distribution Function

Unlike the pdf, the cumulative distribution function describes the statistical distribution of the random variable as that representing all regions (intervals) of data set. Cumulating probabilities can give an idea about the influence of each interval.

3.3.3 Spatial Variability Analysis

The analysis of the spatial variability is generally performed through the construction of variograms, which provide the spatial correlation of data in space. The geostatistical evaluations need an analytical variogram model (Gringarten and Deutsch. 2001) which can be defined as;

$$2\,\gamma(h) = Var\,[Y(u) - Y(u+h)] = E\{[Y(u) - Y(u+h)]^2 \tag{3.23}$$

The Semivariance is the measurement of spatial dependency between samples in data set. This relation depends on the distance between data points, the larger the distance, the larger semi-variance. Depending on this concept, Matheron introduced the semivariogram in 1962 as half of the squared difference between points separated by a distance (h). Hence, the semivariogram. Hence, the semivariogram is a graphical representation of semivariance. This graph is used to build the mathematical models that reflect the variance of measurements with location.

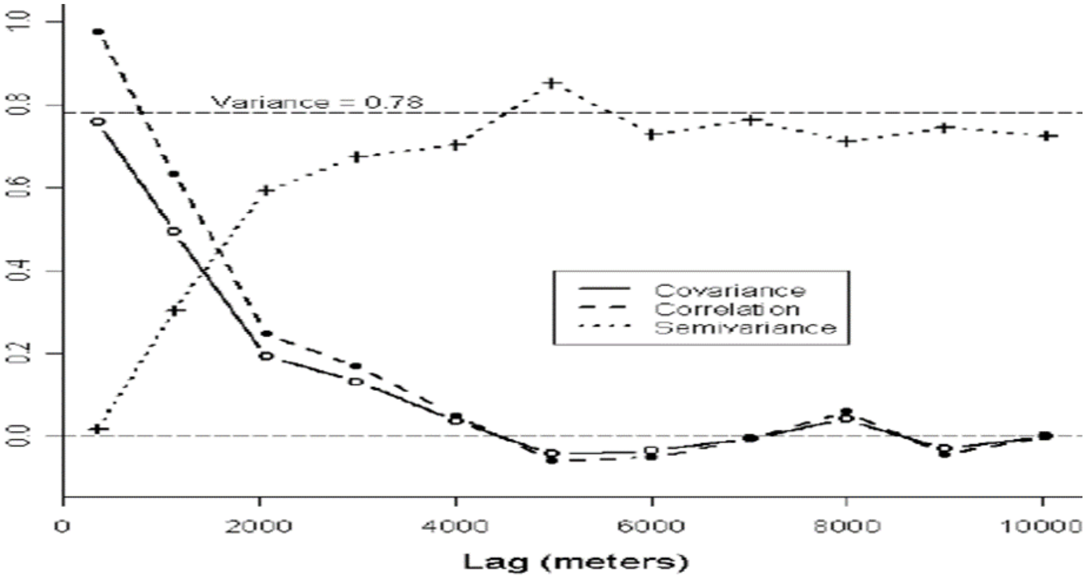

Figure 3.3 Graphical diagram for the relation between the covariance, correlation, and semi-variance for porosity data (Bohling, 2005).

The increase of semi-variance with distance continues until a certain point. The distance between the origin and this point is called “range”. Mathematically, the semivariogram is the half of variogram (Bohling, 2005).

$$\gamma(\Delta x, \Delta y) = \frac{1}{2}\,\varepsilon[\{Z\,(x + \Delta x, y + \Delta y) - Z(x, y)\}^2] \qquad (3.24)$$

Where: *Z(x, y)* = value of a variable in specific location *(x, y)*.

From the graphical representation of semivariogram (Figure 3.4), three parameters are identified: sill, nugget variance, and range. Sill value (C_0+C), represents the value at which the variogram levels off. Nugget variance (C_0) theoretically represents the intuitive zero variability at the origin, while the nugget effect is the ratio between nugget variance and sill value. Range (a) represents the distance to a threshold value of the variance (sill) after which the variance shows constant value (Isaaks and Srivastava, 1989, and Bohling. 2005).

The semivariogram is computed for pairs of data that fall inside a specific band with specific direction (directional semivariogram) and limited lag distance (h). These bands are identified by a known bandwidth, angular tolerance, and azimuth direction (Figure 3.5).

In general, there are two sets of variogram models depending on the presence or absence of the sill value. Transition models are models with sill value and drift models are models without sill. The transition models which are of interest in this study have several types. However, the most common transition models include models with linear behavior at the origin such as the exponential and the spherical models and the models with parabolic behavior (Gaussian model) (Figure 3.6).

The mathematical expression of these three models;

Spherical Model;

$$\gamma(h) = \begin{cases} c \cdot \left(1.5 \left(\frac{h}{a}\right) - 0.5 \left(\frac{h}{a}\right)^3\right) & if\ h \leq a \\ c\ otherwise \end{cases} \qquad (3.25)$$

Exponential Model;

$$\gamma(h) = c \cdot \left(1 - \exp\left(\frac{-3\,h}{a}\right)\right) \qquad (3.26)$$

Gaussian Model;

$$\gamma(h) = c \cdot \left(1 - \exp\left(\frac{-3\,h^2}{a^2}\right)\right) \qquad (3.27)$$

Where (a) represents range value, c represents the sill, and h refers to the lag distance.

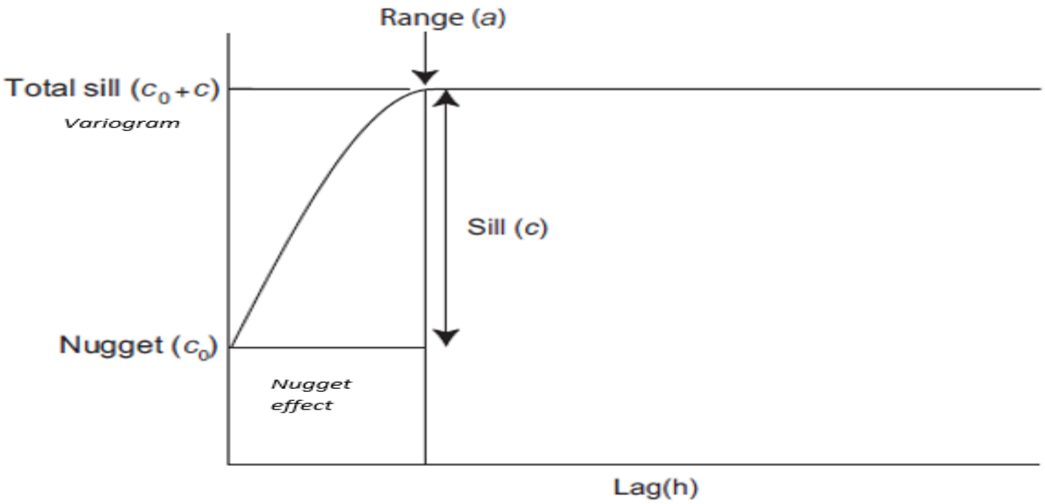

Figure 3.4 Graphical diagram showing the variogram parameters where X-axis represents the separation distance between data pairs of one variable; Y-axis represents the variability (Lloyd. 2011).

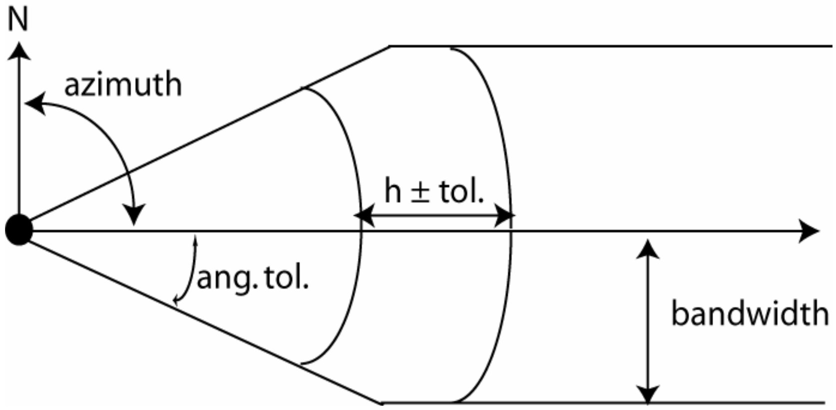

Figure 3.5 Sketch showing the methodology of estimating the directional semivariance (Bohling. 2005).

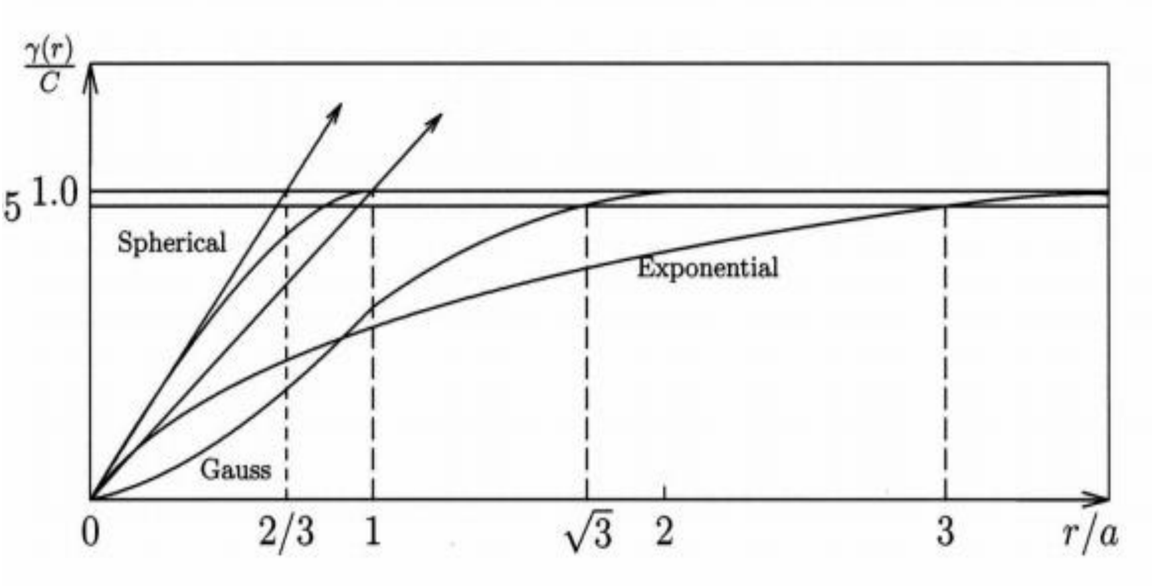

Figure 3.6 Graphical diagram representing the three main transition models the spherical, Gaussian and exponential models with their Sill values, equivalent lag distances, and relation to the range values (a). (Lloyd. 2011).

3.3.4 Kriging Estimates

The kriging is a name given to a group of generalized least-square regression methods. There are number of kriging techniques that are dependent on the same concepts of redundancy and data correlation (Eq. 3.29). The kriging estimation differs from the common interpolation approaches such as invers distance weighting, where the weights are considered inversely proportional to the distance between data location and the location of the point to be estimated. The kriging estimation depends on capturing the spatial variability described by the variogram.

$$Z^*(U) = \sum_{\alpha=0}^{n} \lambda_\alpha Z(U_\alpha) \tag{3.28}$$

Where: U, U_α vector location for point estimation (U) from neighboring unknown point (U_α), *n*, the number of neighboring data paints that used for estimating Z*(U), and λ_α is the kriging weight.

Kriging estimator is the best “linear unbiased estimator”. This implies that among all linear unbiased estimators, there is no “better” than the kriging estimator on average. In kriging, the average square difference between the estimator and the true value is minimized for all unsampled locations.

$$\text{Error} = [z^{*}(u)\text{-}z\ (u)]^{2} \tag{3.29}$$

In a case of variable with global mean equal to 0 and variance equal to 1, and the kriging weights (λ_a) , the following system of equations are used:

$$\begin{bmatrix} 1 & \rho(h12) & \cdots & \rho(h1n) \\ \rho(h12) & 1 & \vdots & \rho(h2n) \\ \vdots & \cdots & \ddots & \vdots \\ \rho(h1n) & \rho(h2n) & \cdots & 1 \end{bmatrix} \times \begin{bmatrix} \lambda 1 \\ \lambda 2 \\ \vdots \\ \lambda n \end{bmatrix} = \begin{bmatrix} \rho(h10) \\ \rho(h20) \\ \vdots \\ \rho(hn0) \end{bmatrix} \tag{3.30}$$

Where ρ (h) = 1-γ (h). The left side matrix accounts for the data redundancy, while vector on the right accounts for the data correlation. The resulting weight is then utilized in Eq. 3.32 to acquire the estimate. This estimate z*(u) is evidently not equal to the true value z (u), the degree of error is expressed as an error variance, an average squared error known as the kriging variance.

$$\sigma^{2}_{E} = 1\text{-}\sum_{\alpha=0}^{n} \lambda\alpha\rho\ (h_{\alpha 0}) \tag{3.31}$$

3.3.5 Simulation Models

The Interpolation approaches such as the kriging provide only one estimate per location. In practice, a number of equal probable values could be generated at each unsampled location. The geostatistical simulation generates multiple realizations or predictions that mimic the reality (Issaks, and Srivastava, 1989). In the petroleum industry, this ability makes the geostatistical simulation a preferable approach in characterizing and capturing the reservoirs heterogeneity. The selection of a simulation method depends on the output needed from the process as well as the data availability. In general, the stochastic simulation is preferred because of better heterogeneity capturing, integrating and honoring multiple data sets, and ability to assess the uncertainty.

Conditional or stochastic simulation requires the spatial analysis models (variograms) and the sample distribution (CDF) remain intact within a given geological zone or interval.. The framework (structural and stratigraphic models) of the 3-D volume remains constant. Each realization starts with random and different seed number and has a distinctive path through the 3-D grid. This distinctive and rather random navigation provides simulated values differing from one realization to another.

There are two principle types of stochastic simulation methods: A pixel-based and object-based methods. The pixel-based methods simulate on pixel-to-pixel basis and operate both on continuous and categorical data type. The object-based methods simulate a group of pixels that are fit together to form a shape of a geological phenomenon. The pixel-based models require the simulated variable to be in a form of Gaussian random function. By utilizing the spatial analysis model, the search ellipsoid and the control data, this method simulate on node-by-node basis. The sequential simulation (Gaussian and indicator) is the most popular pixel-based simulation method.

In the sequential simulation, the simulated value is driven from the Cumulative Distribution Function (CDF), which is calculated from the observed and formerly simulated values around this location. The simulation process conventionally starts with a randomly selected node, hence, progresses sequentially through the grid that represent the simulated area. However, the movement order is not theoretically specified, instead it is usually followed random sequence (Issaks and Srivastava, 1989). Consequentially, at every node, the program searches for the point values to be included in the calculation of the unknown point in a predefined neighborhood (search radius/ellipse). These points may consist of both points simulated in previous step, and the points introduced as input data. From the values at these points, a probability distribution is calculated.

The Sequential Gaussian Simulation approach requires a single semivariogram model based on the transformed data when the simulation at every node is achieved, the results are transformed back to the original values (units).

$$y_i = G^{-1}\left(\frac{C_i + C_{i-1}}{2}\right) \tag{3.32}$$

$$Z_i = F^{-1}\left(G\left(y_i\right)\right) \tag{3.33}$$

Where; $G_{(x)}$ is tha standard normal CDF, G^{-1} is the corresponding standard normal quantile, C_i is the cumulative probabilty associated with Z_i, $F_{(z)}$ is the Cumulative Disribution Function (CDF) of the original data.

3.3.6 Simulation Validation

Leuangthong and others (2004) extensively discussed the basic verifications and the minimum accepted criterion that should be performed on a constructed geostatistical model. They reinforce the necessity for the precise verifications to insure the adequacy of the geostatistical simulation. The affirmation that the generated model reproduces the original data considered the minimum criteria of validation. This input data for the key target represents the actual data and the spatial variability measure (variogram).

Several validation approaches exist and should be incorporated in the modeling workflow:

1. Realization visualization

This validation aims to highlight the high and low areas, their variability, and overall spatial distribution, which should satisfy the geological constraints.

2. Cross validation and Jackknife

The cross validation implies removal of a data value and utilizing the surrounding data to estimate the removed data at their location. Hence, this validation is known as “leave one out”. The jackknife implies re-estimation without the removal or replacement, which is known as “keep some back” (Deutsch, 2002). This two approaches should produce a model with high correlation coefficient in a cross plot between the true and the estimated values. Symmetrical distribution of the errors with low variance and zero mean, and centering around zero error in cross plot between estimates and the errors satisfy the conditional unbiasedness (Issak and Srivastava, 1989; Krige, 1999; Krige and Assibey-Bonsu 2000)

3. Reproduction of data

The property of kriging insures that estimate at location of data are exactly the data value with zero error variance (Journel and Huijbregts, 1978; and Goovaerts, 1997). The simulation depends on the kriging estimates as well as the kriging variance to define the conditional cumulative distribution function (CCDF). Hence, the data are re-produced at their location by the simulation. The verification is then accomplished by cross plot between the true values and the estimates to ensure that the data were reproduced (Figure 3.7).

4. Histogram reproduction

This is to insure that the original histogram of the data values is reproduced. However, the de-clustering approach adopted to construct the model should be clear. For example, the polygonal de-clustering is recommended over the cell-based when the geological architectures are available. However, it is impractical to analyze histograms of all the realization. Yet, selection of a few random realizations should fulfill this task. In this type of visual verification, one must analyze the shape of the histogram, ranges of simulated values and the statistical summary (Figure 3.8a)

Alternatively, the Quantile-Quantile (Q-Q) plot (Figure 3.8b) may result in a better indication on the reproduction of the histogram. Multiple realizations can be visualized in the same Q-Q plot.

5. Summary statistics

Each one of the generated realization has a global variance and global mean. These parameters can be checked by plotting the histograms of the variance and the mean from all the generated realizations. This implies that the mean of the means should be equal to the target mean and the mean of the variances should be equal to the target variance (Figure 3.8c).

6. Variogram reproduction

This means the calculation of the variogram for multiple generated realizations and comparing them with the variogram of the original values (input) data. The variogram of the model should be reproduced adequately (Figure 3.8d).

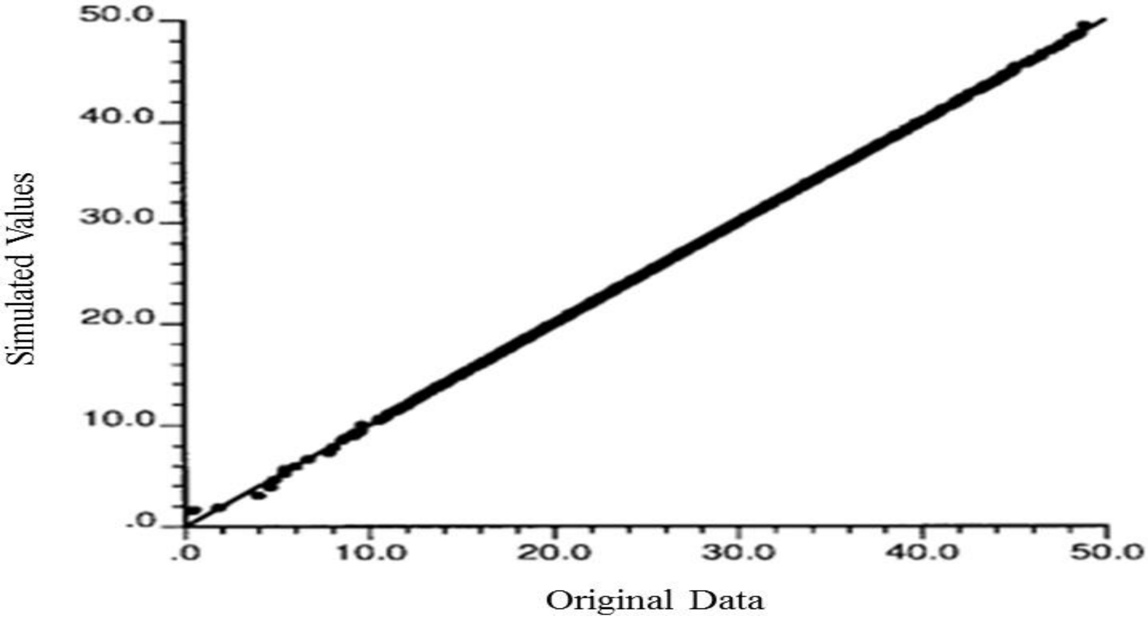

Figure 3.7 A cross-plots of the simulated values against the original data reveals a 1:1 correspondence between the two set of the values (Leuangthong et al., 2004).

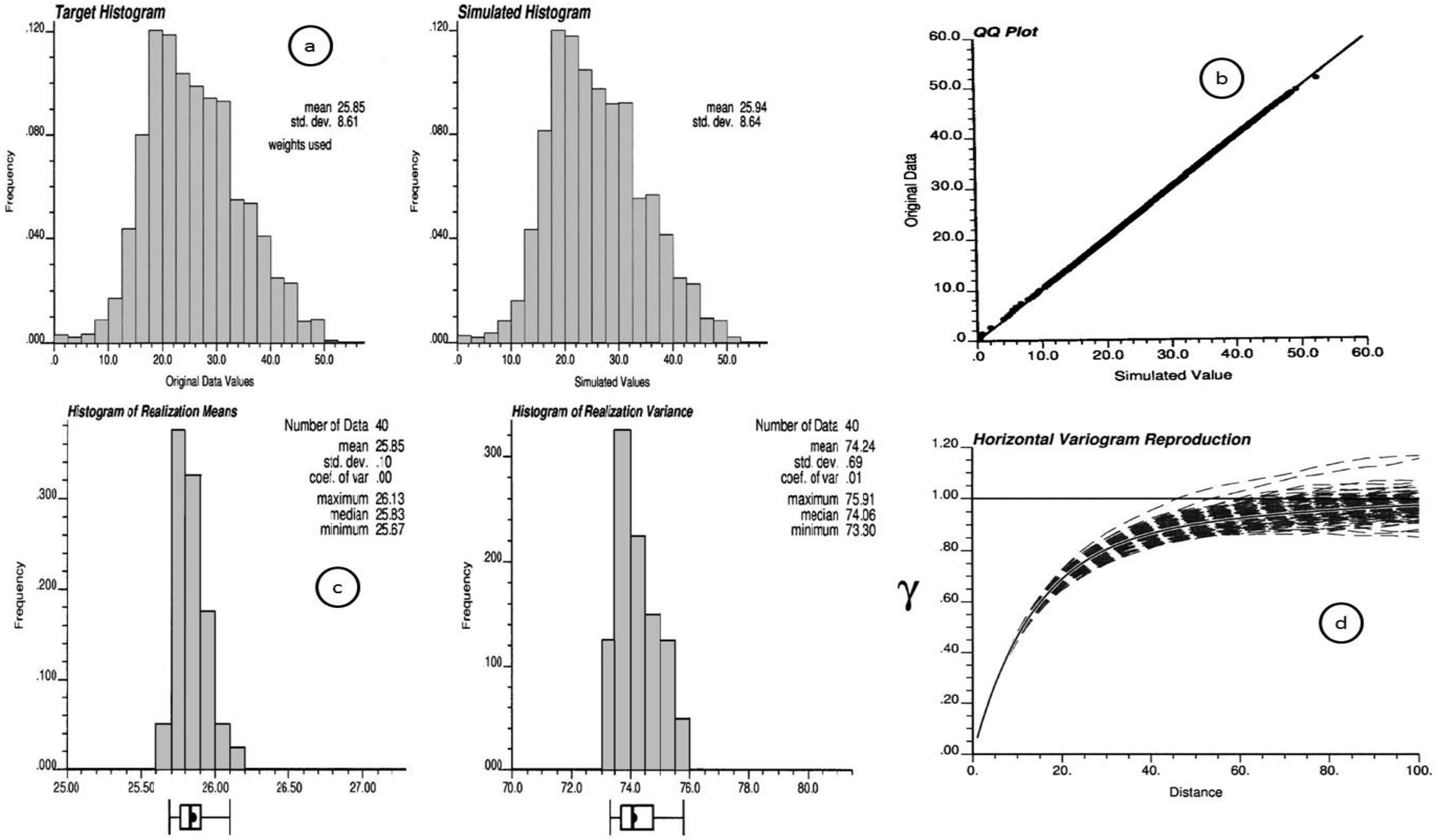

Figure 3.8 Illustrating (a) the reproduction of histogram for the data of interest (target vs. simulated). (b) Q-Q cross-plot of the simulated data distribution against the original data distribution. (c) Summary statistics reproduction of the means of the realizations (left) and variance (right). (d) Horizontal variogram reproduction, the original variogram model is outlined by white line and the rest represents the modeled variograms of the multiple realizations (dashed lines). After Leuangthong et al., 2004.

CHAPTER 4

Lithofacies Classification and Petrophysical Evaluation

4.1 Introduction

This chapter gives a detailed account of the petrophysical and lithofacies analysis in the Bentiu-1 reservoirs interval. The data from 20 wells (Figure 4.1) were used for evaluation of porosity, permeability and water saturation. Also, the results of lithofacies determination and classification based on well logging information gathered from the 20 wells and core analysis reports are accounted for in this chapter.

Out of the full suite of logging curves available from 20 wells used in this study, certain logging curves were found appropriate to fulfill the objectives of this study. The details of these curves are provided in Table 4.1 below.

4.2 Lithofacies Classification

Idriss (2002) and Eltom (2007) presented the Bentiu-1 reservoirs interval (Upper Bentiu Member) to be dominated by gravel sand and sandstone facies. These dominant facies are interbedded vertically and laterally with shale facies of varying thickness and lateral extent. RRI (1991) described the facies association in this interval to be composed of sandstone facies of coarse-to-medium grain and occasionally conglomeratic. They are generally poorly consolidated compared with the overlying sandstone facies of the Aradeiba

Formation. The shale facies are commonly massive varying in thickness from thin interbedded layers to well-developed layers (Kheiralla et al., 2012).

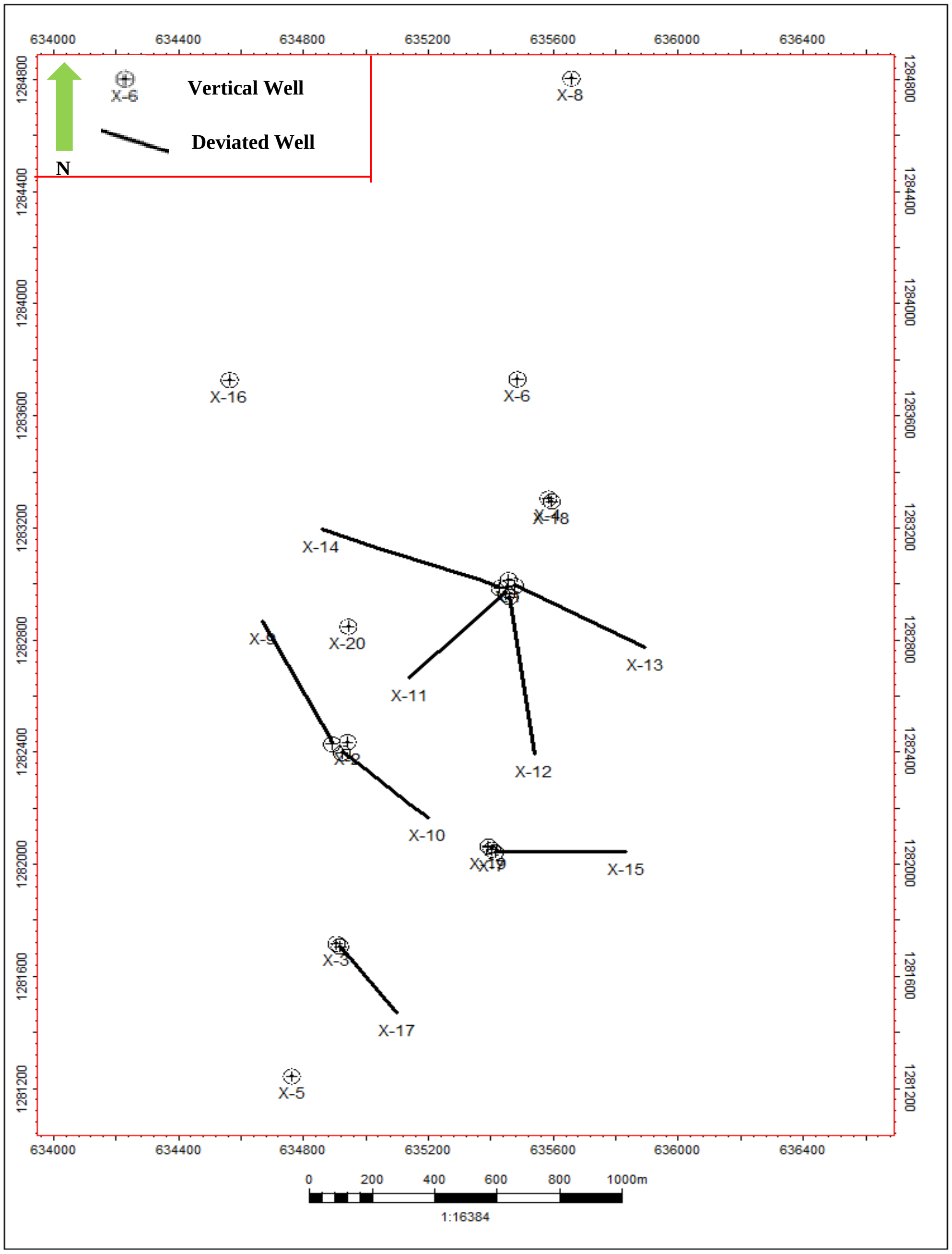

Figure 4.1 Base map for the location of the 20 wells used in this study. Eight wells are deviated and 12 wells are vertical (see legends).

Table 4.1 The well logging curves used in this study and brief information about these curves.

Curve	Description	Unit	Min	Max	Mean
BS	Bit Size	in	12.25	12.25	NA
CAL	Caliper	in	6.35	24.4	11.09
GR	Gamma Ray	API	22.72	290.22	85.45
SP	Spontaneous Potential	mV	NA	NA	NA
RMSL	Micro Spherical Focus log	Ohmm	0.06	44.62	2.44
RS	Shallow Resistivity	Ohmm	1.29	19832.34	42.26
RD	Deep Resistivity	Ohmm	1.72	30591.2	81.91
NPHI	Neutron Porosity	V/V	0.24	0.1	0.4
RHOZ	Density	G/Cm^3	1.38	2.67	2.30
DT	Sonic Transite Time	µs/ft	59.62	179.23	93.03
PEFZ	Photo Electric Cross Section	Barns/Electron	0.89	10	2.6

Table 4.2 The four conventional cores used in this study for the lithofacies determination.

Well	Core #	Depth (m)	Length (m)
X-2	Core A	1449.60-1455.70	6.10
	Core B	1509.00-1516.50	7.58
	Core C	1533.00-1534.40	1.80
X-3	Core D	144.97-1458.02	9.55

In this study, the main lithofacies associations were evaluated based on four conventional cores (Table 4.3) recovered from two wells (X-2 and X-3) with a total length of 25 meters, in addition to side well cores recovered from the same wells at specific intervals.

From the initial examination of the four conventional cores, three main lithofacies have been determined as described in the following paragraphs.

Medium to Coarse Grained Sandstones Facies

This facies consists mainly of medium to coarse-grained sandstones that are occasionally associated with pebbles. In one case, it was observed to have formed a conglomeratic base (Figure 4.2). The sandstones were found in all four cores to be of light grey to light brown in color with poor to moderate consolidation and often poorly sorted with sub-angular to sub-rounded grains (Figure 4.2). The detrital grains of this facies are composed mainly of monocrystalline quartz with notable amount of polycrystalline quartz, few micaceous grains and some heavy minerals such as iron oxide and few lithic fragments (Figure 4.3). This mineralogical assemblage suggests that this facies is sub-lithic arenite that is structurally characterized by trough cross bedding. In addition, this facies is often associated with visible light brown oil staining.

Fine to silty Sandstone Facies

This facies is composed predominantly of fine-grained sandstones which occasionally changings into siltstones (Figure 4.4). The sandstones of this facies are found in all four cores to be of light brown with traces of light grey in color, moderate to well sorted. Mineralogically, this facies is characterized by the abundance of microcrystalline quartz with lesser amount of polycrystalline quartz, few feldspars, some micas as well as negligible amount of heavy minerals as free or enclosed grains and notable amount of lithic fragments that are mostly of muddy nature (Figure 4.5). This mineralogical assemblage indicates that this is a sub-felsic arenite to arenite sandstone facies with occasional light-brown oil staining. Structurally, this facies is characterized by a clear trough cross-bedding.

Shale/claystone Facies

This facies is composed mainly of grey, moderately hard sub-blocky claystones. It is found to be silty in parts and often interbedded with light-grey, very fine-grained, well sorted arenitic sandstones with argillaceous matrix. Structurally, this facies is found with blocky nature that varies in dimension and thickness and few visible mud cracks. This facies appears in all recovered cores to have no oil staining even within the silty intervals associated with the claystones (Figure 4.6).

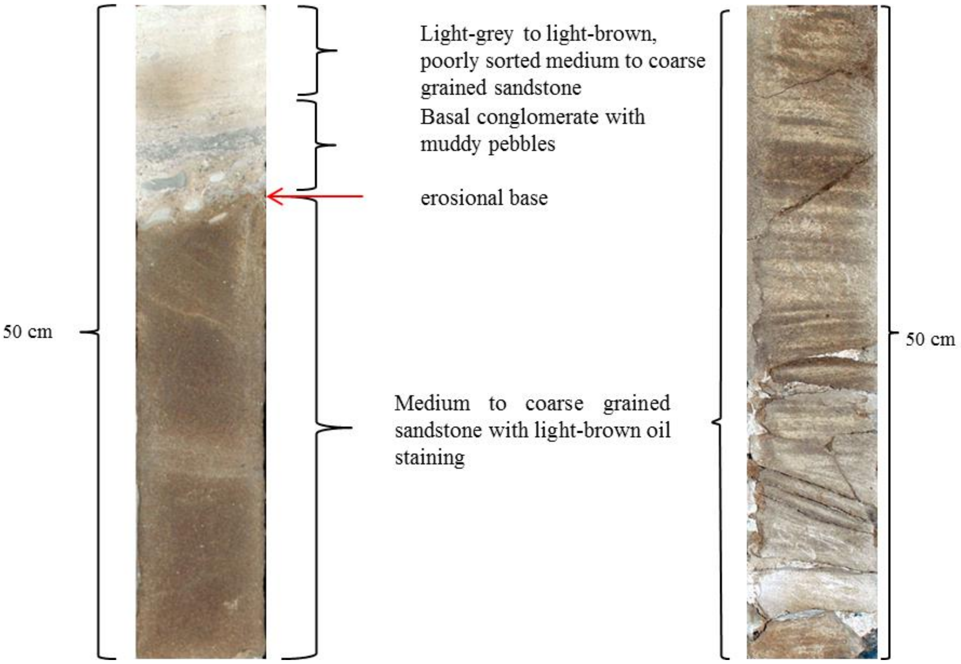

Figure 4.2 One meter of core slab showing an example of the medium to coarse grained sandstone facies.

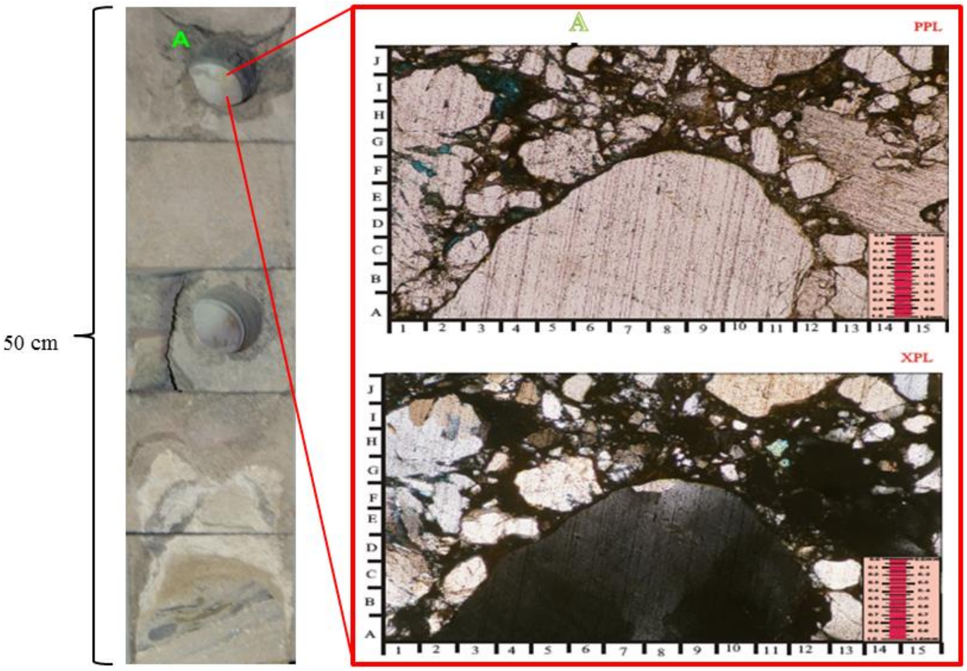

Figure 4.3 50 cm core slab (left) of medium to coarse, poorly sorted sandstones with some lithic fragments, and a thin-section (right) for this facies composed of mono and poly crystalline quartz with some mica minerals and iron oxides.

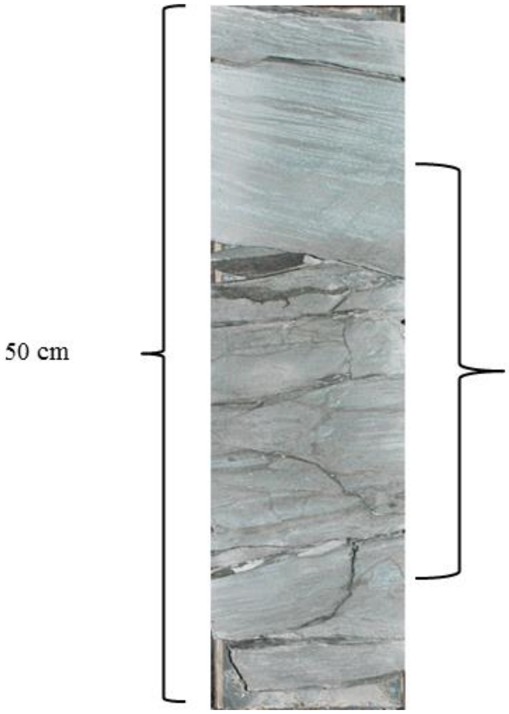

Light-grey, moderate to well sorted, fine silty sandstones, with trough cross-bedding and some lithic fragments that are muddy in nature

Figure 4.4 50 cm of a core slab showing well sorted, light-grey fine to medium grained sandstone facies.

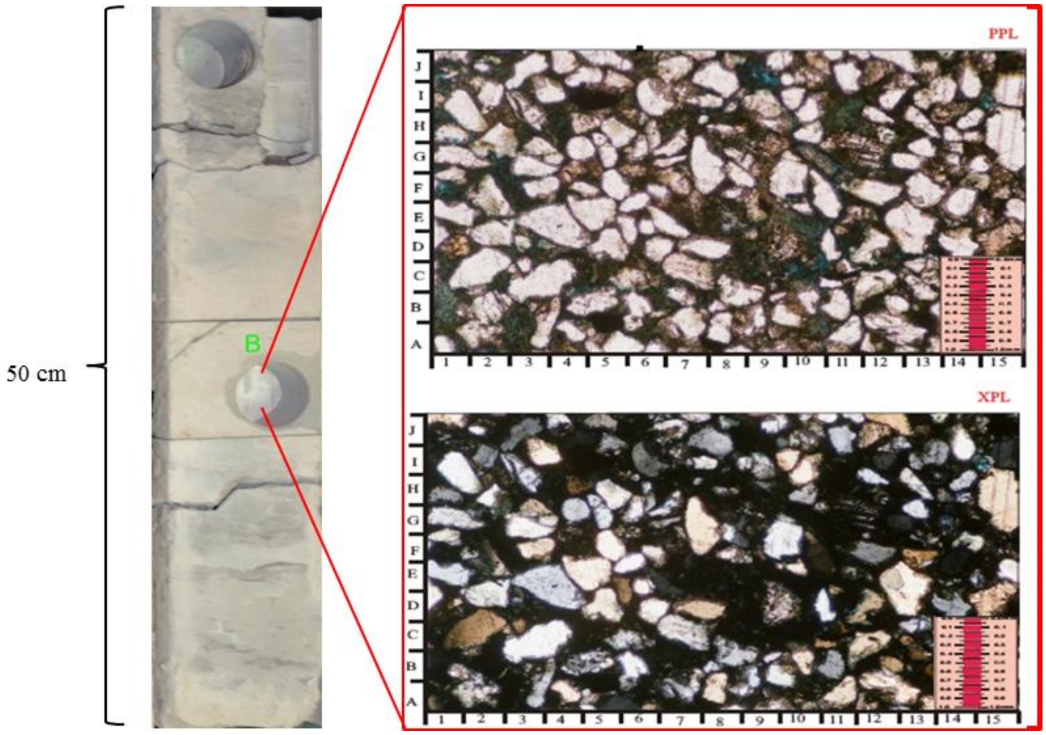

Figure 4.5 50 cm of a core slab (left) showing a part of fine to silty sandstone with some lithic fragments, and a thin-section (right) of this facies composed of quartz (mono and poly crystalline), feldspars, micas, and few iron oxides.

Figure 4.6 85 cm of a core slab showing an example of shale/claystone facies with sub-blocky nature.

Due to the lack of an extensive cores coverage, the concept of Electro-Facies, first introduced by Serra and Abbot (1980), was adopted to evaluate the lithofacies in the whole interval. Hence, the cluster analysis module was implemented to generate a discrete curve describing the lithofacies that was previously determined from the core examination. Prior to applying the model-based cluster analysis, a set of well logging curves were selected and compared with the representative three lithofacies defined earlier from the core examination (Table 4.3 and Figure 4.7). Out of the full suite of logs available for this study, six curves were chosen according to their characteristics in defining the lithological differences with a varying prospective (Table 4.3). Analyzing and examining the logging responses for the three lithofacies identified from the cores, very distinctive characteristics were revealed. These characteristics are represented by various cross-plots between the selected well curves as illustrated in Figure 4.7.

Table 4.4 The well logging responses in the cored interval for the three identified lithofacies.

Log	**Sand Facies**			**Shaly-Sand Facies**			**Shale Facies**		
	Min	Max	Mean	Min	Max	Mean	Min	Max	Mean
GR	51.74	104.91	70.73	86.57	121.44	106	97.86	132.06	123.94
CLV	0.0	.29	.05	.23	.80	.53	.24	1	.83
PEFZ	1.6	3.11	2.03	2.21	2.92	2.64	2.46	3.18	2.92
RHOZ	2.12	2.42	2.25	2.32	2.49	2.42	2.14	2.48	2.41
NPHI	.10	.40	.24	.19	.31	.25	.24	.59	.31
RD	2.32	1261.4	192.56	26.29	250.19	12.5	1.94	22.9	7.41

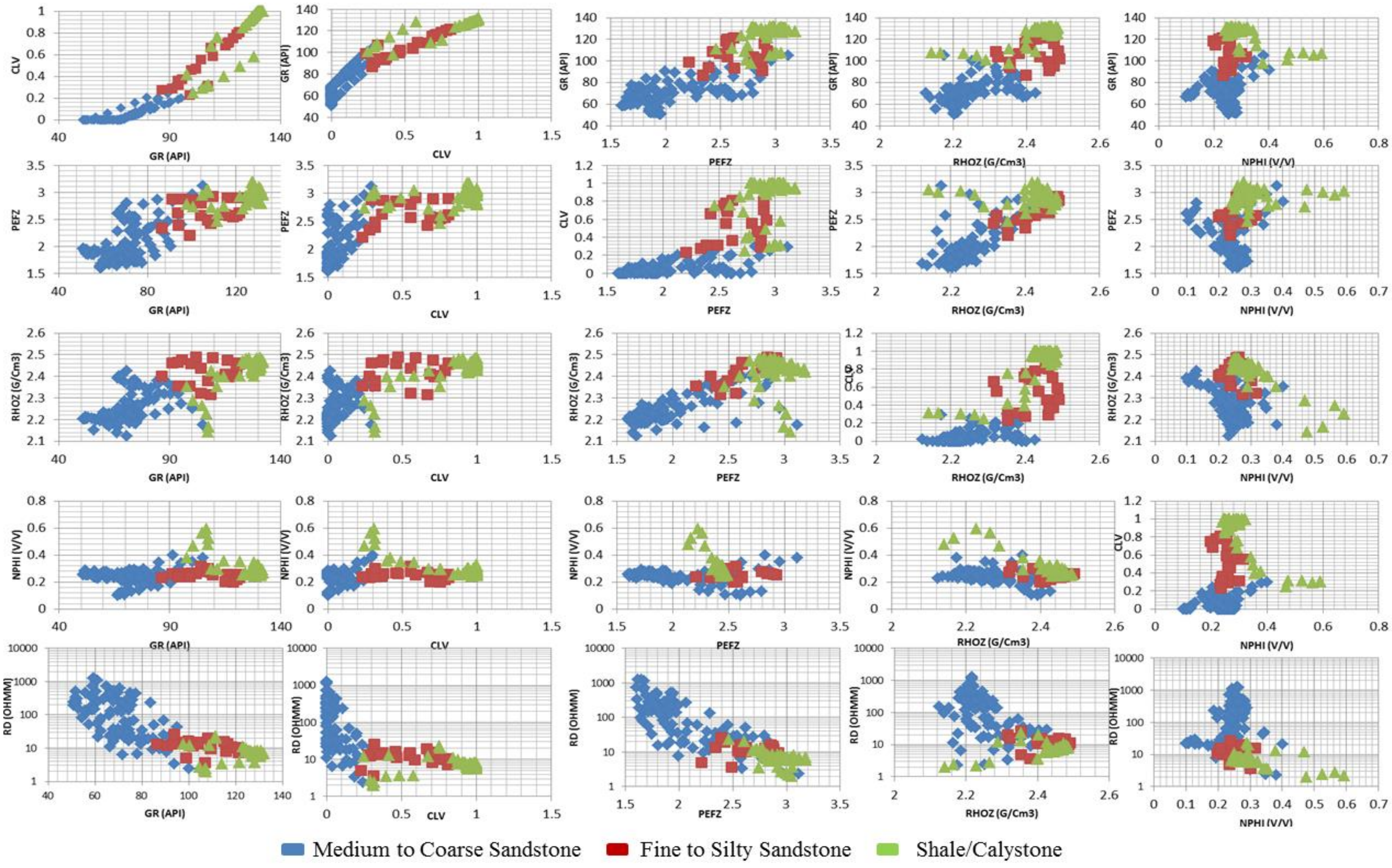

Figure 4.7 Cross-plots of the six well-logging curves to classify the three identified lithofacies from the core data of X-2 and X-3 wells.

The cluster analysis model used to generate a discrete electro-facies curve is based on a set of routines that are statistically standardized (Ataei, 2012). In this study, the available data from 20 wells were used as input to the cluster analysis module to generate a training model according to the upper and lower cutoffs of the six selected curves. These statistical routines enabled the clustering of the input curves into groups corresponding to a sole electro-facies. Three main clustering groups have been generated based on six well-logging curves (Tables 4.4 and Figure 4.8).

The application of the cluster analysis started by setting initial values of the mean and standard deviation for each one of the input curves (Table 4.4). Accordingly, each class (electro-facies) was generated with its own statistical characteristics acquired from the input curves (Table 4.4). The three generated electro-facies have been assigned three different colors, a yellow indicating a sand facies, grey indicating fine to silty sand and green indicating a claystone/shale lithology (Figure 4.9). Figure 4.9 shows the cross-plots and histograms of the selected well logging curves. It illustrate that the electro-facies identified as sand is characterized by zero clay volume, less than 80 API gamma ray, neutron porosity between 15 to 40%, density of less than 2.7 g/cm^3, photo-electric cross-section from 2 to 4.5 barns/electron, and deep resistivity of over 10 ohmm excluding a few points. The electro-facies identified as shale is characterized by a clay volume of over 60%, gamma ray of 100 to 110 API and neutron porosity of 30% and higher, density between 1.8 to 2.5 g/cm^3, photo-electric cross-section of 5 barns/electron and higher, and a deep resistivity of less than 10 ohmm in general. The third electro-facies, which is correlated to the fine to silty sandstone facies, is intermediate between the two previous electro-facies. It is characterized by clay volume between 20 to 60%, gamma ray dominantly between 80 to 110 API, neutron porosity of 15 to 40 % and density of 2 to 2.6 g/cm^3, a photo-electric cross-section between 2 to 6 barns/electron, and deep resistivity between 10 to 100 ohmm.

Table 4.5 The well logging responses in the cored interval for the three identified electro-facies.

Log	Class #1		Class #2		Class #3	
	Mean	St. Dev.	Mean	St. Dev.	Mean	St. Dev.
GR	63.54	13.6	111.37	22.46	121.79	20.56
CLV	.09	.08	.41	.11	.64	.14
PEFZ	1.12	91.87	2.89	.62	3.91	1.62
RHOZ	1.13	91.88	2.39	.08	2.28	.19
NPHI	.21	.04	.25	.04	.41	.07
RD	94.97	211.4	22.32	24.79	5.35	8.25

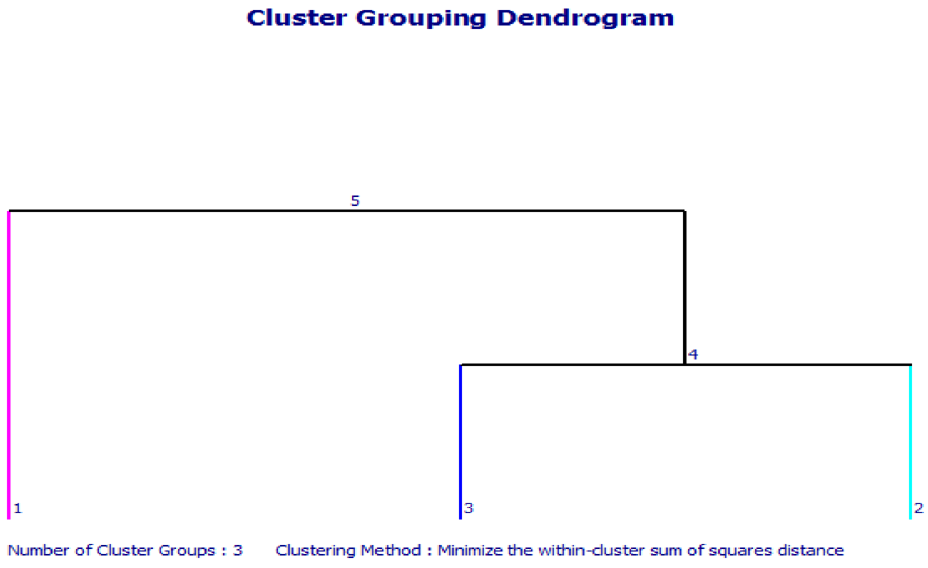

Figure 4.8 Cluster grouping dendogram for clustering the well-logging responses by minimizing the within-cluster sum of square distance.

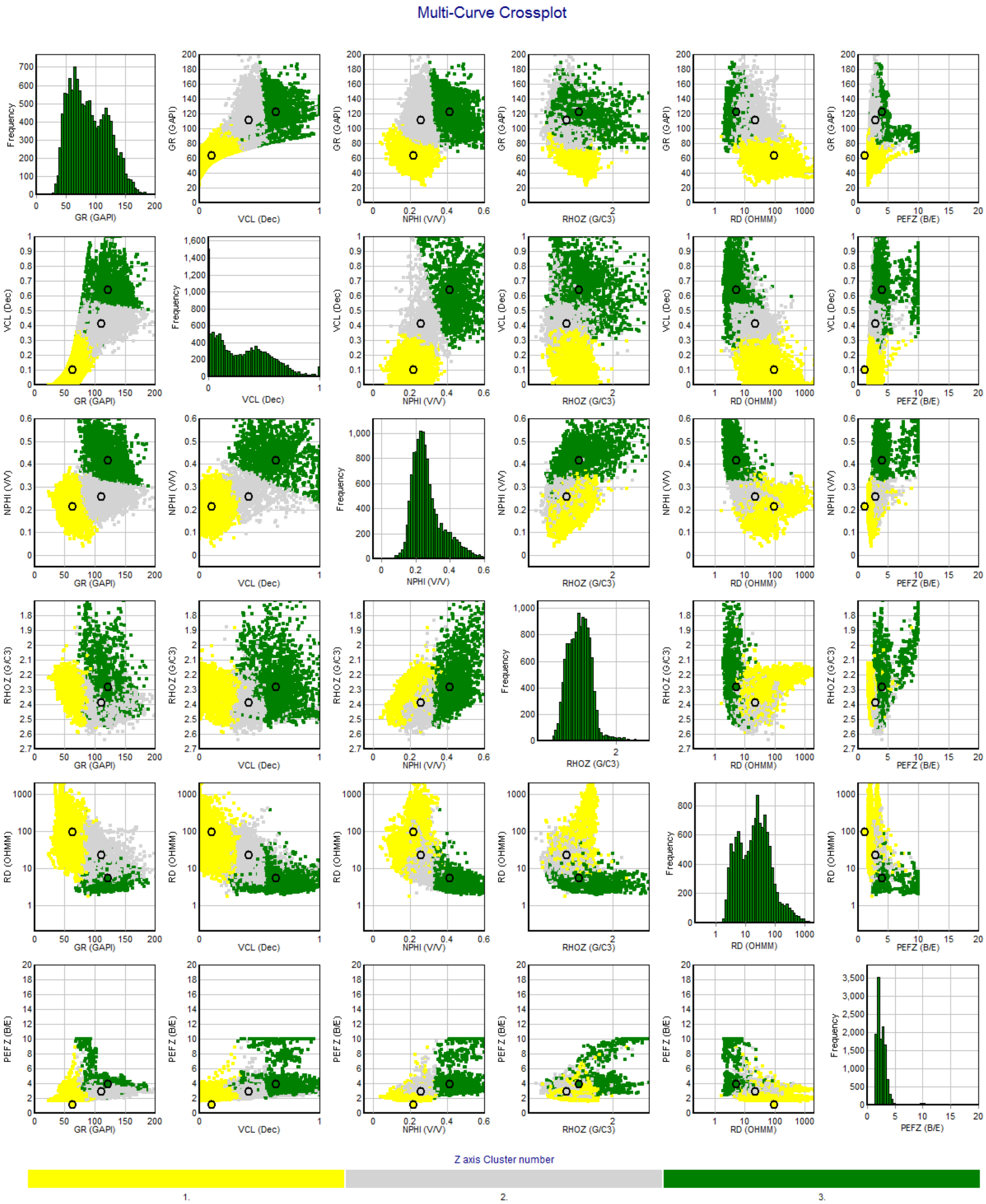

Figure 4.9 The cross-plots and histograms of the selected logging curves for the cluster analysis module. The three cluster groups represent the three electro-facies: 1 sand facies, 2 shaly_sand, and 3 shale.

For the validation of the constructed lithofacies based on the cluster analysis, side-well cores recovered from two wells (X-2 and X-3) were compared to the generated electro-facies curve. The results illustrated in Figure 4.10 and Figure 4.11 show good correlation between the side well cores and the electro-facies. Moreover, the generated electro-facies were compared with the interpreted lithology from the mud logging for all the available wells (20 wells). Good agreement between the constructed electro-facies was obtained from the comparison, between the sand/clay lithology interpreted and the sand/shale facies constructed from the cluster analysis based-module (Figure 4.10 and 4.11).

4.3 Evaluation of the Petrophysical Parameters

This section gives a brief description of the petrophysical parameters' evaluation and estimation, namely the clay volume, porosity, permeability, and water saturation. In addition, the various aspects of the petrophysical parameters' calculation will be also summarized.

4.3.1 Clay Volume Estimation

The very common erroneous results in porosity and water saturation calculation are in many cases related to the presence of clay. Clay or shales can be present in one or more of the following three forms in reservoir rocks (Figure 4.12) (Schlumberger, 1987). In *structural shale,* the sand grains are partially replaced with shale grains. This rearrangement changes the matrix density while the porosity remains the same. In *laminated shale,* thin layers of shale occur within the reservoir matrix; both the matrix density and porosity are affected. In *dispersed shale,* the shale minerals are caught within

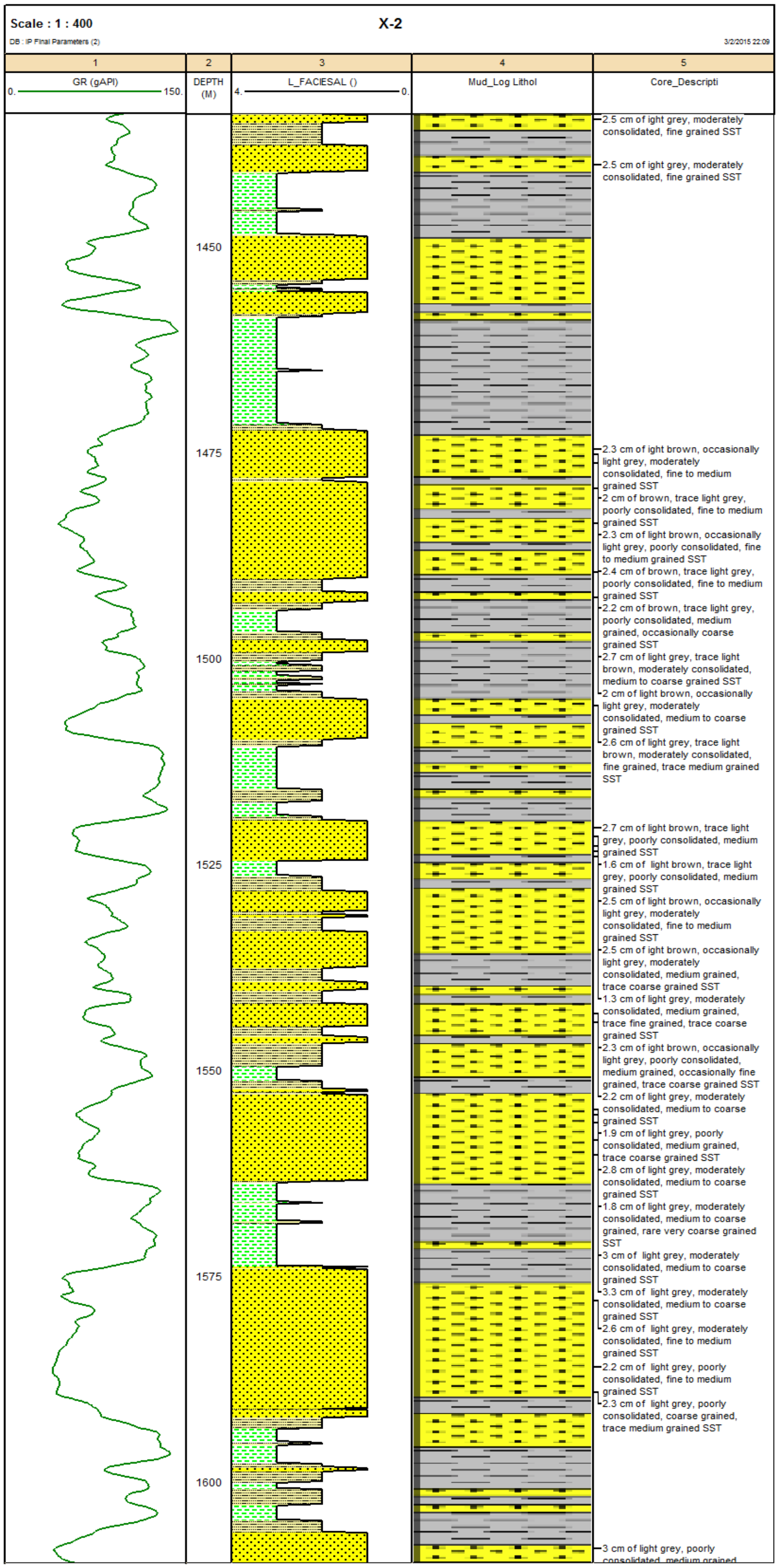

Figure 4.10 Shows a comparison between the generated electro-facies, the mud-logging interpreted lithology and the side-well core description of the well X-2.

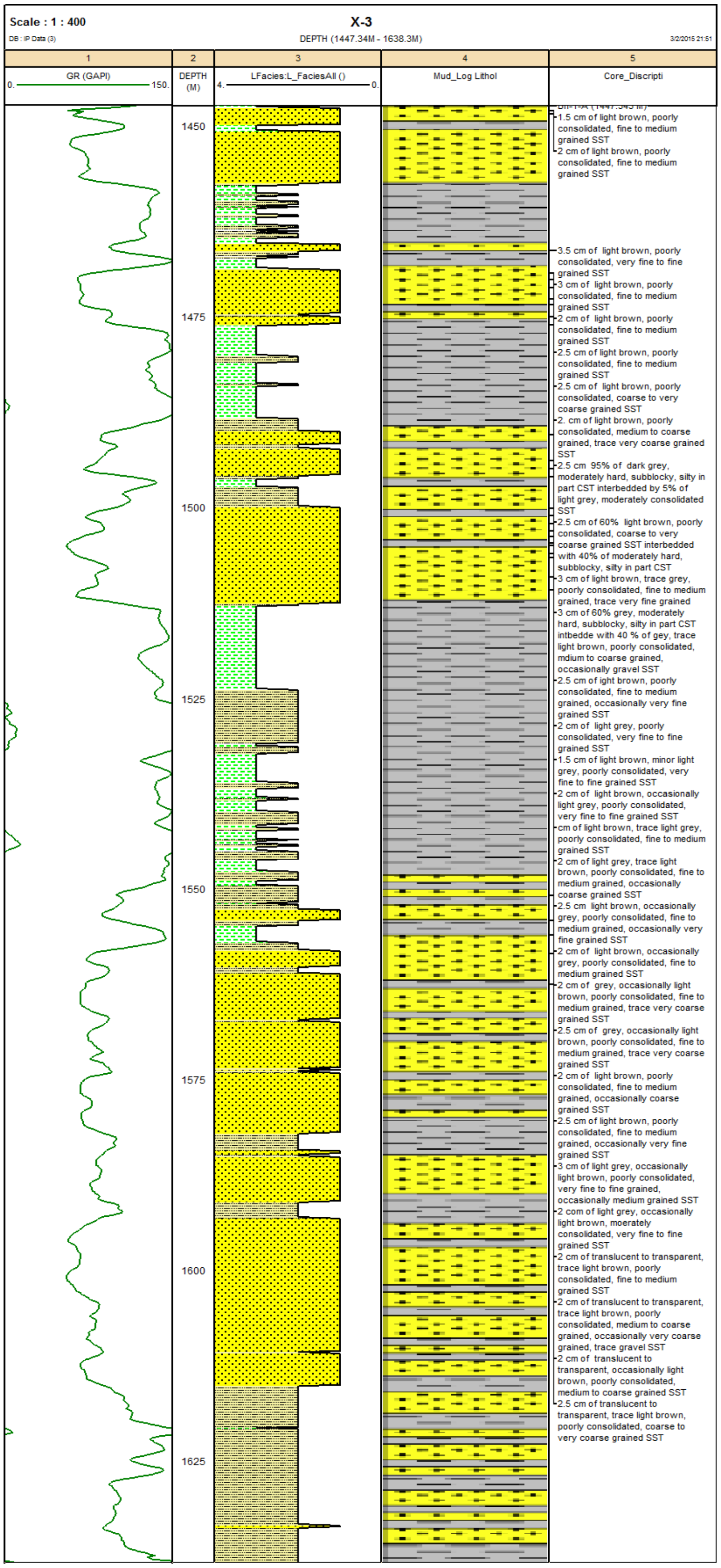

1.5 cm of light brown, poorly consolidated, fine to medium grained SST

2 cm of light brown, poorly consolidated, fine to medium grained SST

3.5 cm of light brown, poorly consolidated, very fine to fine grained SST

3 cm of light brown, poorly consolidated, fine to medium grained SST

2 cm of light brown, poorly consolidated, fine to medium grained SST

2.5 cm of light brown, poorly consolidated, fine to medium grained SST

2.5 cm of light brown, poorly consolidated, coarse to very coarse grained SST

2. cm of light brown, poorly consolidated, medium to coarse grained, trace very coarse grained SST

2.5 cm 95% of dark grey, moderately hard, subblocky, silty in part CST interbedded by 5% of light grey, moderately consolidated SST

2.5 cm of 60% light brown, poorly consolidated, coarse to very coarse grained SST interbedded with 40% of moderately hard, subblocky, silty in part CST

3 cm of light brown, trace grey, poorly consolidated, fine to medium grained, trace very fine grained

3 cm of 60% grey, moderately hard, subblocky, silty in part CST intbedde with 40 % of gey, trace light brown, poorly consolidated, mdium to coarse grained, occasionally gravel SST

2.5 cm of ight brown, poorly consolidated, fine to medium grained, occasionally very fine grained SST

2 cm of light grey, poorly consolidated, very fine to fine grained SST

1.5 cm of light brown, minor light grey, poorly consolidated, very fine to fine grained SST

2 cm of light brown, occasionally light grey, poorly consolidated, very fine to fine grained SST

cm of light brown, trace light grey, poorly consolidated, fine to medium grained SST

2 cm of light grey, trace light brown, poorly consolidated, fine to medium grained, occasionally coarse grained SST

2.5 cm light brown, occasionally grey, poorly consolidated, fine to medium grained, occasionally very fine grained SST

2 cm of light brown, occasionally grey, poorly consolidated, fine to medium grained SST

2 cm of grey, occasionally light brown, poorly consolidated, fine to medium grained, trace very coarse grained SST

2.5 cm of grey, occasionally light brown, poorly consolidated, fine to medium grained, trace very coarse grained SST

2 cm of light brown, poorly consolidated, fine to medium grained, occasionally coarse grained SST

2.5 cm of light brown, poorly consolidated, fine to medium grained, occasionally very fine grained SST

3 cm of light grey, occasionally light brown, poorly consolidated, very fine to fine grained, occasionally medium grained SST

2 com of light grey, occasionally light brown, moerately consolidated, very fine to fine grained SST

2 cm of translucent to transparent, trace light brown, poorly consolidated, fine to medium grained SST

2 cm of translucent to transparent, trace light brown, poorly consolidated, medium to coarse grained, occasionally very coarse grained, trace gravel SST

2 cm of translucent to transparent, occasionally light brown, poorly consolidated, medium to coarse grained SST

2.5 cm of translucent to transparent, trace light brown, poorly consolidated, coarse to very coarse grained SST

Figure 4.11 Show a comparison between the generated electro-facies, the mud logging interpreted lithology and the side-well core description of the well X-3.

the inter-granular spaces changing the porosity but do not affecting the matrix density significantly (Poupon and Gaymard, 1970 in Migdad 2013) (Figure 4.12).

Commonly, one should differentiate between two types of shale based on their Cation Exchange Capacity (CEC): these are *passive shale* and *effective shale*. The passive shale which comprises chlorite and kaolinite, is characterized by it is predominantly CEC. On the other hand, the effective shale which is mainly made of montmorillonite characterized by high CEC. The clay/shale volume present in a certain interval of a reservoir can be identified by the common logging curves such as gamma ray logs, density logs, neutron log, and resistivity logs. These logs often referred to as a "shale indicators" (Poupon and Gaymard, 1970). They can also be used to differentiate between the two types of shale. Most of the indicators can detect the effective shales, while neutron logs can only detect the passive shales.

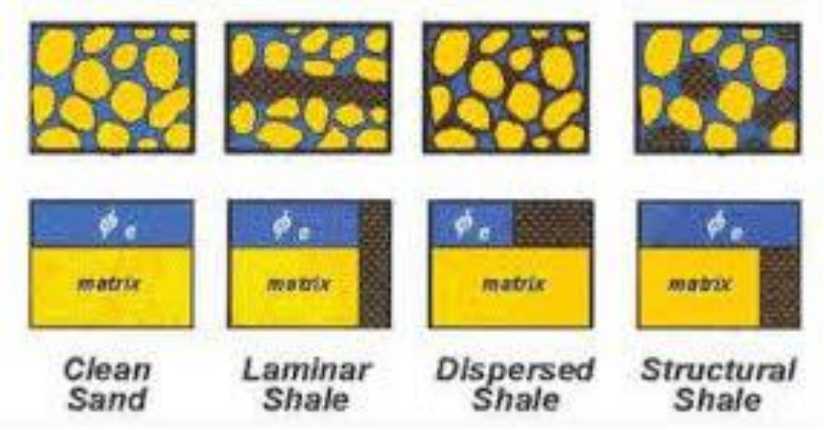

Figure 4.12 The three common forms of the shale present in a sandstone (Schlumberger, 1987).

In this study, I used the gamma ray log as shale indicator due to absence of passive shale and radioactive sands (Figure 4.13). Evaluation of clay volume based on the gamma ray used in this study requires calculation of the gamma ray index based on the Eq. 3.1. A nonlinear equation (Eq. 3.3) stated by Larinov (1969) for older rocks was used to calculate the clay volume in the Bentiu-1 reservoirs interval.

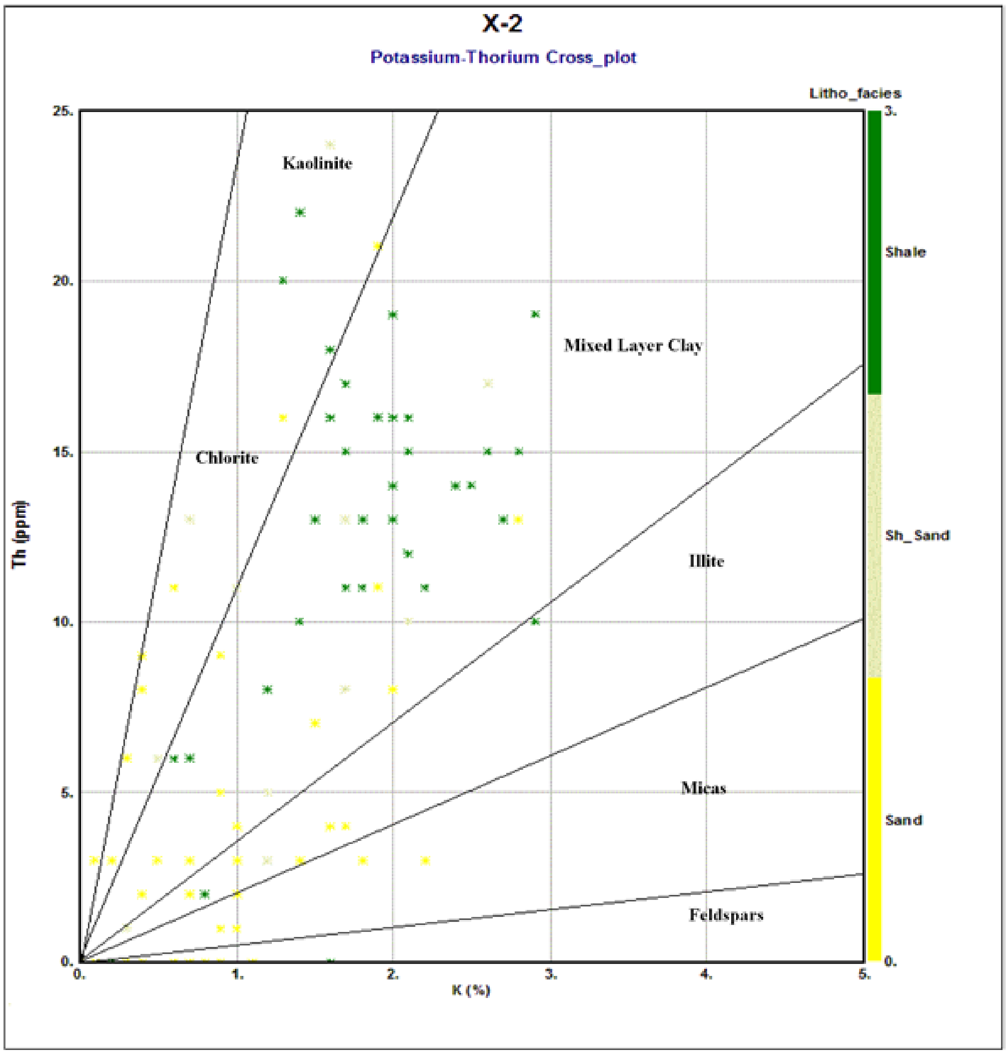

Figure 4.13 Shows a cross-plot between the potassium (K) in % and the thorium (Th) in ppm to illustrate different types of clay minerals in the study interval.

The shale volume calculated in this study was used primarily for the elimination of the clay effect from the porosity and water saturation estimations. The clay volume has been used also as one of the input curves for the electro-facies evaluation (Section 4.1). This is because the vertical and lateral distribution of the clay is governed by some depositional attributes (Figures 4.14). Histograms presented in Figure 4.14 show the clay distribution in five wells located in different parts throughout the study area. The clay volume increases from north to south towards the central parts of the area and from the rims of the structure in the west towards the central highs.

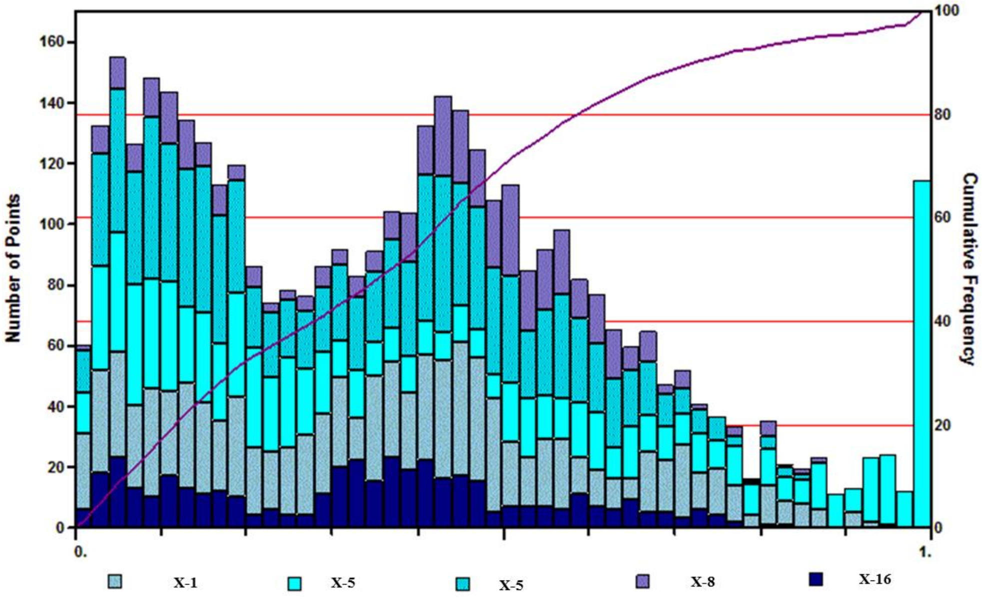

Figure 4.14 The clay volume histogram of five wells form north to south. More volume is encountered at the central part of the study area.

4.3.2 Porosity Evaluation

To determine the optimum porosity value for model building in this study, four types of porosity have been calculated. The density porosity was calculated by the Eq.3.10, for the clean (free of clay) wet formations, while the Eq. 3.11 is applied to eliminate the erroneous values caused by the presence of shale and/or clay minerals. Neutron porosity was calculated by the Eq. 3.12 after correcting the log responses to the sandstone porosity unit. The sonic porosity was determined from the sonic interval transit by Eq. 3.7 (Wyllie and others equation) for clean, unconsolidated formations. This equation, when modified in the form of the Eq. 3.8 accounts for the compaction factor. This modified Wyllie equation was used to calculate the sonic porosity in the Bentiu-1 reservoir interval (Figure 4.15).

Finally, the average of the four types of porosity is calculated and used later as one of the modeling input parameters. The average porosity was plotted against the core porosity from two wells, namely X-2 and X-3 (Figures 4.16 and 4.17). A good correlation was found between the calculated average porosity and the core porosity. The goodness of fit (R^2) was 0.85 for Well X-2 and 0.79 for Well X-3.

4.3.3 Permeability Evaluation

The permeability is controlled mainly by the pore size and the pore throat size distributions. However, the presence of clay in the reservoir layers in any of the three common forms (Figure 4.12) may drastically reduce permeability. With the current state of there is no available technique that could directly measure the permeability downhole. Therefore, a number of empirical models (such as the Timur and Morri-Bigg's oil equation) have been developed to overcome this problem (Schlumberger, 1987).

A predefined relation between the porosity and permeability from core analyses as well as other analysis such as irreducible water saturation, grain size analysis and repeated formation testing often provides a good approximation of the reservoir's permeability.

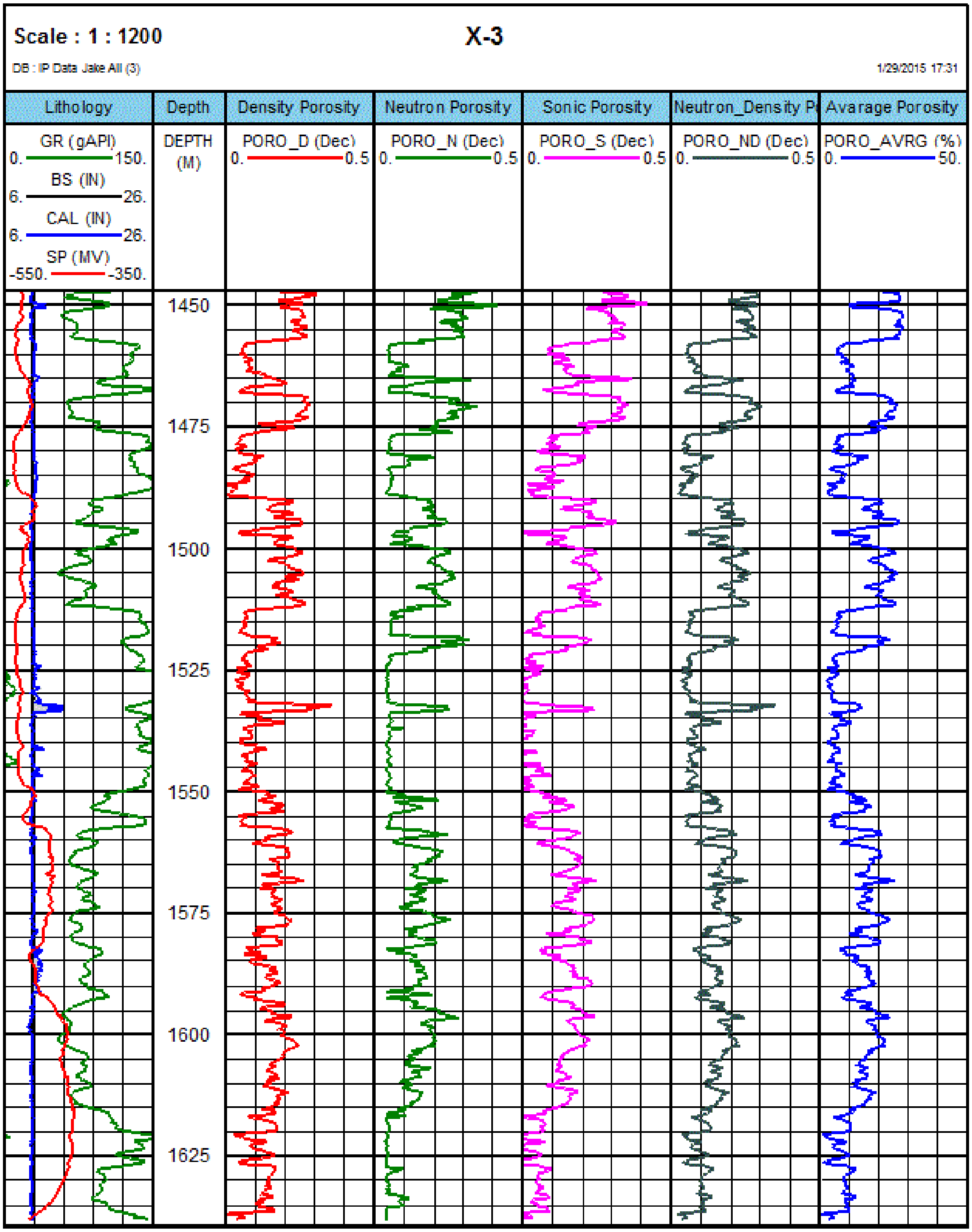

Figure 4.15 The four types of porosity calculated in Well X-3 namely, the Density porosity (Track #3), Neutron porosity (Track #4), Sonic porosity (Track #5), Neutron_Density porosity (Track #6) and average (Track #7).

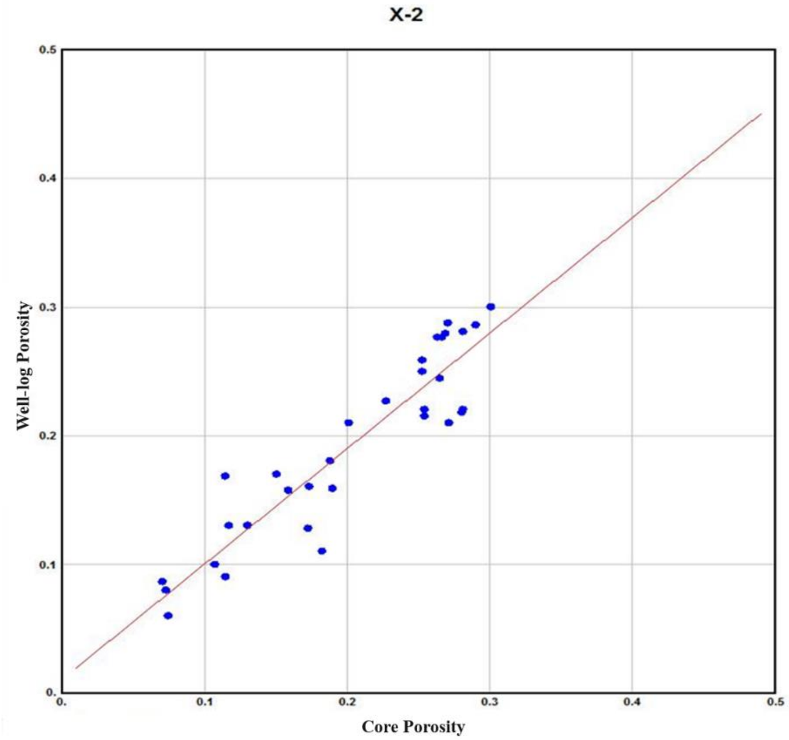

Figure 4.16 Cross-plot between the core porosity and the well logging average porosity of well X-2.

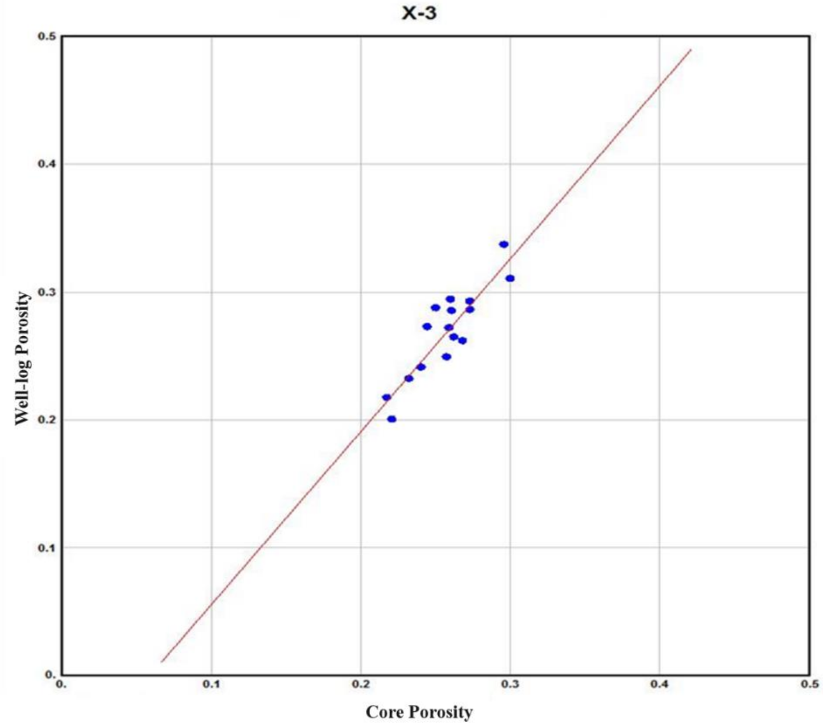

Figure 4.17 Cross-plot between the core porosity and the well logging average porosity of well X-3.

In this study, the permeability values were determined based on a pre-established relationship between core-porosity and the core-permeability (Eq. 4.1). This relationship was based on the cross-plot between the porosity and the permeability (Figure 4.18) of the cores recovered from Wells X-2 and X-3.

$$K\ (mD) = 0.1845 \times e^{.3568\phi} \tag{4.1}$$

This relationship is then applied to calculate the permeability from the average porosity curve. Figure 4.19 shows an example for the calculated permeability curve from the average porosity on the Eq. 4.1 from (X-2 Well).

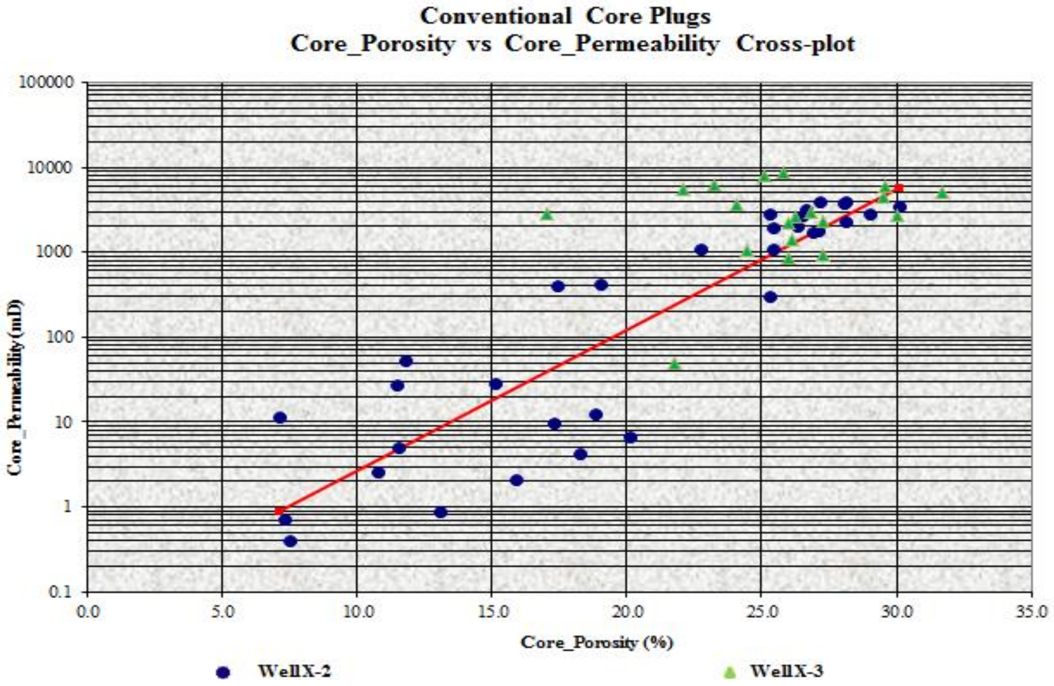

Figure 4.18 Cross-plot between the core porosity and the core permeability on a semi-logarithmic paper (Petroenergy E&P, 2006).

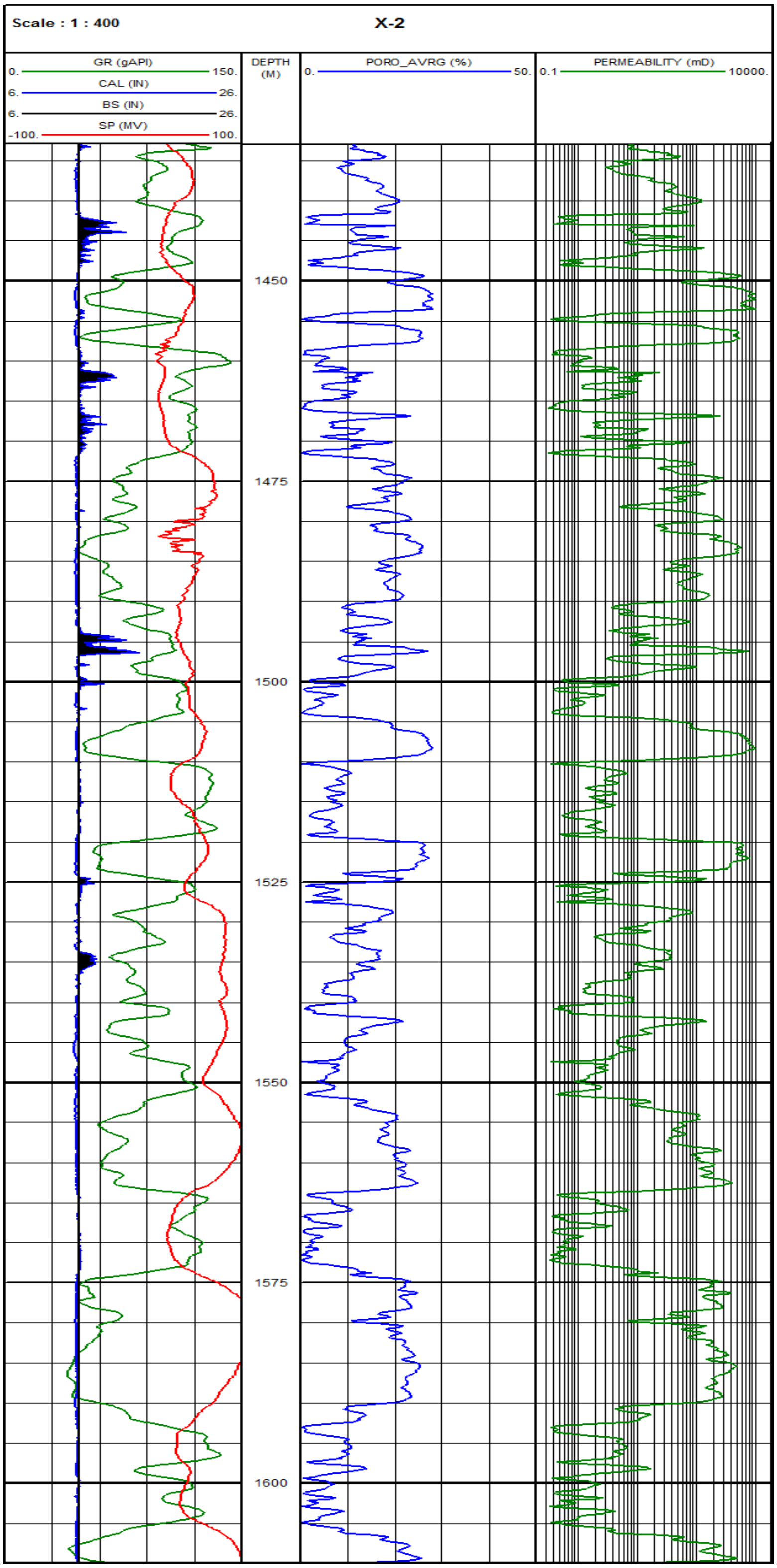

Figure 4.19 The log-derived permeability (Track #4) based on the average porosity (Track #3) calculated form the four types of porosity.

4.3.4 Water Saturation Evaluation

The water saturation is a ratio of water volume to pore volume excluding the shale-bound water. Among the various methods and models available for the water saturation calculation discussed in Section 3.1.4, the Indonesian Equation (1971) modified for shaly formations (Eq. 3.18) was used in this study. This equation found to be adequate for determining the water saturation in the Bentiu-1 interval due to the similarities of the conditions upon which the Indonesian equation was based, namely the shale percentage present (Poupon, and Leveaux, 1971).

The parameters required to apply the modified Indonesia Equation (Eq. 3.18) were acquired from the core analysis reports of Well X-2 and Well X-3. The cementation index (m) was determined from Archie's first law (Eq. 4.2 and Figure 4.20). The cementation index is 1.9 for the study interval (Figure 4.20). The saturation exponent (n) has values commonly between 1.8 and 2.0. In this study the saturation exponent was obtained from the core analysis reports by cross-plotting the resistivity index and the water saturation (Figure 4.21). From this doubly logarithmic cross-plot, the slope gives the saturation exponent based on the empirical second Archie's law (Eq. 4.3). Hence, the saturation exponent is found to be 1.77 for the Bentiu-1 reservoir interval. The formation water resistivity (R_w) was defined to be 0.12 ohmm for the same reservoir from the laboratory analysis of the water samples.

Archie's first law $$F = \phi^{-m} \tag{4.2}$$

Archie's second law $$I = S_w^{-n} \tag{4.3}$$

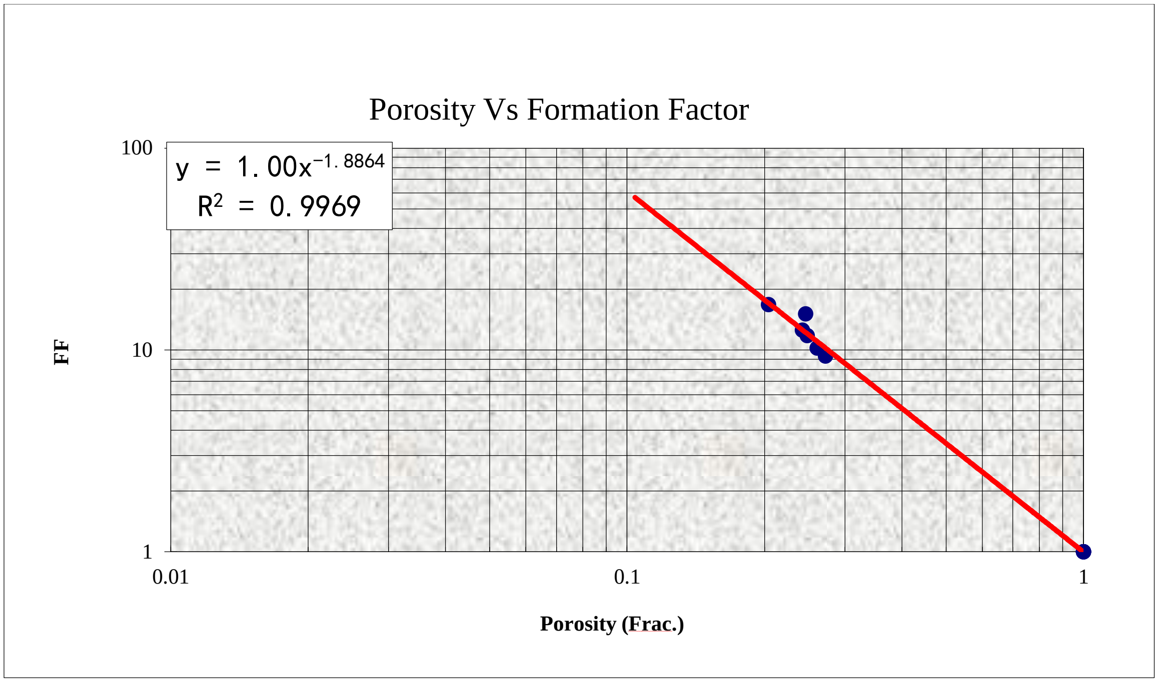

Figure 4.20 Cross-plot of the porosity and the formation factor. The slope gives the cementation exponent according to Archie's first law (Petroenergy E&P, 2006).

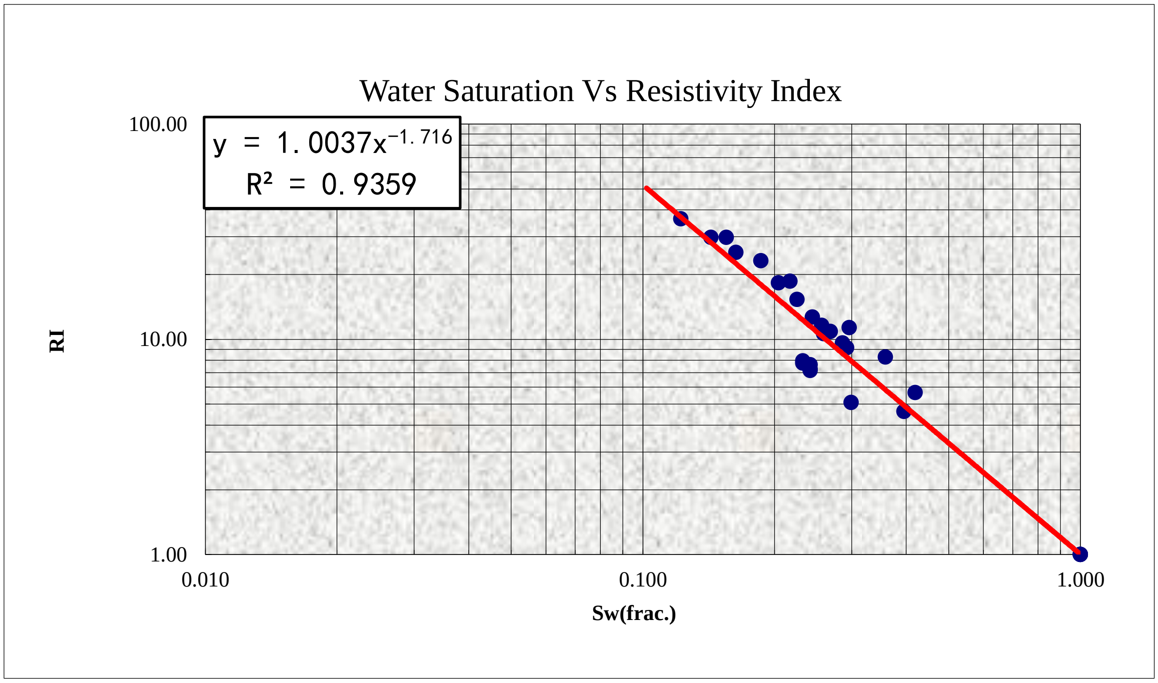

Figure 4.21 Cross-plot between the water saturation and the resistivity index. The slope gives the saturation exponent according to Archie's second law (Petroenergy E&P, 2006).

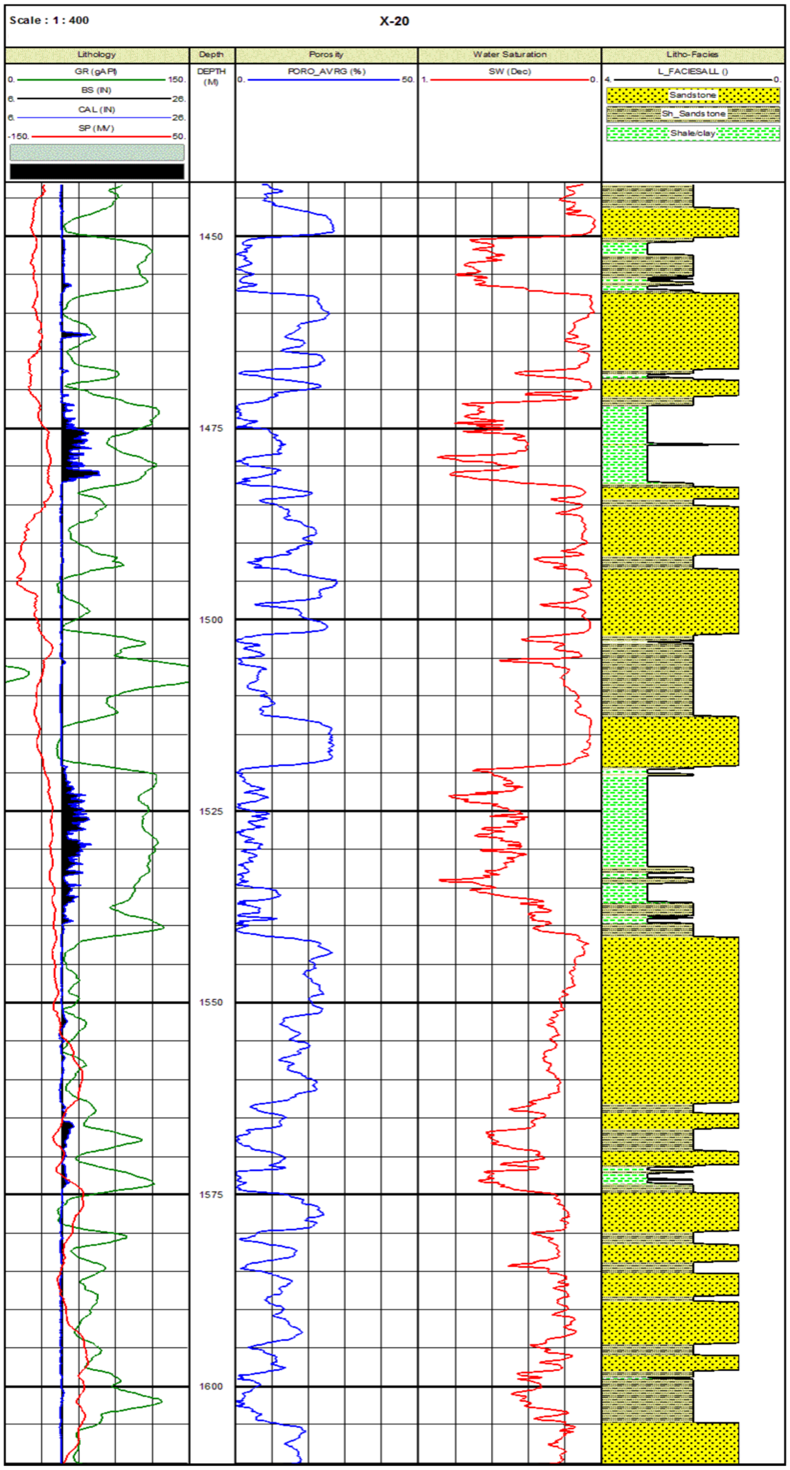

Figure 4.22 The calculated water saturation (Track #4) along with the porosity curve (Track #3) used to calculate water saturation and the generated lithofacies (Track #5) for comparison.

CHAPTER 5

Structural and Geostatistical Modeling

5.1 Introduction

This chapter has two sections devoted to the results of the structural and geostatistical modeling. The first section gives in details the results of the seismic data interpretation leading to the structural framework necessary to establish the structural control over the study interval using existing faults and the bounding horizons. The second section discusses in detail the results of geostatistical modeling in a hierarchical manner. In this section, all previous information and results will be integrated to complete the final step in the study workflow and to provide answers to the stated problems.

5.2 Structural Modeling

In order to establish a meaningful structural framework that can serve as a basis for the structural control over the study interval, a cropped 3-D post-stack migrated seismic was interpreted. The seismic cube is composed of 181 Inlines from 60 to 240 and 261 Xline from 150 to 410 (Figure 5.1). This cube was acquired with surface disposal element of 30×15 and total area of 21062 km^2 (3.9×5.4 km). The main objective behind the seismic cube interpretation is to define the major faults that affect the study interval and the bounding (top and bottom) horizons.

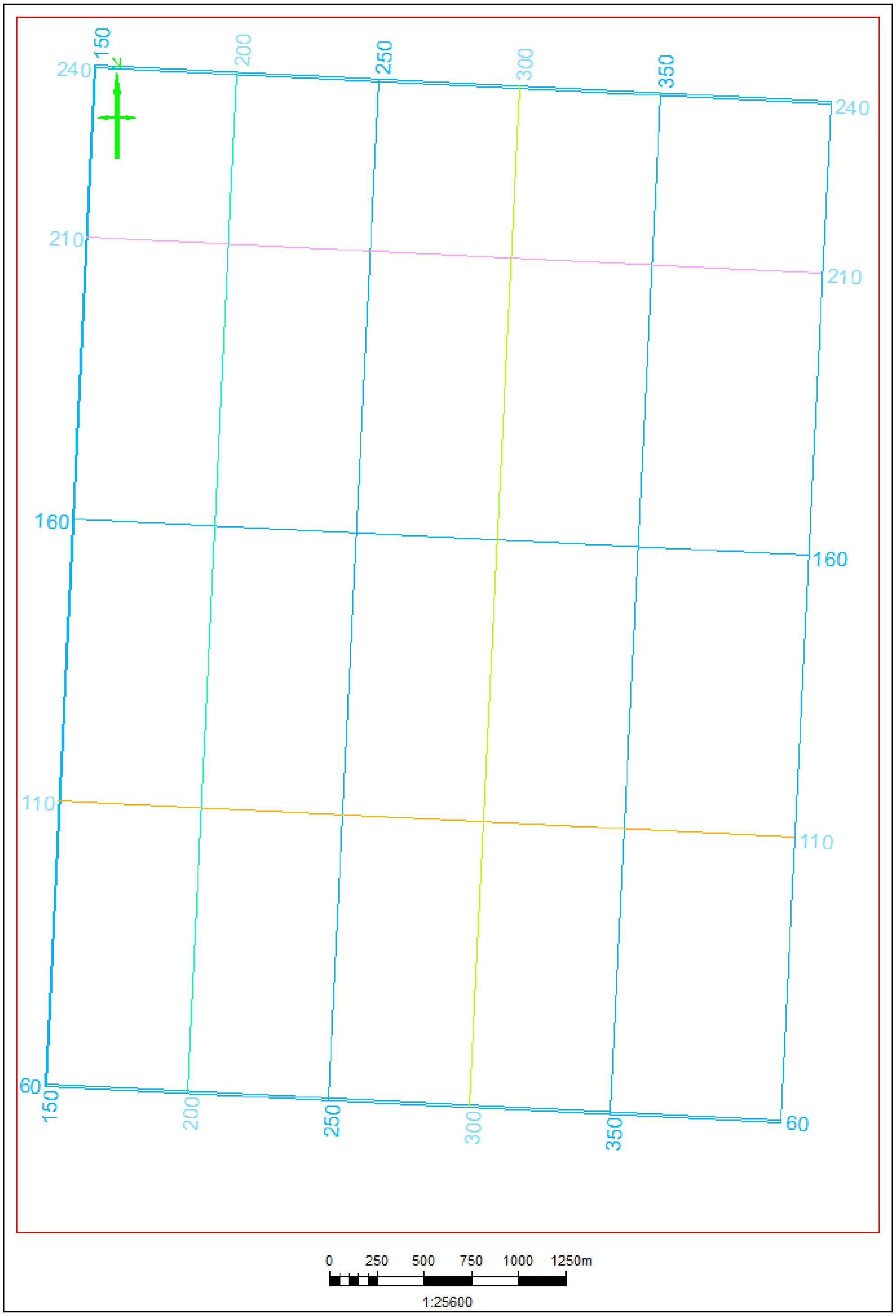

Figure 5.1 Base map of the seismic cube surface survey.

5.2.1 Horizons Interpretation

The seismic cube was interpreted in terms of horizons based on the well tops (formation markers) defined from the wells. The well tops have been interpreted form the GR, DT logs, and the mud logging (master log) information. These formation markers were then matched with the corresponding reflectors from the seismic cube to infer the surfaces in general and the top and bottom of the study interval in particular (Figure 5.2). A number of horizons (Formation Tops) such as Amal, Baraka, Ghazal, Aradeiba, Bentiu, and Abu Gabra have been interpreted in a few lines (Figure 5.3, 5.4 and 5.5). However, all the 3-D volume was interpreted for the Bentiu-1 interval with fine resolution (two lines increments). This interval is defined by its top and bottom horizons that identify the formal Upper Bentiu Member. The top horizon represents the top of Bentiu Formation and termed the Bentiu-1 Top. The bottom horizon corresponds to the top of the Middle Bentiu Member and this horizon is termed the Bentiu-1 Bottom (Figure 5.6).

Bentiu-1 Top; this surface represents a regional surface that is identified easily across the study area and the Muglad Basin. In principle, this surface separates between the sag phase of the first rifting cycle characterized with coarser sediment of the Bentiu Formation and the lower part of the second rifting phase characterized with fine sediments of the Aradeiba Formation. Hence, this surface (Formation marker) is identified from the mud logging (master log) by the change in deposition from large packages of sand into abrupt change towards clay/shale sediment. This conclusion was supported by the GR and DT curves. The GR reveals a big kick to the right and remains high for over 25m.

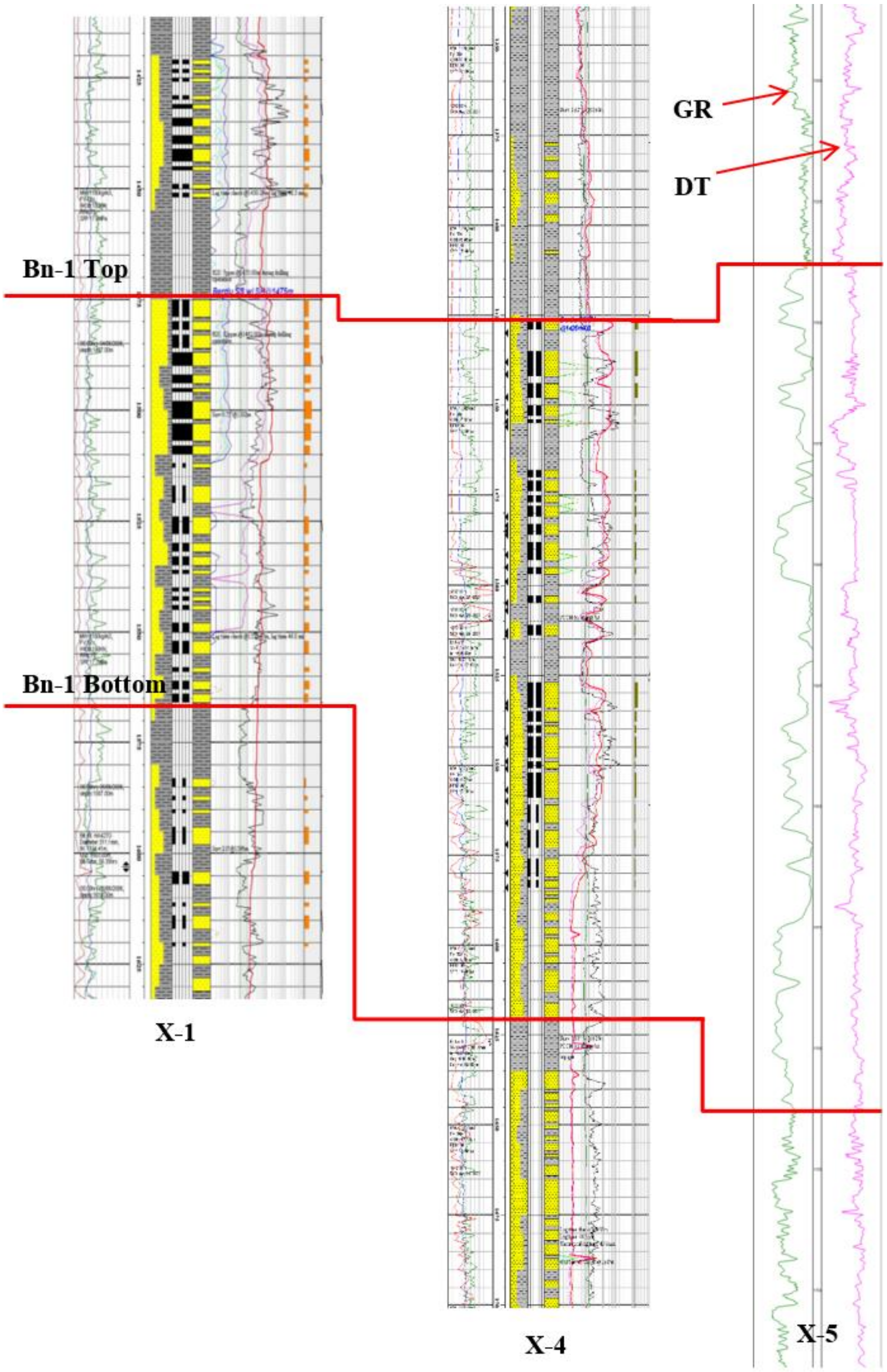

Figure 5.2 Top and bottom interval markers picked from the logging information of three wells.

The DT curve shows a left-hand deflection (high transit time) and follows the GR curve's pattern for the aforementioned 25m (Figure 5.2). The Bentiu-1 Top marker identified from the wells was matched to a reflector in the seismic data. This reflector is found to be of poor quality, discontinuous and broken near the well location due to the proximity of the major fault (Fault_major). However, towards the center of the study area, this reflector was found with fair quality and good continuity (Figure 5.3). The interpretation was carried out using a package-by-package approach. In this fashion the conformable horizons on one side of a fault were interpreted first before moving to the other side of the fault and so on. This approach is found to be appropriate to work due to poor to fair quality of the seismic data. After completing the interpretation of this horizon throughout the study area, the depth-structural map (Figure 5.7) was generated.

Bentiu-1 Bottom; this horizon represents the surface that separates the upper and lower Bentiu members. Lithologically, this surface is placed to separate two members (upper and lower) with variable depositional environments. The upper member (the interval under consideration) is dominated by sandstone facies and high sand to shale ratio (Upper Bentiu Member) due to the deposition in braided shallow channels (Idriss, 2002). The lower member (Middle Bentiu Member) is characterized by lower sand to shale ratio due to the deposition in sand-bed dominated streams. Hence, this surface is placed at the top of the well-developed fluvio-lacustrine shale occurring within approximately 200m of Bentiu Formation (Figure 5.2). The aforementioned information is corroborated by with the lithology description from the master log (mud logging). Moreover, a good signature for the position of this surface is found from the GR and DT curves (Figure 5.2).

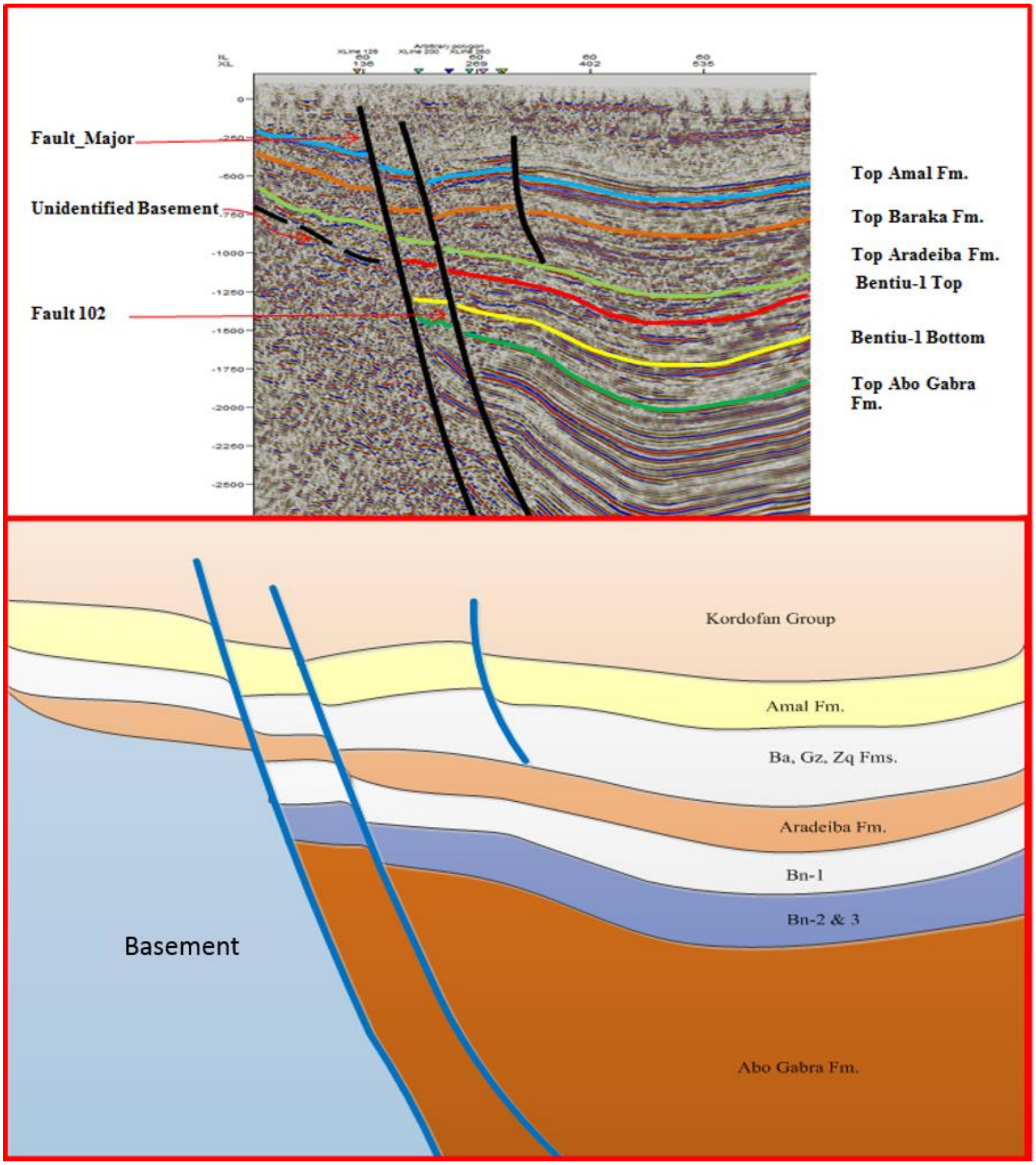

Figure 5.3 The interpretation result of the Inline 60 (top), and the inverted geological 2D section of this inline (bottom).

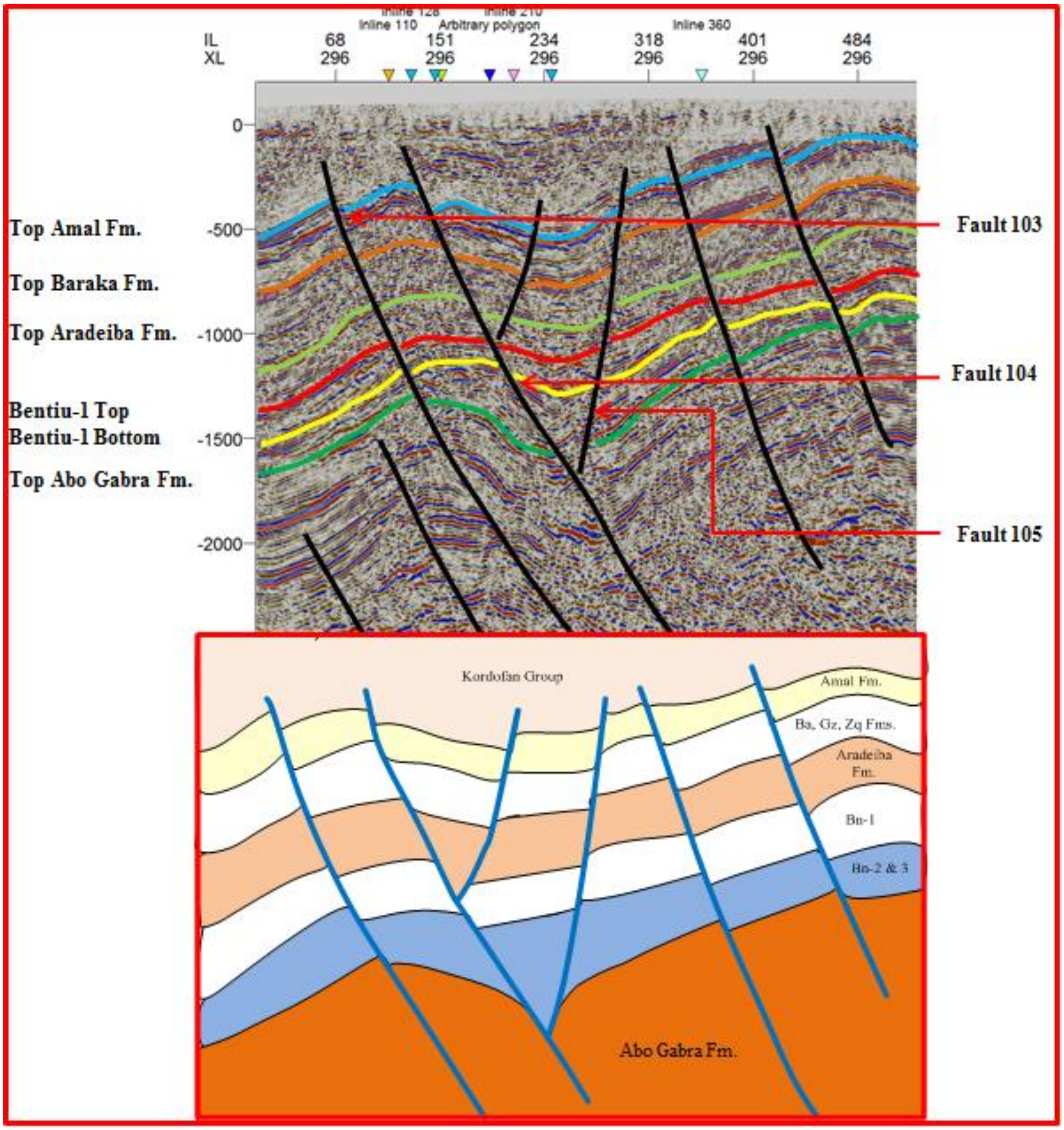

Figure 5.4 The interpretation result of Xline 296 for a number of formation markers (top), and the geological 2D inverted cross section based on the interpretation (bottom).

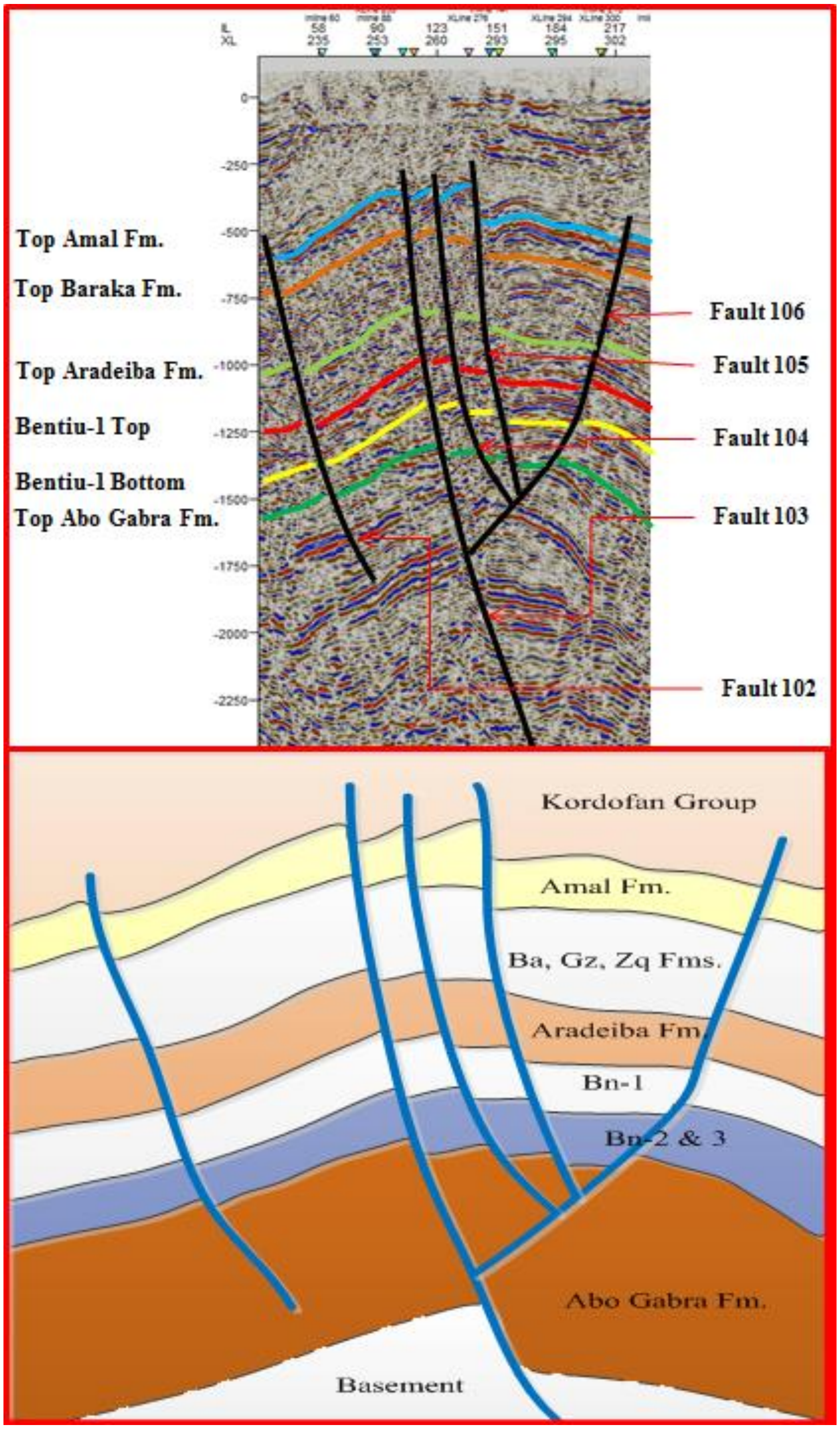

Figure 5.5 An arbitrary seismic section interpreted for a number of markers identified from the wells (top) along with 2D geological cross-section constructed upon the arbitrary seismic line interpretation (bottom).

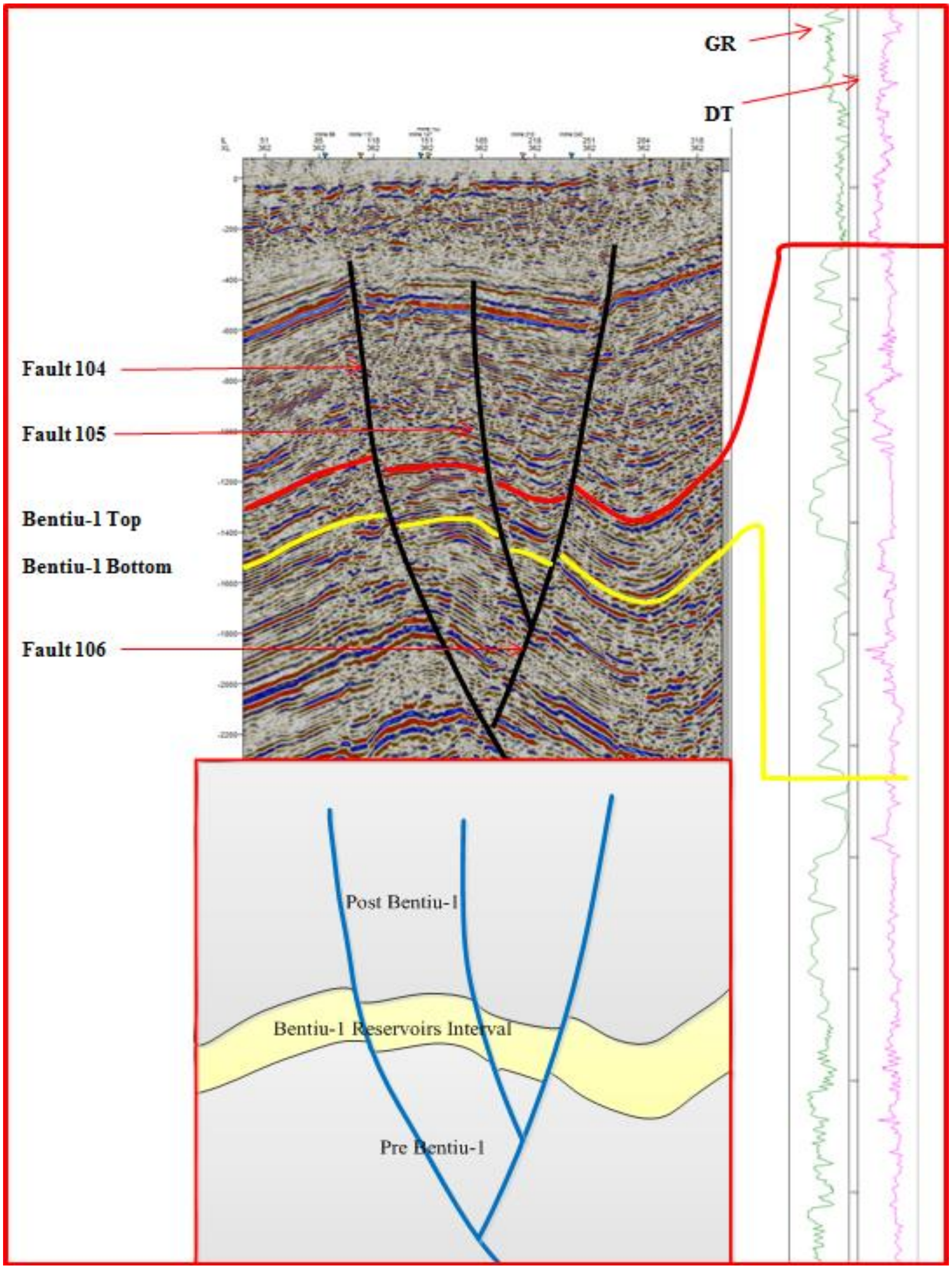

Figure 5.6 Xline 362 interpreted for the top and bottom of Bentiu-1 reservoirs interval (top left) based on the markers identified from the well logs (right side). The bottom of the figure represents a 2D geological cross-section of the study interval.

The GR curves show a significant right kick and follow a 20 m thick shale unit. The DT curves show left-hand deflection that match with the GR pattern for the 20 m shale unit. This bottom marker is found corresponding to a fair reflector in the seismic data. Once again, this reflector is found with the same characteristics with the Bentiu-1 top marker in terms of resolution, quality, and continuity (Figures 5.3 to 5.6). The same interpretation approach used for the Bentiu-1 top marker interpretation was followed here. Hence, this marker is interpreted throughout the 3-D volume in two line-based increments leading to the generation of the depth-structural map (Figure 5.8).

Based on the isochore map (Figure 5.9), the interpreted seismic cubes, and the inverted 2D cross-sections (Figure), the study interval thickens generally from the center eastwards. Hence, a cross-section of the study interval (Figures 5.3 to 5.6) shows that it forms an anticline. This conclusion is consistent with the structural regime over the Fula Sub-basin (Figure 1.1). The thickness of the interval increases eastward with the eastern rims of the area representing a depo-center. These results are comparable with the published work from the different parts of the Muglad Basin. Schull (1988) described the presence of anticlines among other structures such as rollover anticlines and drape folds (Figure 2.3).

Based on the generated depth-structural maps of the two horizons (Figures 5.7 and Figure 5.8) the study interval represents a dome-like structure (Figure 5.10). This structure is characterized by a major axis that extends in north-south direction across five of the interpreted six faults and parallel to the major fault (see section 5.2). Moreover, the minor axis is extending in east-west direction is terminated against the major fault (fault_major in Section 5.2).

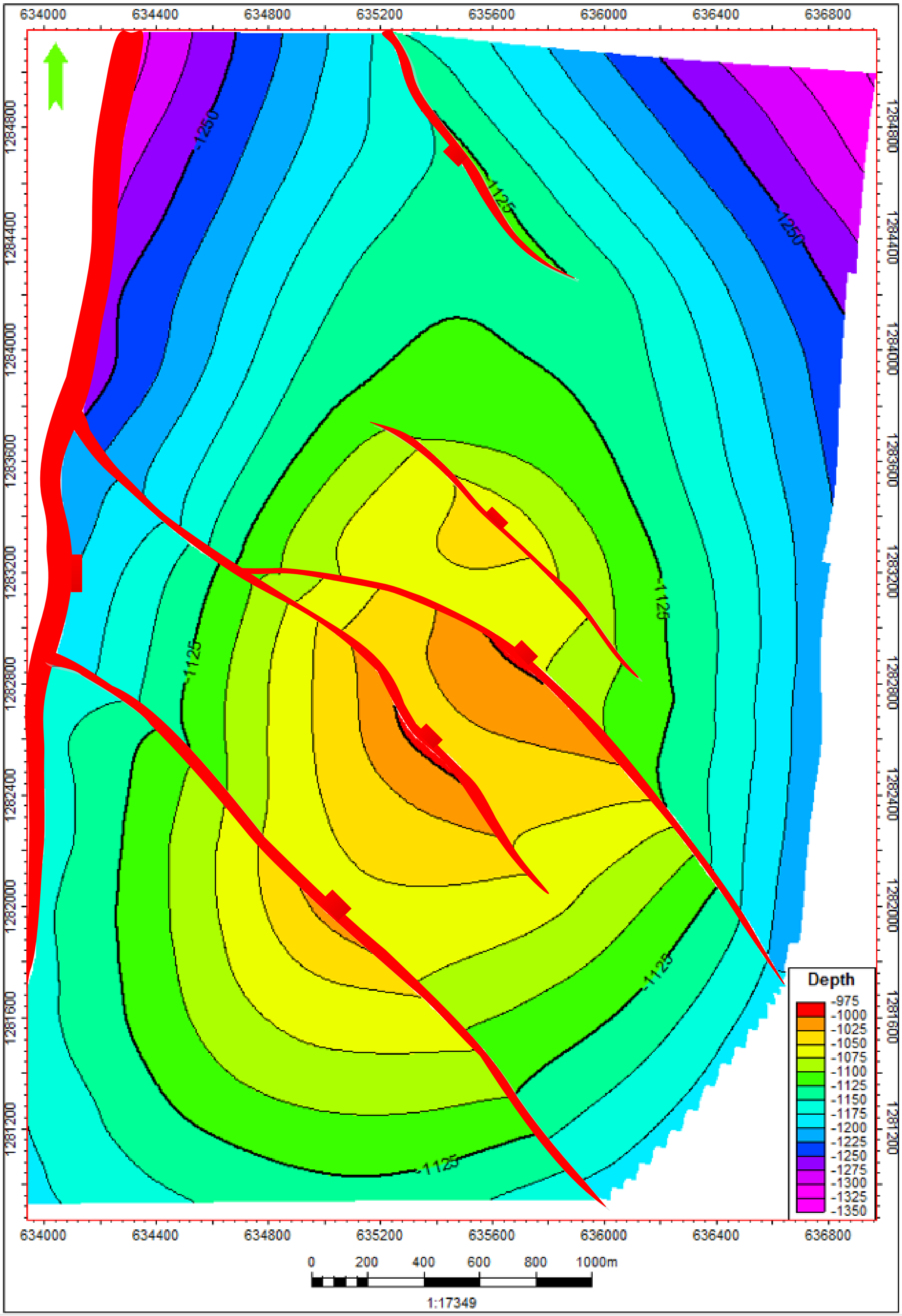

Figure 5.7 The depth-structural map to the top of the Bentiu-1 reservoir interval.

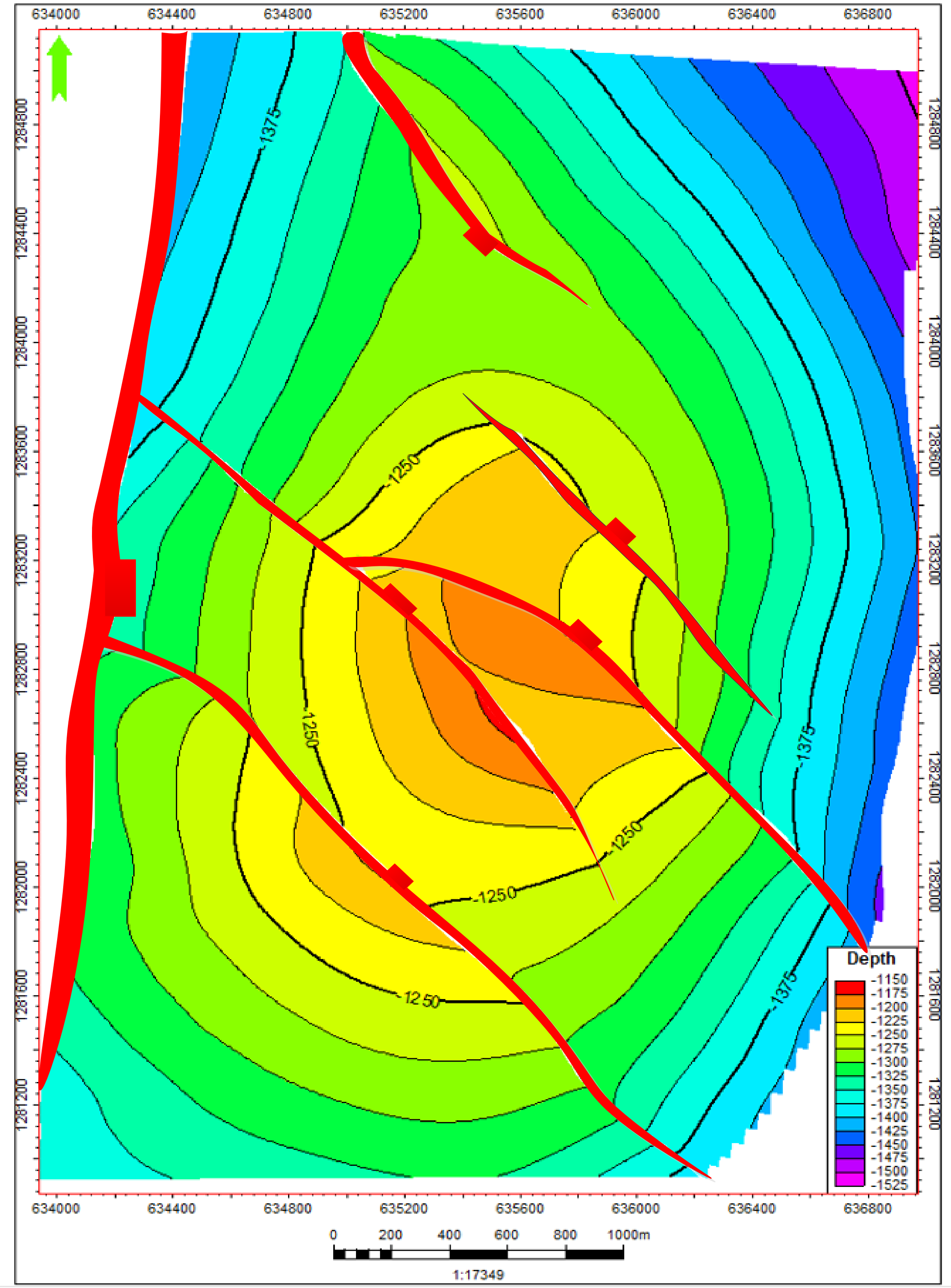

Figure 5.8 The depth-structural map to the bottom of the Bentiu-1 reservoir interval.

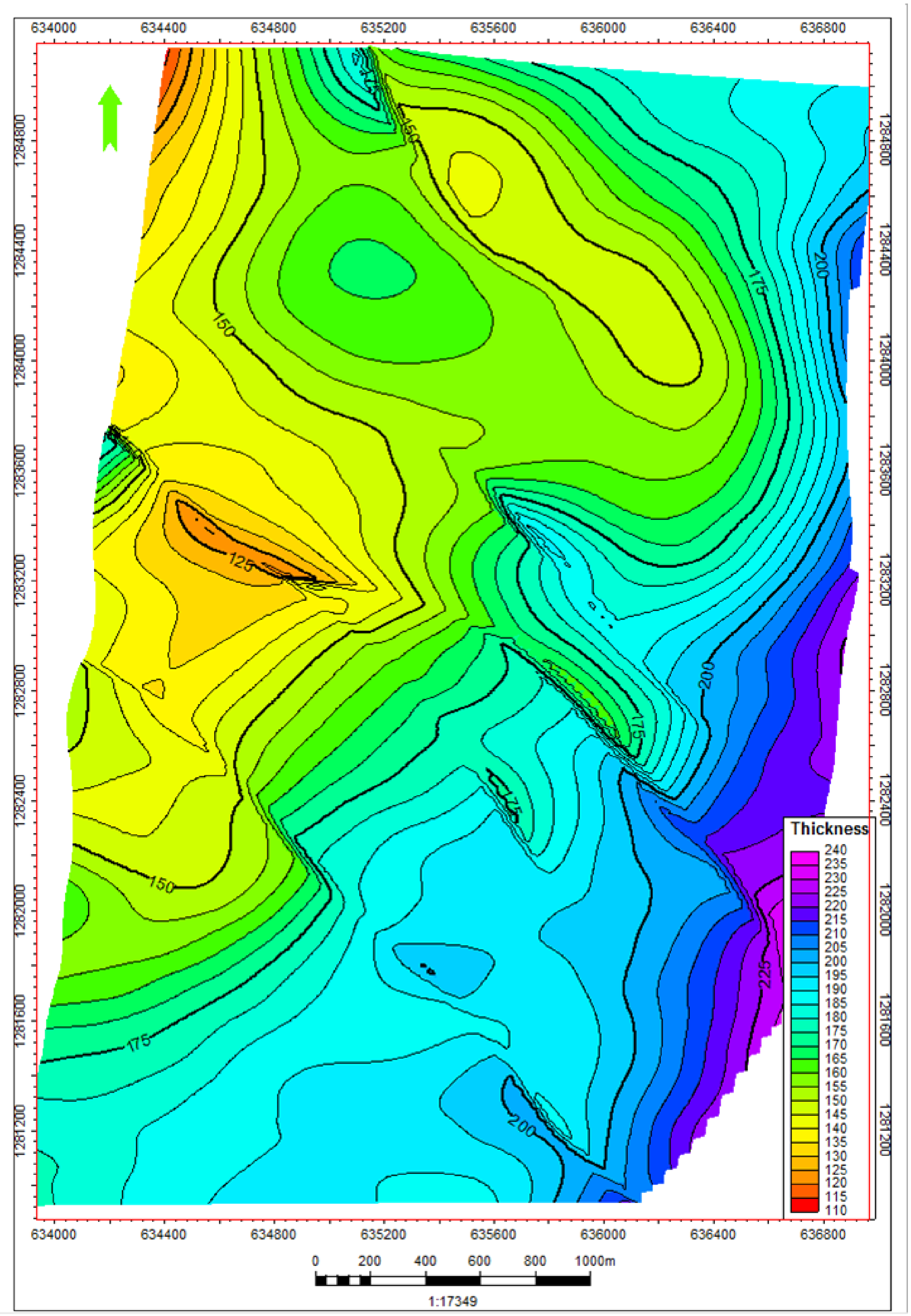

Figure 5.9 The isochore map of the Bentiu-1 reservoirs interval showing the variation of vertical thickness. It thickens away from the center of structures to the rims in the east and west.

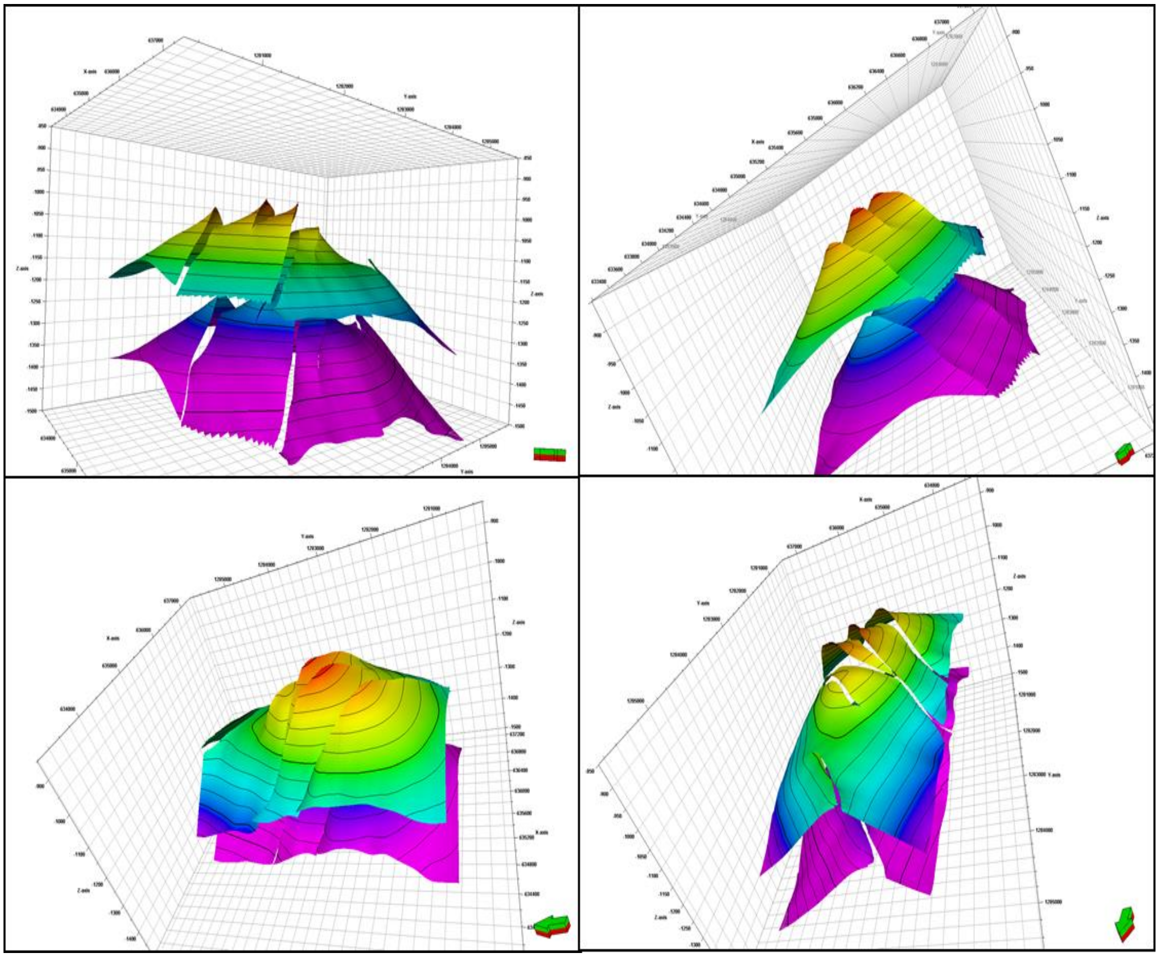

Figure 5.10 A different 3-D views of the Bentiu-1 reservoirs interval.

5.2.2 Faults Interpretation

A faults interpretation has been carried on the 3-D seismic data to determine those faults affecting the study interval. The results provided basis of the structural modeling (geological framework). As with the horizons interpretation, the fault interpretation started with interpreting a number of seismic lines with coarse (10 lines increment) resolution (Figure 5.4). Then, a fine (two lines increment) resolution was applied to determine the fault that has directly displaced the Bentiu-1 reservoir interval (Figures 5.5 and 5.6). Altogether, six faults have been found directly affecting and involved in the displacement of the Bentiu-1 reservoirs interval (Table 5.1). The major fault (Fault_major) represents a deep-seated normal fault that dips towards the east with a north-south strike and marks the western boundary of the study area. The minor faults (Fault-102 to Fault-105) represent a set of normal faults varying in length and throw (Table 5.1). These faults were probably associated with the major fault. They have a steep northeast dips and approximately northwest strike. The sixth fault (Fault 106) represents a normal fault that dips to the southwest with northwest-southeast strike. This fault behaves as an antithetic fault for the previous four faults (Figures 5.6, 5.7, and 5.8). It was again originated from the major fault where they connect north of the study area.

Table 5.1 Faults associated with the Bentiu-1 reservoir interval.

Fault	Length (m)	Heave (m)	Throw (m)
Fault_Major	4236.37	50	100
Fault 102	2730	15	50
Fault 103	2224.73	15	10
Fault 104	16020	23	15
Fault 105	15780	10	10
Fault 106	1287	25	70

5.2.3 Structural Model

The structural model in this study has been achieved through a process in which the interpreted faults, top and bottom horizons of the study interval were integrated to define the 3-D geological framework for the subsequent steps. The process of generating the 3-D framework consists of following four main processes: fault modeling, pillar gridding, horizons defining, and layering.

In the *fault-modeling* process, the six interpreted faults were transformed into a 3-D framework in conjunction with the second step (pillar gridding). The fault sticks generated in the seismic interpretation were connected and gridded where appropriate (Figures 5.11 and 5.12). Moreover, all the fault truncation, inter-fault connection, and fault horizons intersections were taken into account in these two steps. The fault modeling process may be defined as the development of the 3-D skeleton, which defines the boundary of study area (Figure 5.13). The resolution is acquired from the 3-D seismic survey resolution (Figure 5.1); more precisely it is the Inline-Xline spacing (30×15 meter).

The *horizons defining* process involves incorporating the previously generated two surfaces (Bentiu-1 Top and Bentiu 1 Bottom) and the six faults into the 3-D skeleton. This process is applied to limit the 3-D skeleton to the study interval top and bottom horizons, which are designed to define the vertical layering, constraints. Moreover, the top and bottom of the interval were also used to limit the faults previously defined in the building of the 3-D skelton (Figure 5.14). The layering process revolves mainly around defining the vertical resolution of the 3-D grid. In this study, the whole interval was treated as one single zone. Hence the study interval was divided vertically to be as close as possible to the well logs resolutions (Figure 4.24). This process depends on finding the appropriate number of layers to be built according to the thickness variations of the study interval (Figure 5.9). The average thickness of the study interval from the isochore map is about 170 m. Therefore, the interval is subdivided into 170 layers vertically (Figure 5.15). This subdivision provided the resolution needed to fulfill my study objective and to capture details to assess the heterogeneity in reservoirs entities.

Figure 5.16 shows the final structural model of the Bentiu-1 reservoirs interval that was built in successive manner using the steps described earlier. In this figure, the top and bottom of the interval represent the vertical constraints of the study interval. The major fault represents the western boundary of the area where a polygon helped in securing the remaining boundaries of the study area. The faults aided in segmenting the study area into three from south to north according to their length. The first segment occupies the area between the southern boundary and the Fault-102. The third area lies between the northern boundary and the Fault-104. Whereas the second segment falls between the previous two segments, more precisely between the Fault-102 and the Fault-104. This structural model included the structural and stratigraphic constraints needed for the generation of the various geostatistical models.

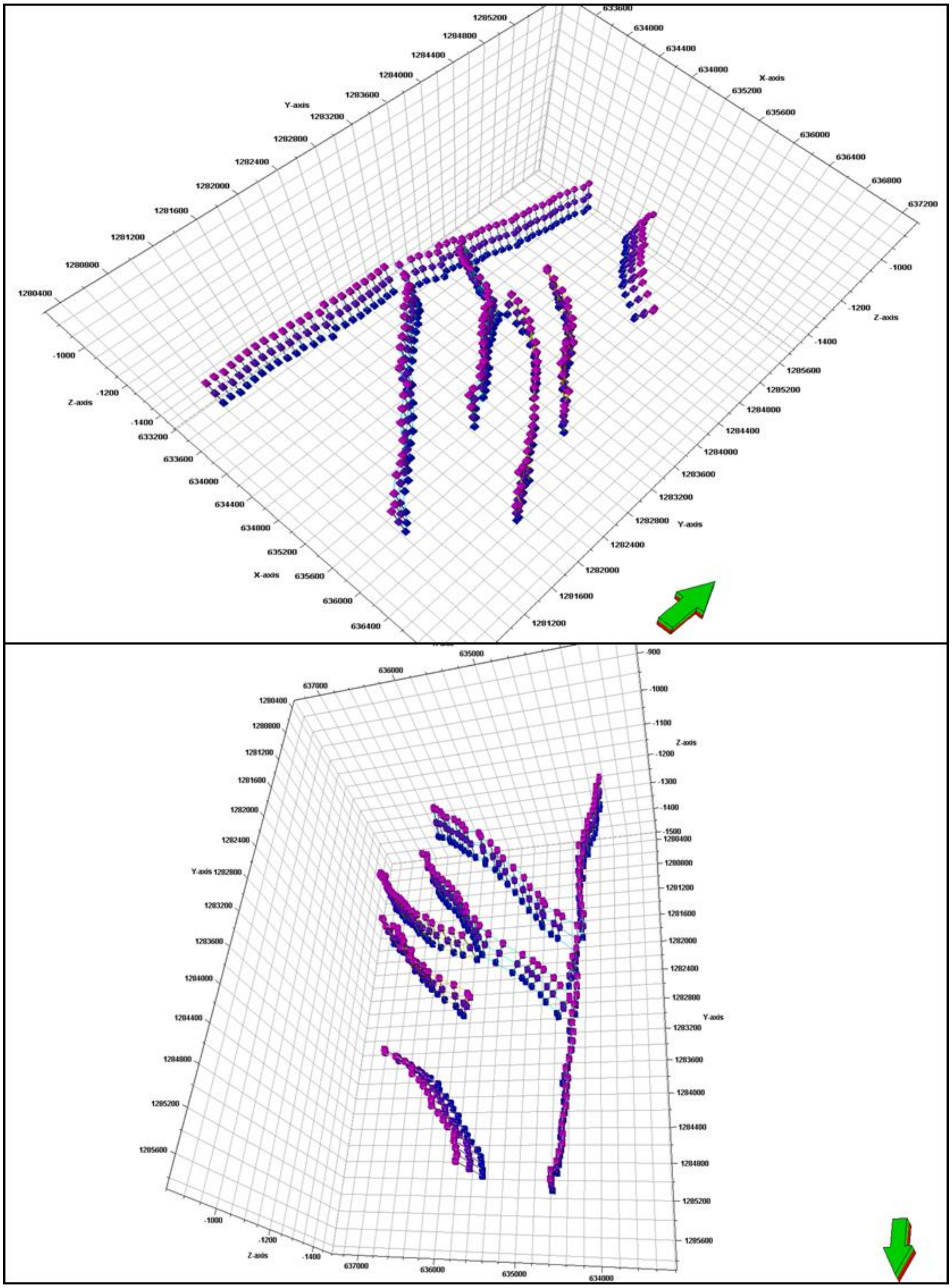

Figure 5.11 A pre-fault model with faults sticks interpreted from the 3-D seismic.

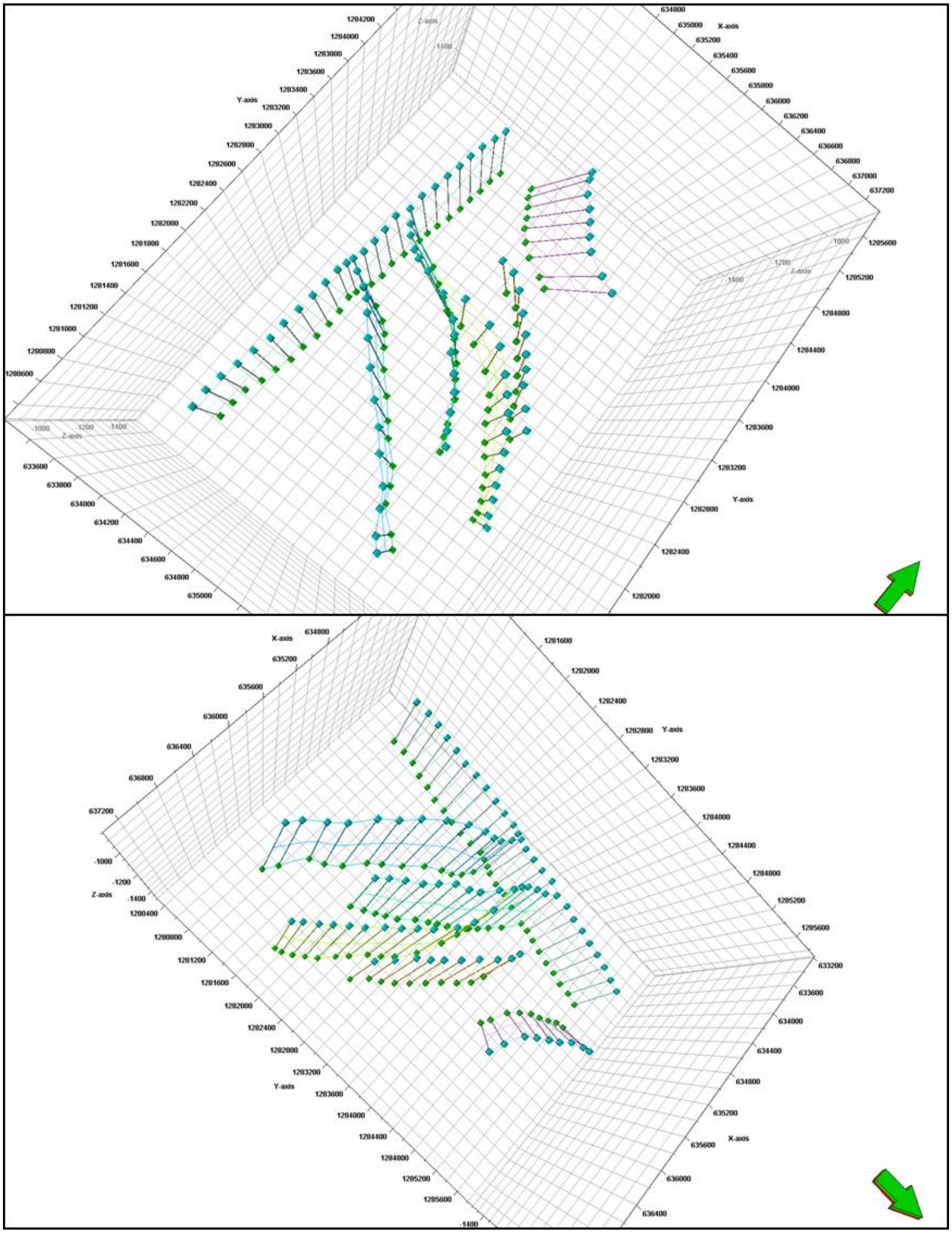

Figure 5.12 Results of the fault modeling through the pillar gridding process. The faults are gridded firmly where appropriate.

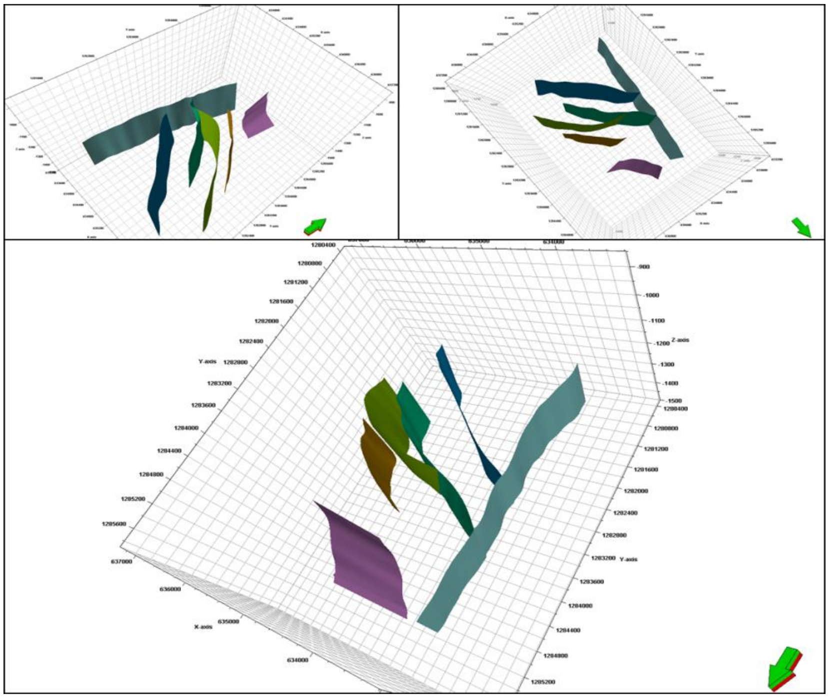

Figure 5.13 The final results of the fault modeling where the fault sticks have been limited to the study interval top and bottom.

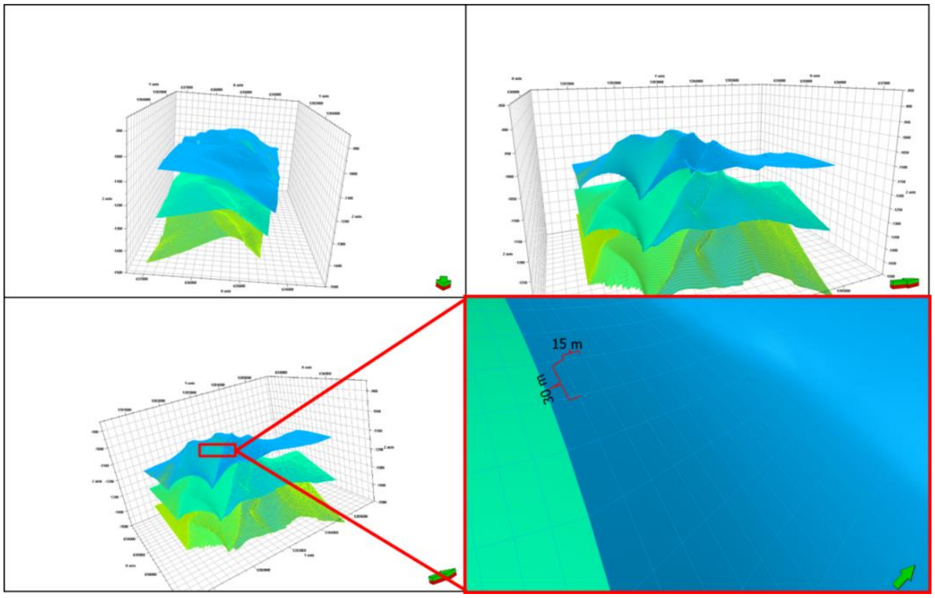

Figure 5.14 The constructed 3-D skeleton for the study interval based on the horizontal resolution acquired from the seismic 3-D survey.

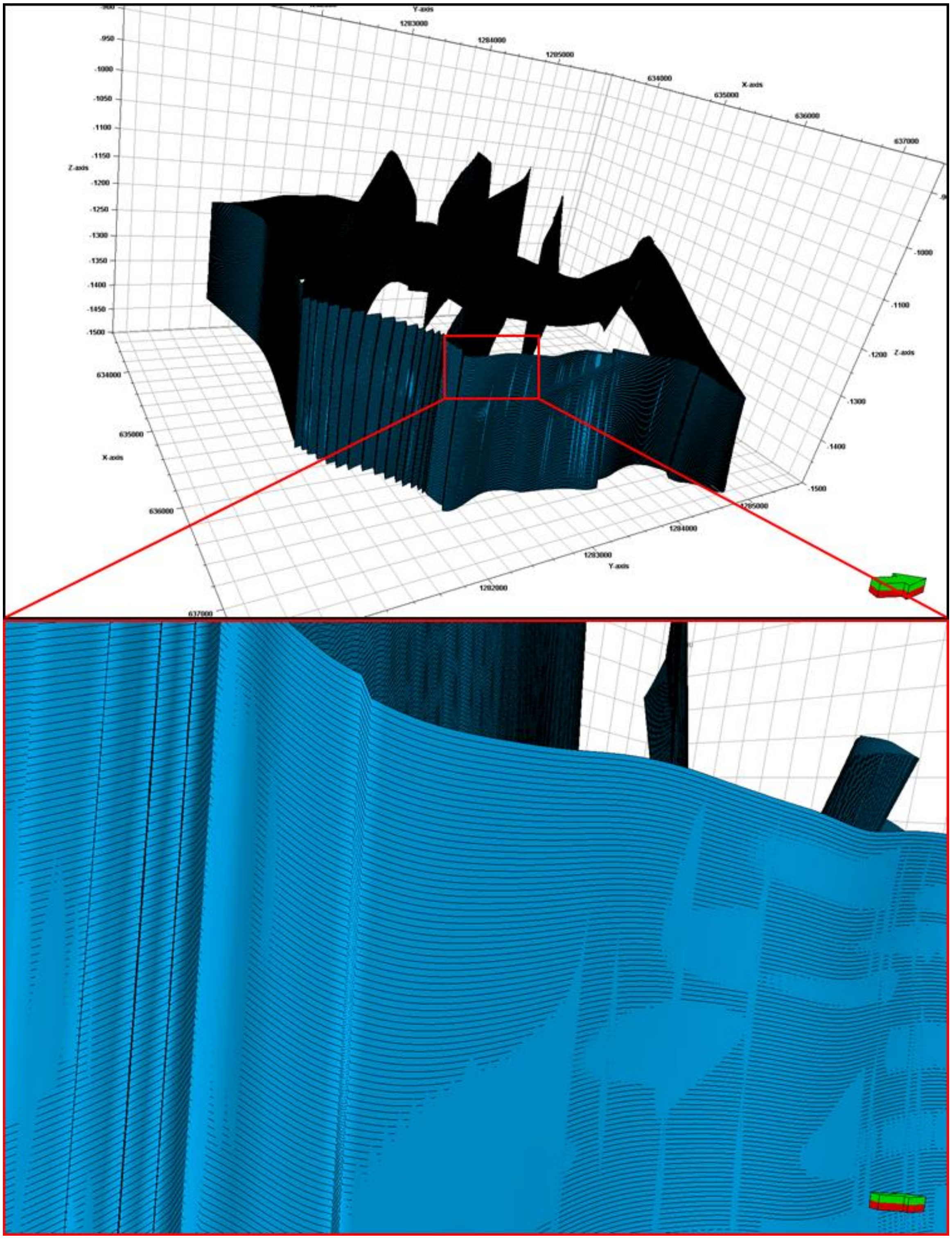

Figure 5.15 A general and a close-up view of the study interval to show the vertical resolution imposed on the edges of the study area.

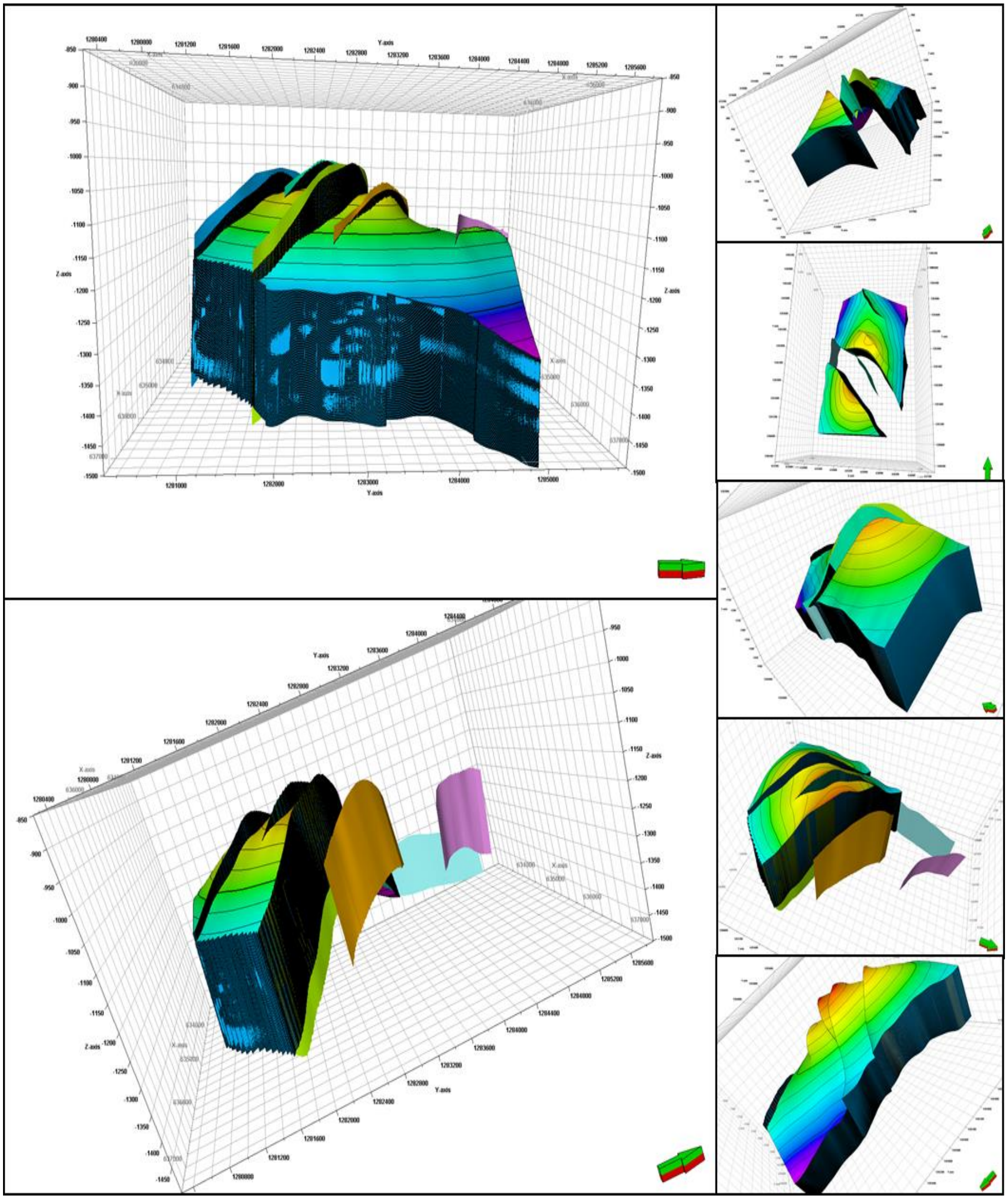

Figure 5.16 The final structural model of the Bentiu-1 reservoirs interval based on the interpretation of the seismic 3-D data and the markers picked from the wells information.

5.3 Geostatistical Modeling

This section gives the results of the geostatistical modeling in hierarchal manner. The descriptive statistics provides a comprehensive description to the data distribution through various measures and plots. In addition, brief investigations of the normal distribution fit for all the parameter distributions to define a proper path in the upcoming steps were also account for. Upscaling the reservoir's properties and lithofacies evaluated to the 3-D structural framework of the Bentiu-1 reservoirs interval defined earlier. The modeling of the spatial variability in the reservoirs properties in different directions was conducted by means of semivariogram. The estimation of the reservoirs properties in the unsamplesd locations (away from wells) was carried out through the ordinary kriging. The sequential indicator simulation (SIS) was adopted to model the lithofacies based on the stratigraphic and geological templates defined earlier. The Sequential Gaussian Simulation was used to model the petrophysical parameters within the individual lithofacies. The validation and verification of the simulation and modeling results are based on the verifications and the minimum accepted criterion stated Leuangthong and others (2004).

5.3.1 Descriptive Statistics

Table 5.2 gives a comprehensive account to statistical parameters for the petrophysical properties within each of the three lithofacies. The distribution and correlation of these parameters often provide a good knowledge about the reservoir characteristics. Saner and Sahin (1999) indicated that each dominant lithology (distinct zone and/or layer) within the reservoir is characterized by a distinct set of porosity and permeability with a distinct statistical distribution. The previous statement can be adequately stated about the statistical distribution of the porosity, permeability, and water saturation for the reservoir interval under consideration.

The lithofacies abundance in the Bentiu-1 reservoirs interval is best summarized by a histogram (Figure 5.17). The lithofacies histogram shows that the sand had the highest percentage (44.6%) and the shale the lowest. These results indicate the high sand/shale percentage in the Bentiu-1 reservoirs interval.

The mean, median and the mode of the porosity values of the sand lithofacies are consistently higher than those of the shaly-sand and the shale lithofacies. These statistical parameters are closely similar (especially the mean and the median) indicating the symmetry of the distributions within each of the three lithofacies (Table 5.2). A critical parameter for evaluating the heterogeneity or the homogeneity is the coefficient of variation (Corbett and Jensen, 1992). This parameter is very low for the sand porosity (0.27) indicating the homogeneity of the porosity distribution within this lithofacies. However, the coefficient of variation values for the porosity within shaly-sand and shale lithofacies are relatively high (> 0.5) indicating more heterogeneous nature of distributions (Table 5.2).

The statistical analysis of the permeability distributions revealed considerable differences between the permeability values within the three lithofacies (Table 5.2). The results indicates asymmetric nature of the permeability distribution within each lithofacies when comparing the mean, median and mode. The asymmetry of the permeability distributions is also indicated by the positive skewness values of permeability within the three lithofacies. The coefficient of variation values are relatively high (1.29, 3.7 and 5.19) for the sand, shaly-sand and shale lithofacies respectively, indicating significant heterogeneity in the permeability values (Sahin and Saner, 2001).

Some differences observed between mean, median and mode values of water saturation within each lithofacies point to the asymmetric nature of distributions. The skewness coefficient values revealed positive values for the sand and the shaly-sand lithofacies and negative values for the shale lithofacies (Table 5.2). The coefficient of variation values are considerably high for the water saturation within three lithofacies (> 0.5) indicating some heterogeneity (Sahin and Saner, 2001).

Table 5.2 The main statistical parameters of the petrophysical properties within each lithofacies identified.

Property	**Porosity (%)**			**Permeability (mD)**			**Water Saturation (Frac)**		
Measure	Sand	Sh_Sand	Shale	Sand	Sh_Sand	Shale	Sand	Sh_Sand	Shale
Mean	20.1	10	7.2	736.6	88.6	47.7	0.15	0.28	0.51
Median	20.9	9.1	5.7	324.8	4.7	1.5	0.12	0.25	0.53
Mode	25.6	15.53	4.5	1712.6	47	0.9	0.1	0.2	1
Min	0	0	0	0.2	0.2	0.2	0	0.01	0.02
Max	29	28.7	28.7	7356.1	5260	4126.8	1	1	1
Variance	28.7	36.6	29.3	915431	112918	61320	0.01	0.03	0.05
Std. Dev.	5.4	6.1	5.4	956.8	336	247.6	0.12	0.18	0.22
Coef. Var	0.27	0.61	0.75	1.29	3.7	5.19	0.8	0.6	0.5
Range	29.7	28.7	28.1	7355.9	5259.9	4126.7	1	0.99	.098
Skewness	-1	0.6	1.3	2	7	9.1	2.48	0.98	-0.21
Kurtosis	1	-0.2	1.6	4.6	63.1	100	9.7	0.77	-0.29

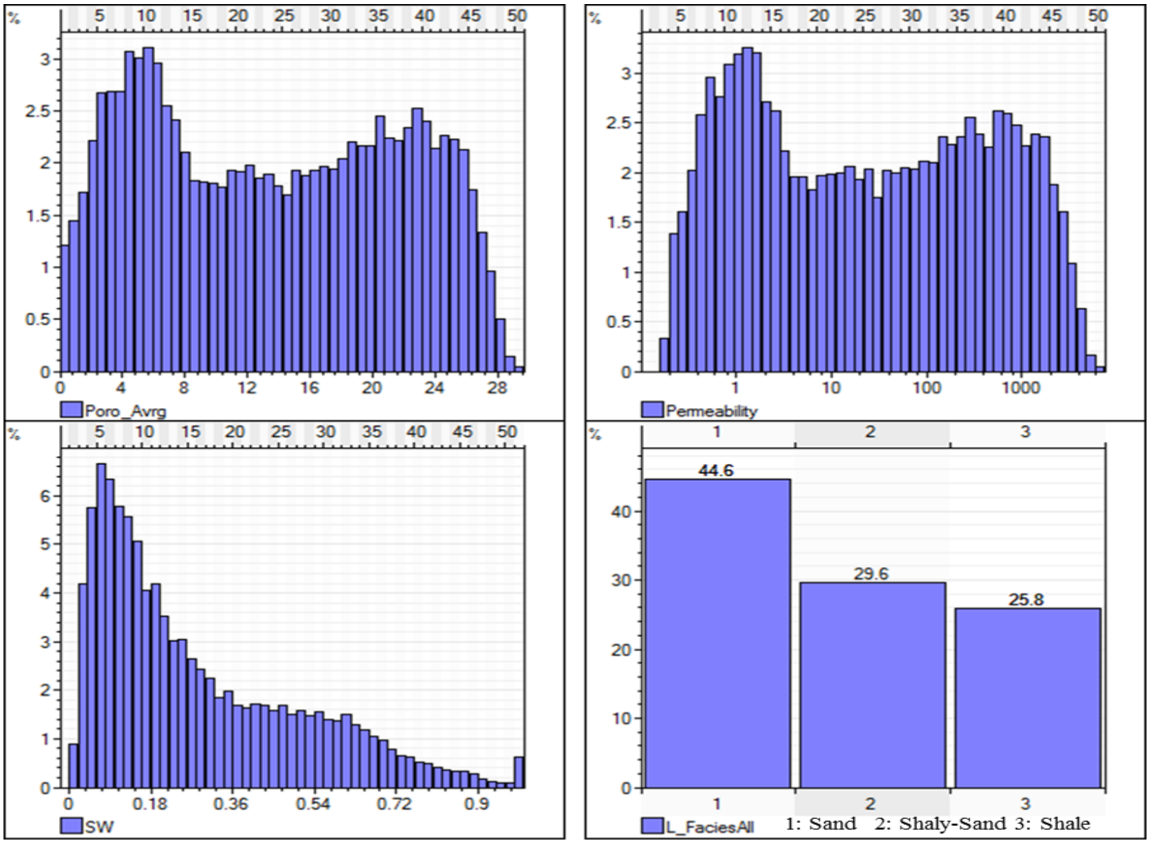

Figure 5.17 The histograms of the petrophysical properties; porosity (upper left), permeability (upper right) and water saturation (lower left), and the lithofacies (lower right).

5.3.2 Properties and Lithofacies Upscaling

The discrete (lithofacies) and continuous (porosity, permeability and water saturation) properties derived from the wells need to be upscaled to represent 3-D reservoir. This necessity emerges from the fact that the reservoir properties were estimated from the well logging with a resolution of approximately 15 cm and must be resampled to build the 3-D grid (approximately 1m dimension).

The upscaling process assigns the log values to the cells in the 3-D grid that are penetrated by the wells. Two main data types including both continuous and discrete were scaled-up to the reservoirs 3-D grid. The continuous data which are composed of the porosity, permeability, and water saturation estimated from the well logs. These parameters were upscaled based on the arithmetic averaging technique to avoid the biased in combining properties from different lithofacies (Figure 5.18). The discrete data which mainly consists of the lithofacies was also upscaled through same techniques as the continuous data (Figure 5.18). Histograms for validation and quality assurance (Figure 5.19) were generated to insure the validity of upscaling processes.

5.3.3 Data Coding and Transformation

The data coding process is often used for generating or assigning discrete logs from the continuous logs. In this study, the coding of the data acquired from the cluster analysis module was used to generate the lithofacies from the well log information (electro-facies). Table 5.3 gives a description of the codes of the cluster analysis module-based electro-facies along with their correlative core lithofacies.

A normally distributed data is necessary to evaluate the lateral and vertical variability, more precisely to construct the semivariogram. This requires investigating and testing the normality of the data in hand. In other words, determine whether the data follows the Gaussian standard distribution or not. Figure 5.20 gives description of the normality test accomplished for the porosity, permeability, and water saturation data. Unsurprisingly, all the normality tests proved that all the parameters differ from the normal distribution. The differences could be firmly correlated to the different lithofacies present in the reservoirs interval, precisely the depositional and post depositional heterogeneity imposed within each of prevailed lithofacies.

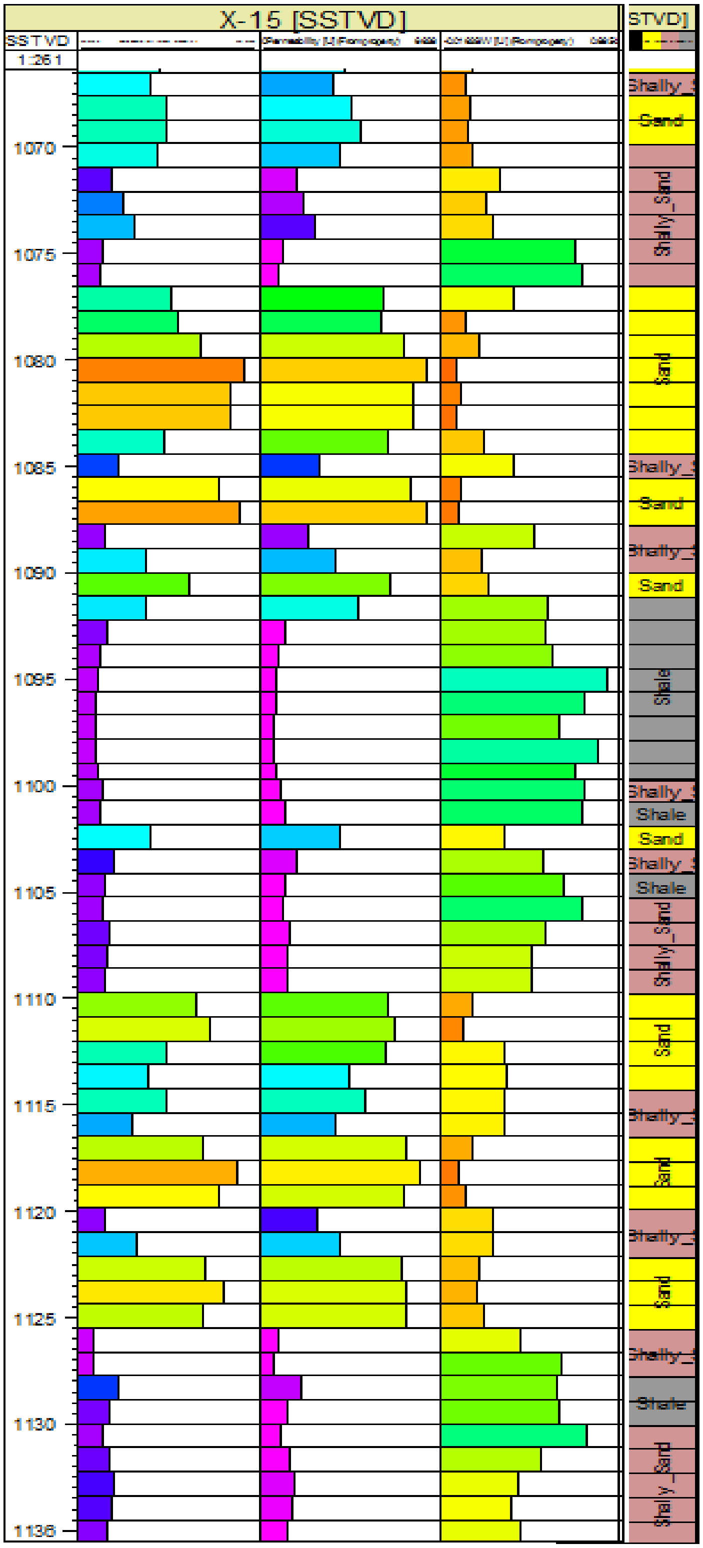

Figure 5.18 The result of the upscaling process for the lithofacies (Track #5) and petrophysical properties; porosity (Track #2), permeability (Track #3), and water saturation (Track #4).

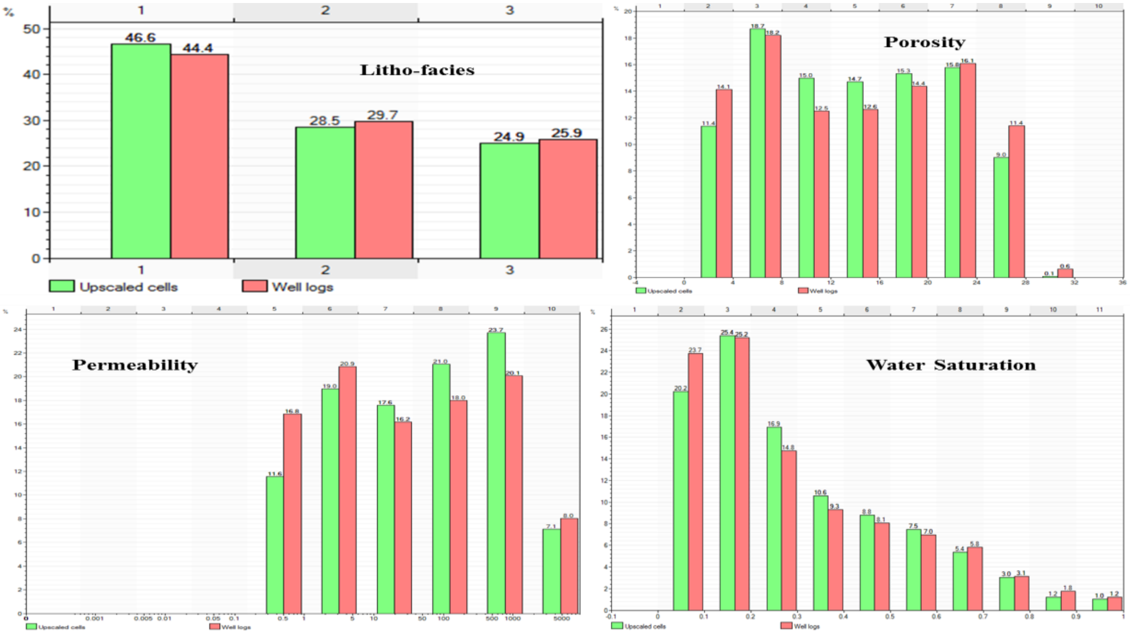

Figure 5.19 The upscaling validation histograms. The figure indicates that all the parameters were upscaled properly.

Table 5.3 The codes used to describe the elctro-facies generated using the cluster analysis.

Facies Code	Elecro-Facies	Core Facies
1	Sand Facies	Medium to Coarse Grained Sandstones Facies
2	Shaly Sand Facies	Fine to silty Sandstone Facies
3	Shale Facies	Shale/claystone Facies

In this study, two main transformation techniques were used to acquire a Gaussian distribution for the porosity, permeability, and water saturation. The normal score transformation technique, which is used to transform the porosity and water saturation directly and the logarithmic transformation technique for the permeability data. In the normal score transformation, the input data is forced to mimic a standard normal distribution (zero mean and unit standard deviation).

This means that most of the sample points in the data are close to the mean value with relatively few sample points behave as high and low extremes (Figure 5.21). The logarithmic transformation is particularly useful for the lognormally distributed data such as permeability in this study. The primary objective of this transformation is to reduce the skewness of the data distribution (Figure 5.22).

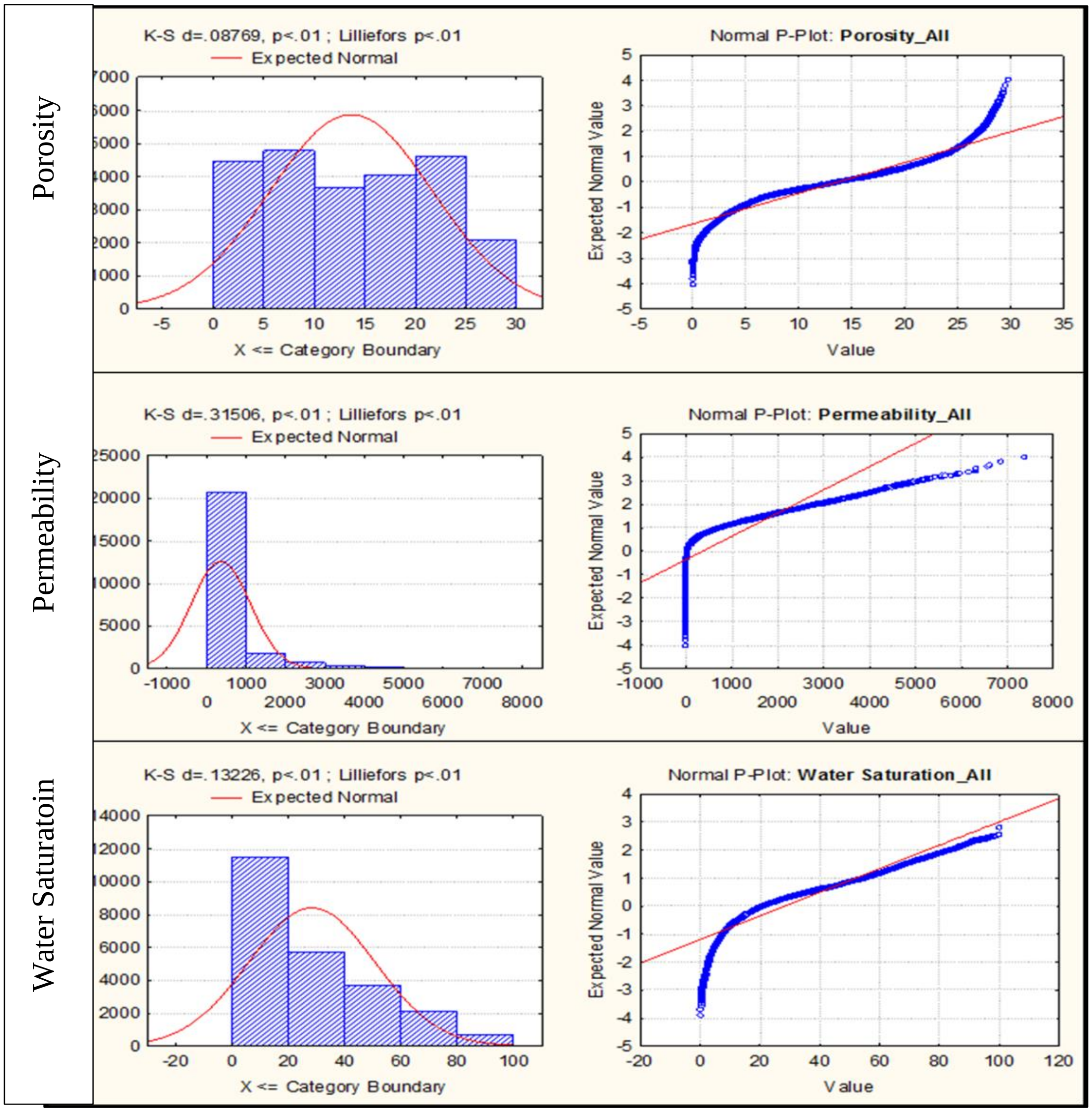

Figure 5.20 The results of the four normality tests performed on the petrophysical properties; Kolmogrov-Smirnov test (K-S), Lilliefors Test, Normal Histograms, and Normal Probability Plots.

Property	**Original Data**	**Transformed Data**
Porosity	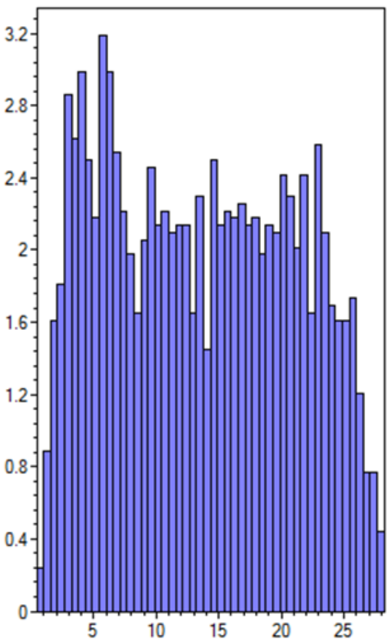	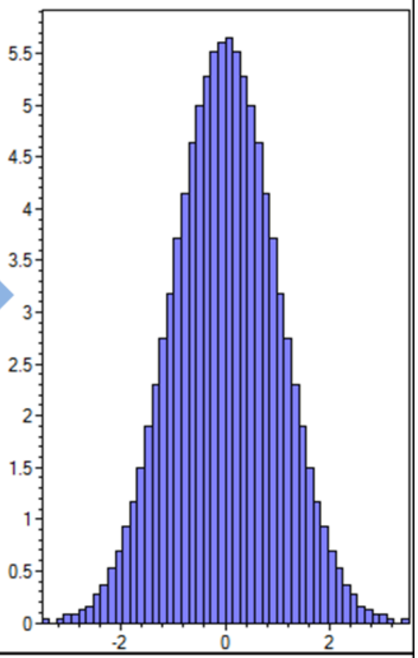
Water Saturation	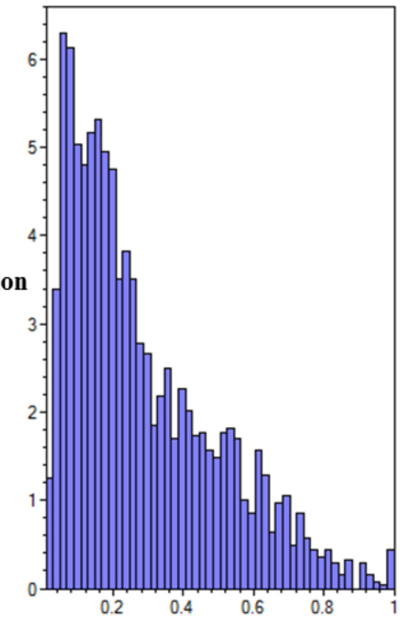	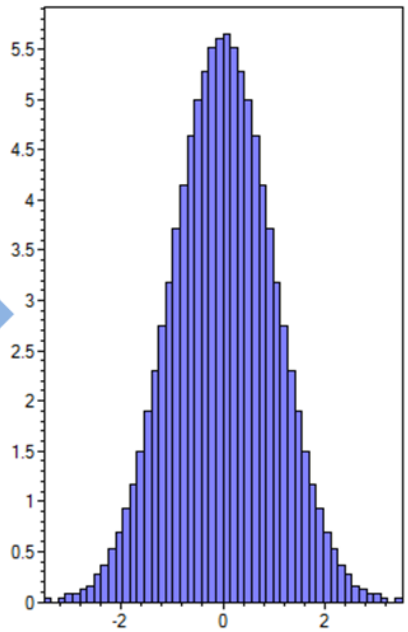

Figure 5.21 The results of normal score transformation applied on the porosity and water saturation data.

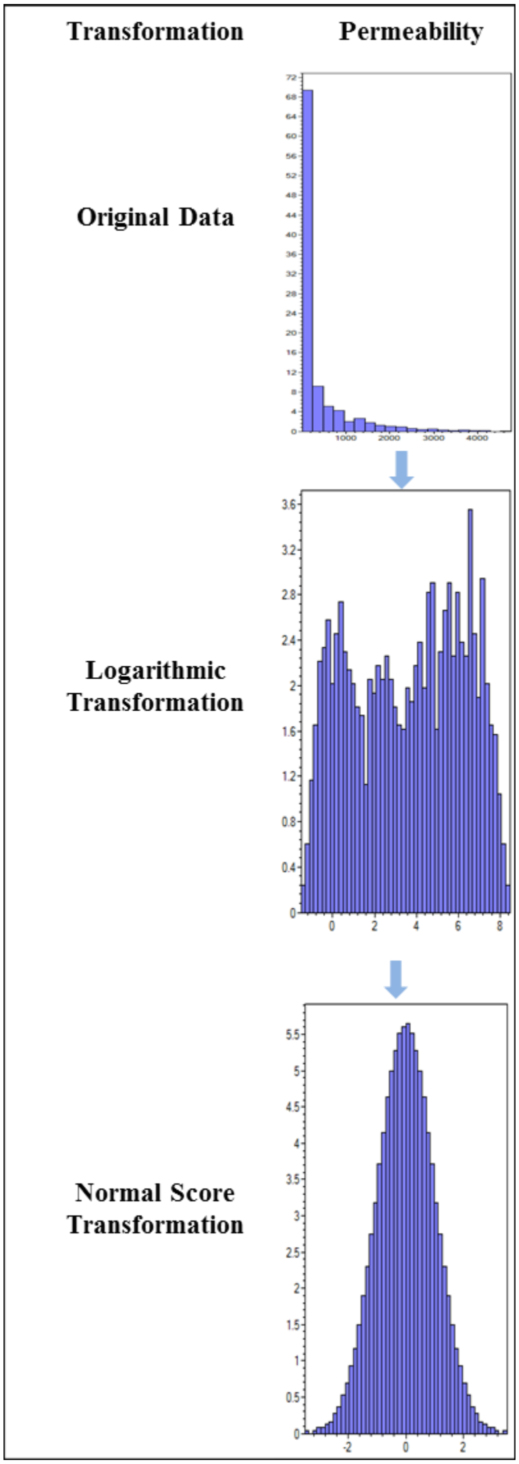

Figure 5.22 The result of the logarithmic and normal score transformations applied on the permeability data.

5.3.4 Spatial Variability

The spatial analyses was accomplished using semivariograms calculated vertically and laterally. The directional semivariograms was constructed in two main directions coinciding with the major and minor trends of the variability. Moreover, the vertical semivariogram was constructed in the vertical direction for all the data sets. The semivariograms were constructed in three main directions: a major direction (10°NE); aligned to the major sub-basin boundaries and perpendicular to depositional direction, a minor direction (80°NW) and a vertical direction. A spherical model (Eq. 3.25) was used to model all the semivariograms constructed.

Lithofacies semivariograms: Indicator semivariograms were used to capture the variability among each of the three lithofacies. The lithofacies thickness upscaled to the 3-D grid cells (Figure 5.18) was used as basis the experimental variogram construction. Firstly, an experimental semivariograms were constructed for the all the lithofacies combined together to acquire a general information on their variability (Figure 5.23). Although this setup may mix pairs of points from different lithofacies into the semivariogram constructed leading to unrealistic results about lithofacies continuity. Yet, some qualitative interpretation can be observed (Figure 5.23). These outlines can be seen in appropriate number of pairs versus lags, approximate leveling of the sill, adequate lag distance. A particular importance was given to the lag distance appropriate for this study.

The lithofacies semivariogram parameters used for the 3-D model were acquired based on the semivariograms constructed for the lithofacies separately. The lag size in the vertical directions varied between 1 and 2 meter depending on the vertical stacking of the three lithofacies.

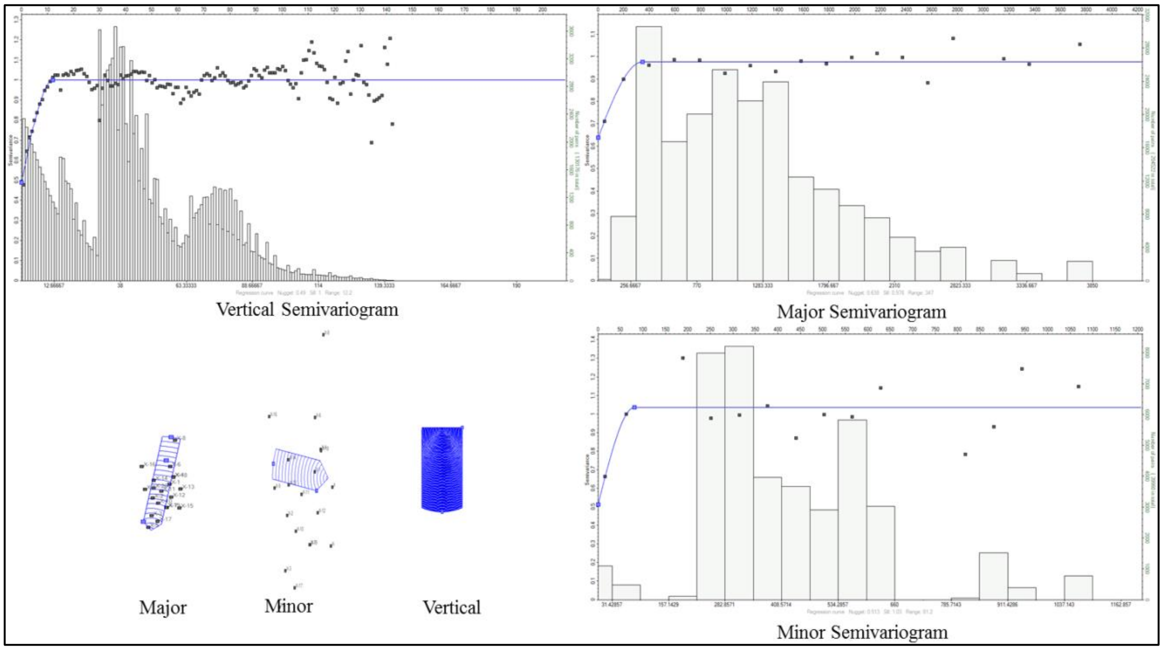

Figure 5.23 The semivariograms in the three principle direction constructed for all lithofacies combined.

Sand lithofacies semivariograms**:** the indicator semivariogram model for this lithofacies showed a good structural behavior, moderate nugget value for both major and minor directions. The sill values are nearly equal for the three directions. However, the range values are varying greatly between the major, minor and the vertical directions (Figure 5.24 and Table 5.4). In the vertical direction, the semivariogram model fairly fits the data and shows an expected short range (~ 12m). The difference in the range values (Table 5.4) between different directions and equality in sill values suggest the prevalence of a geometrical anisotropy

Geologically; this lithofacies represents the dominant lithofacies in the study interval representing the bed-load deposition of the main channel. The semivariogram for this lithofacies indicate a good spatial continuity where the vertical semivariogram displays a periodic behavior known as the hole-effect. This perfectly reflects the deposition and the lateral migration of the fluvial channel indicating the zonal nature of the interval (Sahin and Al-Salem, 2001).

Shaly Sand lithofacies semivariograms: The semivariograms in the major and minor directions revealed good structural behavior (Figure 2.25). The nugget value is somewhat high for the major direction compared with that of the minor direction (Table 5.4). The sill values are nearly equal for the minor, major and vertical directions. The range for the major direction is slightly higher than that of the minor direction (Table 5.4). This indicates a slight tendency toward a geometrical anisotropy.

Geologically, this lithofacies is the second common in the Bentu-1 reservoir interval. The relatively high nugget value indicates relatively higher variation within this lithofacies as commonly observed in fluvial-origin deposition.

Shale lithofacies semivariograms: the indicator semivariogram model of this lithofacies is characterized by poor structure for the minor direction where the model loosely fits the data points. However, the vertical direction reveals a good structure compared to the minor and major directions (Figure 5.26). The relatively higher nugget value reflects the variability at the close lag intervals. The sill values are approximately equal for the vertical, major and minor directions. However, the range values for the major and minor directions indicate slight difference (Table 5.4).

This lithofacies stand as the least abundant in the Bentiu-1 reservoir interval. It reflects the deposition of fluvio-lacustrine environments. The vertical semivariogram better describes such characteristics of this lithofacies. The clear periodic behavior as for the previous lithofacies reflects the stacking pattern of the fluvial channels.

Table 5.4 The parameters of the indicator semivariograms for each lithofacies.

Lithofacies	Direction	Azimuth	Model	Lag Size (m)	Sill	Nugget	Range (m)
Sand	Major	10°	Spherical	294.1	0.99	0.337	377.6
	Minor	280°	Spherical	113	0.926	0.291	142.8
	Vertical	0°	Spherical	1	1.01	0.407	11.6
Shaly Sand	Major	10°	Spherical	185.2	0.982	0.724	151
	Minor	280°	Spherical	114.3	1.043	0.493	141.3
	Vertical	0°	Spherical	1	1.00	0.63	9.3
Shale	Major	10°	Spherical	185.2	1.00	0.659	177.6
	Minor	280°	Spherical	126.3	0.791	0.476	159.1
	Vertical	0°	Spherical	1	1.00	0.391	13.2

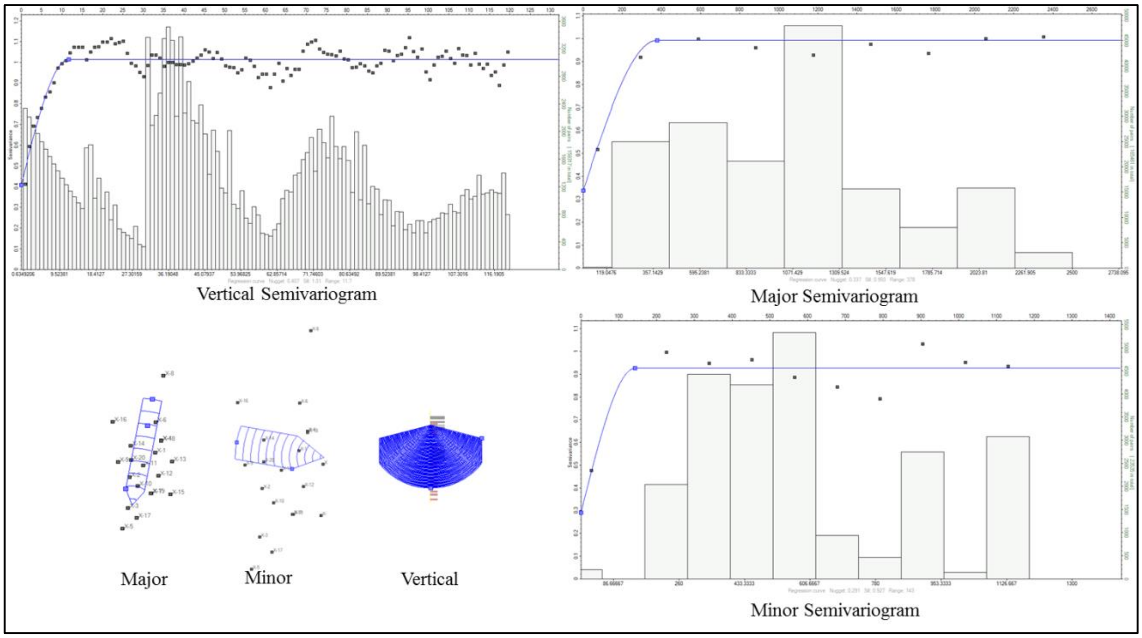

Figure 5.24 The semivariograms in the three principle directions for the sand lithofacies.

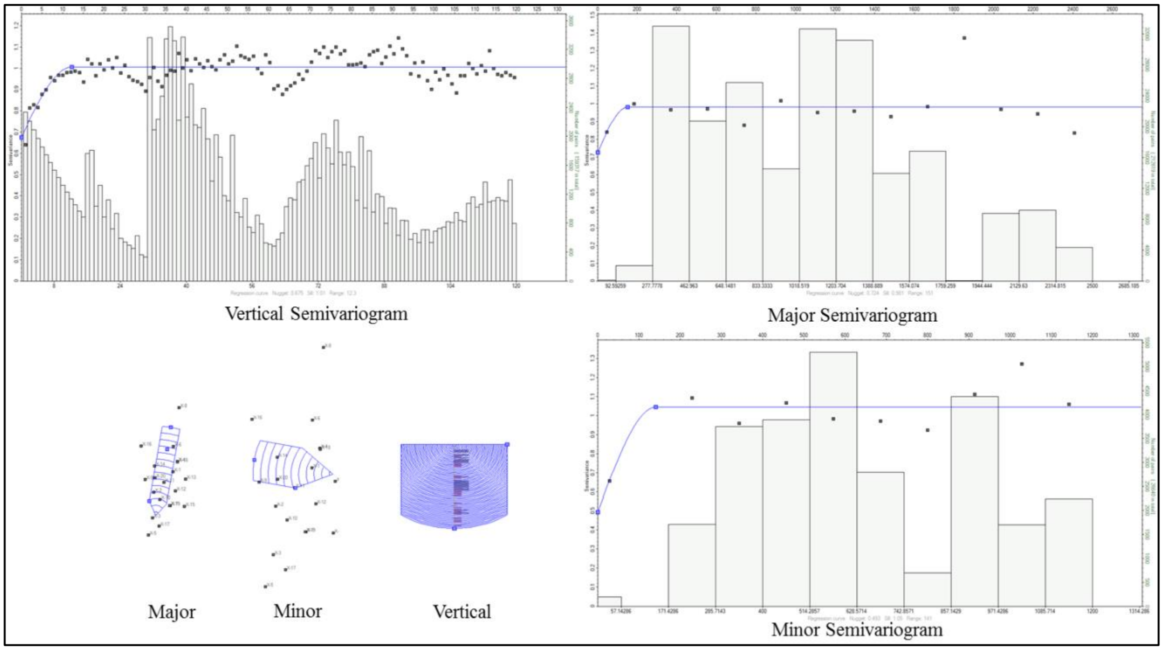

Figure 5.25 The semivariograms in the three principle directions for the shaly sand lithofacies.

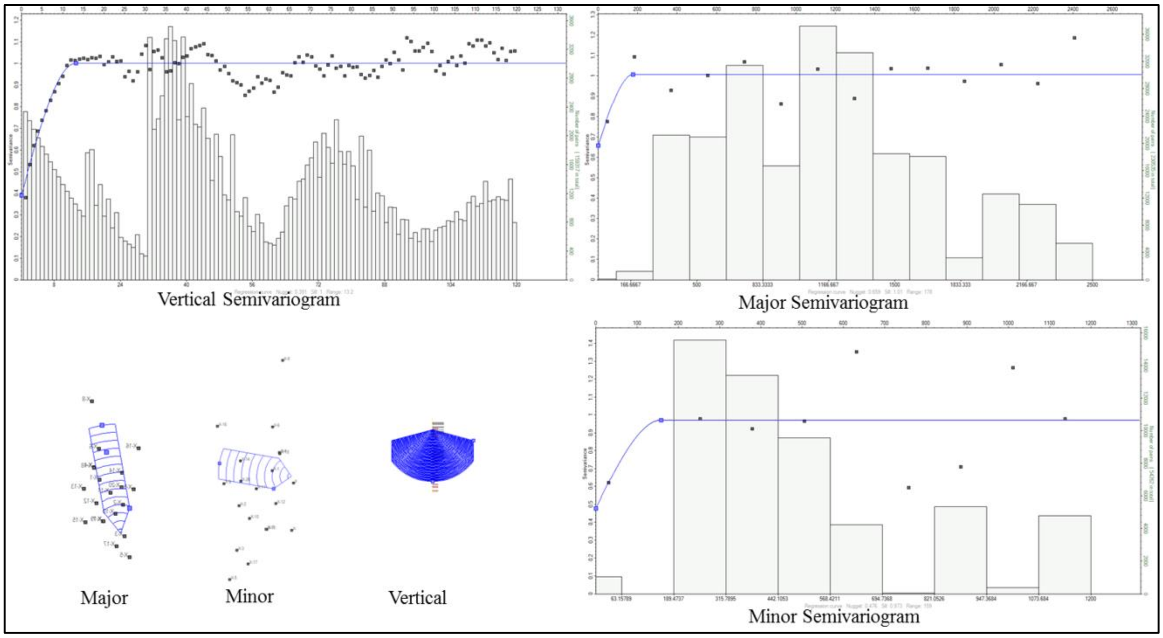

Figure 5.26 The semivariograms in the three principle directions for the shale lithofacies.

Petrophysical parameter semivariograms: the evaluation of the spatial variability of petrophysical parameters was carried out on lithofacies conditioning basis. Semivariogram for each parameter was constructed within each lithofacies.

The semivariogram parameters for capturing the vertical and lateral variability were selected to be close to those of indicator semivariograms. The major search radius is around 2500 m approximately half of the study area. The minor search radius is around 1200-1500m and the same azimuth used for the lithofacies semivariograms was selected.

Sand lithofacies porosity semivariograms: the semivariogram models for the porosity in this lithofacies poorly fitted the data points especially for the major and minor directions (Figure 5.27). The sill values are nearly equal in all directions. However, a notable difference in the range values was observed between the three directions with vertical semivariogram showing the shortest range (Table 5.5). The vertical semivariogram of this lithofacies porosity shows the same periodical behavior previously observed in the lithofacies indicator semivariogram (Figure 5.27). This behavior is best attributed to the syn-and-post depositional settings.

Shaly-sand lithofacies porosity semivariograms: the semivariogram model of the porosity in this lithofacies shows a good fit in both major and minor directions (Figure 5.28). However, the vertical semivariogram of the porosity loosely fits the data points which form several scattered groups (Figure 5.28). The notable differences between the range values in three directions suggest the presence of geometrical anisotropy (Table 5.5).

Shale lithofacies porosity semivariograms: the semivariogram models for this lithofacies are poorly fits the data points especially for the minor direction (Figure 5.29). The nugget value of the minor and the vertical directions show relatively lower, closely similar values indicating relatively small variability at the small distances.

Lithofacies permeability semivariograms: the semivariogram models for the permeability revealed parameters that are similar to the porosity semivariogram models (Table 5.5 and Figures 30, 31 and 32). As pointed out earlier, the permeability data was originally calculated from the porosity data based on exponential pre-established relation (refer to Section 4.2.3). The same periodic behavior previously observed in the lithofacies indicator semivariograms and the porosity semivariograms are present. Moreover, the vertical semivariogram models for the permeability in the three lithofacies show short-range structures. The major and the minor directions for permeability in all the three lithofacies revealed different range values indicating the prevalence of the geometrical anisotropy (Table 5. 5 and Figures 30, 31 and 32).

Sand lithofacies water saturation semivariograms: the semivariogram models for the water saturation in the sand lithofacies showed poor fit to the data points in the minor and major directions (Figure 5.33). The nugget values for the three directions are quite small indicating lower variability at small lag distances (Table 5.5). The sill values are nearly equal in all directions. One again a geometrical anisotropy is present as reflected in the differences in the range values (Table 5.5).

Shaly-sand lithofacies water saturation semivariograms: the water saturation semivariogram model for this lithofacies shows poor fit to the experimental points in all directions (Figure 5.34). The vertical semivariogram revealed some grouping or clustering of the data.

Shale lithofacies water saturation semivariogram: this show a good fit for the experimental points in the major direction (Figure 3.35). However, the minor and vertical semivariogram models poorly fit the experimental points. The sill values are nearly equal for all directions. The nugget values are considerably low especially for the major and minor directions (Table 5.5 and Figure 5.35).

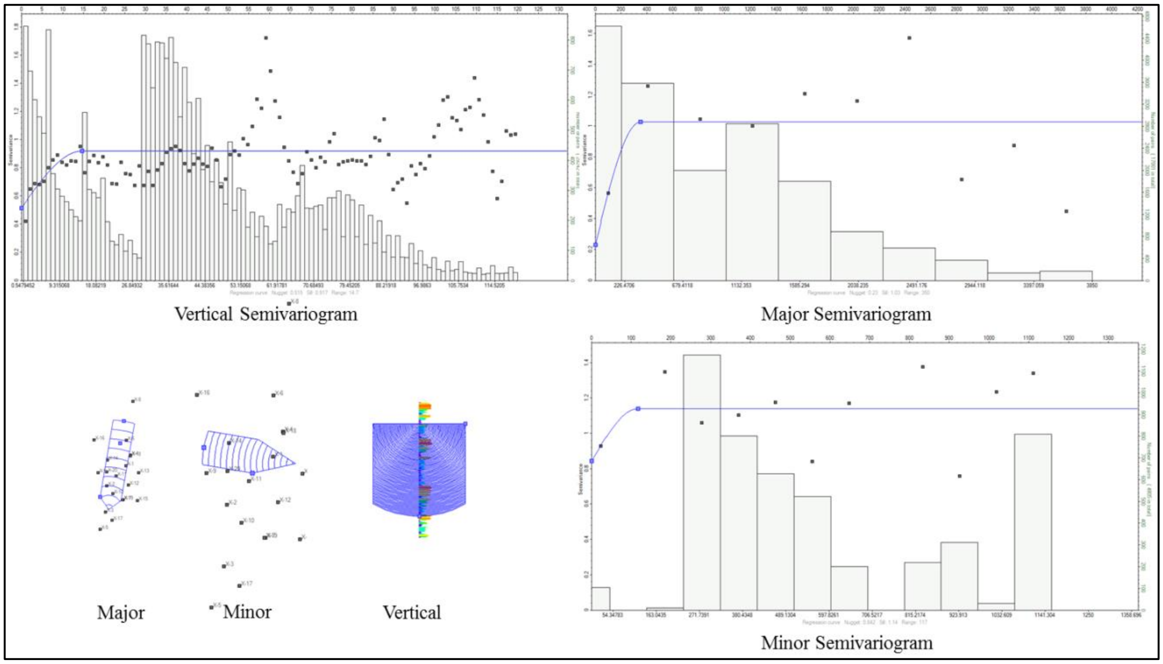

Figure 5.27 The semivariograms in the three principle directions for the sand-based porosity.

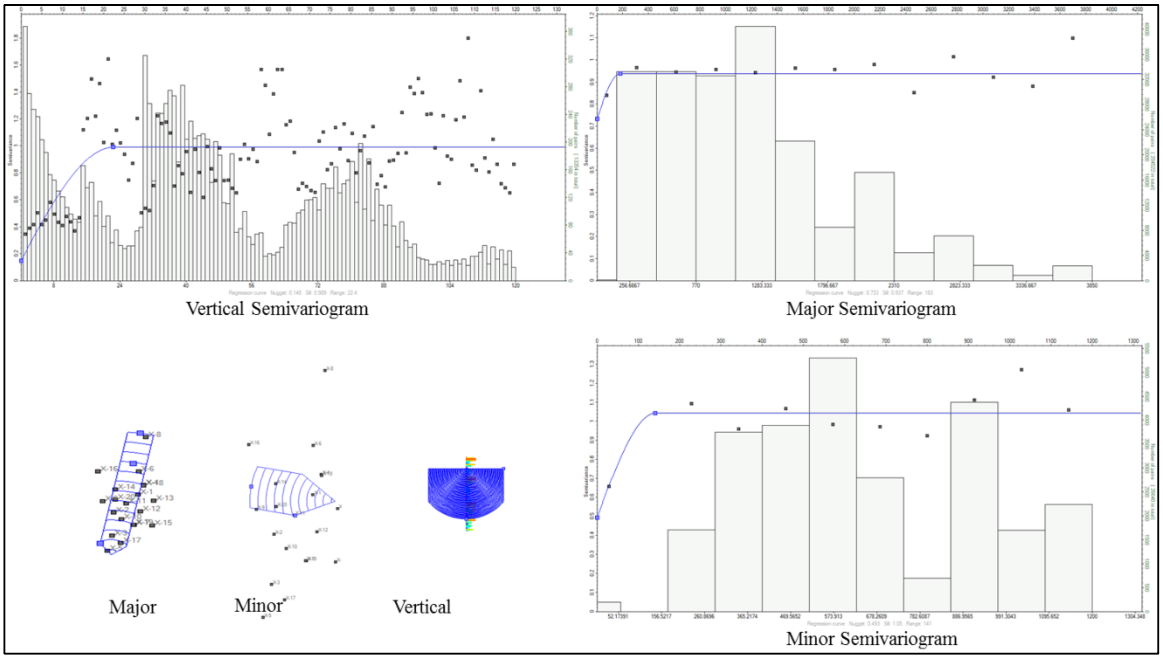

Figure 5.28 The semivariograms in the three principle directions for the shaly sand-based porosity.

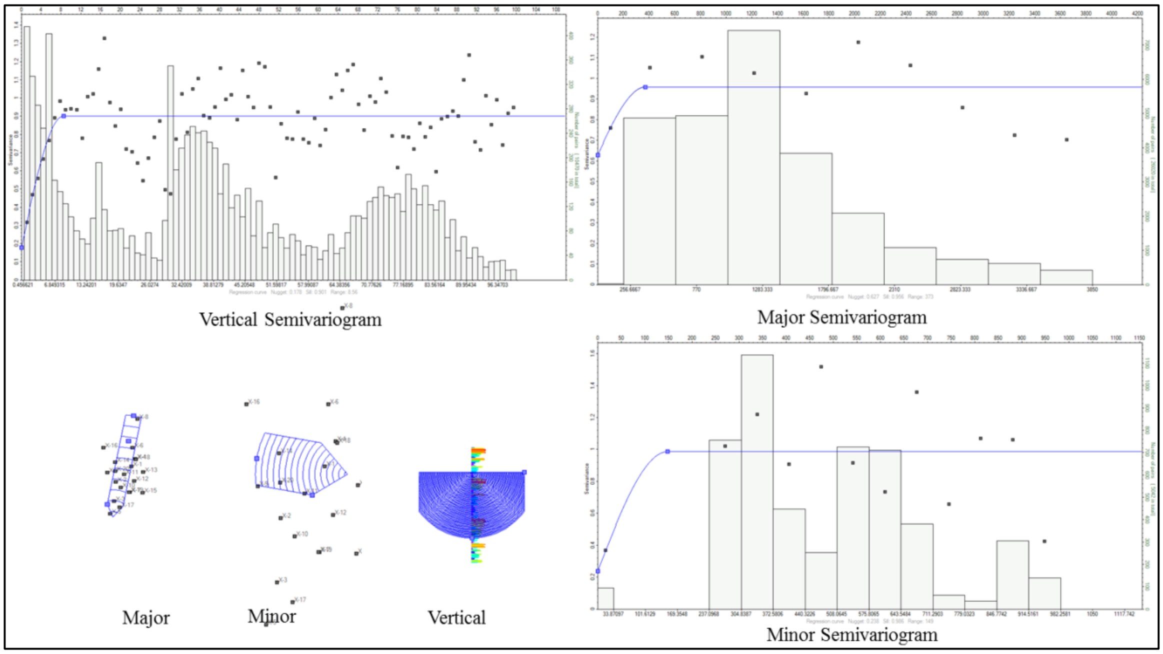

Figure 5.29 The semivariograms in the three principle directions for the shale-based porosity.

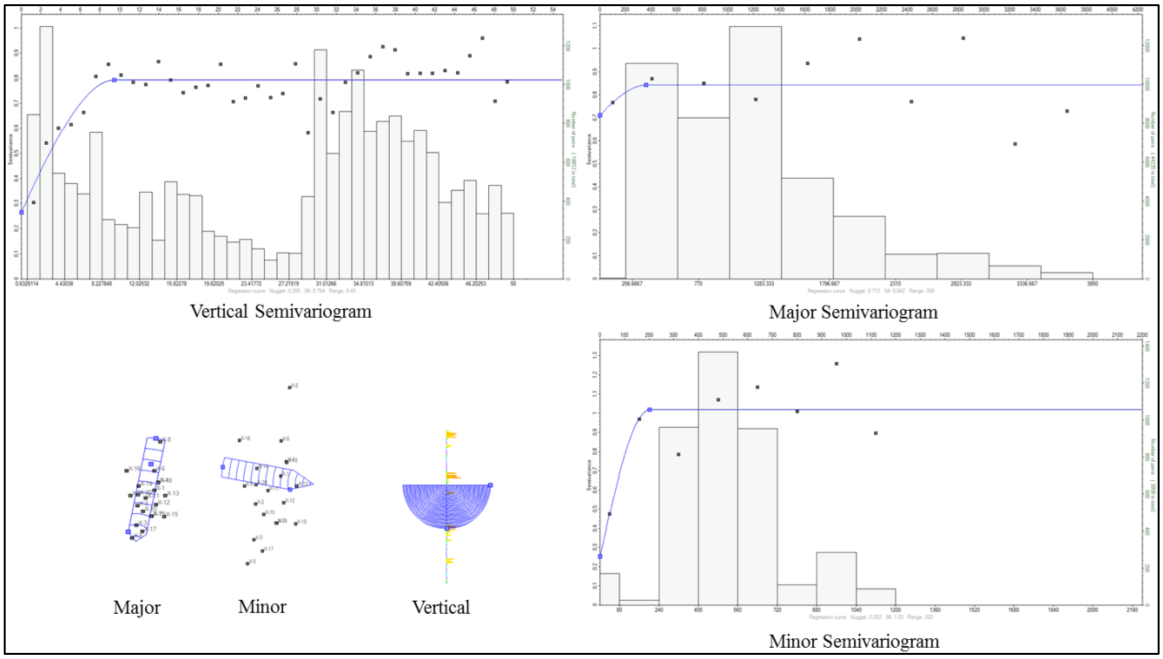

Figure 5.30 The semivariograms in the three principle directions for the sand-based permeability.

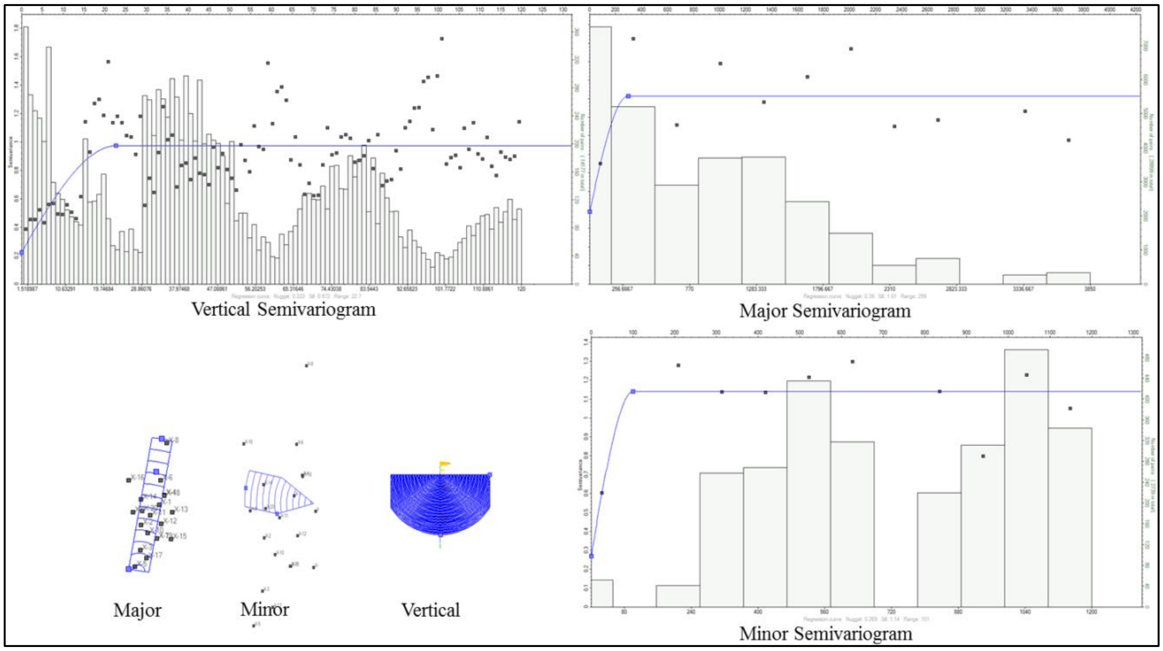

Figure 5.31 The semivariograms in the three principle directions for the shaly sand-based permeability.

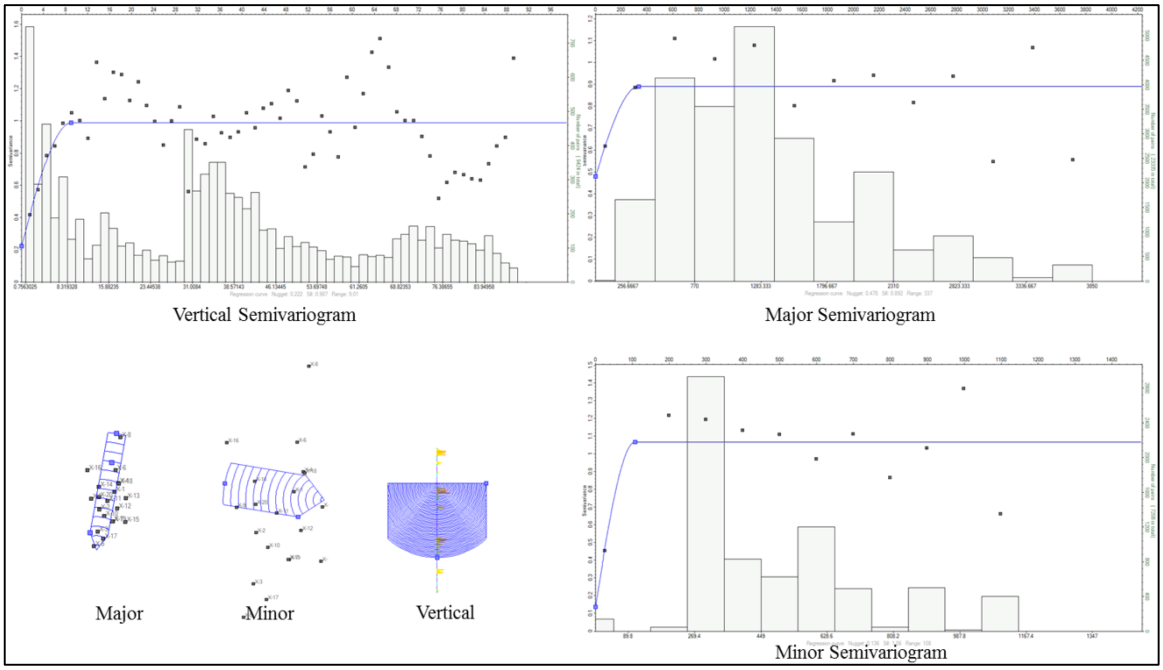

Figure 5.32 The semivariograms in the three principle directions for the shale-based permeability.

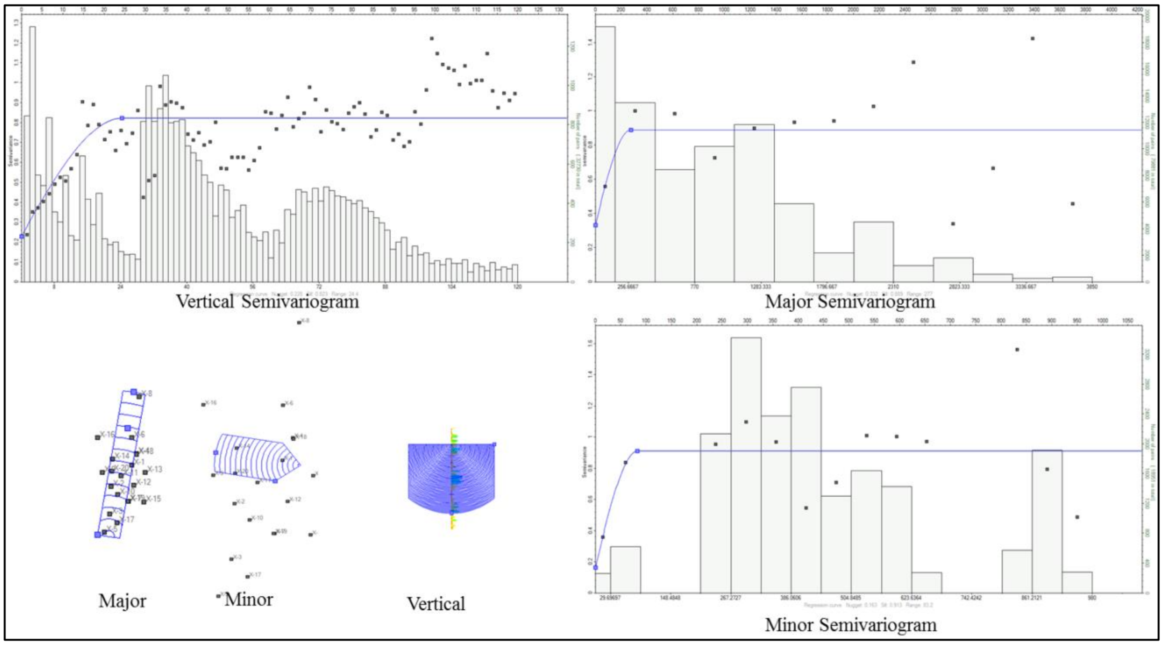

Figure 5.33 The semivariograms in the three principle directions for the sand-based water saturation.

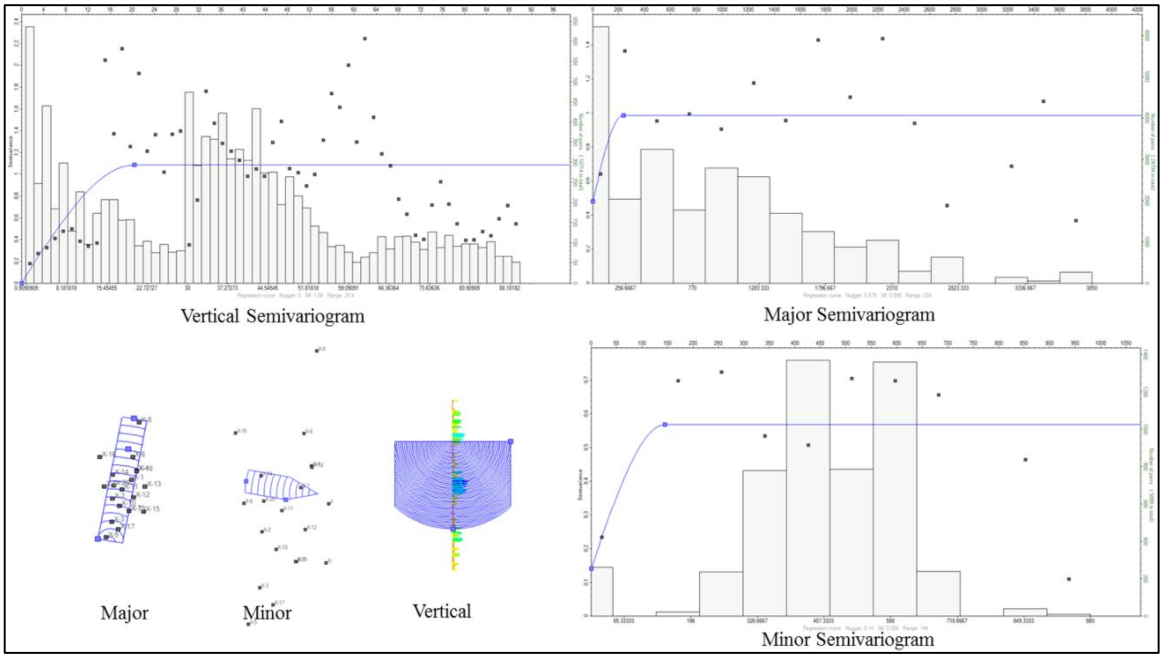

Figure 5.34 The semivariograms in the three principle directions for the shaly sand-based water saturation.

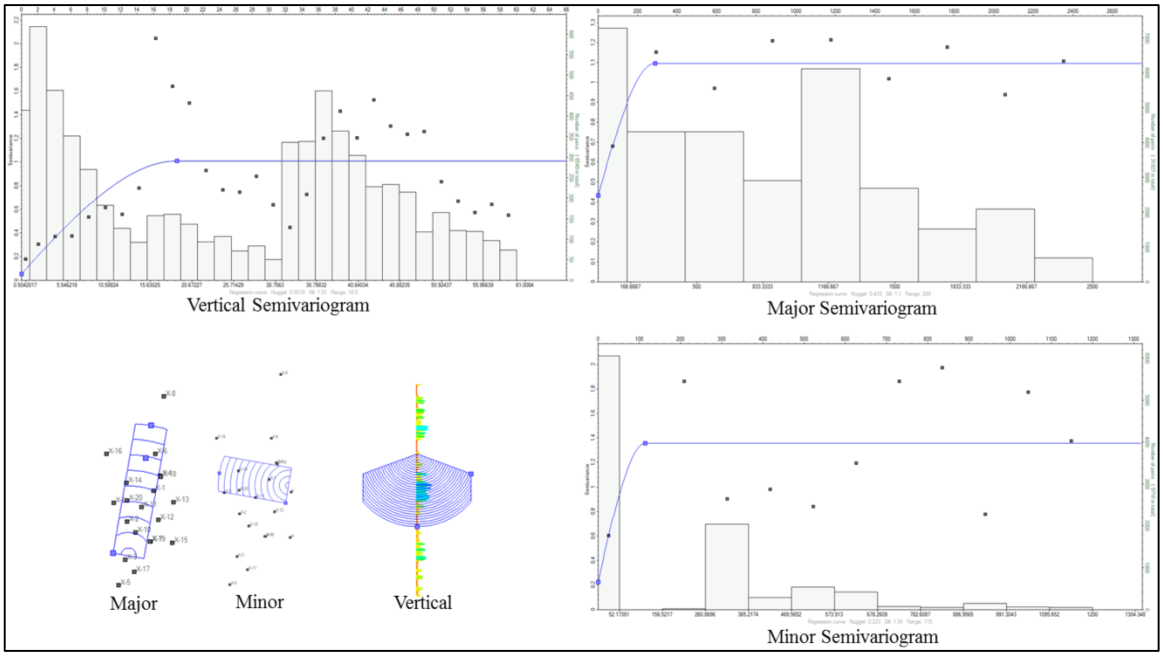

Figure 5.35 The semivariograms in the three principle directions for the shale-based water saturation.

Table 5.5 Parameters of the semivariograms for the three petrophysical properties within each lithofacies.

Semivariogrms	Direction	Azimuth	Model	Lag Size (m)	Sill	Nugget	Range (m)
Sand_Porosity	Major	10°	Spherical	263.2	0.941	0.547	232.7
	Minor	280°	Spherical	71	1.06	0.166	112.6
	Vertical	0°	Spherical	1.1	0.919	0.515	14.7
Sh_Shale Porosity	Major	10°	Spherical	405.3	1.026	0.23	350.4
	Minor	280°	Spherical	92.6	1.138	0.842	116.7
	Vertical	0°	Spherical	1	0.148	0.989	22.4
Shale Porosity	Major	10°	Spherical	405.3	0.958	0.627	372.8
	Minor	280°	Spherical	67.7	0.985	0.238	148.5
	Vertical	0°	Spherical	1.1	0.9	0.178	8.6
Sand Permeablity	Major	10°	Spherical	405.3	0.922	0.584	319.5
	Minor	280°	Spherical	93.3	1.093	0.446	100.5
	Vertical	0°	Spherical	1.3	0.792	0.265	9.4
Sh_Sand Permeability	Major	10°	Spherical	334.8	1.015	0.390	298.6
	Minor	280°	Spherical	104.3	1.141	0.269	100.5
	Vertical	0°	Spherical	1.1	0.974	0.222	22.7
Shale Permeablity	Major	10°	Spherical	308	0.889	0.478	337.1
	Minor	280°	Spherical	99.8	1.067	0.136	108.2
	Vertical	0°	Spherical	1.5	0.988	0.222	9
Sand Water_Saturaion	Major	10°	Spherical	405.3	0.889	0.332	276.7
	Minor	280°	Spherical	59.4	0.910	0.163	83.2
	Vertical	0°	Spherical	1.3	0.822	0.228	24.4
Sh_Sand Water_Saturaion	Major	10°	Spherical	284.4	0.986	0.479	237.7
	Minor	280°	Spherical	85.2	0.568	0.14	144.4
	Vertical	0°	Spherical	1.5	1.08	0	20.4
Shale Water_Saturation	Major	10°	Spherical	294.1	1.09	0.433	289
	Minor	280°	Spherical	285.2	1.01	0.093	115
	Vertical	0°	Spherical	2	1.009	0.05	18.8

5.3.5 Estimation

The estimation of the lithofacies and the petrophysical properties at the un-sampled locations in this study was based on the indicator and ordinary kriging respectively. Kriging estimator depends on the variogram parameters in capturing the spatial variability (Bohling, 2005). The ordinary kriging applies a random function model of the spatial correlation to estimate a weighted linear combination of the available data to predict the value at un-sampled location. The ordinary kriging method used in this study assumes a constant unknown mean over the search neighborhood. This method is preferred because of its ability to minimize the error variance (Yamamoto, 2005). The indicator kriging method used for the lithofacies interpolation is a simple non-parametric method applied for categorical data.

Lithofacies estimation: Figures 5.36 and 5.37 show the results of the lithofacies interpolation by means of indicator kriging. The 3-D interpolation of the lithofacies exhibits a good spatial continuity in a north-south direction. This direction is approximately parallel to the major direction selected in semivariogram computation. However, rather smooth features were observed at the rims of the study area (Figure 5.36 and 5.37). These features are a typical smoothing behavior imposed by the kriging interpolation. The smoothed values are mostly associated with areas that are located away from the well controls. These values are also associated with a high uncertainty related to distance between the point to be estimated and the real data points (Sahin and Aboukhodair, 1988). Vertically, the kriging interpolation showed a good vertical stacking of the identified lithofacies (Figure 5.36). The central parts of the structure had the better estimation of the lithofacies due to the proximity of the wells (Figure 5.36). Table 5.7 provides comparison of the input lithofacies and the corresponding kriging results.

Table 5.6 Comparison between the input lithofacies percentage and the kriged lithofacies output percentage.

Lithofacies	Input Lithofacies (%)	Kriging Results (%)
Sand	44.6	52.22
Shaly Sand	29.6	24.52
Shale	25.5	23.63

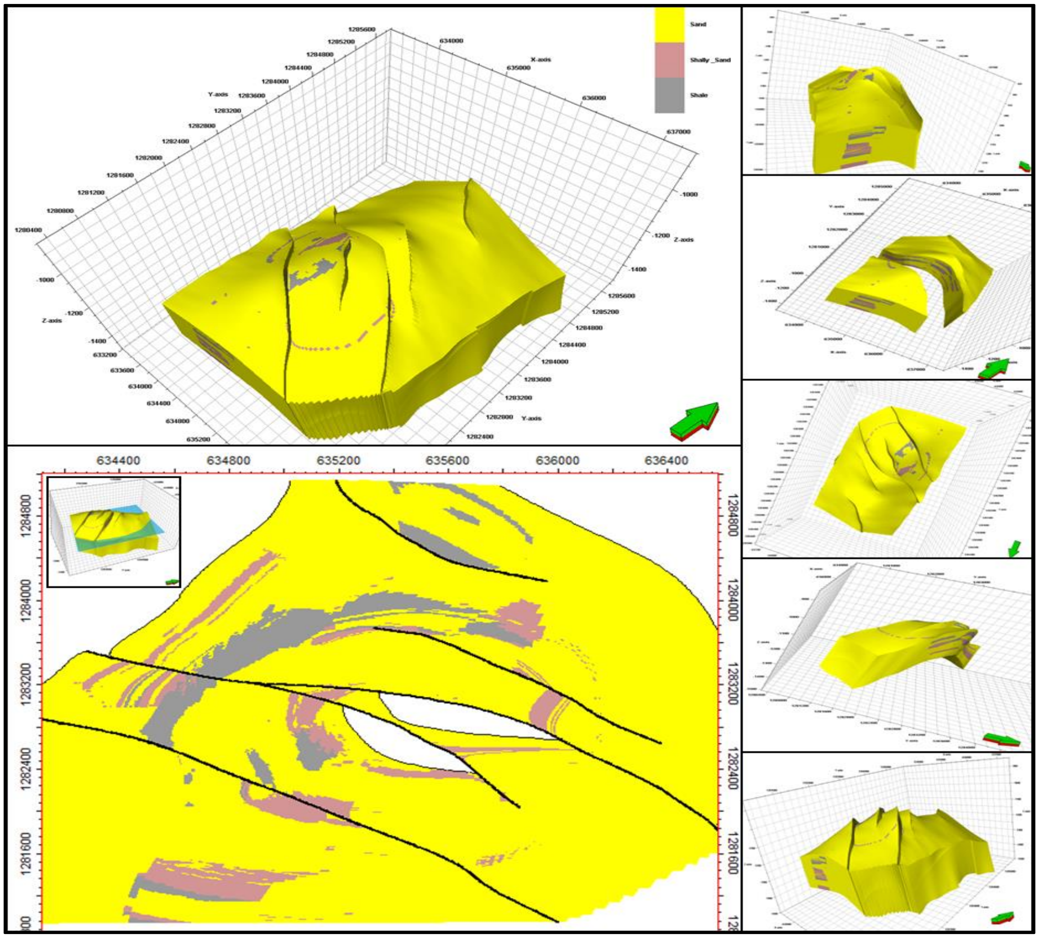

Figure 5.36 Various 3-D views and a depth slice (1188.41m) of the lithofacies resulted from the kriging interpolation.

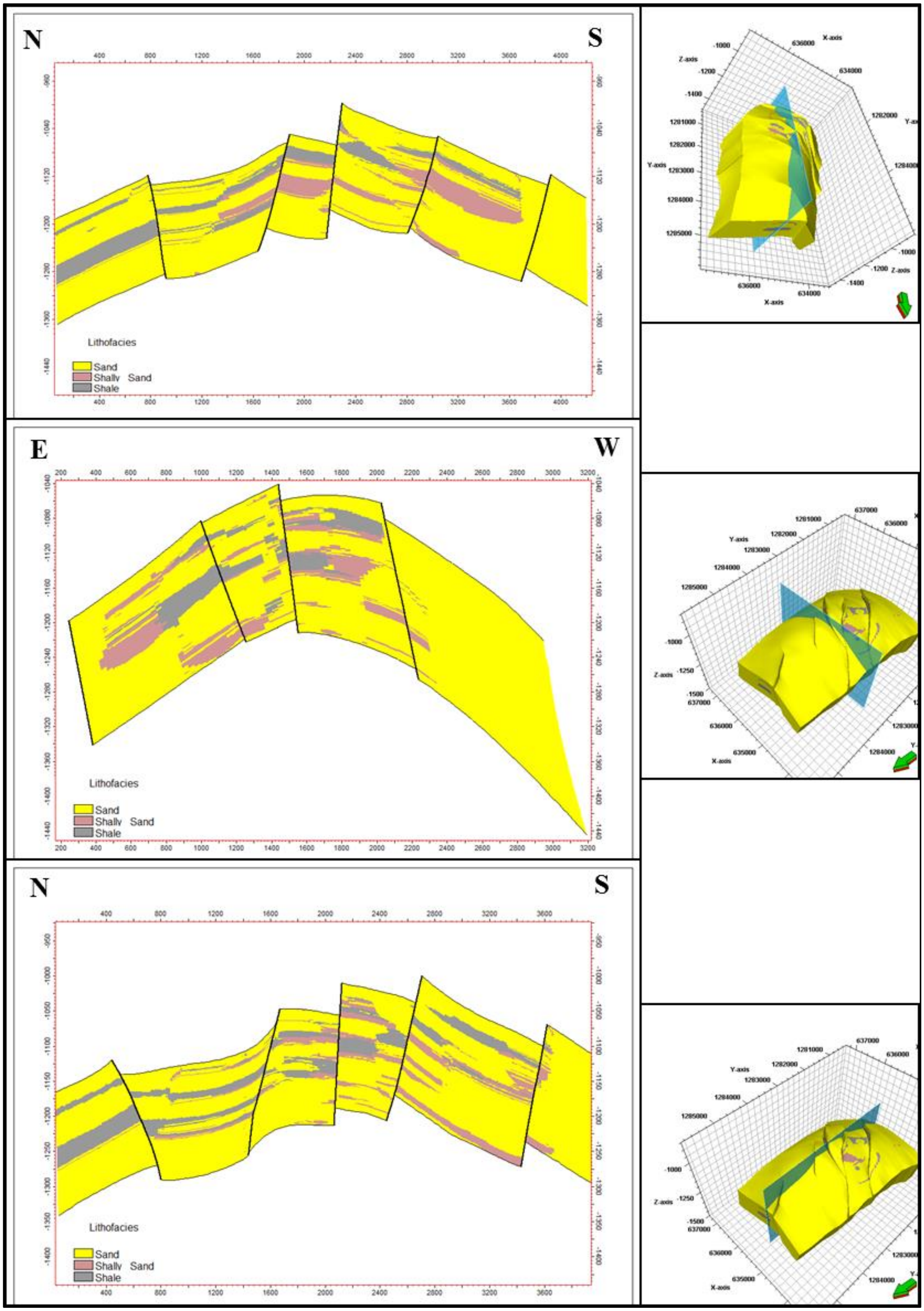

Figure 5.37 Three cross-sections of the lithofacies generated through kriging interpolation.

Petrophysical properties estimation: Figures 5.38 to 5.43 illustrate the results of the petrophysical properties estimated using the ordinary kriging technique. The porosity, permeability and water saturation properties at the un-sampled locations were estimated based on the respective semivariograms constructed earlier. The same search radius and number of cells used for the lithofacies interpolation were adopted for the petrophysical properties interpolation.

Porosity estimation: the porosity kriging results display expected lateral and vertical continuity. Continuous areas of high and low porosity generally extend laterally. This pattern was perfectly observed in Figure 5.38 from south to north.

Vertically, the porosity interpolation showed a good zonation. These zones were observed to be vertically stacked in a repetitive manner (Figure 5.39). Moreover, these zones can be directly linked to the lithofacies model in Figure 5.37.

Permeability estimation: the interpolation of permeability data by the ordinary kriging followed the same lateral and vertical trends of the porosity interpolation (Figure 5.40 and Figure 5.41). High permeability areas are often associated with the sand lithofacies. However, the interpolation of the permeability data is also biased toward the dominant values range. The absence of the smooth transition in the vertical stacking emphases the role of the depositional attributes (Figure 5.41). Aerially, as observed in the depth slice presented in Figure 5.40 at the top of the study interval, the permeability interpolation showed a good distribution with three distinctive areas generally extending north-south direction. The deepest part of the interval to the east and west revealed relatively low permeability compared with the central shallow areas (Figure 5.40).

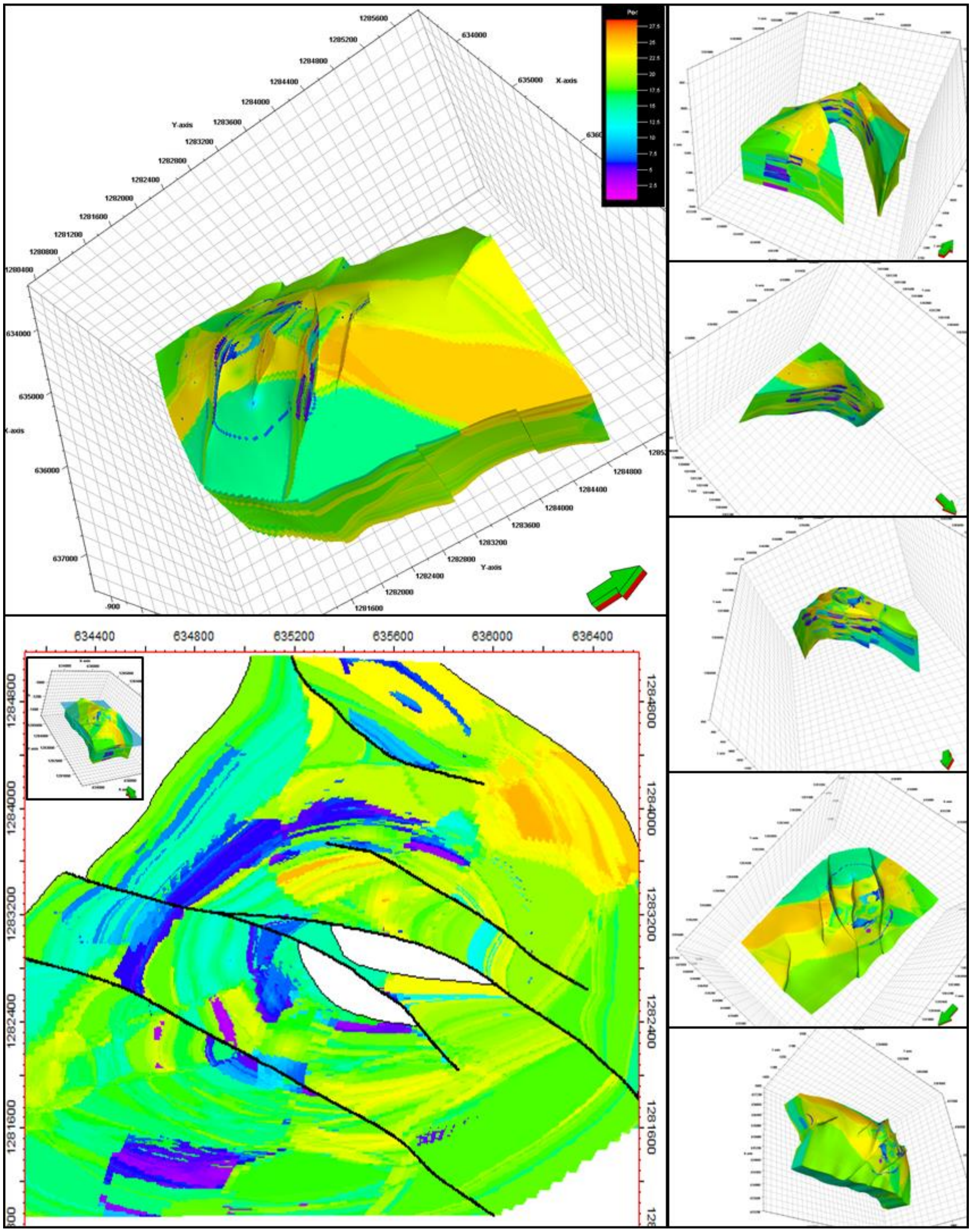

Figure 5.38 Various 3-D views and a depth slice (1188.41m) of the porosity estimation through ordinary kriging.

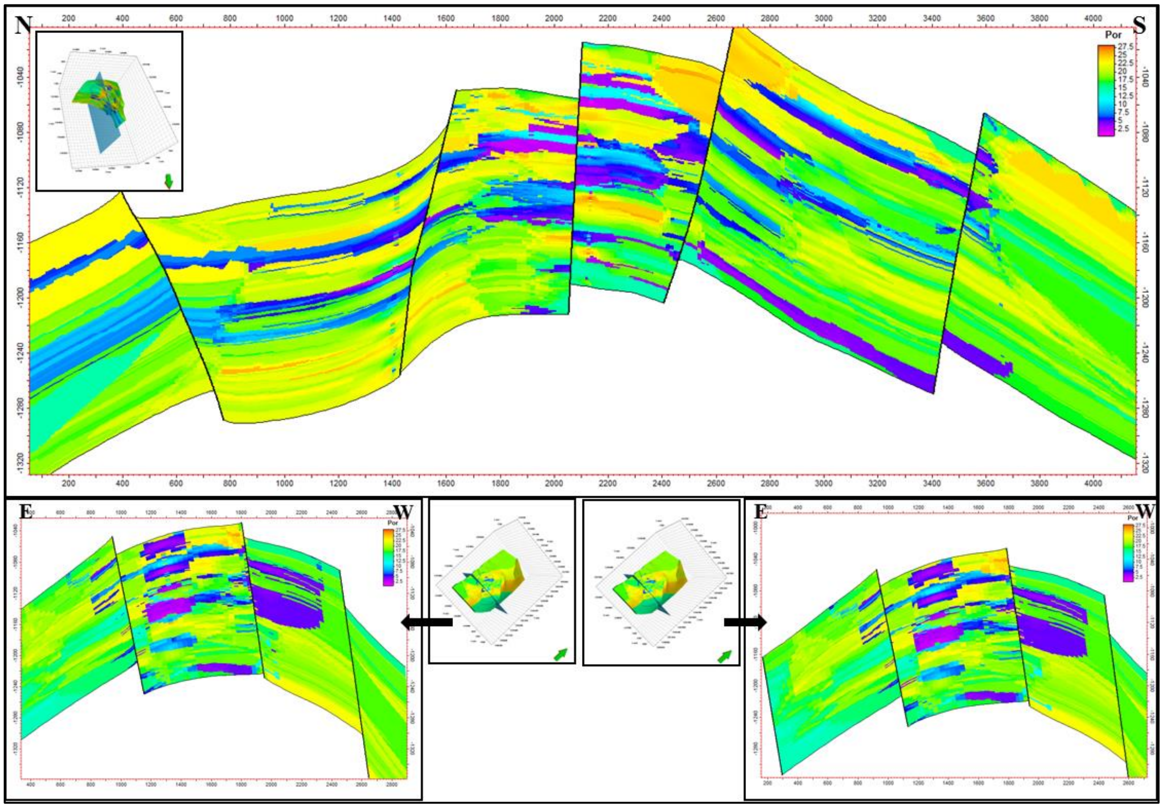

Figure 5.39 Three cross-sections of the porosity estimated through ordinary kriging.

Water saturation estimation: the kriging of the water saturation is presented in Figure 5.42. The aerial distribution (Figure 5.43) reveals some continuity especially within the central parts. Vertically (Figure 5.42), a clear zonation of the water saturation is observed. A number of zones have been vertically stacked with clear water saturation cutoffs. The zonation is best observed at the central part of the area, more precisely between the first and fifth fault from the north (Figure 5.42). Once again, the remote areas reveal clear smoothing, similar to that observed earlier in the interpolation of the porosity and the permeability data.

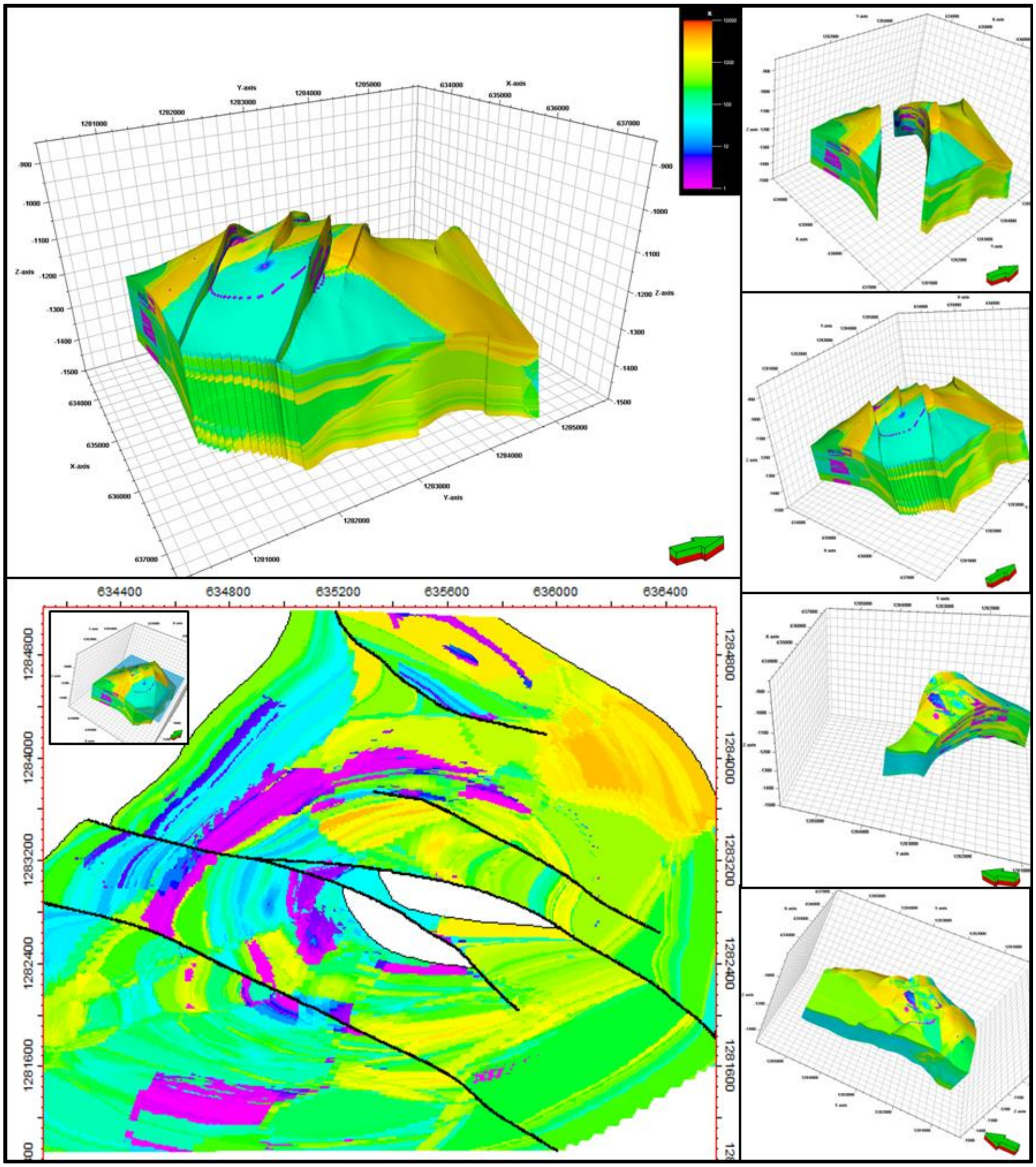

Figure 5.40 Various 3-D views and a depth slice (1188.41m) of the estimated permeability through ordinary kriging.

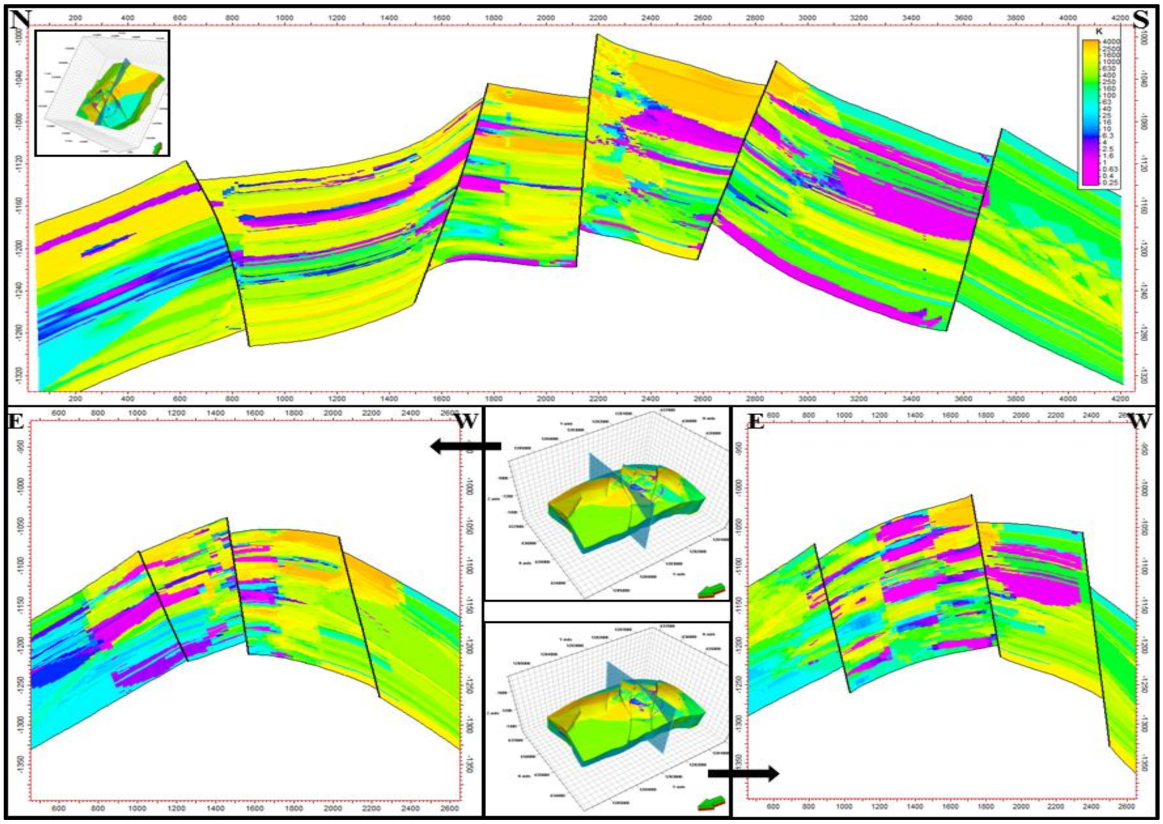

Figure 5.41 Three cross-sections of the permeability estimated through ordinary kriging.

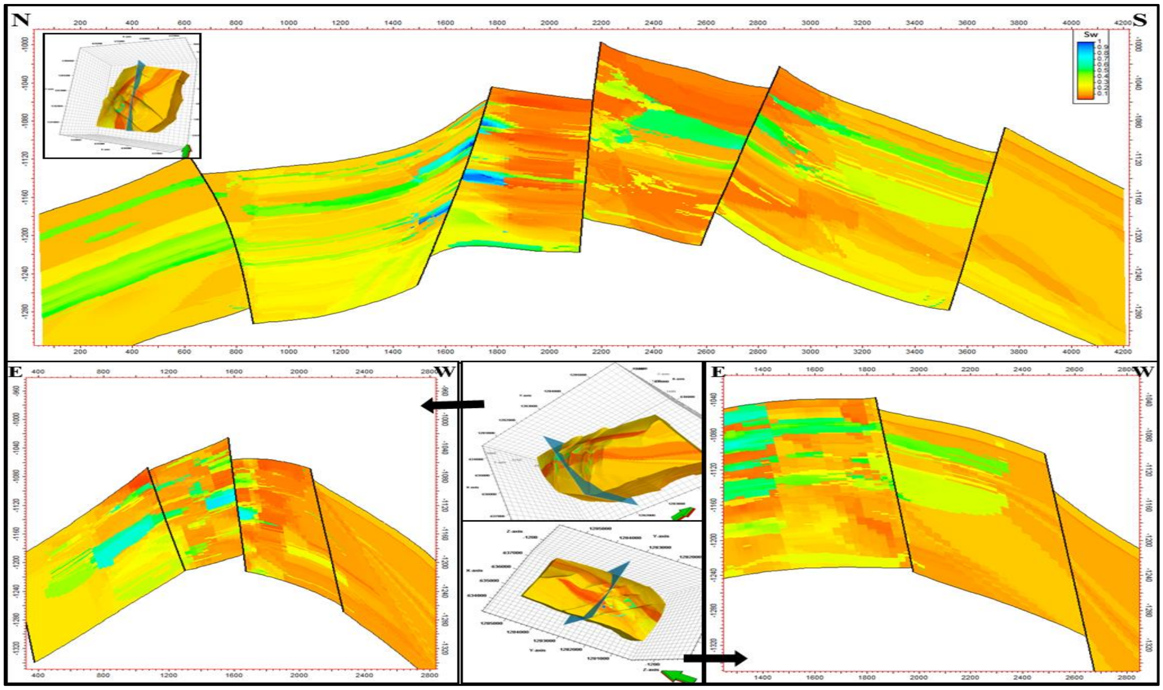

Figure 5.42 Three cross-sections of the water saturation estimated through ordinary kriging.

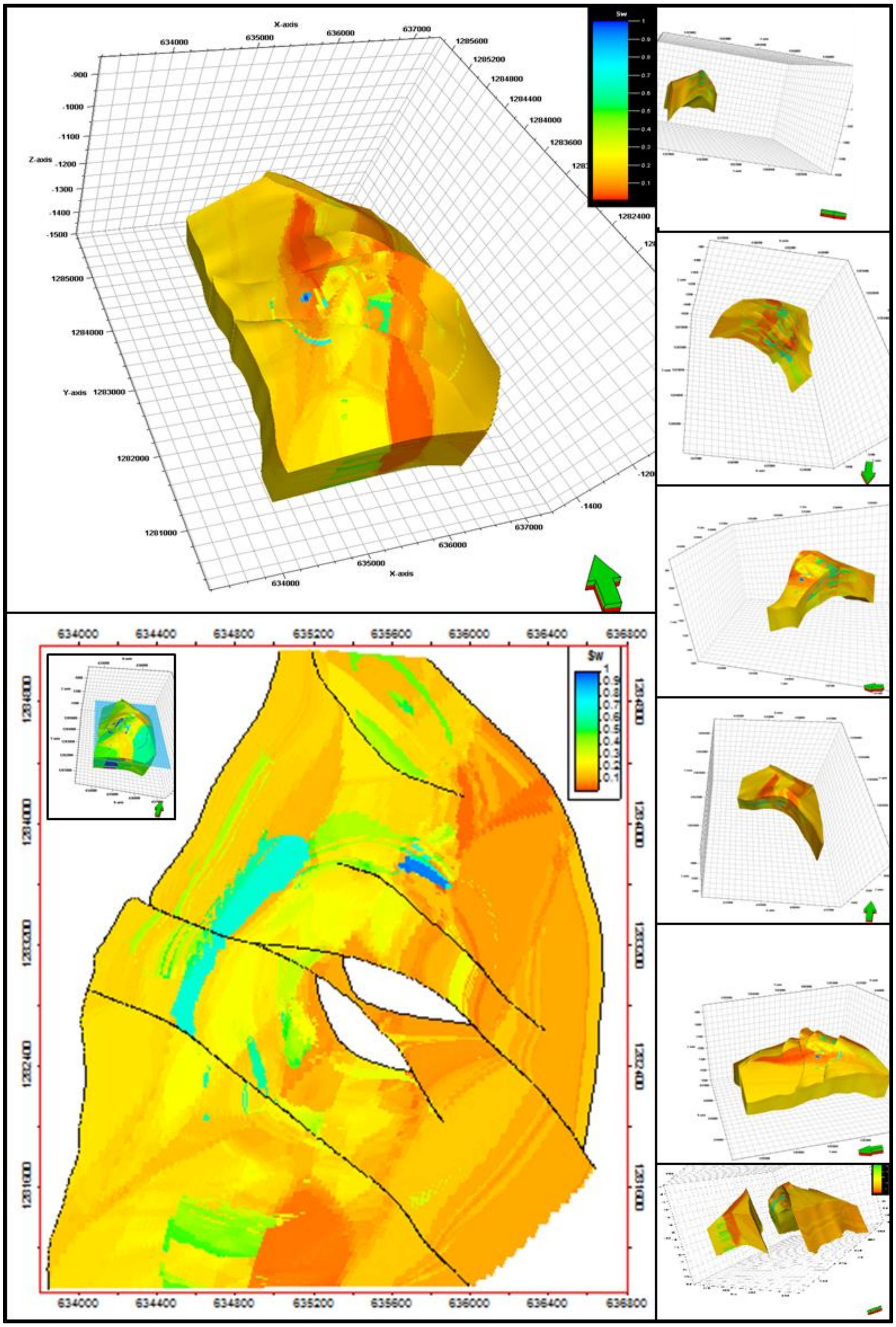

Figure 5.43 Various 3-D views and a depth slice (1188.41m) of the water saturation estimation through ordinary kriging.

From geological point of view, the interpolation of the petrophysical properties generally follows the same spatial and vertical distribution of the lithofacies. The zonation resulted from kriging interpolation observed in the three petrophysical properties represents a distinctive flow units that could be easily correlated with the lithofacies distribution. Figure 5.44 shows a part of cross-sections of lithofacies, porosity, permeability, and water saturation. Based on these cross-sections, four generally finning upwards lithological units can be identified. Each one of these units is dominated by sand at the bottom and capped with shale. Each one of these units is characterized by relatively high porosity where the sand lithofacies dominates. Porosity decreases upwards where the finer lithologies prevail becoming about 2.5% in the capping shale at the top (Figure 5.45). The permeability vertical distribution follows the same trend as observed in porosity. The zones characterized by higher porosity often associated with higher permeability and vice versa. The water saturation also revealed some interesting characteristics. The lower part for each of the four units, characterized with dominant sand lithofacies display lower water saturation. On the contrary, the interval where the shale lithofacies prevails is characterized by relatively higher water saturation values (Figure 5.44 and 5.45). It could be concluded that the petrophysical properties in the Bentiu-1 reservoir interval are generally controlled by the lithofacies.

5.3.6 Simulation

The kriging interpolation is accomplished by various methods such as the ordinary kriging where a randomized spatial function that is non-stationary and has varying means. These algorithms lead to smoothing and to some extent biased toward the sample points of higher occurrence (Yamamoto 2005).

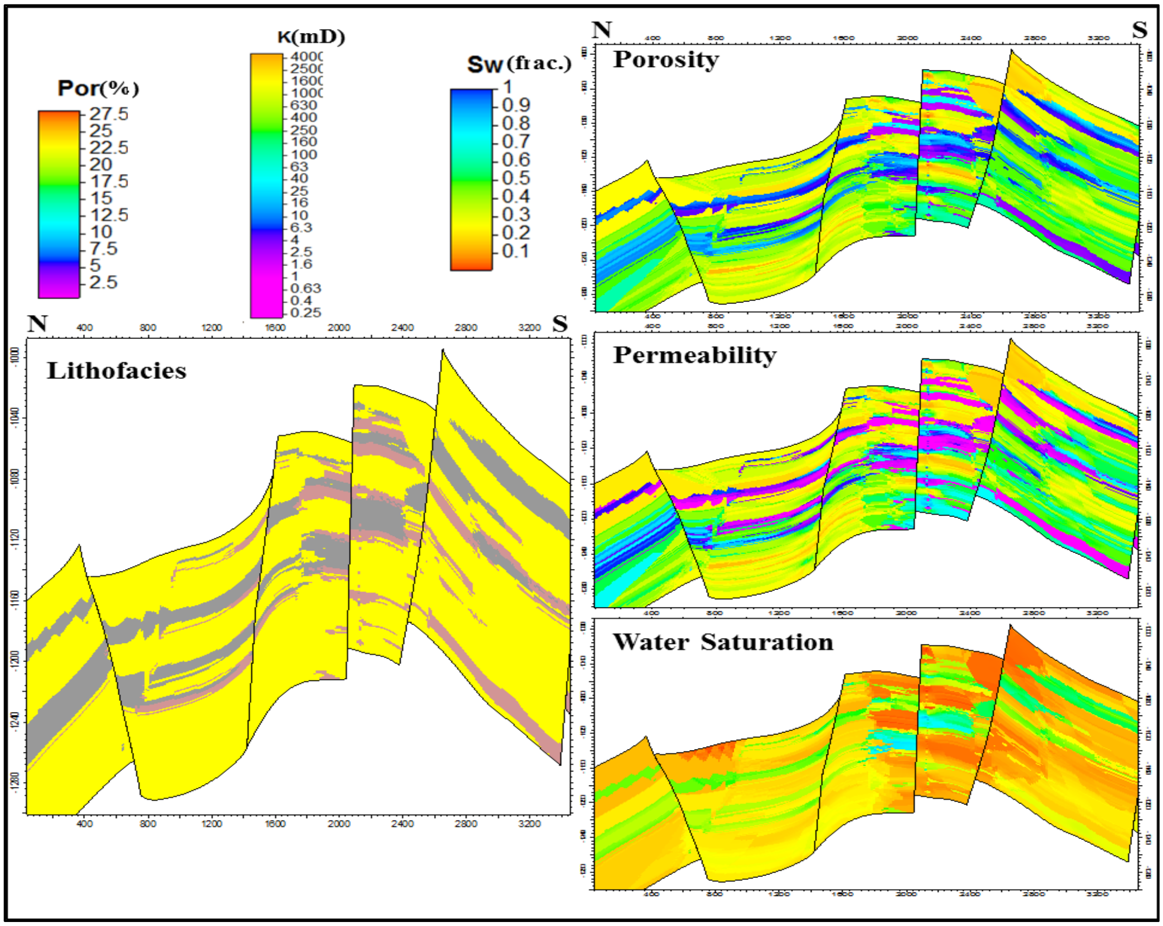

Figure 5.44 Cross-section from the lithofacies, porosity, permeability, and water saturation derived using kriging.

Therefore, various stochastic simulation approaches become available to reproduce the spatial variability. Hence, delivering models that display the spatial variability of a given phenomenon based on a predefined variogram model (Matheron, 1973 and Journel, 1977). Two simulation techniques were applied in this study: the Sequential Indicator Simulation (SIS) and the Sequential Gaussian Simulation (SGS). The Sequential Indicator Simulation (SIS) was used to simulate the lithofacies, while the SGS was applied to model the porosity, permeability and water saturation.

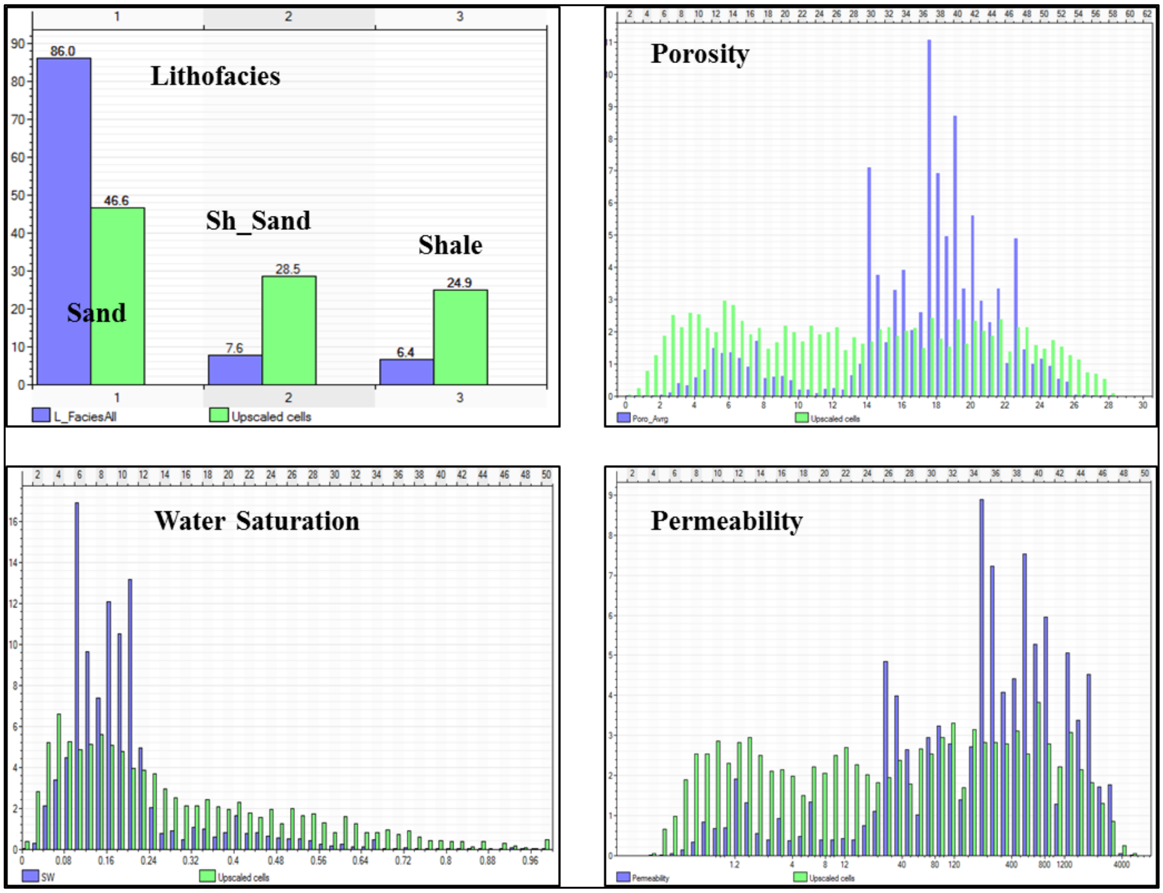

Figure 5.45 A comparison between the original input data (green) and the kriging results (blue) of the lithofacies porosity, permeability, and water saturation.

Lithofacies simulation: the data from twenty wells, indicator semivariogram parameters, and the initial kriging model were used to construct 3-D lithofacies model by applying the SIS. The structural model constructed previously was used to limit the study interval and to define the structural control over the study area (Figure 5.16). As a result, 25 equi-probable- simulated realizations were generated. The percentage of the simulated lithofacies in each of the 25 realizations accounted for and compared with the percentage of the input lithofacies.

Figure 5.46 shows various 3-D views of the model generated along the horizontal slice at 1188.41m depth. Moreover, three cross sections were also generated to check the quality and adequateness of the generated lithofacies model. The 3-D view of the generated lithofacies model shows high percentage of continuity between the three lithofacies in a north-south direction. Moreover, the sand lithofacies is dominant lithofacies in the four lithological units as identified earlier from the kriging results (Figure 5.37).

Aerially, a good continuity of the lithofacies is observed, especially at the central and western areas (Figure 5.46). The mild curvature in the sand lithofacies (Figure 5.47), which represent lag deposits, indicate a low sinuosity stream that generally extend in N-S direction as reported in the literature (Idriss, 2002; Eltom, 2007 and Dou Lirong et al., 2013). The distribution of shaly sand lithofacies follows the same general vertical and aerial distribution. However, the thicknesses of this lithofacies are considerably smaller than that of the sand lithofacies (Figure 5.47). Aerially, the shale occurs as isolated sheets and in some areas terminates and bounds the sand lithofacies. This lithofacies most probably represents the flood plain of the low sinuosity stream according to low sand to shale percentage. Vertically, the four fining upward cycles identified earlier from the kriging interpolation do not appear clearly in the SIS models (Figure 5.347). However, the SIS model reveals a more realistic vertical succession. Moreover, the high sand to shale ratio is also preserved. The vertical cross-sections shown in Figure 5.47 illustrate that the sand is the dominant lithofacies vertically through the succession. On the contrary, the shale was well developed in the middle of the interval with the maximum thickness of approximately 20 meters. The shale lithofacies is often discontinuous and gave a lenses-like view to the sand lithofacies (Figure 5.47).

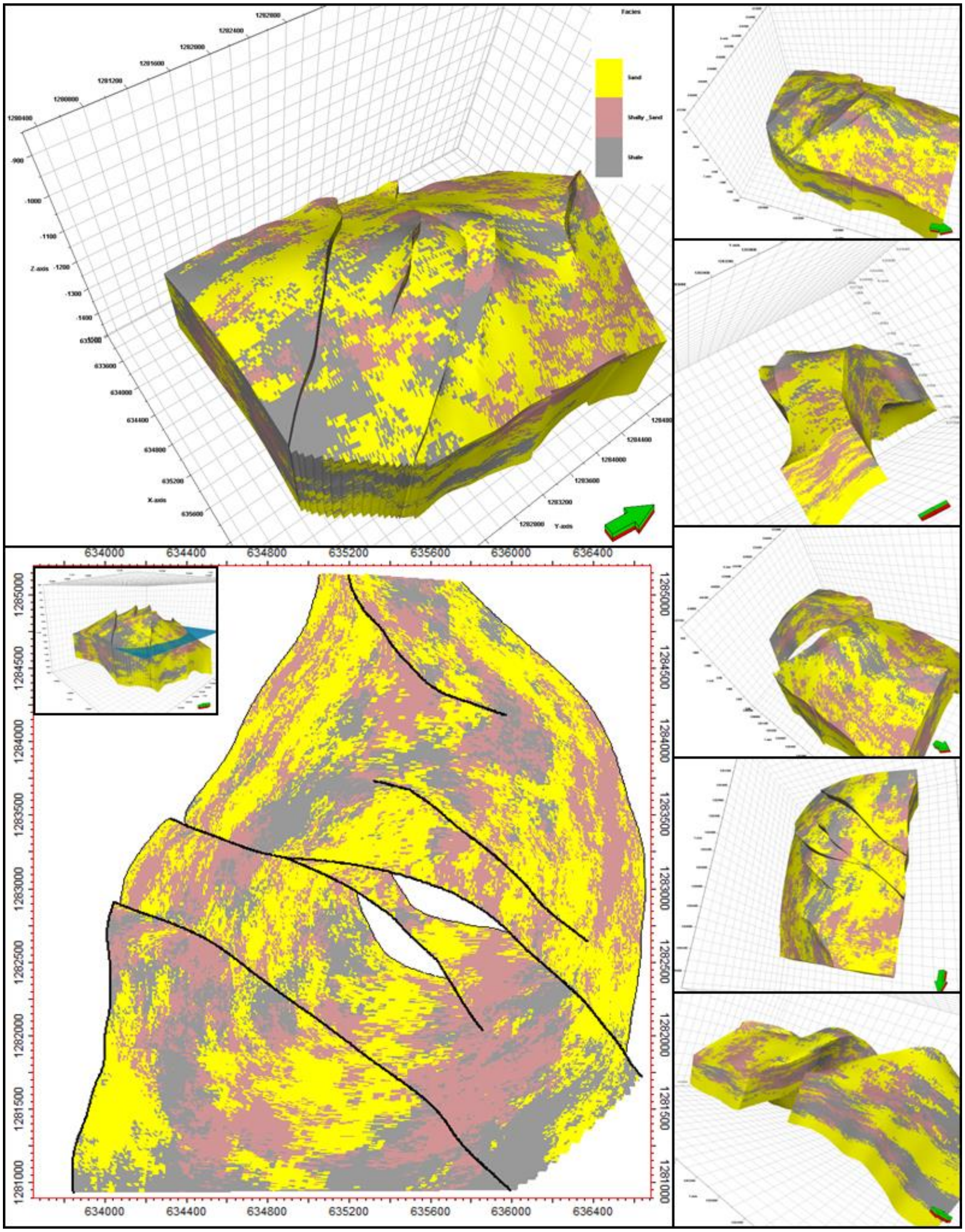

Figure 5.46 A number of 3-D views and a depth slice (1188.41m) from the lithofacies simulation model by the SIS.

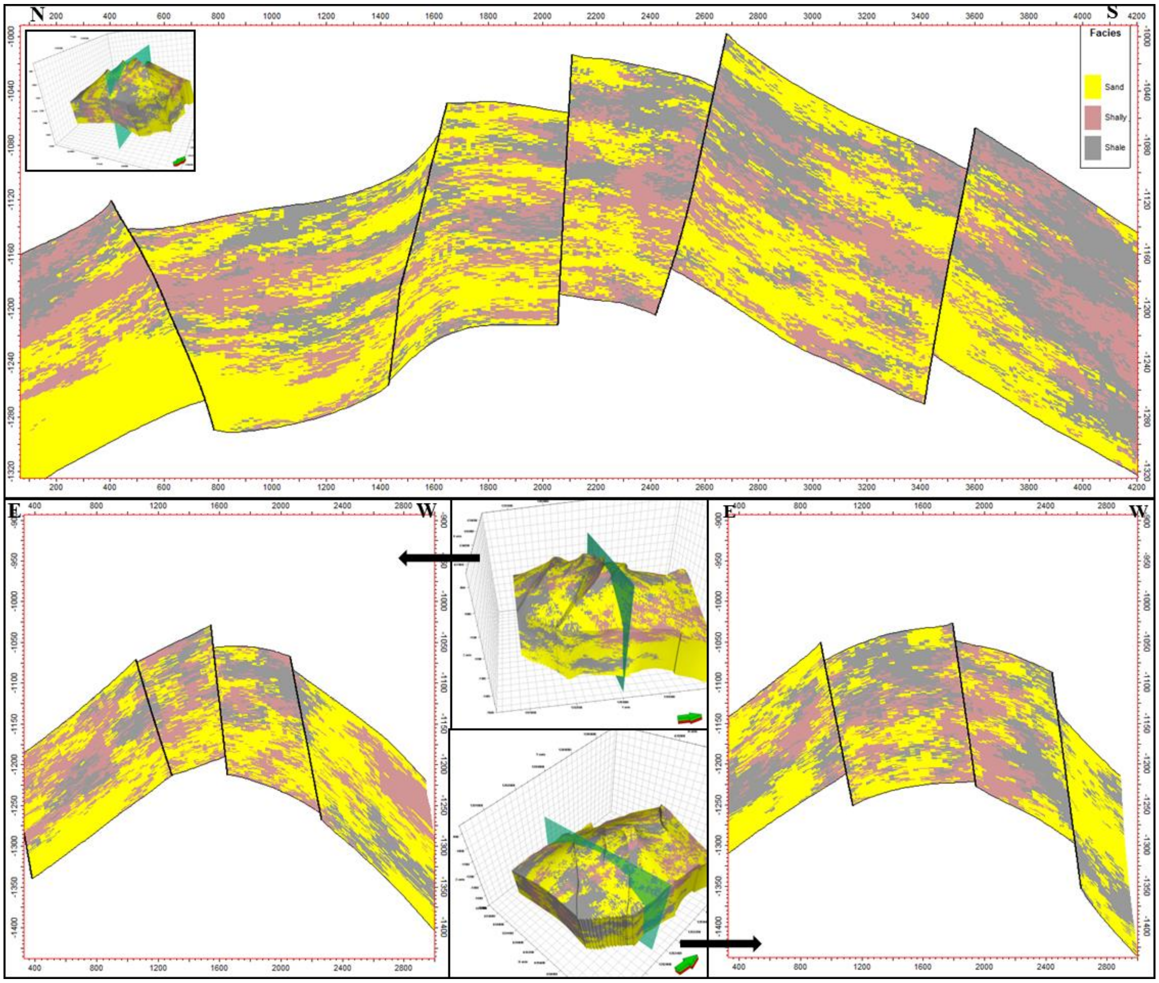

Figure 5.47 Three cross-sections from the lithofacies simulation model by the SIS.

Property Simulation: the generated lithofacies model provides a firm geological framework that would lead to 3-D property simulation. Several authors reported the improvement of the 3-D porosity model when guided by the lithofacies model (Al-Qassab and Heine, 1998).

The porosity, permeability and water saturation models in this study were generated by using the SGS technique. The procedure and algorithms of the SGS were discussed in Section 5.2.6. The petrophysical parameters were first conditioned to the lithofacies when the semivariograms constructed (Section 5.4.1). The benefits of this conditioning are correlating the petrophysical parameters to their representative lithofacies. The 20 wells, semivariogram parameters and the initial kriging models were used as input to the SGS. Accordingly, 25 equi-probable realizations were generated for each of the three petrophysical parameters. The descriptive statistics of the simulation results, simulation validation and honoring of the input data were accounted for and they will be discussed in Section 5.5.

Porosity modeling: an example of the constructed porosity models is illustrated in Figure 5.48 and Figure 5.49. The 25 generated realizations of porosity simulation revealed a good spatial and vertical distribution. The 3-D view (Figure 5.48) of the porosity model shows a good continuity between the porosity values. In this sense, the high porosity values are indicate the sand lithofacies while the low porosity the shale lithofacies. The depth slice (1188.41m) presented in Figure 5.48 displays a quite interesting structure with the circular belt of a low porosity occupying the central part of the area. The formation of this belt can be attributed to the influence of the structural control over the area. The vertical cross-sections of 3-D porosity model (Figure 5.49) reveal a clear stacking of porosity zones. The four lithological fining upward units identified earlier from the kriging maps can be clearly observed here. In general, the four low-porosity belts have a good lateral continuity in the north-south direction. These belts can be directly correlated to the shale lithofacies. Although the sand often reveals high porosity, the varying ranges within this facies indicate its heterogeneity (Figure 5.49). This heterogeneity could be related to the different origin of the sand deposition, varying geological control, and/or pre-and-post depositional factors.

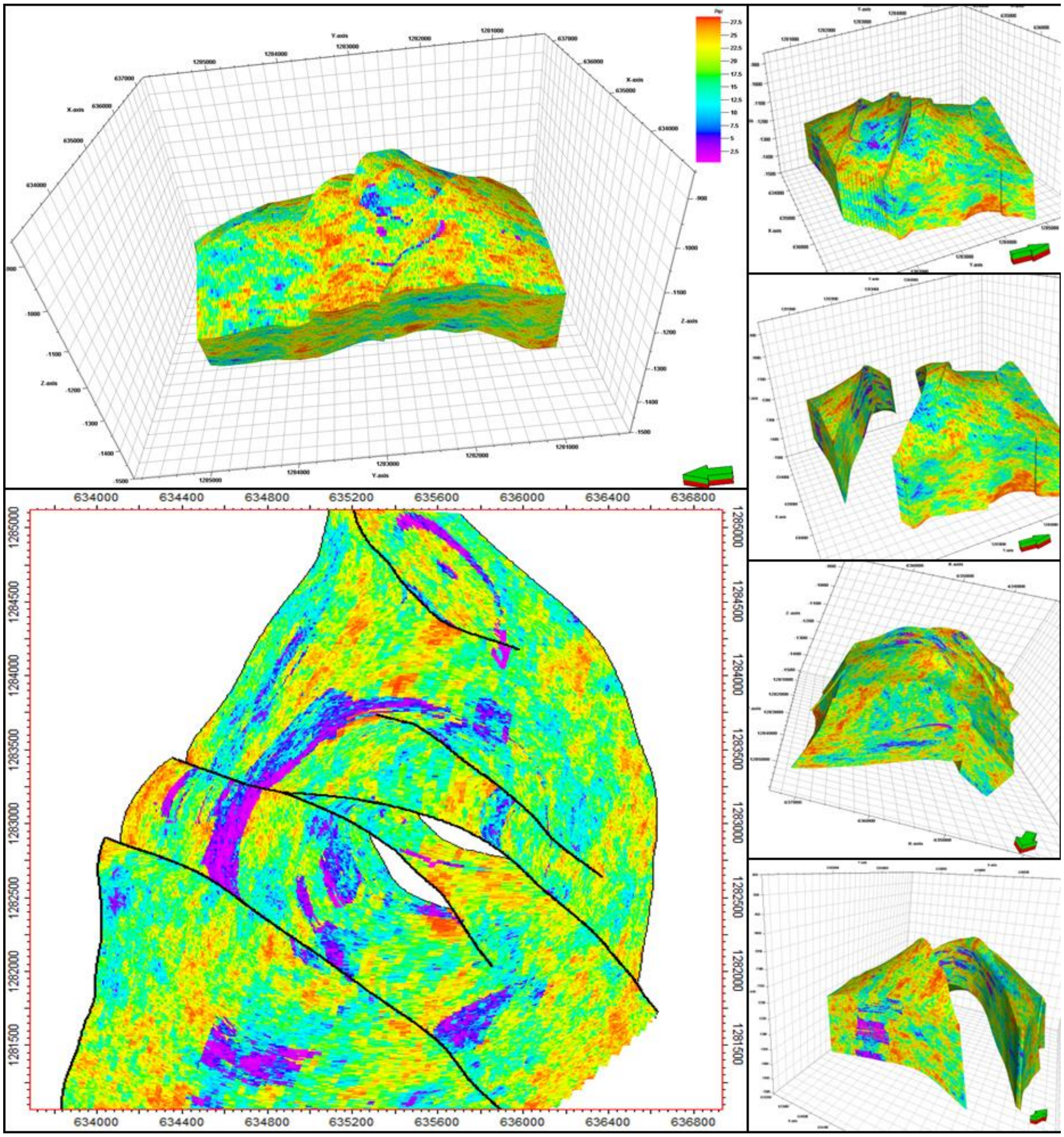

Figure 5.48 A number of 3-D views at a depth slice (1188.41m) from the porosity simulation model obtained using the SGS.

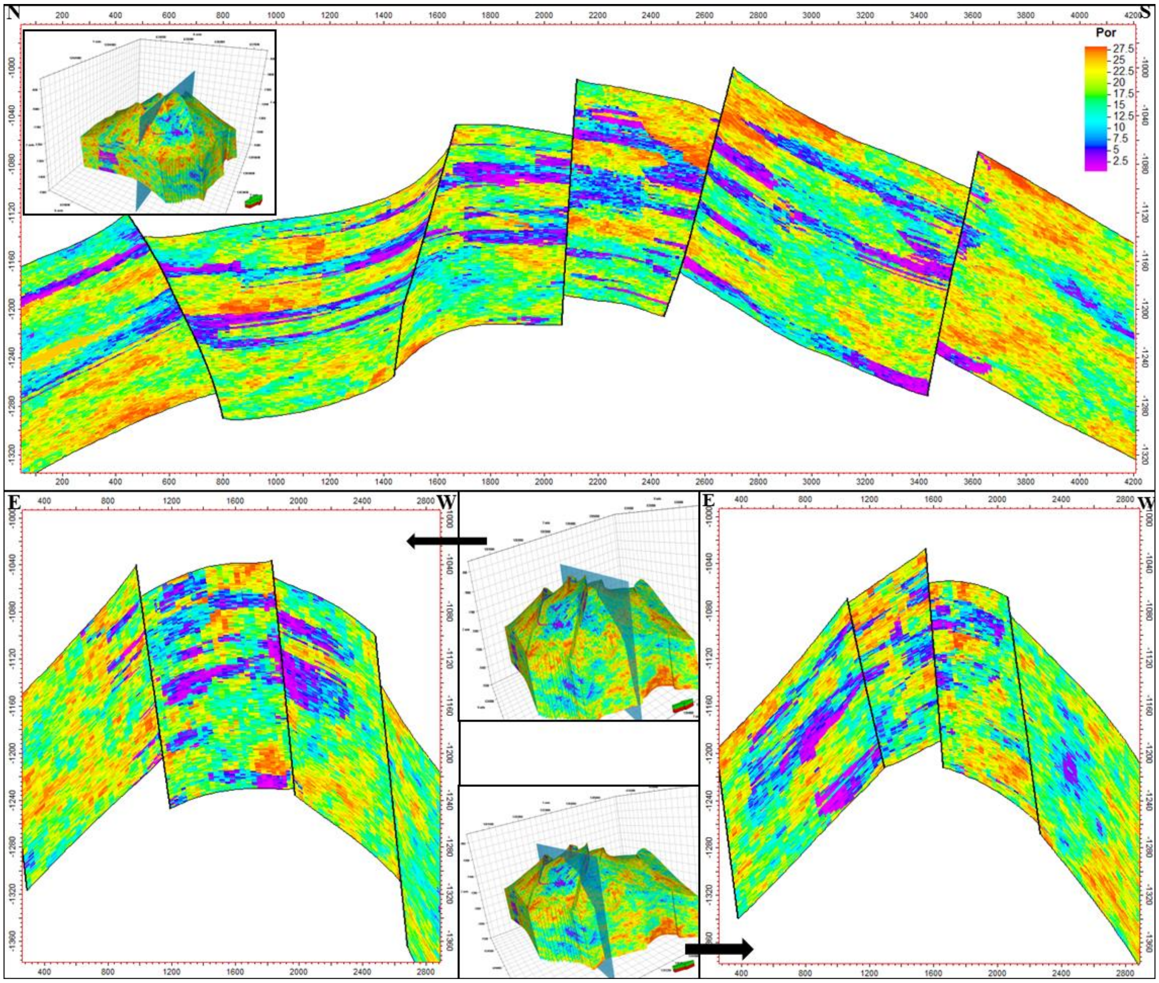

Figure 5.49 Three cross-section taken from the 3-D model of the porosity generated using the SGS.

Permeability modeling: generated model of the permeability is given in Figure 5.50. Since permeability data was calculated from the porosity data as outlined earlier (see Section 4.3), its lateral, and vertical distributions generally follows the respective distributions of the porosity. However, the vertical cross-sections (Figure 5.51) reveal an improved continuity and lateral distribution when compared with the porosity cross-sections.

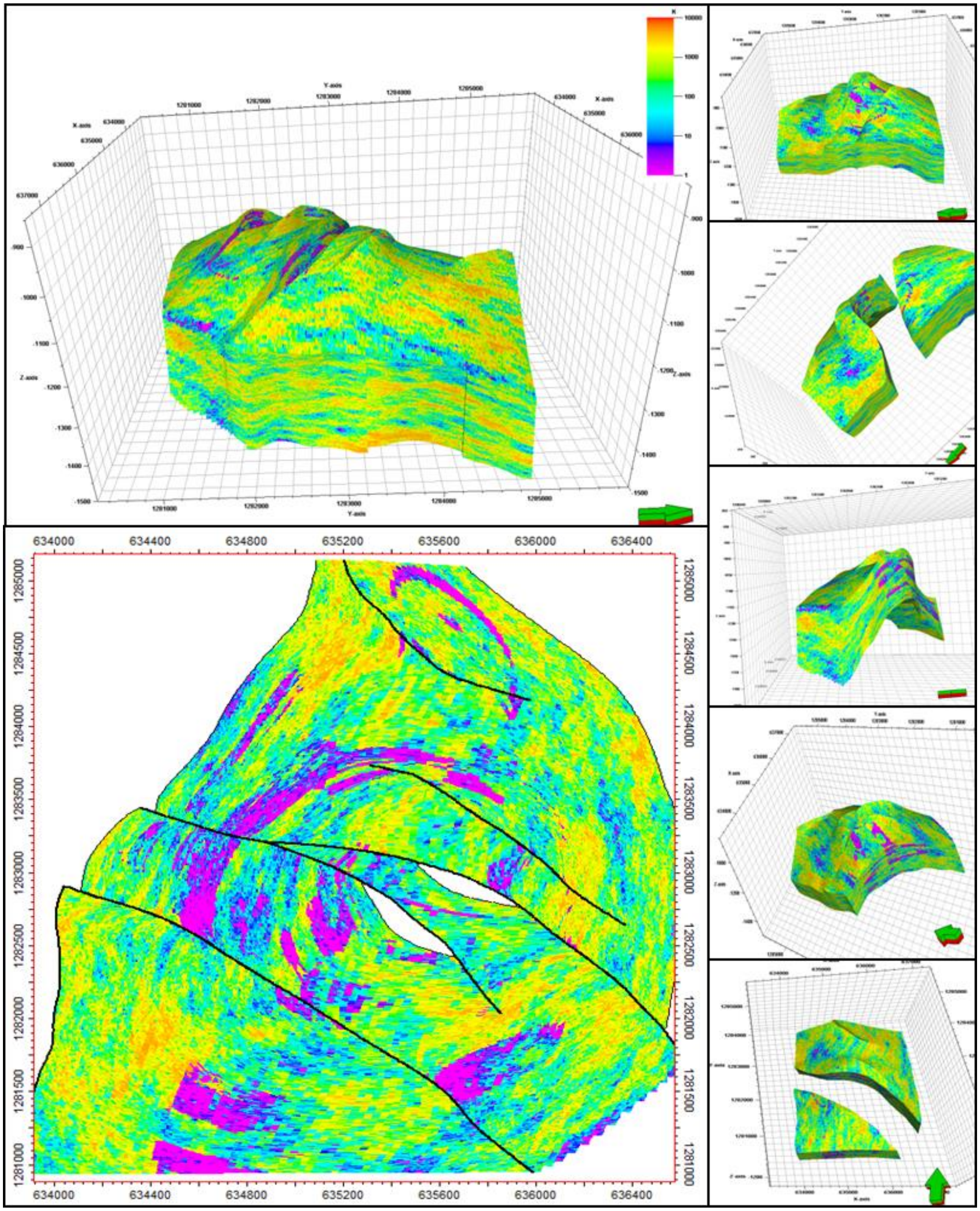

Figure 5.50 A number of 3-D views and depth slice (1188.41m) from the permeability simulation model obtained using the SGS.

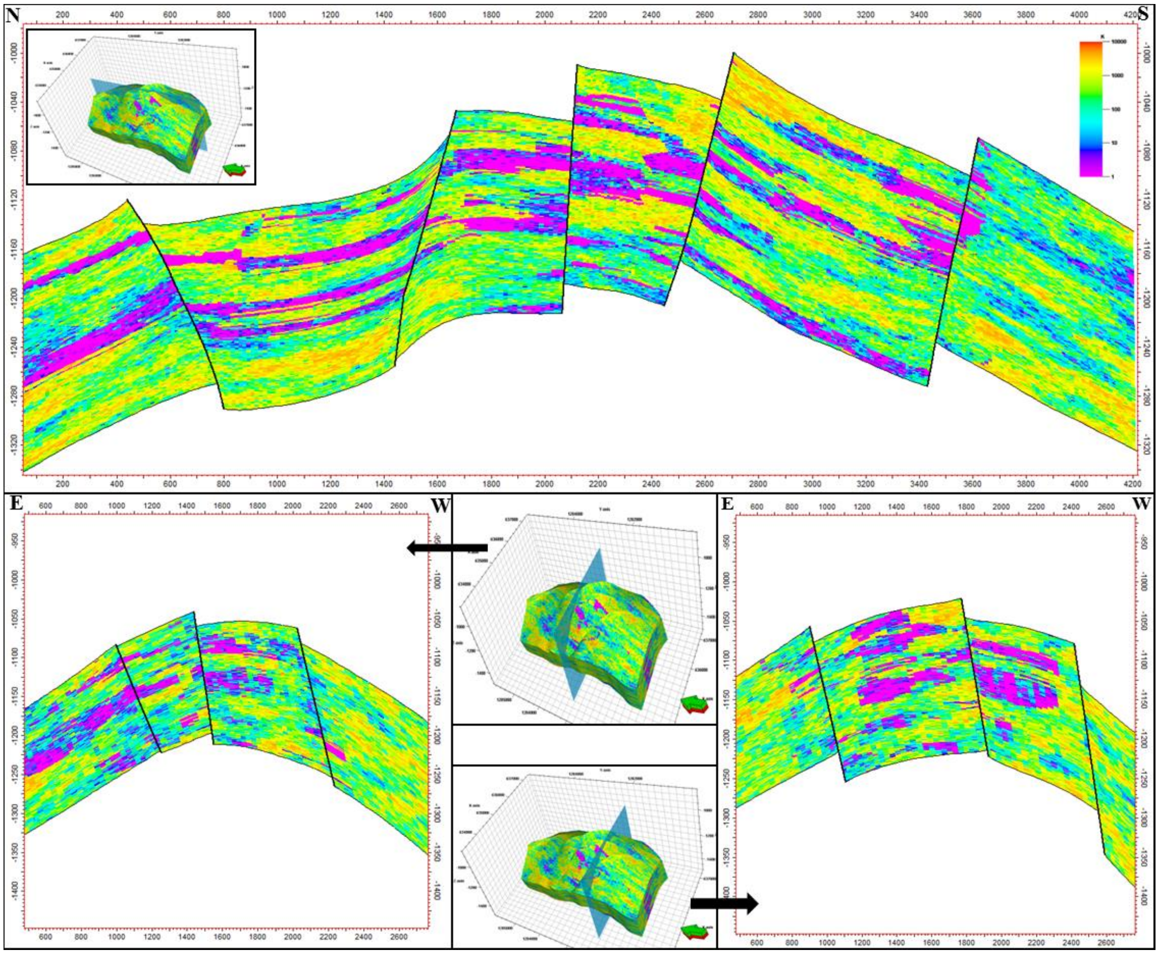

Figure 5.51 Three cross-sections taken from the 3-D model of the permeability generated by the SGS.

Water Saturation models: These models were also generated by gathering the water saturations calculated from the logs of the 20 wells, conditioned semivariogram parameters, and the initial water saturation kriging model. The water saturation simulation was accomplished by applying SGS algorithms discussed in Section 5.2.6.

Figure 5.52, illustrates a various 3-D view of the water saturation model in addition to a horizontal slice taken at depth of (1188.41 m) within the Bentiu-1 reservoir interval. The 3-D model of the water saturation shows a good lateral and vertical continuity. However, a more distinct lateral continuity was observed especially in the north-south direction (Figure 5.52 and Figure 5.53).

Aerially, the same low porosity, low permeability circular belt observed in the porosity and permeability simulation models were also observed in water saturation models. Accordingly, the three depth slices of the porosity, permeability and water saturation were compared at the same depth slice (1188.41 m) from the respective models.

The lateral enhanced continuity observed in the N-S cross-section (Figure 5.53) reveals the tendency of the water saturation to occur in preferred zonation. This zonation extends along the N-S direction and could be directly related to the lithofacies within the Bentiue-1 reservoir interval. In addition, the three cross-sections illustrated in Figure 5.53 reveal a notable vertical stacking. Once again, this vertical stacking of the water saturation resembles the lithofacies simulated (Figure 5.47). The shale lithofacies corresponds to a clear water saturation cutoff of more than 40%, whereas the sand corresponds to a water saturation cutoff of less than 30%.

5.3.7 Validation and Ranking

Qualitative and quantitative validation approaches were carried out in this study to assess the validity of the simulation results. In the qualitative approach, a comparison is made between the wells data location to insure honoring the data points at their locations. While in the quantitative approach, some of the basic verification and minimum acceptance criterion that should be performed at the simulation model (Leuangthong and others 2004) were carried out. Moreover, an adaptive approach is also used to rank the 25 realizations resulted from the SIS of the lithofacies and the 25 realizations from the SGS for each of the porosity, permeability, and water saturation. This ranking is meant to rearrange the multiple realizations representing various simulation alternative based on the best and worst case scenarios.

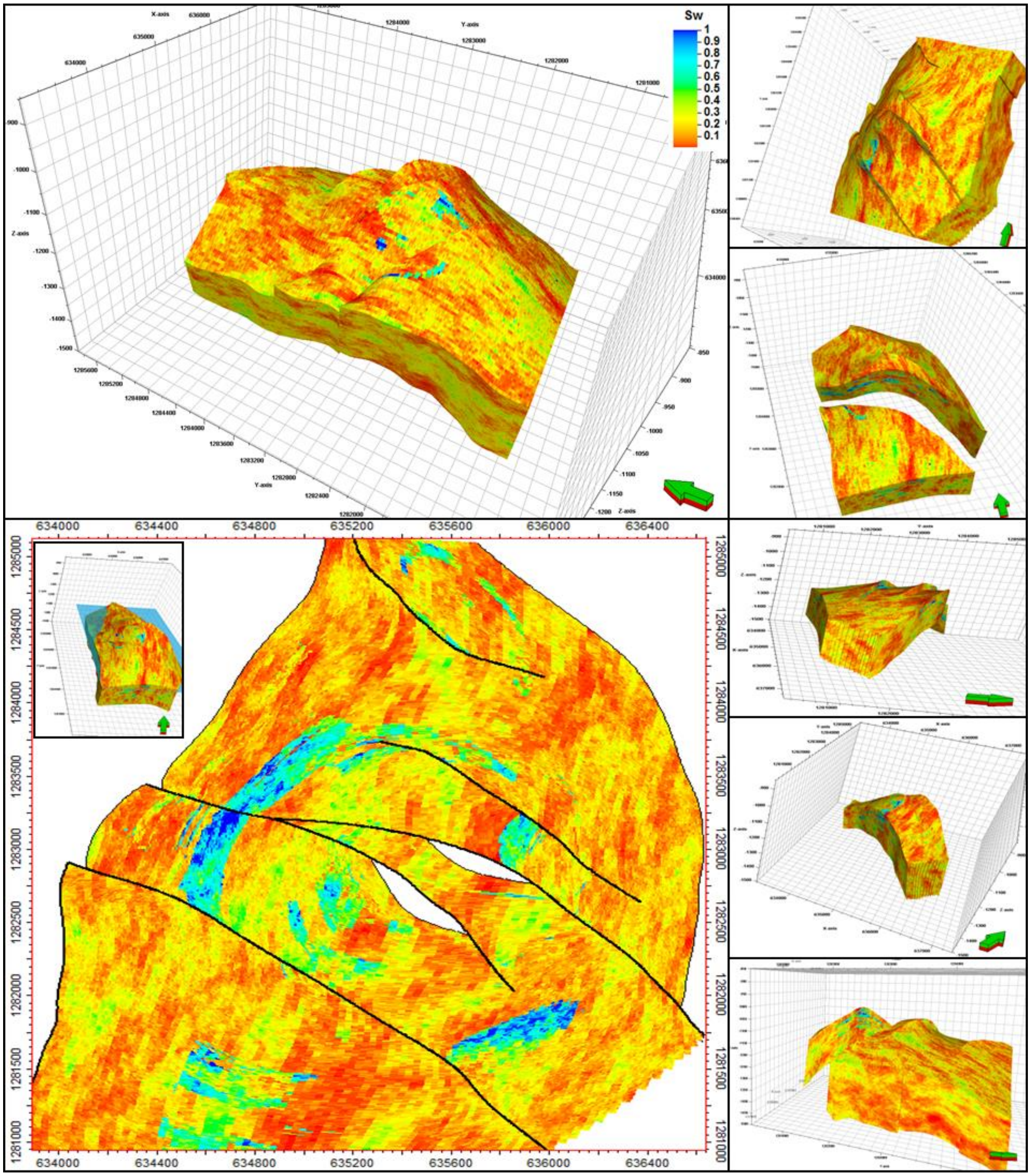

Figure 5.52 A number of 3-D views and depth slice (1188.41m) from the water saturation simulation model obtained using the SGS.

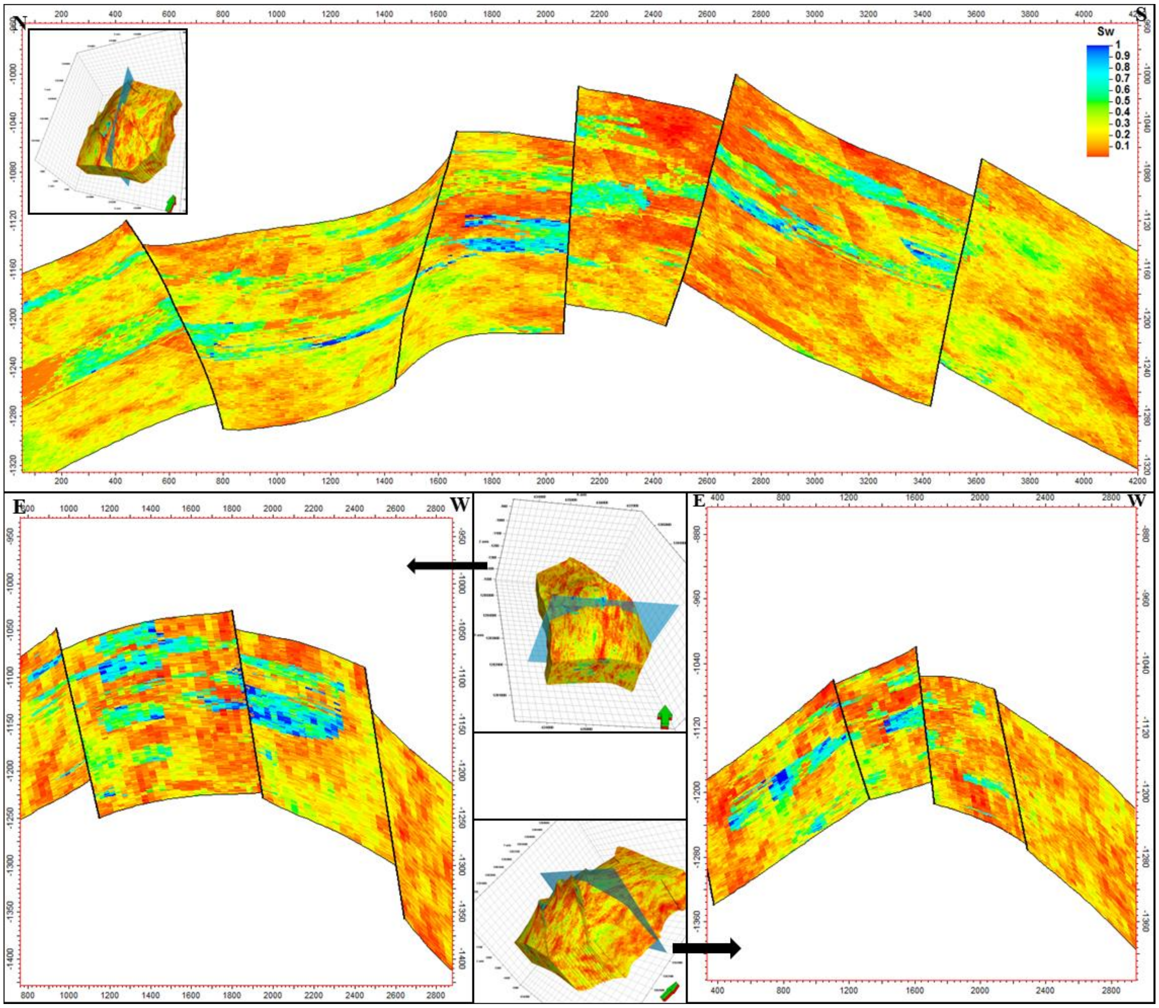

Figure 5.53 Three cross-sections taken from the 3-D model of the water saturation generated using the SGS.

A visual comparison between the simulated data and the original data at the wells was carried out qualitatively; Figure 5.54 shows an example of this comparison. The simulated properties were shown next to the original well data in this figure. This comparison revealed great similarity between the original data and the simulated data indicating that the simulation algorithms honored the original data at their location. Moreover, several model slices were randomly selected and compared with other petrophysical parameters and lithofacies. During this comparison, the same depth for the slices and the same cross-section for the simulation results were maintained. The qualitative approach followed in this study confirmed the adequacy of the simulation results.

In the quantitative validation approach, the descriptive statistics and their plots have been used. Table 5.7 and Figure 5.55 show the relative percentage of the 25 realizations resulted from the SIS simulation of lithofacies. A 5% threshold error from the original input data was used as an indication on the acceptance or rejection of a given realization (Table 5.7). Accordingly, 12 lithofacies realizations were accepted out of the 25 realization and the rest were rejected. The accepted realizations show great resemblance to the original input lithofacies in terms of percentages (Table 5.7).

Table 5.8 gives the descriptive statistics of the petrophysical properties simulation. The 25 realizations for each of the petrophysical properties were sorted out to determine the best and worst case scenarios. Figures (5.56, 5.57 and 5.58) show the histograms and Cumulative Distribution Function (CDF) of the porosity, permeability and water saturation plotted against the original input data.

The porosity histogram and CDF revealed a slight difference between the original and the simulated porosity distribution for the 25 realizations generated. These differences are mainly due to the 3-D interpolation by means of the ordinary kriging algorithms without adequate well control. Hence, the three realizations (8, 9, and 21) closely matching the original input data (Table 5.8 and Figure 5.56) were defined as the best-case scenarios, and the three realizations lying away from the input data as the worst-case scenarios (realizations 4, 5, and 6).

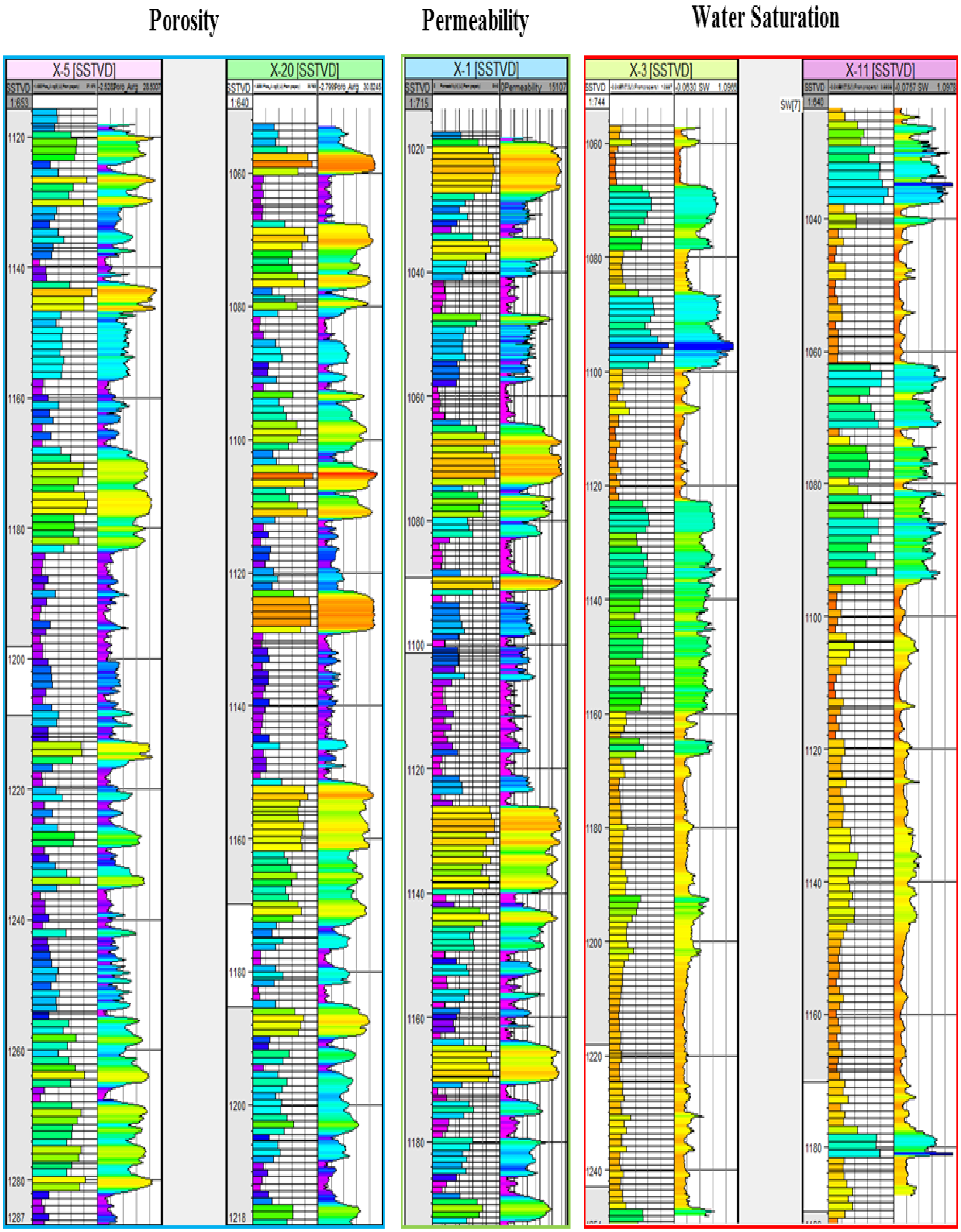

Figure 5.54 A visual comparison between the original input data (Track #1) and the simulated data (Track #2) at the well location for the porosity, permeability, and water saturation.

Table 5.7 The 25 realizations resulted from the Sequential Indicator Simulation of lithofacies.

Realization No	Lithofacies Percentage			Status
	Sand	Shaly_Sand	Shale	
Rel. # 1	42.02	38.16	19.82	Rejected
Rel. # 2	54.01	25.63	20.36	Rejected
Rel. # 3	45.11	32.36	22.53	Accepted
Rel. # 4	40.74	33.90	25.37	Accepted
Rel. # 5	41.22	32.16	26.62	Accepted
Rel. # 6	48.55	28.78	22.67	Accepted
Rel. # 7	49.11	28.70	22.19	Accepted
Rel. # 8	50.17	28.56	21.27	Rejected
Rel. # 9	40.34	32.81	26.85	Accepted
Rel. # 10	41.12	39.26	19.63	Rejected
Rel. # 11	43.90	31.67	24.43	Accepted
Rel. # 12	47.28	27.28	25.44	Accepted
Rel. # 13	31.57	35.60	32.83	Rejected
Rel. # 14	36.75	34.21	29.05	Rejected
Rel. # 15	43.16	34.04	22.80	Accepted
Rel. # 16	34.87	41.23	23.90	Rejected
Rel. # 17	40.59	33.17	26.24	Accepted
Rel. # 18	42.91	33.98	23.11	Accepted
Rel. # 19	44.76	32.24	23.00	Accepted
Rel. # 20	46.64	34.00	19.36	Rejected
Rel. # 21	40.33	40.31	19.36	Rejected
Rel. # 22	35.08	36.43	28.49	Rejected
Rel. # 23	36.51	36.65	26.84	Rejected
Rel. # 24	33.84	39.89	26.26	Rejected
Rel. # 25	43.26	30.95	25.79	Accepted

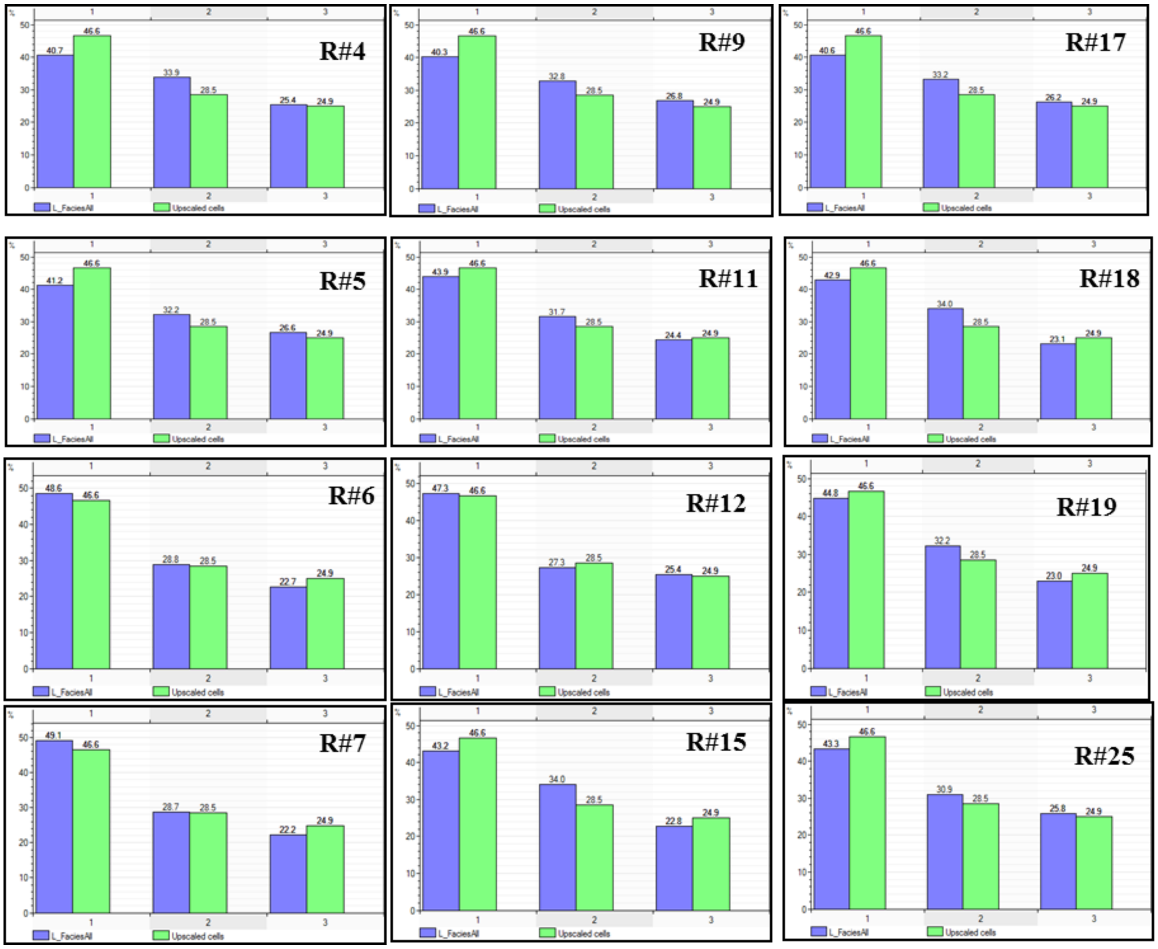

Figure 5.55 The histograms of the 25 generated realizations from the SIS simulation: blue –simulated lithofacies and green – original input lithofacies.

The same approach was followed to assess the validity of the realization of permeability simulation. Figure 5.57 shows the histogram and the CDF of the 25 realizations resulted from the permeability simulation. The distribution of the 25 realizations in this case showed a notable resemblance to the distribution of the original input data (Figure 5.57). Once again, the closest three realization (7, 8 and 17) to the original input data were selected as the best-case scenarios and the three realizations (5, 13 and 15) as the worst-case scenario.

The 25 realization generated from the water saturation simulation were validated following the same approach used for the porosity and permeability quantitative validation. Table 5.8 lists the mean and variance of the 25 realizations resulted from the water saturation simulation. Moreover, the 25 realizations of the water saturation simulation were plotted in a histogram and CDF against the original input data (Figure 5.58). Based on this plot, a notable resemblance in the distribution between the input data and the 25 realizations was observed. Accordingly, realizations number 4, 19 and 21 were chosen as best scenarios and realization number 8, 17 and 22 represent the worst possible scenarios.

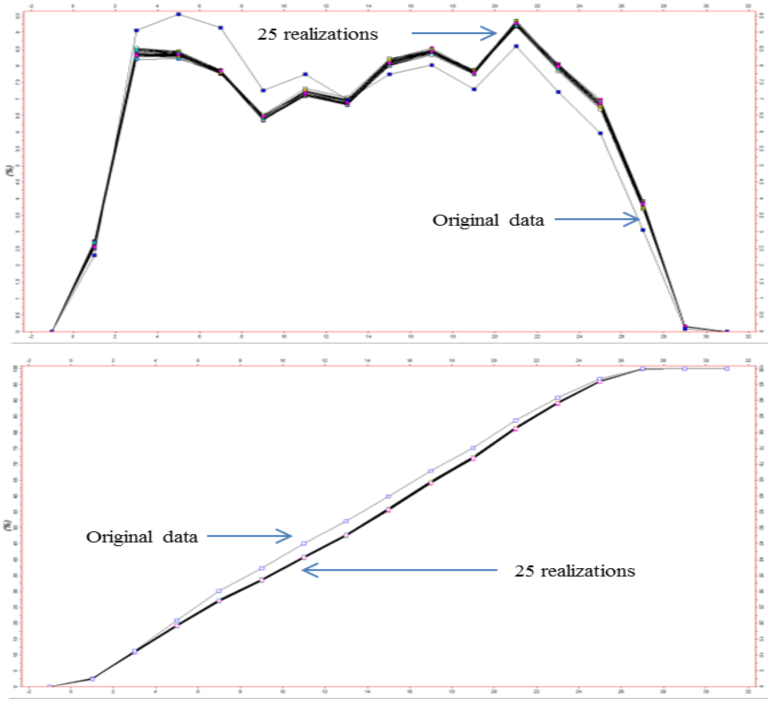

Figure 5.56 The histogram (upper) and CDF (lower) of the porosity realizations.

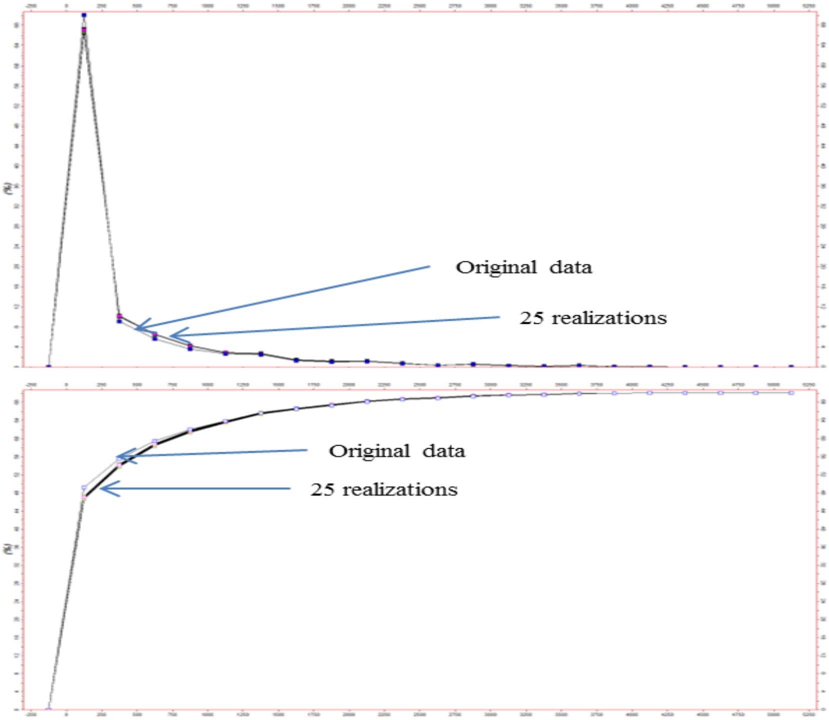

Figure 5.57 The histogram (upper) and CDF (lower) of the permeability realizations.

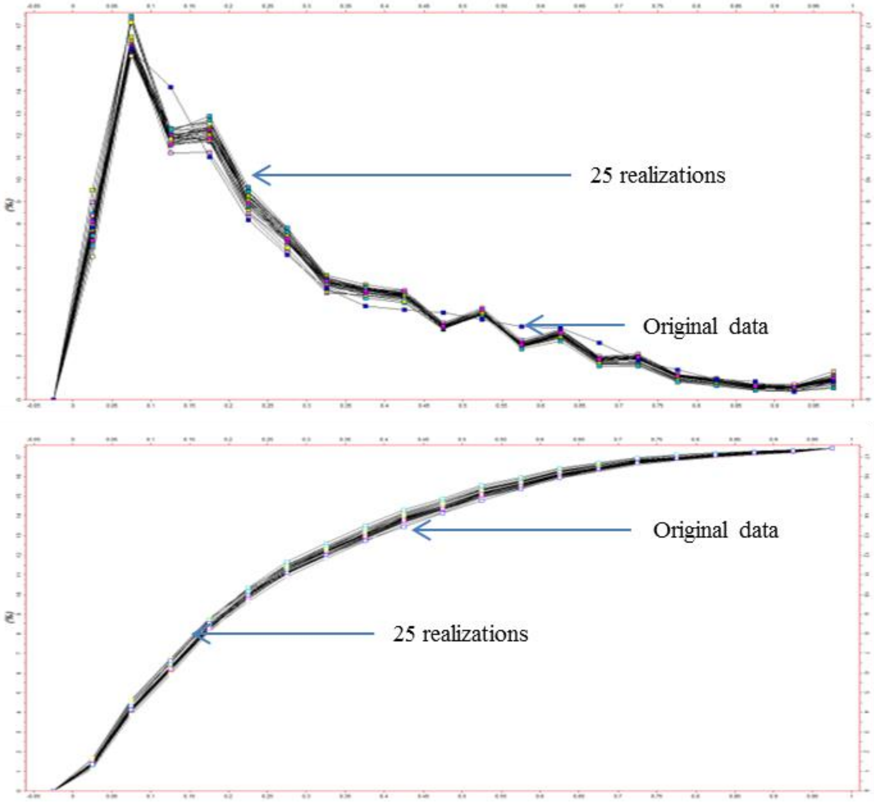

Figure 5.58 The histogram (upper) and CDF (lower) of the water saturation realizations.

Table 5.8 Mean and variance of the 25 realizations generated for each of the three petrophysical parameters.

Realizations	Porosity		Permeability		Water Saturation	
	Mean	Variance	Mean	Variance	Mean	Variance
Rel. # 1	14.22	55.57	364	404801	27.73	4.63
Rel. # 2	14.20	56.37	366	411307	27.81	4.79
Rel. # 3	14.22	56.03	365	403626	27.63	4.79
Rel. # 4	14.27	56.12	365	404546	28.20	5.01
Rel. # 5	14.27	55.93	373	420481	26.75	4.54
Rel. # 6	14.25	56.17	366	409023	27.76	4.90
Rel. # 7	14.19	56.18	360	396467	27.16	4.89
Rel. # 8	14.16	56.18	360	398723	26.63	4.47
Rel. # 9	14.15	55.72	366	406693	27.33	4.45
Rel. # 10	14.17	56.18	365	405662	28.02	4.93
Rel. # 11	14.22	55.80	366	409961	28.15	4.90
Rel. # 12	14.19	56.44	358	392826	27.50	4.57
Rel. # 13	14.24	56.15	368	412453	27.53	4.79
Rel. # 14	14.20	55.79	361	397866	27.83	4.87
Rel. # 15	14.20	56.15	372	419200	26.89	4.88
Rel. # 16	14.24	56.47	364	406528	27.66	4.72
Rel. # 17	14.20	55.83	360	398074	26.77	4.23
Rel. # 18	14.19	56.30	364	404935	27.20	4.60
Rel. # 19	14.21	55.74	365	405367	28.57	5.13
Rel. # 20	14.20	56.63	365	409011	27.84	4.92
Rel. # 21	14.16	55.44	362	400201	28.66	5.07
Rel. # 22	14.23	56.20	367	410204	28.06	4.92
Rel. # 23	14.17	56.06	362	402211	26.18	4.17
Rel. # 24	14.21	55.57	368	409434	27.79	4.84
Rel. # 25	13.6	64.6	359.97	558237	28.36	5.00

CHAPTER 6

Conclusions and Recommendations

6.1 Conclusions

This study presents a comprehensive lithofacies and petrophysical integration and modeling of the Bentiu-1 reservoir interval formally known as the Upper Bentiu Member. This study provided a high-resolution 3-D geocellular model of thick sandstone sequences of this interval. These 3-D structurally-based stochastic models were deemed to delineate the lithological and petrophysical heterogeneity that develop within the complex structural and stratigraphic settings of the Muglad Rift Basin. The following paragraph summarizes the results and findings of this study.

Three main lithofacies were determined from the investigation of the cores recovered from two wells; X-2 and X-3. A medium to coarse-grained sandstone lithofacies that is sub-lithic arenite in composition and often found with light-brown oil stains. A fine to silty sandstone lithofacies composed predominantly of fine grained sandstone, sub-felsic arenite to arenite in composition and occasionally characterized by light-brown oil staining. A Shale/Claystone lithofacies that is arenite in composition with argillaceous matrix with no visible oil staining. However, due to the lack of core coverage, the electro-facies concept adopted to generate a discrete log describing the lithofacies from the 20 wells available for this study. Accordingly, the cluster analysis-based module was utilized to ease this lithofacies log generation. Subsequently, three electro-facies were determined from this process by integrating the responses of six logging curves; gamma ray, shale volume, photo electric cross-section, density porosity, neutron porosity and deep resistivity logs. These three electro-facies are: the sand electro-facies, shaly sand electro-facies and shale electro-facies. Moreover, the three electro-facies determined according to the cluster analogue-based module were correlated to the three lithofacies inferred from the core examination by comparing the log responses of the six logging curves. Accordingly, the sand electro-facies corresponded to the medium to coarse grained sandstones facies, shaly sand-electro facies to the fine to silty grained sandstones and the shale electro-facies to the shale/claystone lithofacies.

Three petrophysical parameters were calculated in this study, these are the porosity, permeability and water saturation. The porosity was taken as the average of the four porosities calculated from the density porosity, Neutron porosity, sonic porosity and a combination of Neutron-Density porosity. The permeability was determined based on a pre-defined relationship acquired from the core analysis reports. The water saturation was calculated based on a modified Indonesian equation.

The porosity values within the Bentiu-1 interval were found ranging between 0.01 and 30% with the average of 13.6%. The higher porosities were found in the sand lithofacies and the lowest within shale lithofacies with 20% and 7%, respectively. The permeability values range between 0.18 mD and 7.4 D with an average of 360 mD. The highest permeability values were found within the sand lithofacies with average of 737 mD and the lowest within shale lithofacies with average of 48 mD. The water saturation in the Bentiu-1 reservoir interval ranges between 0 and 100% with 28.4% on average. Not surprisingly, the highest water saturation was found within the shale lithofacies with average of 51% and the lowest within the sand lithofacies with average of 15%.

A 3-D structural model (framework) was built based on the interpretation of a cropped 3-D seismic cube. This seismic cube was interpreted for the top and bottom of bounding horizons and the main faults that affect the Bentiu-1 reservoir interval. Moreover, six faults have been determined with direct impact on this reservoir interval under consideration. One major fault with the north-south strike that marks the western boundary of the area and five minor faults intersect the area with north-west strike. The lateral resolution acquired from the 3-D seismic survey was (15x80 m). The vertical resolution is chosen to be as close as possible to the well log resolution based on the above. The fault model was built and this model will be used as structural framework to limit and bound the stochastic modeling.

A comprehensive stochastic modeling workflow was used in this study to model the lithofacies and the three petrophysical parameters. The data were first tested for their normality and transformed where appropriate. Two main transformation techniques were used in this study: normal score transformation and logarithmic transformation. The normal score transformation was used for the porosity and water saturation, and the logarithmic transformation was used for the permeability data. The spatial variability of the lithofacies and petrophysical properties was investigated by means of semivariogram. The indicator semivariogram model for the lithofacies indicates a good lateral continuity. However, the indicator semivariogram in the vertical direction displays a periodic behavior. This periodic behavior can be directly related to deposition, lateral channel migration and the vertical stacking. The semivariograms of the three petrophysical properties revealed an alternative good to poor lateral continuity especially where the semivariogram model barely fits the data pairs. However, the smivariograms in the vertical direction showed similar periodic behavior observed in the lithofacies semivariograms. This behavior can be attributed to the difference in petrophysical properties between the three lithofacies and within each of these lithofacies.

The indicator and ordinary kriging interpolation techniques were used to estimate the lithofacies and their properties between the wells. The lithofacies 3-D interpolation showed a good lateral continuity and a distinctive vertical stacking pattern. Four lithological fining upwards units can be observed. Each of these units dominated by sands at the bottom and capped with shales at the top. The interpolation of the three petrophysical parameters generally follows the same spatial and vertical distribution. A distinctive flow or petrophysical units were observed from the interpolation that can be easily correlated to the four lithological units. In each lithological unit where the sand dominates, high porosity, high permeability and low water saturation prevail. However, where the shale lithologies dominate, low porosity, low permeability and high water saturation prevail.

Two main stochastic simulation techniques were used in this study to model the lithofacies and their petrophysical properties. Sequential Indicator Simulation (SIS) was used for lithofacies modeling and Sequential Gaussian Simulation (SGS) for petrophysical properties modeling. Accordingly, 25 equi-probable realizations were generated for the lithofacies, porosity, permeability and water saturation. The results of the SIS improved the smoothing effect observed earlier in the kriging interpolation. The lithological heterogeneity observed in the lithology simulation is emphasized by the sand-shale interaction laterally and vertically. Moreover, the mild curvatures observed in the lithofacies model indicate a deposition in low sinuosity streams which is confirmed by previous studies.

The simulation results for the lithofacies and their petrophysical properties were validated in a qualitative and quantitative manner. Based on this validation, 12 lithofacies realizations were accepted ad 13 were rejected. The realization of the porosity, permeability and water saturation were ranked based on their validation and simulation adequacy. The ranking was deemed to determine the best and the worst case scenarios of the realizations.

6.2 Recommendations

The following recommendations are made for the future modeling studies in the same reservoirs interval.

1. To increase the accuracy of the lithofacies and the petrophysical properties evaluation, it is essential to have more core data. The permeability data in this study was calculated based on the predefined relationship between the porosity and permeability as pointed out earlier. This relation may overestimate or underestimate the real permeability since it is only a function of porosity. Accordingly, the availability of more core-permeability data can reduce the uncertainty in the permeability calculations.
2. The periodic behavior observed in the vertical semivariograms can be better accounted for if the vertical interval subdivided into a number of stratigraphic subzones. This subdivision will allow the calculation of the semivariogram for each zone separately. Moreover, the availability of more wells in the study area can improve the

semivariogram model fitting especially in the major and minor direction in the shaly-sand lithofacies and its petrophysical properties.

3. The smoothing effect especially observed on kriged estimates at the rims of the study area and away from the well control points can be reduced through a number of methods. One of these methods is utilizing the co-kriging technique to link the lithofacies and the petrophysical parameters to the acoustic impedance or other seismic attributes. Another method is by adding more data especially at the rims of the study area when available.
4. Two methods have been used in this study for stochastic simulation: SIS and SGS. However, other simulation algorithms can be adopted to improve the results. The application of the Object-Based Modeling (OBM) can enhance the finding of the study since the area has been subjected to a fluvio-lacustrine deposition. Moreover, training images drawn from a recent deposition environment can be used for the 3-D simulation of the lithofacies through Multi-Points Geostatistics (MPS).
5. The modeling results can be further quantitatively validated through the history matching. In this process, the simulation results will be adjusted in a stepwise manner to firmly reproduce the past behavior of a reservoir. This approach depends mainly on the production data and the quality of the reservoir model.

References

Abdullatif O. M., (1992). Sedimentological Investigation of Cretaceous, north margin of Muglad basin. Unpublished report.

Abdullatif O. M., (2002). Burial Diagenesis and Thermal Maturity Evaluation of The North West Muglad Rift Basin, Sudan, AAPG conference. Cairo 2002: Ancient Oil-New Energy.

Ahmed H. B. M., (1994). A Palynological Investigation of the Lower Section of the Abanus No. 1 Well; Muglad Basin, South Central Sudan. Unpublished M. Phil. Thesis, University of Sheffield. 185 pp

Al-Qassab, H. M., & Heine, C. J. (1998). A Geostatistical Approach to Attribute Interpolation Using Facies Templates, and Advanced Technique in Reservoir Characterization. Saudi Aramco Journal of Technology, 54–66.

Ataei, M., (2012). Log Facies Evaluation and Property Modelling of a Turbidite Reservoir, the Gulf of Mexico, Master Thesis, NTNU, Norway

Babiker M. E., (1993). Basin evolution and sedimentry facies with reference to the petroleum exploration in Muglad Basin. M. Sc, University of Portsmouth U.K

Bohling, G., 2005. Introduction to Geostatistics and Variogram Analysis., pp.1–20.

Browne, S.E. and Fairhead, J.D. (1983). Gravity Study of the Central African Rift System: a Model of Continental Disruption. 1. The Ngaoundere and Abu Gabra rifts. In: P. Morgan (Editor), Processes of Continental Rifting. Tectonophysics, 94: 187-203.

Corbett, P. W. M. And Jensen, J. L., (1992). Estimating mean permeability: how many measurements do we need? First Break, 10, (3), 89-94.

Damsleth, E., C Harlote, B. T. & Haldorsen. H. H. (1992). A Two-Stage Stochastic Model Applied to a North Sea Reservoir. The 1990 SPE Annual Technical Confer-Ence and Exhibition Held in New Orleans, (April), 402–486.

Deutsch, C.V., 2002. Geostatistical Reservoir Modeling. New York: Oxford University Press, 376p

Dou Lirong, Cheng Dingsheng and Zhang Zhiwei, (2002). Division of petroleum systems by using integrated geological and geochemical analyses. Chinese Journal of Geology, 37(4), 495-501 (in Chinese with English abstract).

Dou Lirong, Zhang Zhiwei & Cheng Dingsheng., (2006). Control of regional seal on oil accumulations in the Muglad Basin, Sudan. Acta Petrolei Sinica, 27(3), 22-26.

Dou Lirong., Dingsheng, C., Zhi, L., Zhiwei, Z., & Jingchun W., (2013). Petroleum Geology of The Fula Sub-Basin, Muglad Basin, Sudan Journal of Petroleum Geology, Vol. 36(1), January 2013, pp 43 – 60

Eltom, H. A. (2007). Sedimentology and Sequence Stratigraphy of fluviallacustrine, Mesozoic, Abu Gabra and Bentiu formations, Muglad rift basin, Sudan. M.Sc.Thesis, KFUPM (Saudi Arabia).

Fairhead, J. D. (1988). Mesozoic Plate Tectonic Reconstructions of the Central South Atlantic Ocean: The Role of the West and Central African Rift System. Tectonophysics, 155(1), 181-191.

Giedt, N. R., (1990). Unity Field, Muglad Rift Basin, Upper Nile Province. In: Beaumont, E.A., Foster, N.H. (ed), Structural Traps; III, Tectonic Fold and Fault Traps, American Association of Petroleum Geologists Treatise of Petroleum Geology, Atlas of Oil and Gas Fields, A-019, 177-197.

Goovaerts, P., (1997). Geostatistics for natural resources evaluation: Oxford Univ. Press, New York, 483 p.

Gringarten, E, and C V Deutsch. 2001. “Variogram interpretation and modeling.” Mathematical Geology 33(4): 507–534.Lloyd. 2011

Guiraud, R. and. Maurin, J.C., (1992). Early Cretaceous rift of Western and Central Africa: An Overview. Tectonophysics, 213, 153-168

Haldorsen, H, Damsleth E., (1990). Stochastic modeling. Journal of Petroleum Technology, 42: 404–412.

Hewang, R. J., Ahmed, A. S., & Moldowan, J. M. (1994). Oil Composition Variation and Reservoir Continuity: Unity Field, Sudan. Org. Geochem., 21(2), 171-188.

Holden L, Hauge R,. & Skare O., (1998). Modeling of fluvial reservoirs with object models. Mathematical Geology, 30: 473–496.

Hussein, R. A. M., (2012). Sequence Stratigraphy and Sedimentary Facies of Fula Sub-basin, Muglad Basin (Sudan), Journal of Science and Technology vol. 13.

Idriss K. (2002). Lateral Seal- a Major Exploration Risk in the Faulted Traps of the Cretaceous Petroleum System - Central Muglad Basin, Sudan 2004. AAPG International Conference and Exhibition.

Idriss K. (2005). An Integrated Petroleum System Study for the Aradeiba and Bentiu Plays, Block 4 Central Muglad Basin, Sudan 2005. AAPG International Conference and Exhibition.

Isaaks, E., & Srivastava, R. M., (1989). An introduction to applied geostatistics: Oxford Univ. Press, New York, 561 p

Journel A G., (1977a). The abuse of principles in model building and the quest for objectivity. In: Baffi E, Shofield N (eds.), Geostatistics-Wollongong. Dordrecht: Kluwer Academic Publ., 1: 3–24.

Journel A G., (1977b). Deterministic geostatistics: a new visit. In: Baffi E, Shofield N (eds.), Geostatistics-Wollongong. Dordrecht: Kluwer Academic Publ., 1: 174–187.

Journel, A. G., & Stanford, U. (1990). SPE 20750 Geostatistics for Reservoir Characterization. In the 65th Annual Technical Conference and Exhibition of the Society of Petroleum Engineers held in New Orleans, LA, (pp. 353–358).

Journel, A. G., and Huijbregts, C. J., (1978). Mining geostatistics: Academic Press, London, 600 p.

Kaska, H. V. (1989). A spore and pollen zonation of Early Cretaceous to Tertiary non-marine sediments of central Sudan. Palynology, 13(1), 79-90.

Krige, D. G., (1951). A statistical approach to some mine valuations and allied problems at thewitwatersand. Master's Thesis. South Africa: University of Witwatersand.

Krige, D., (1999). Conditional bias and uncertainty of estimation in geostatistics: 1999 APCOM Intern. Symp., Soc. Of Mining Engineers, Golden, Colorado, p. 3–14.

Kumar, B. and Kishore, M. (2006). Electrofacies classification- a critical approach, 6th International Conference and Exposition on Petroleum Geophysics, Kolkata, 822-825Davis, 2002

Leuangthong, O., McLennan, J. a., & Deutsch, C. V. (2004). Minimum Acceptance Criteria for Geostatistical Realizations. Natural Resources Research, 13(3), 131–141.

Lilliefors, H. W. (1967), On the Kolgomorov- Smirnov test for normality with mean and variance unknown, J. Am. Stat. Assoc., Vol. 62, pp. 399-401. Kolgomorov-Smirnov test for normality with parameters estimated from the same sample.

Mann, D. C. (1989). Thick-skin and thin-skin detachment faults in continental Sudanese rift basins. Journal of African Earth Sciences (and the Middle East), 8(2), 307-322.

Matheron G., (1962). Traité de géostatistique appliquée. Volume 2, Technip, Paris.

Matheron G., (1965). Les variables régionalisées et leur estimation. Doctoral Thesis. Masson, Paris.

Matheron G., (1973). The intrinsic random functions and their application. Advances in Applied Probability5: 439–468.

Mc Hargue T. R., Heidrick J. L., Livingstone J. E. (1992). Tectonostratigraphic development of the interior Sudan rifts, Central Africa. Tectonophysics 213, 187– 202.

Mohamed, A. Y., Ashcroft, W. A., & Whiteman, A. J. (2001). Structural development and crustal stretching in the Muglad Basin, southern Sudan. Journal of African Earth Sciences, 32(2), 179-191.

Mohamed, A. Y., Pearson, M. J., Ashcroft, W. A., & Whiteman, A. J. (2002). Petroleum maturation modeling, Abu Gabra–Sharaf area, Muglad Basin, Sudan. Journal of African Earth Sciences, 35(2), 331-344.

Mohamed, A. Y., Pearson, M. J., Ashcroft, W. A., Iliffe, J. E., & Whiteman, A. J. (1999). Modeling Petroleum Generation in the Southern Muglad Rift Basin, Sudan. AAPG Bulletin, 83(12), 1943–1964.

Mohammed, A. & Mohammed, M.S., (2008). Stratigraphy and Tectonic Evolution of the Oil Producing Horizons of Muglad Basin, Sudan. Journal of Science and Technology, 9(1), pp.1–8.

Mohammed, A. A. (2006). Enhancement of OIP through Reservoir Modeling of a Multilayered Siliciclastic Reservoir: A Case Study from Muglad Basin, Sudan. Geo 2006 Conference, Manama, Bahrain.

Morelon, I. F., Doligez, B., Guerillot, D. R., Rahon, D., & Touffait, Y. (1991). An Application of a 3D Geostatistical Imaging to Reservoir Fluid Flow Simulations. In the Sixth SPE Petroleum Computer Conference held in Dallas, Texas (pp. 223–231). Society of Petroleum Engineers.

Moulin, M., Aslanian, D., and Untenehr, P., (2010). A new starting point for the South and Equatorial Atlantic Ocean. Earth Science Review, 98, 1-37.

Mustafa, A. A., & Tyson, R. V. (2002). Organic Facies of Early Cretaceous Synrift Lacustrine Source Rocks from the Muglad Basin, Sudan. Journal of Petroleum Geology, 25(3), 351-366.

Oluseyi, E., Osemoahu, O., Uchenna, O., & Ugochukwu, A. (2013). Insights from the 3D Modeling of a Densely Faulted , Stacked Reservoir System. In the Nigeria Annual International Conference and Exhibition held in Lagos, Nigeria (SPE 167558) (pp. 1–9).

Petroenergy E&P (2006), Unpublished report

Poupon, A., & Leveaux, J. (1971). Evaluation of water saturation in shaly formations. The Log Analyst, 11, 3-8.

Poupon, A., and Gaymard, R. (1970). The evaluation of clay content from logs. Trans., SPWLA 11th Annu. Logging Symp., Pap. G..

Sahin, A. and A. Aboukhodair, (1988). Geostatistical Approach in Design of Sampling Pattern for Jabal Sayid Sulfide Deposits, Western Saudi Arabia. Journal od African Earth Sciences. Vol. 7, No. 4, pp, 679-690.

Sahin, A. and Al-Salem, A. A. (2001). Stochastic Modeling of Porosity Distribution in a Multi-Zonal Carbonate Reservoir. SPE 68113 Middle East Oil Show, Bahrain

Sahin, A. and Saner, S. (2001). Statistical distributions and correlations of petrophysical parameters in the eastern Saudi Arabia. Journal of Petroleum Geology, vo1.24(1), pp 101-114.

Saida, O. Mohammed and Abdullatif O. M. (2002). Facies and Reservoir Quality of Zarqa Formation (Turonian-Late Senonian) in Heglig and Unity Fields, Muglad Rift Basin. AAPG conference Cairo 2002: Ancient Oil-New Energy

Saner, S. and Sahin, A., 1999. Lithological and zonal porosity-permeability distributions in the Arab-D reservoir, Uthmaniyah field, Saudi Arabia. AAPG Bul., 83, (2), 230-243.

Schlumberger (1987). Log Interpretation Principle/ Application, New York

Schull T. J., 1988, Rift basins of interior Sudan: petroleum exploration and discovery. AAPG Bull., 72, 1128-1142.

Serra, O. and Abbott., H. T. (1980). The contribution of logging data to sedimentary and stratigraphic, Paper SPE 9270, 55th Annual Fall Technical Conference and Exhibition, Dallas Texas, 19pp.Vail (1978)

Shauib, M. A., (2013). Seismic Attributes and Petrophysical Modelling of the Aradeiba-D Member, Muglad Rift Basin, Sudan, Master thesis. KFUPM, Saudi Arabia

Tong X., Dou Lirong, Tian, Z., PAN X., & Zhu X., (2004). Geological Mode and Hydrocarbon Accumulating Mode in Muglad Passive Rift Basin, Sudan. Acta Petrolei Sinica, 25(1), 19-24.

Trivedi K. B,, Idris K. Eltayeb M., (2005). Porosity versus Depth: A Case Study from Neem Field of Muglad Basin, Sudan, Africa2005. AAPG International Conference and Exhibition

Wilson, M. and Guiraud, R., (1992). Magmatism and rifting in Western and Central Africa, from Late Jurassic to recent times. Tectonophycics, 213, 203-225.

Wycisk, P., Klitzsch, E., Jas, C. and Reynolds, O., (1990). Intracratonal sequence development and structural control of Phanerozoic strata in Sudan. Berl. Geowiss. Abh.,

Yamin, Z. & Qin, G., (2011). Petroleum System of the Fula Depression at the Muglad Basin in the Central African Fault Zone, Journal of Earth Science, Vol. 22, No. 3, p. 363–370.

Yu, Y. X., Tang, L. J., & Yin, J. Y., (2009). Tectonic and Hydrocarbon Accumulation Elements Characteristics of the Tethyan Realm in South China. Acta Geologica Sinica, 83(6): 1214–1223

Vitae

Name	Mohammed Ali Hammad Jabir
Nationality	Sudanese
Date of Birth	6/ April/1986
Email	mjabir@uofk.edu
Address	Department of Geology, University of Khartoum
Academic Background	Bachelor of Sciences in Geology
Research Interests	My research interests revolve around the reservoirs characterization, modeling and simulation through the geostatistical approaches and the different ways of reducing the uncertainties emerges from these approaches.

Publications:

Jabir M., Sahin A., Abdullatif O., Korvin G., Makkawi M., and Kaka I. (2015). High-Resolution stochastic mapping of the lithofacies within late cretaceous Upper Bentiu Member, Muglad Rift Basin, Sudan. Submitted to the Geo2016 Conference in Bahrain.

Jabir, M. and Abdullatif, O. (2015) Artificial intelligence based approach towards accurate facies determination; a case of Late-Cretaceous Upper Bentiu Member of NW Muglad Basin. Presented at the 11th International Conference for Geoscience (SSG), Riyadh.